공학박사 학위논문

Enzyme-Mimetic Carbon-based Catalysts for Photoelectrochemical Water Splitting

생체 촉매를 모방한 탄소기반의 광전기화학 물분해 촉매 연구

2016년 2월

서울대학교 대학원

재료공학부

심 욱

Abstract

Enzyme-Mimetic Carbon-based Catalysts for Photoelectrochemical Water Splitting

Uk Sim
Department of Materials Science and Engineering
College of Engineering
Seoul National University

The development of efficient catalysts represents one of the most important and challenging issues for the electrochemical hydrogen production. Learning from the biomolecular catalysts such as an enzyme or photosystem in nature provides clues to resolve the related kinetic issues. For example, hydrogenase, which occurs in bacteria, archaea, and some eukarya, catalyzes a proton into a hydrogen evolution reaction (HER) with high activity very near the thermodynamic efficiency limit. The reaction takes place at a specialized metal active center. Functional protein assemblies surrounding a metal active site act as ligands for the metals, pockets for the catalytic reaction, and pathways for reactants and products. Inspired by biomolecular system, we have designed enzyme-mimetic carbon-based catalysts for HER and investigated the effect of each component with a systematic approach.

As the simplest model carbon-based platform, 2D monolayer graphene was chosen as a HER catalyst. Graphene possesses excellent transmittance and superior intrinsic carrier mobility. For the first time, we have investigated

new possibilities of monolayer graphene as the efficient HER catalyst. The catalytic activity can be further enhanced by generating more active sites. Treatment with N_2 plasma also induces N doping and abundant defects. The catalyst exhibits a lower Tafel slope (45 mV/decade) and a higher exchange current density (7.1×10^{-5} mA/cm^2) than those of other previously reported carbon-based HER catalysts, indicating performance comparable to that of Pt catalyst. Based on the electrochemical analysis, the active sites of the N-doped graphene have been identified and quantified.

As an intermediate stage of extension from the single 2D platform to a complicate 3D structure, we have transferred graphene layer-by-layer as a well-defined model of the pseudo-3D system and investigated the layer dependence of catalytic activity. Comprehensive electrochemical analysis shows that there is an optimized structure of stacked graphene for the best catalytic activity and the highest charge transfer rate. Based on the understanding of the optimized carbon platform, metal active sites have been incorporated with high controllability and tunability. Moreover, another type of the biomimetic carbon-based nanosheets is addressed as a new HER catalyst.

Our synthetic bioinspired HER catalysts are also highly transparent and are applicable to the co-catalyst for the Si photoelectrochemical (PEC) cell. The results indicate the applied bias photon-to-current efficiency of 2.29%, which is higher than that of any other carbon-based PEC catalysts reported to date. Controlling surface structure of the light-absorbing photoelectrode and the deposition of the co-catalyst represent a significant step toward enhancing the hydrogen production.

Keywords: photoelectrochemical cell, silicon, carbon, catalyst, bioinspired, water splitting, hydrogen production

Student Number: 2011-30188

Contents

List of Tables

List of Figures

Chapter 1. Introduction

1.1 Demand for hydrogen energy as sustainable energy source

Development of sustainable energy sources is an urgent issue in the future due to the amount of energy consumption.[1.1-1.3] The world energy consumption rate is projected to double from 13.5 TW in 2001 to 27 TW by 2050 and to triple to 43 TW by 2100.[1.4] At present, energy sources, such as coal and oil, can provide sufficient energy to humankind. However, renewable and sustainable energy sources must be developed for our future because present energy sources have several disadvantages. Carbon dioxide gas is emitted when coal and oil are burned because their main component, carbon, combines with oxygen in the air. 1 kg of coal emits 2.31 kg of CO_2 and 1 gallon of gasoline emits 8.9 kg of CO_2.[1.5-1.9] Because high CO_2 concentrations accompany high average temperature of the earth,[1.10] CO_2 emission should be inhibited. In addition to this, severe energy depletion will occur unless renewable and sustainable energy is developed because deposits of fossil fuel are limited. Thus, many researchers have been trying to develop sustainable energy sources, such as solar, wind, biomass, biofuel, geothermal and hydrogen.

Among the various types of sustainable energy, hydrogen is the most common element that can be used as an energy source for fuel cells. Hydrogen is an ideal fuel source because when it is used, by-products are water, heat and electricity without CO_2 emission. Hydrogen is also non-toxic while nuclear energy, coal, and gasoline are all either toxic or hazardous to the environment. Moreover, hydrogen energy is a very efficient fuel source compared to traditional sources of energy (Figure 1.1). It has a high energy density of 142 kJ/g while gasoline has an energy density of 46 kJ/g and natural gas has an energy density of 47.2 kJ/g (Figure 1.2).[1.11] Unlike non-renewable sources of energy, hydrogen energy can be produced on demand

(Figure 1.3 and Figure 1.4).

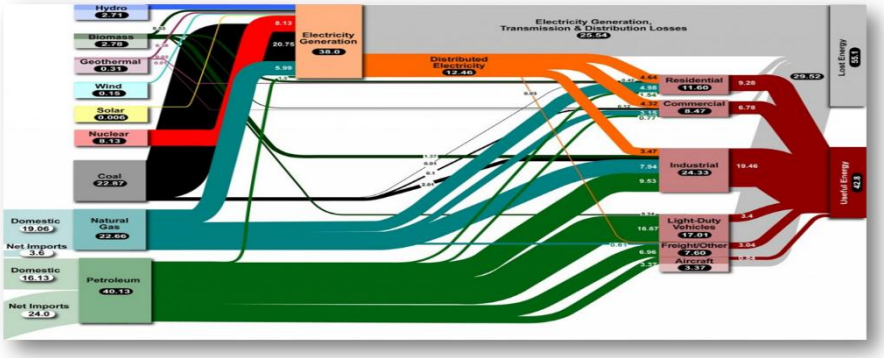

Figure 1.1. Spaghetti diagram showing the portion of the each energy which is produced, transported, and dissipated.

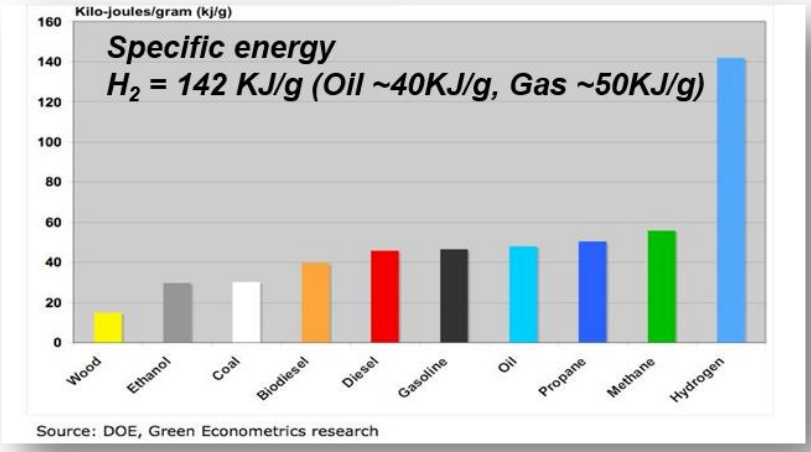

Figure 1.2. Specific energy diagram of hydrogen and fossil fuel sources.

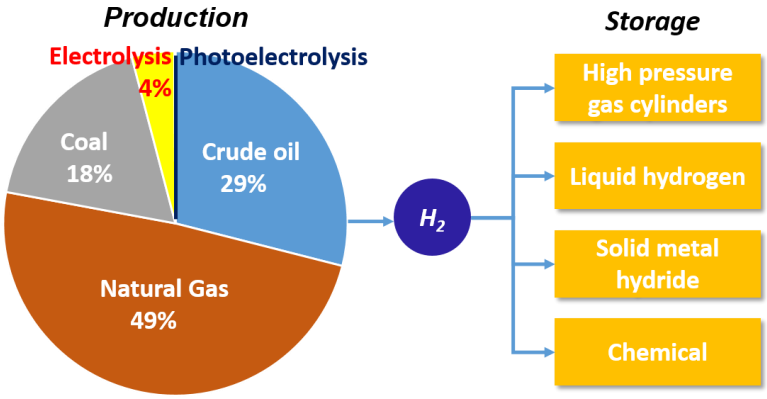

Figure 1.3. Sources of hydrogen production and the kinds of hydrogen storage.

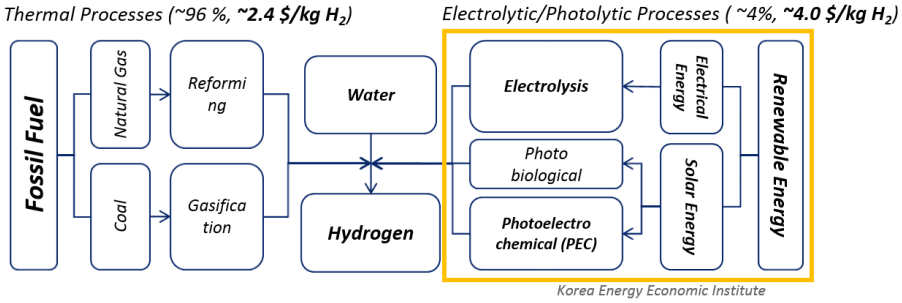

Figure 1.4. The methods of hydrogen production: thermal processes, electrolytic, and photolytic processes.

1.2 Demand for water splitting reaction catalyst

Hydrogen production using solar energy is an important energy and environmental issue. The development of efficient photoelectrodes and related co-catalyst for water splitting is one of the fundamental challenges in hydrogen production. Considering the thermodynamic potential, a single-component semiconductor that possesses a higher band gap than 1.23V can generate hydrogen and oxygen gas from water simultaneously as long as its conduction and valence bands are in their proper positions. However, overall water splitting by one single-component semiconductor is usually limited by the kinetic overpotential. Until now, the maximum solar-to-hydrogen conversion efficiency using single-component semiconductor still does not exceed 5%.[1.12] Because of such inherent weakness of one-component approaches, many developments have been made in photoelectrochemical cells that have separate cathode and anode and are easily implementable in terms of tunability and efficiency. Moreover, efficient co-catalysts for water splitting also represent one of the most important and challenging issues for the implementation of photoelectrochemical hydrogen production (Figure 1.5). A critical requirement for outstanding catalysts in a photoelectrochemical cell is not only the ability to boost the kinetics of a chemical reaction but also durability against electrochemical and photoinduced degradation.

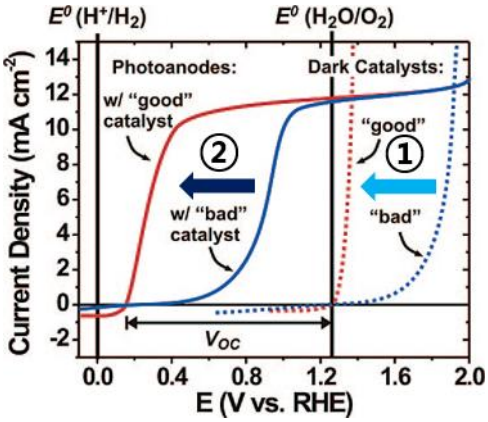

Figure 1.5. The example of current density vs. applied potential plot of photoanode under illumination or dark state. The effect of co-catalyst on the photoelectrode.

1.3 Lessons from natural enzyme

Lessons from the biomolecular catalysts such as an enzyme or photosystem in nature provides clues to resolve the related kinetic issues. Biological systems, with their ability to create materials with precisely defined architecture in nanoscale, offer an unprecedented approach in dealing with this problem. (Figure 1.6) For example, hydrogenase, which occurs in bacteria, archaea, and some eukarya, catalyzes a proton into HER with high activity very near the thermodynamic efficiency limit. Functional protein assemblies surrounding a metal active site act as ligands for the metals, pockets for the catalytic reaction, and pathways for reactants and products. Another example, in photosystem II of plant chloroplasts, manganese calcium clusters are stabilized and surrounded by specific peptides. These complexes exhibit unique electrochemical properties that is not achievable in synthetic manganese calcium crystals alone. Inspired by biomolecular system, we have designed enzyme-mimetic carbon-based catalyst for HER and investigated the

effect of each component with a systematic approach.

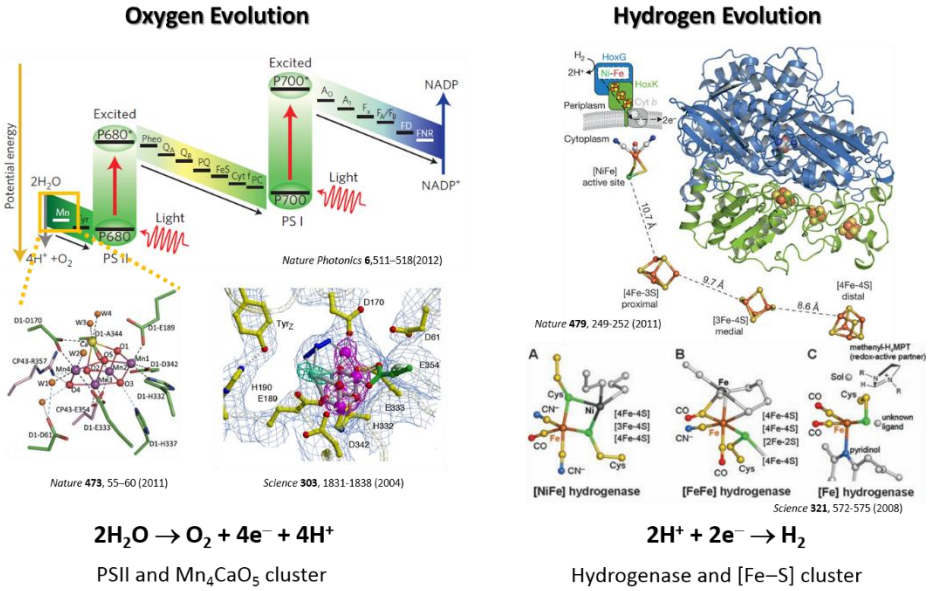

Figure 1.6. Representative natural enzymes: photosystem II and hydrogenase.

1.4 Objective of the thesis

The aim of the thesis is the development of efficient hydrogen evolution reaction catalyst in photoelectrochemical water splitting. Development of sustainable energy sources is an urgent issue to meet growing demand in world energy consumption. Among the various types of sustainable energy, hydrogen is the most promising renewable energy source with a high energy density. The discovery of efficient catalysts represents one of the most important and challenging issues for the implementation of PEC hydrogen production. A critical requirement for outstanding catalysts in a PEC cell is not only an ability to boost the kinetics of a chemical reaction but also a durability against electrochemical and photo-induced degradation. Generally, precious metals, such as platinum, exhibit superior performance in these requirements; however, high cost of the precious metal is the biggest barrier to

widespread commercial use. To address this critical and long-standing technical barrier, we have focused on an intense search for efficient, durable, and inexpensive alternative catalysts. Our research have been concentrated on four subjects; (1) new possibilities of an atomic-scale catalyst as the efficient HER catalyst, (2) interface control between electrode and catalysts for lower activation energies and higher current density, (3) new type of the enzyme-mimetic carbon-based catalyst for greener and more environmentally benign approach, (4) the application to the co-catalysts for the PEC cell with high efficiency and long-term stability. We pioneered the field of the graphene-based catalyst for HER in PEC cell that have never been made before. Inspired by biomolecular approach, we also have made a breakthrough in the limit of recent photo-to-current efficiency through the incorporation of a non-noble transition metal into carbon-based catalysts.

Learning from the biomolecular catalysts such as an enzyme or photosystem in nature provides clues to resolve the related kinetic issues. For example, hydrogenase, which occurs in bacteria, archaea, and some eukarya, catalyzes a proton into the HER with high activity very near the thermodynamic efficiency limit. The reaction takes place at a specialized metal active center. Functional protein assemblies surrounding a metal active site act as ligands for the metals, pockets for the catalytic reaction, and pathways for reactants and products. Inspired by biomolecular system, we have designed enzyme-mimetic carbon-based catalyst for HER and investigated the effect of each component with a systematic approach.

In part I, as the simplest model carbon-based platform, 2D monolayer graphene is chosen as a HER catalyst. For the first time, we have investigated new possibilities of monolayer graphene as the efficient HER catalyst. The catalytic activity can be further enhanced by generating more active sites. Based on the electrochemical analysis, the active sites of the N-doped graphene have been identified and quantified. As an intermediate stage of

extension from the single 2D platform to a complicate 3D structure, we have stacked graphene layer-by-layer as a well-defined model of the pseudo-3D system and investigated the layer dependence of catalytic activity. Comprehensive electrochemical analysis shows that there is an optimized structure of stacked graphene for the best catalytic activity and the highest charge transfer rate. Based on the understanding of the optimized carbon platform, metal active sites have been incorporated with high controllability and tunability.

In part II, another type of the biomimetic carbon-based nanosheets has been addressed as a new HER catalyst. Carbon nanosheet is synthesized by polydopamine, which are natural adhesive proteins secreted by marine mussels. Based on the understanding about the synthesis of the biomimetic carbon platform, earth-abundant metal active sites have been incorporated with high controllability and tunability, which results in a further decrease in kinetic overpotential. Fe-doped carbon nanosheet exhibits better photoelectrochemical performance in terms of the applied bias photon-to-current efficiency than those of any other reported non-noble metal-based catalyst/p-Si system. This significant enhancement achieved in this study emphasizes the strategies for the application of bioinspired materials as the HER catalyst. Our bioinspired catalysts paradigm can revolutionize the catalyst materials that have traditionally made by alloying inorganic metal composite or have had little interest in surrounding carbon platform, opening the way to the design of atomic-scale controlled catalysts, materials inspired from biomolecular precursor approach, and learning design rules for interfacing semiconductor and catalysts.

Our synthetic bioinspired HER catalyst is also highly transparent and is applicable to the co-catalyst for the PEC cell. The results indicate the applied bias photon-to-current efficiency of 2.29%, which is higher than any other carbon-based PEC catalysts reported to date. In PEC cell system, negative

effects from metal-based catalysts should be considered: reflection by the overlaid catalyst, an unfavorable band structure such as a Schottky barrier, photocorrosion, and recombination sites at the interface. To design catalysts for PEC water splitting, the optical properties, stability, and interfacial issues must be comprehensively considered. Silicon, the most promising photocathode material for absorbing of large part of visible spectrum, precise controllability, and its abundancy, however, cannot durably operate in aqueous electrolyte because of surface oxidation. Thus, passivation of silicon surface is essential for the durable operation of the silicon photocathode in neutral water. Our transparent carbon catalysts on silicon acts as a passivation layer against surface oxidation without attenuating the photon incidence. Controlling a surface structure of the light-absorbing photoelectrode and the deposition with the co-catalyst also represent a significant step toward enhancing the hydrogen production. This transparent catalysts with a capability of passivation effect can result in a paradigm shift for catalytic materials research and discovery for energy application.

The significant meaning of this research is the construction of transparent catalyst that only consists of carbon materials and the possibility of extension to a variety of biomimetic HER catalysts with excellent activity. Scientifically, it provides an importance to understand the interactions at the solid/solution interface to exploit its amazing potential. The conducted research would advance my understanding how the carbon-based catalysts can alter the band structure of the electrode and its photo-electrochemical behaviors. This understanding would allow development of catalysts with unique and highly tunable properties with broad energy applications as well as the efficient solar-driven hydrogen production.

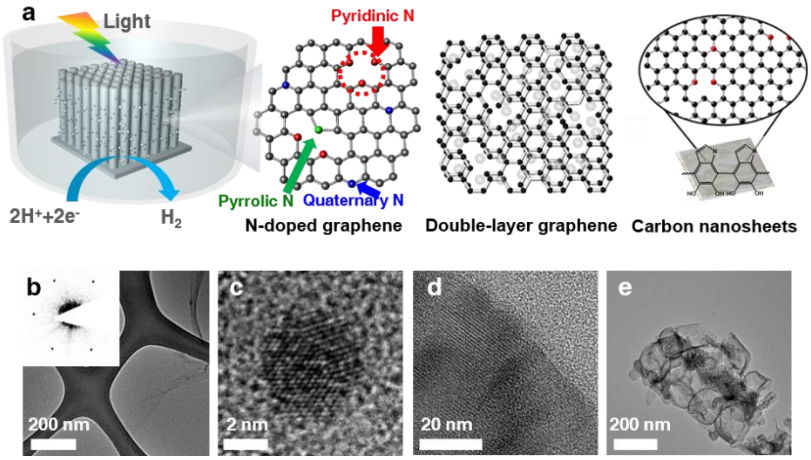

Figure 1.7. Carbon-based catalysts for efficient hydrogen evolution reaction. (a) Schematic of carbon-based catalysts on p-silicon photocathode. TEM images of (b) monolayer graphene grown by chemical vapor deposition, (c) N-doped graphene quantum sheets by N_2 plasma treatment, (d) carbon nanosheets inspired from marine adhesive proteins, and (e) Fe-incoporated carbon nanosheets.

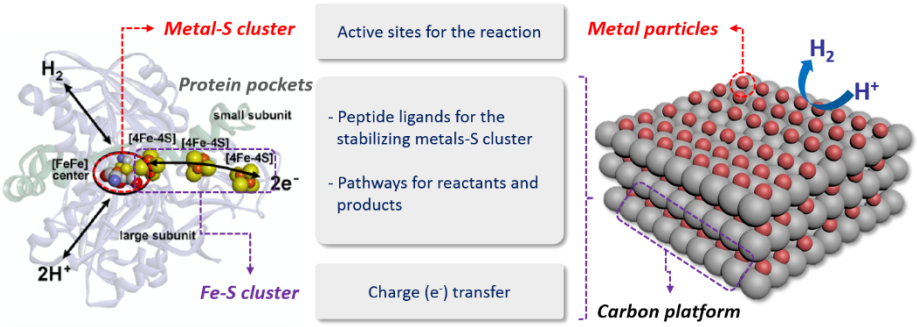

Figure 1.8. Schematic of model system study. Part 1: Study of carbon platform: From 2D monolayer graphene to pseudo-3D system of multi-layer of graphene and graphene quantum sheets. Part 2: Study of metal active sites: Synthetic bioinspired carbon-based catalyst.

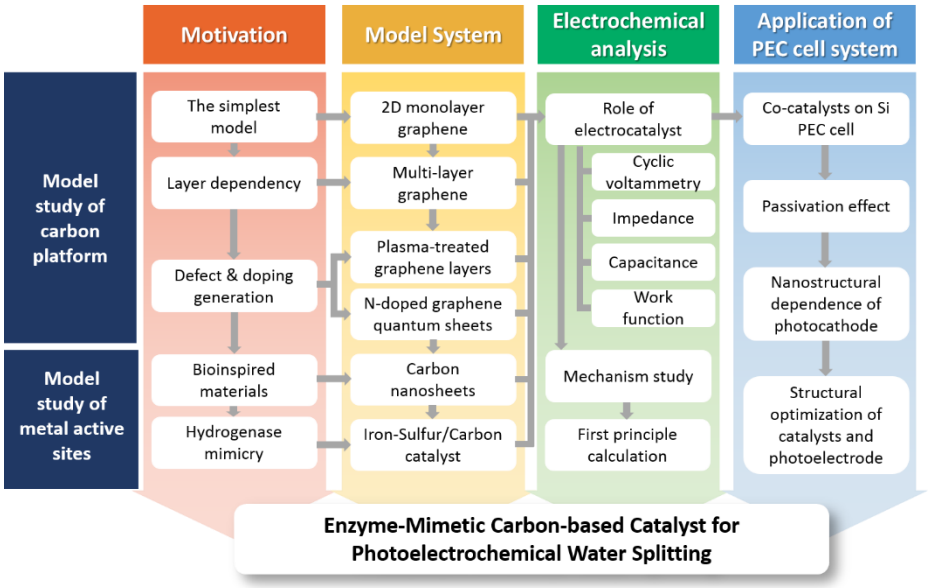

Figure 1.9. Research scheme of the thesis.

Bibliography

1.1. D. G. Nocera, *Daedalus* 2006, ***135***, 112-115;

1.2. N. S. Lewis, D. G. Nocera, *Proceedings of the National Academy of Sciences* 2006, ***103***, 15729-15735;

1.3. A. J. Esswein, D. G. Nocera, *Chemical reviews* 2007, ***107***, 4022-4047.

1.4. U. S. E. I. Administration., 2013.

1.5. P. M. Cox, R. A. Betts, C. D. Jones, S. A. Spall, I. J. Totterdell, *Nature* 2000, ***408***, 184-187;

1.6. J. R. Petit, J. Jouzel, D. Raynaud, N. I. Barkov, J. M. Barnola, I. Basile, M. Bender, J. Chappellaz, M. Davis, G. Delaygue, M. Delmotte, V. M. Kotlyakov, M. Legrand, V. Y. Lipenkov, C. Lorius, L. Pepin, C. Ritz, E. Saltzman, M. Stievenard, *Nature* 1999, ***399***, 429-436;

1.7. J. L. Sarmiento, C. Le Quéré, *Science* 1996, ***274***, 1346-1350;

1.8. S. Solomon, G.-K. Plattner, R. Knutti, P. Friedlingstein, *Proceedings of the National Academy of Sciences* 2009, ***106***, 1704-1709;

1.9. K. Caldeira, M. R. Rampino, *Geophysical Research Letters* 1991, ***18***, 987-990.

1.10. C. Ronneau, *Energie, pollution de l'air et developpement durable*, 2004.

1.11. L. M. Gandia, G. Arzamedi, P. M. Diéguez, *Renewable Hydrogen Technologies: Production, Purification, Storage, Applications and Safety*, Newnes, 2013.

1.12. A. Kudo, Y. Miseki, *Chemical Society Reviews* 2009, ***38***, 253-278.

Chapter 2. Theoretical background of water splitting reaction

2.1 Introduction

Hydrogen production using solar energy is an important energy and environmental issue. The development of efficient photoelectrodes and related co-catalyst for water splitting is one of the fundamental challenges in hydrogen production. Considering the thermodynamic potential, a single-component semiconductor that possesses a higher band gap than 1.23V can generate hydrogen and oxygen gas from water simultaneously as long as its conduction and valence bands are in their proper positions. However, overall water splitting by one single-component semiconductor is usually limited by the kinetic overpotential. Until now, the maximum solar-to-hydrogen conversion efficiency using single-component semiconductor still does not exceed 5%.[2.1] Because of such inherent weakness of one-componentapproaches, many developments have been made in photoelectrochemical cells that have separate cathode and anode and are easily implementable in terms of tunability and efficiency. Moreover, efficient co-catalysts for water splitting also represent one of the most important and challenging issues for the implementation of photoelectrochemical hydrogen production. A critical requirement for outstanding catalysts in a photoelectrochemical cell is not only the ability to boost the kinetics of a chemical reaction but also durability against electrochemical and photoinduced degradation. Here, we will discuss hydrogen evolution reaction (HER) and oxygen evolution reaction (OER) from overall water splitting reaction. Issues of catalysts for HER, OER and photoelectrochemial hydrogen production from light absorbing photoelectrodes will also be described.

2.2 Hydrogen evolution reaction (HER)

General description of HER and catalyst for HER

The oxidation reaction in the electrolysis of water is:

$O_2 + 4e^- + 4H^+ \leftrightarrow 2H_2O$ $E_{anodic} = 1.23\ V - 0.059(pH)\ V$ (vs. NHE) (2.1)

while the reduction reaction is:

$4e^- + 4H^+ \leftrightarrow 2H_2$ $E_{cathodic} = 0\ V - 0.059(pH)\ V$ (vs. NHE) (2.2)

where, NHE is the Normal Hydrogen Energy and the standard potential is dependent on pH ($E_{half} = E - 0.059(pH)$ vs NHE). In these two equations, the thermodynamic potential of water splitting ($E^o_{cell} = 1.23V$) is observed by subtracting (2) from (1). Kinetically, however, when a voltage of 1.23V is applied, electrolysis occurs with difficulty, which results in no current flow. In this situation, additional potential is needed to drive a reaction at a certain rate, which is called overpotential, η. Meanwhile, if a current of i_c flows at the cathode, the same current of i_a must flow at the anode to complete the circuit. Because of this, both electrodes (anode and cathode) need the overpotential.

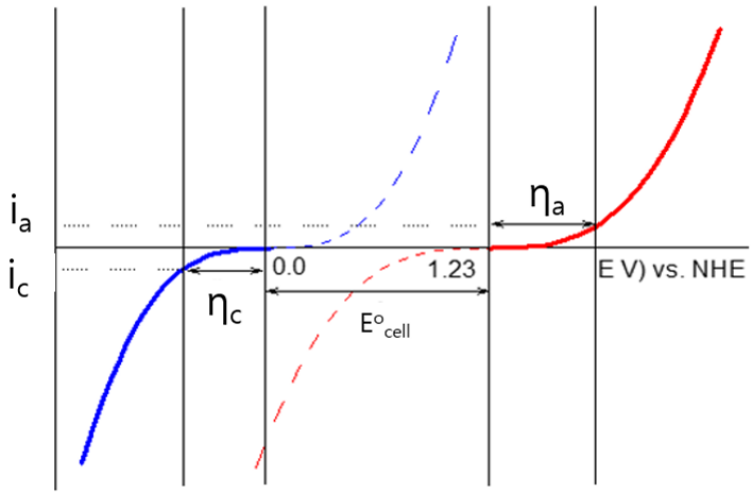

Figure 2.1. Schematic of the current to potential curve of water splitting reaction.

Figure 2.1 shows current to potential curve for the water-splitting reaction. The red line and blue line indicates oxidation and reduction reaction of water electrolysis, respectively. The overpotential at the cathode and anode is written η_c and η_a, respectively. Therefore, total applied potential, E_{appl}, is:

$$E_{appl} = 1.23V + \eta_c + \eta_a \quad (2.3)$$

Higher overpotential requires higher total applied voltage. Using an electrocatalyst for water splitting can reduce the overpotential required for electrolysis of water.

The hydrogen evolution reaction can be written as:

$$H^+ + e^- \rightarrow 1/2H_2 \quad (2.4)$$

Its standard potential is 0 V vs. NHE and the potential is dependent on pH (E = 0 V – 0.059(pH) vs NHE). Mechanistically, for the HER in acidic solution, the following possible reaction steps have been suggested.[2.16]

$$H_3O^+ + e^- \rightarrow H_{ads} + H_2O \quad (2.5)$$

$$H_{ads} + H_3O^+ + e^- \rightarrow H_2 + H_2O \quad (2.6)$$

$$H_{ads} + H_{ads} \rightarrow H_2 \quad (2.7)$$

where H_{ads} is the adsorbed hydrogen atom on the surface. Eq. (2.5) is a discharge step (the Volmer reaction), eq. (2.6) is a desorption step (the Heyrovsky reaction), and eq. (2.7) is a recombination step (the Tafel reaction). Therefore, two different pathways for HER can occur. A combination of eq. (2.5) and (2.7) step is known as the Volmer-Tafel mechanism. In this mechanism, protons from the solution are discharged on the surface, forming adsorbed hydrogen atoms. Then, two adjacent adsorbed hydrogen atoms combine to form molecular hydrogen. The combination of eq. (2.5) and (2.6) is known as the Volmer-Heyrovsky mechanism. A proton from the electrolyte solution is discharged on the catalyst surface to form an adsorbed hydrogen atom. This step is followed by combination with another proton and electron to form molecular hydrogen. However, for the reaction to proceed at a sufficient rate, it needs to be catalyzed on an electrode surface. Possible

candidates for an HER catalyst include various metals such as Pt, Pd, and Ru as well as metal oxide, carbon, and enzymes with active centers. Using Pt catalyst for HER, equations (2.8) – (2.10) can be described as follows:[2.11]

$Pt + H^+ + e- \rightarrow H\text{-}Pt$ Volmer reaction (2.8)

$2(H\text{-}Pt) \rightarrow H_2 + 2Pt$ Tafel reaction (2.9)

$H\text{-}Pt + H^+ + e- \rightarrow H_2 + Pt$ Heyrovsky reaction (2.10)

HER activity of the catalyst can be characterized by representative parameters; the exchange current density and the bond energy of hydrogen adsorbed to the catalyst.[2.12] During hydrogen evolution, a current I can be described as:[2.13]

$$I = -e(r_+ - r_-) \quad (2.11)$$

where, $r_+ - r_-$ is the net rate of Eq. (2.4). The exchange current is the forward and backward rate when Eq. (2.4) is in equilibrium. The ability of a given metal to catalyze the hydrogen evolution reaction is usually measured by the exchange current density, which is the rate of hydrogen evolution per surface area at the electrode potential when the reaction is at equilibrium. The exchange current density (J_0) is also defined to be the current density at zero overpotential.[2.14] The catalytic effect originates from improving the rate of charge transfer at the interface between the electrode and electrolyte or from lowering the activation energy barrier for a chemical reaction; these catalytic effects are represented by J_0. A higher J_0 indicates that electron transfer or the adsorption/desorption of protons at the electrode/electrolyte can occur more easily with a lower kinetic barrier.

The chemisorption of hydrogen at the catalyst is also an indicator of the ability of catalytic activity for HER. ΔG_{H*}, the free energy of the adsorbed state is calculated as:[2.13]

$$\Delta G_{H*} = \Delta E_H + \Delta E_{ZPE} - T\Delta S_H \quad (2.12)$$

where, ΔE_H is the hydrogen chemisorption energy, ΔE_{ZPE} is the difference in

zero point energy between the adsorbed and the gas phase, T is the temperature, and the ΔS_H is the entropy of H_2 in the gas phase at standard conditions. The chemisorption energy of hydrogen is also dependent on the surface coverage of the adsorbates. Electrochemical Quartz Crystal Microbalance is useful to find the surface coverage experimentally, and density functional theory calculation can be applied to calculate the chemisorption energy of hydrogen adsorbed on the catalyst, theoretically.

Good catalytic activity requires moderate binding energy between metal catalyst and hydrogen adsorbed for HER. This tendency forms the shape of a volcano. The volcano shape of HER catalysts can be represented by the exchange current density versus the metal – hydrogen bond strength (Figure 2.2) or the exchange current density versus the calculated free energy for hydrogen adsorption (Figure 2.3). In Figure 2.3, Pt, Pd, and Ru catalysts are near the top of the volcano curve. Their binding energy to hydrogen is neither strong nor weak. Moderate binding energy gives good catalyst behavior.

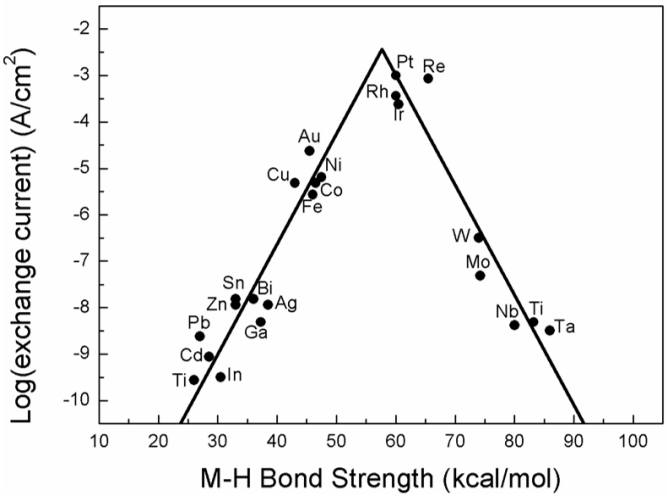

Figure 2.2. Experimentally measured exchange current, log(J_0), for hydrogen evolution over different metal surfaces plotted as a function of the calculated hydrogen chemisorption energy per atom. Data are collected from the previous literature as shown in Table 2.1.

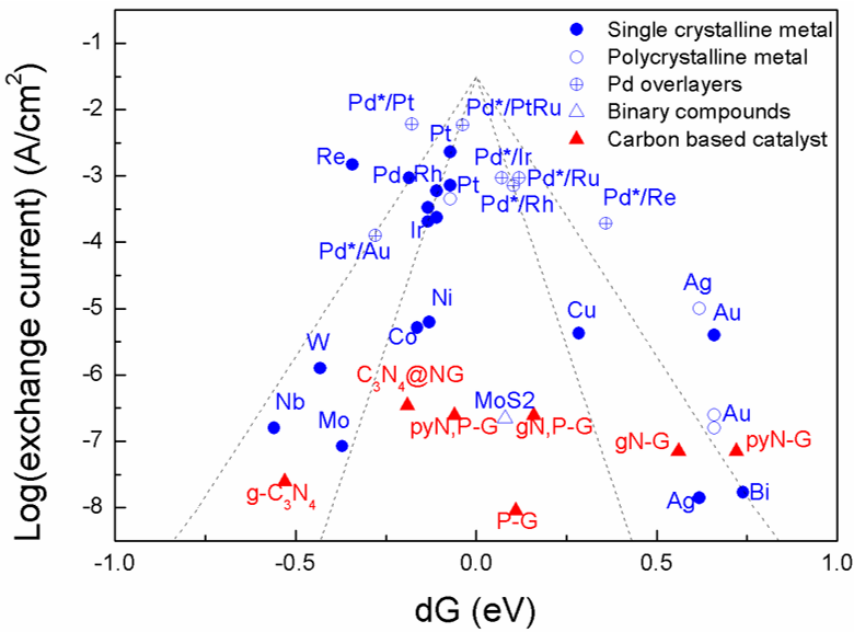

Figure 2.3. Experimentally measured exchange current, log(J_0), for hydrogen evolution over different catalyst plotted as a function of the calculated the free energy for hydrogen adsorption. Data are collected from the previous literature (Table 2.1 ~ 2.3).

The overpotential is the additional energy required to overcome the kinetic barriers inherent to hydrogen evolution reactions at the electrode/electrolyte interface. This overpotential is related to the logarithm of the current density as described by the Tafel law:[2.15]

$$\eta = A \ln (J/ J_0) \quad (2.13)$$

where, parameters η is the overpotential, A is the so-called "Tafel slope", J is the current density, J_0 is the so-called "exchange current density". The exchange current density includes the activity of the catalyst on the electrode and Tafel slope indicates the mechanism of the water splitting reaction on the electrode. Examples of Tafel plot are plotted in Figure 2.6 (c), 2.7 (b), and 2.8 (c). The Tafel slope is also defined to be a measure of the potential increase

required to increase the resulting current by 1 order of magnitude. The Tafel slope is an inherent property of the catalyst that is determined by the rate-limiting step for HER. The value of the Tafel slope also relates to the adsorbed hydrogen coverage (θ_H) on the surface of the electrode.[2.16] If the recombination of adsorbed hydrogen (the Tafel reaction) is the rate-determining step for the HER and if the coverage is very high ($\theta_H \approx 1$), the measured Tafel slope is below 40 mV/decade. However, if the electrochemical desorption step (the Heyrovsky reaction) is the rate-determining step, a Tafel slope of 40 ~ 118 mV/decade is measured and is dependent on the value of θ_H (0 ~ 1).

Types of HER catalysts

Traditionally, pure metals (Pt, Pd, Ni, etc.),[2.17] metal composites/alloys (Ni–Mo, Ni–Co, Ni–Mo–Cd, etc.),[2.18] and compounds including nonmetallic elements (RuO_2, Sr_xNbO_3, Mo_3S_4, etc.)[2.1] have been used for HER catalysts. Table 2.1 ~ 2.3 are the selection of experimental values of exchange current for the hydrogen evolution on metals, metal oxides, bimetallic compounds, and other types of catalysts, respectively. Recently, binary and bimetallic catalysts also have been attracting attention in renewable energy technologies due to the low cost and high stability. Their insufficient activity compared to the pure metallic catalysts is still a challenging issue, however.

Metal based HER electrocatalysts

Metal:

Much HER research in the past few decades has been made for HER of metal based elements or metal as HER electrocatalysts. Among metal based catalysts, Pt, Pd, and Ru are near the top of the volcano curve, showing highly catalytic activity for HER. Their binding energy to hydrogen is neither too strong nor too weak, which leads to the good catalytic behavior. Table 2.1

summarizes a selection of experimental values of exchange current for the hydrogen evolution on metals and metal oxides. Recent progress has been concentrated on the incorporation of noble metal nanoparticle in earth-abundant elements rather than usage of full noble metals only. Notwithstanding these, there has been a report about a highly active and durable class of electrocatalysts by exploiting the structural evolution of Pt-Ni bimetallic nanocrystals, as shown in Figure 2.4.[2.19]

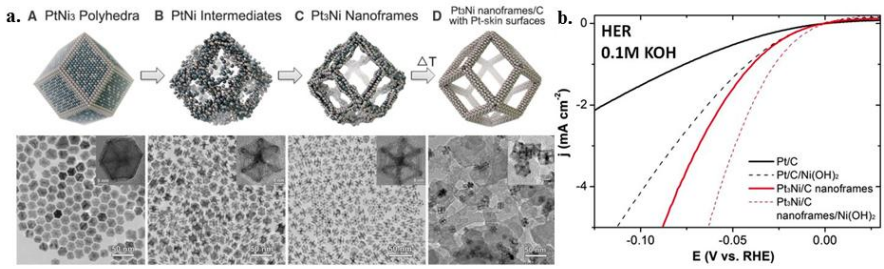

Figure 2.4. Structure and electrochemical property of Pt_3Ni nanoframe (a) Schematic illustrations and corresponding TEM images of the samples obtained at four representative stages during the evolution process from polyhedral to nanoframes. (b) HER activities for Pt/C, Pt/$Ni(OH)_2$/C, Pt_3Ni nanoframes/C, and Pt_3Ni frames/$Ni(OH)_2$/C in alkaline electrolyte. Reprinted with permission (a), (b) from ref. 2.19.

Anode Material	**Loading method**	**Electrolyte**	**Activity**		**Ref. (Year)**
			Tafel Slope (mV/dec)	**Exchange current –log(j_0) (A/cm^2)**	
Ni/Si-micro wire	Electro deposition	KHP, K_2SO_4, KOH (pH 4.5)	N/A	N/A	[2.18](2011)
Ni-Mo/Si-micro wire	Electro deposition	KHP, K_2SO_4, KOH (pH 4.5)	N/A	N/A	[2.18](2011)
Ag	Ag wire	H_2SO_4,	N/A	7.9	[2.20](1967)

		K_3PO_4			
		0.1M H_2SO_4	N/A	7.9	[2.21](1967)
		1M H_2SO_4	N/A	7.8(+) 11.0(-)	[2.22](1970)
		1M H_2SO_4	N/A	7.9	[2.23](1968)
		0.1M HCl 0.4M HCl	(58±2) (57±2)	5.82~6.77 5.11~5.96	[2.24](1957)
Al	Chemipolished Al wire	N/A	N/A	8.0	[2.25](1957)
		0.5M H_2SO_4	114	7.7	[2.26](1968)
Au	Pure Au	0.5M H_2SO_4	N/A	5.9	[2.27](1967)
		0.1M HCl	85	6.7	[2.28](1957)
		0.1M HCl	118	6.3	[2.29](1955)
Bi	Pure Bi	0.45M H_2SO_4	N/A	10.4	[2.30](1964)
		1M H_2SO_4	N/A	7.8(+) 10.0(-)	[2.31](1969)
		0.5M H_2SO_4	N/A	10.8	[2.32](1970)
		0.1M $HClO_4$	N/A	8.1	[2.33](1961)
Cd	Cd wire	1M H_2SO_4	N/A	11.6	[2.34](1970)
		0.25M H_2SO_4	135±12	10.8	[2.35](1964)
Co	Pure Co	0.5M H_2SO_4	N/A	5.3	[2.36](1963)
		0.05M H_2SO_4	N/A	5.6	[2.37](1970)
		1M H_2SO_4	N/A	5.2	[2.38](1946)
Cr	Pure Cr	0.5M H_2SO_4	126	6.5	[2.39](1969)
		0.01M HCl	116	7.25	[2.28](1957)
		0.5M H_2SO_4	N/A	7.4	[2.40](1968)
Cu	Pure Cu	0.5M H_2SO_4	N/A	7.8	[2.41](1966)
		0.5M H_2SO_4	N/A	7.9	[2.42](1969)
		0.5M H_2SO_4	120	7.7	[2.43](1965)
		0.5M H_2SO_4	N/A	7.9	[2.44](1970)
Fe	Pure Fe	0.5M H_2SO_4	N/A	5.1	[2.27](1967)
		0.5M H_2SO_4	120	5.6	[2.43](1965)
		0.01M HCl	118	6.29	[2.28](1957)
		1M H_2SO_4	N/A	6.0	[2.38](1946)
		1M H_2SO_4	N/A	5.9	[2.45](1956)

Ga	Dropped Pure Ga	1M H_2SO_4	N/A	8.4(+) 10.8(-)	[2.31](1969)
		0.5M H_2SO_4	N/A	10.4	[2.46](1969)
		0.5M H_2SO_4	N/A	10.1	[2.47](1965)
		0.1M $HClO_4$	2.63±0.10	9.9	[2.48](1966)
Hg	Dropped Pure Hg	7.5M $HClO_4$	483	12.2	[2.49](1969)
		0.5M H_2SO_4	N/A	12.5	[2.50](1934)
		0.125M H_2SO_4	N/A	12.1	[2.51](1944)
		0.1M HCl	113±1	12.3	[2.52](1949)
		0.05M H_2SO_4	N/A	12.6	[2.53](1965)
In	Pure In	0.1M $HClO_4$	120	11.9	[2.54](1964)
		0.5M H_2SO_4	N/A	9.4(+) 11.0(-)	[2.55](1970)
		0.1M $HClO_4$	120	11.2	[2.56](1965)
		1M H_2SO_4	N/A	9.7	[2.57](1965)
Ir	Pure Ir	0.5M H_2SO_4	N/A	3.4	[2.27](1967)
		0.5M H_2SO_4	N/A	3.7	[2.53](1965)
Mn	Pure Mn	0.05M H_2SO_4	N/A	10.9	[2.58](1962)
Mo	Pure Mo	0.1M HCl	92±12	7.3	[2.28](1957)
Nb	Pure Nb	0.5M H_2SO_4	N/A	8.4	[2.59](1965)
Ni	Ni wire	0.25M H_2SO_4	124±10	5.2	[2.35](1964)
		0.5M H_2SO_4	N/A	5.25	[2.60](1965)
		0.5M H_2SO_4	N/A	5.3	[2.27](1967)
		0.05M H_2SO_4	N/A	5.15	[2.37](1970)
		1M $HClO_4$	125	5.3	[2.61](1964)
Os	Pure Os	1M HCl	124	4.1	[2.62](1970)
Pb	Pure Pb	0.25M H_2SO_4	125±14	11.3	[2.35](1964)
		0.01-1M HCl	N/A	11.5	[2.63](1970)
Pd	Pure Pd	0.1M H_2SO_4	N/A	3.0	[2.53](1965)
		1M H_2SO_4	N/A	3.2	[2.64](1961)
		0.1M HCl	55	3.3	[2.28](1957)

		0.1M HCl	110±5	2.8	[2.65](1960)
		0.5M H_2SO_4	N/A	3.1	[2.27](1967)
Re	Pure Re	1M H_2SO_4	N/A	3.0	[2.66](1950)
Rh	Pure Rh	0.5M H_2SO_4	N/A	3.6	[2.53](1965)
		0.25M H_2SO_4	28±2	3.2	[2.35](1964)
		0.01M HCl	55	3.8	[2.28](1957)
		0.5M H_2SO_4	N/A	3.5	[2.27](1967)
Ru	Pure Ru	1M HCl	117	4.2	[2.62](1970)
Sb	Pure Sb	0.5M H_2SO_4	N/A	8.1	[2.67](1969)
		1M H_2SO_4	N/A	5.1(+), 7.8(-)	[2.31](1969)
		1M H_2SO_4	N/A	9.0	[2.68](1957)
		1M H_2SO_4	N/A	9.3	[2.38](1946)
		1M $HClO_4$	170	5.7	[2.61](1964)
Sn	Pure Sn	1M H_2SO_4	N/A	7.8(+), 9.8(-)	[2.31](1969)
		1M H_2SO_4	N/A	10.5	[2.69](1956)
		1M H_2SO_4	N/A	9.3	[2.38](1946)
		1M HCl	N/A	10.2	[2.53](1965)
Ta	Pure Ta	0.5M H_2SO_4	N/A	8.5	[2.59](1965)
		1M $HClO_4$	N/A	8.6	[2.70](1969)
Te	Pure Te	1M $HClO_4$	48	11	[2.61](1964)
Ti	Pure Ti	1M H_2SO_4	N/A	8.2	[2.71](1962)
		pH2.2 H_2SO_4	150	8.3	[2.72](1970)
		0.5M NaCl	150	8.5	[2.73](1954)
Tl	Pure Tl	0.1M $HClO_4$	N/A	9.5(+), 11.7(-)	[2.74](1970)
		0.8M H_2SO_4	N/A	11.1	[2.75](1951)
		1M HCl	85	9.8	[2.76](1948)
Zn	Pure Zn	1M H_2SO_4	N/A	10.5	[2.77](1957)
		1M H_2SO_4	N/A	10.6	[2.78](1970)
		0.5M HCl	N/A	10.6	[2.79](1969)
		1M HCl	N/A	10.0	[2.80](1963)
Pt	Pure Pt	0.05M H_2SO_4	(26±3)	N/A	[2.81](1952)
		H_2SO_4 Buffer (pH 0.5) (pH 0.9) (pH 1.4) (pH 1.9) (pH 1.95)	 (26) (26) (30) (30) (30)	N/A	[2.82](1954)

		(pH 2.0) (pH 2.25) (pH 2.35) (pH 2.7) $NaHCO_3$ Buffer (pH 8.2) (pH 9.4) (pH 9.6) (pH 10.4) (pH 10.9) (pH 11.2) NaOH buffer (pH 12.1)	(30) (35) (35) (29) (138) (116) (126) (125) (127) (128) (126)		
	Pure Pt	1M H_2SO_4	(25.5±0.5)	2.82(P_{H2}=1.0atm) 3.15(P_{H2}=0.46atm) 3.40(P_{H2}=0.31atm) 3.56(P_{H2}=0.24atm) 3.95(P_{H2}=0.14atm) 4.23(P_{H2}=0.05atm)	[2.83](1959)
	Pure Pt	Prepared in H_2 0.1M HCl 1.0M HCl 1.5M HCl	 28±2 30±22 29±1	 3.45±0.45 2.95±0.55 2.85±0.65	[2.24](1957)
W	W wire	0.1M HCl	60±3	5.96~5.35	[2.24](1957)
Ni	Ni foil	1M NaOH	(115)	5.70	[2.84](1998)
TiO_2-Bi_2O_3 NPs/ Bi-doped TiO_2 NPs/ SnO_2-Bi_2O_3/ IrO_2-Ta_2O_5/Ti	Sequential Coating with heat treatment	50mM NaCl	N/A	N/A	[2.85](2012)
RuO_2-IrO_2/Ti	Chemical Deposition	1M $HClO_4$	40	N/A	[2.86](1994)

*KHP : Potassium Hydrogen phthalate

Table 2.1. Selection of experimental values of Tafel slope and exchange current for hydrogen evolution on metals. Loading method and electrolyte

used are described.

Binary or bimetallic structure ($A_xB_yM_z$ (A =Mo, Ni, Co, W), (B = O, S, Se) , (M =P, C)):

Recent progress has been concentrated on developing low-cost and acidic stable non-noble metal HER catalysts. Table 2.2 summarizes a selection of experimental values of exchange current for the hydrogen evolution on binary or bimetallic structure catalysts. Binary structures such as MoS_2, Mo_2C, Mo_2N, and Ni_2P or bimetallic compounds such as Ni-Mo and Co-Mo-N have been suggested as catalysts with a high activity for HER. Precise tuning of each composition from $A_xB_yM_z$ compounds and nanostructuring increased activity for HER and long-term stability in acidic media. Nanoparticulated molybdenum sulfide catalyst has been known as HER catalyst, which shows HER activity on the edge sites of the crystal structure. Identification and understanding of active sites in thiomolybdate $[Mo_3S_{13}]^{2-}$ nanoclusters improved HER activity greatly, as shown in Figure 2.5 (a) - (c).[2.87] Phase change of crystal structure in MoS_2 nanosheet boosts HER activity, as shown in Figure 2.5 (d) - (f).[2.88] Exfoliation of bulk MoS_2 powders transforms trigonal prismatic (2H and 3R phases) to octahedral 1T phase which is more metallic leading to the high activity for HER.

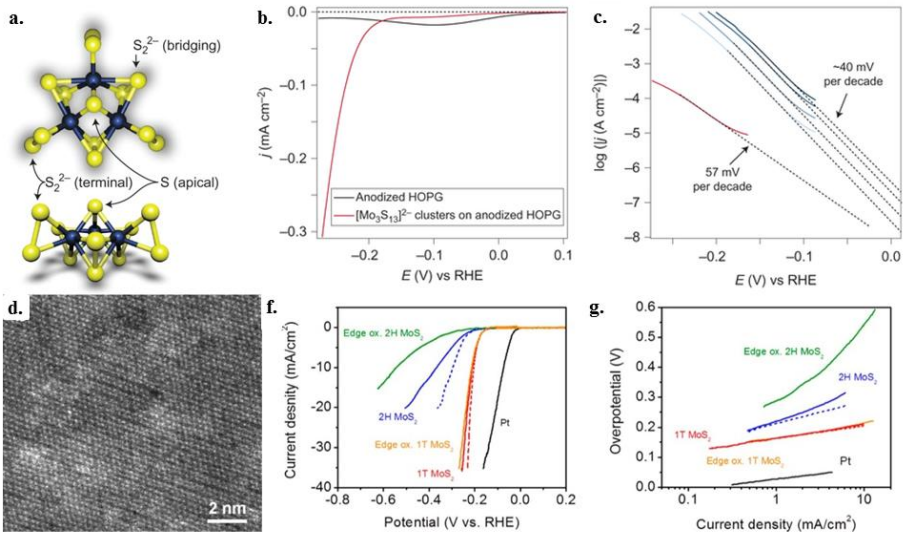

Figure 2.5. Electrochemical properties of Molybdenum sulfide film (a) Model of a single $[Mo_3S_{13}]^{2-}$ cluster, top and side views. (b) Polarization curve of sub-monolayer coverage of $[Mo_3S_{13}]^{2-}$ clusters on HOPG. (c) Tafel plots of the cathodic sweeps of the polarization curves in (b). (d) HAADF STEM image of chemically exfoliated MoS_2 with octahedral coordination (1T phase). The nanosheets are mostly composed of distorted regions with zigzag chains. (e) Polarization curve of 1T and 2H MoS_2 nanosheet electrodes before and after edge oxidation. (Dashed line : iR-corrected) (f) Corresponding Tafel plots obtained from polarization curves. Tafel slopes of ~40 and 75-85mV/dec for 1T and 2HMoS_2, respectively. Reprinted with permission (a), (b), and (c) from ref. 2.87 Copyright 2014 Nature Publishing Group and (d), (e), and (f) from ref. 2.88 Copyright 2013 American Chemical Society.

In the past, tungsten was treated as an element which has a poor activity for HER. Recently, tungsten combined with sulfur or carbide produces better HER catalytic activity through the nanostructuring of the crystal structure, as shown in Figure 2.6. Chemically exfoliated WS_2 nanosheets show improved onset potential for HER, low Tafel slope, and enhanced time of frequency

value (Figure 2.6 (a) - (b)).[2.89] Highly concentrated strain of metallic 1T phase in WS_2 nanosheets can activate HER and promote long-term stability electrochemically and mechanically. Tungten carbide (WC) is also a promising electrocatalyst for HER in pH neutral solution (Figure 2.6 (c) - (d)).[2.90] Research about the dependency of W and C (WC, W, and W_2C) on their composition provides another possibility for tungsten-based HER catalyst.

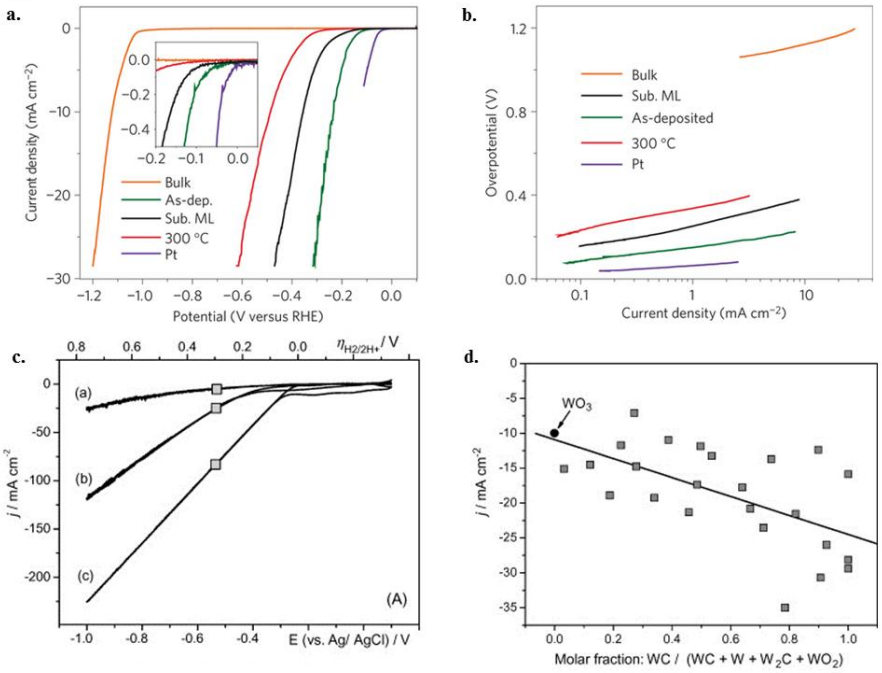

Figure 2.6. Fundamental electrochemical properties of tungsten based materials (a) Polarization curves of bulk and as-exfoliated WS_2 (as-deposited film of 1T phase, sub-monolayer as-exfoliated film, and 2H phase after annealing at 300 ℃) along with those corresponding to Pt nanoparticles and bulk WS_2 powder for comparison. (b) Tafel plots obtained from the polarization curves (exfoliated sample : 60 mV/dec, 2H and bulk samples : higher than 110 mV/dec). (c) Cyclic voltammograms of the hydrogen evolution reaction at (a) polycrystalline graphite, (b) tungsten carbide) and (c) Vulcan XC-72 20% Pt. (100mM H_2SO_4) (d) Dependence of the hydrogen

evolution current densities of different catalyst samples on their composition, as derived from X-ray powder analysis. Reprinted with permission (a), (b) from ref. 2.89 Copyright 2013 Nature Publishing Group and (c), (d) from ref. 2.90 Copyright 2009 Elsevier B. V.

Cobalt- and Co-based compounds are traditionally known as excellent oxygen evolution catalysts. Recent progress shows that Co-based catalysts combined with chalcogenide elements or other metal element can be a highly active catalyst for HER with good stability. $CoSe_2$ nanoparticles grown on carbon nano paper displayed optimal activity for HER recently (Figure 2.7 (a) - (c)).[2.91] In this system Co 3d electrons adopt a low-spin configuration and make $CoSe_2$ a metallic conductor when combined with Se. Four alternative layered mixed close-packed Co-Mo-N allows the 3d transition metal to tune the electronic states of Mo, which catalyze the HER activity (Figure 2.7 (d) - (f)).[2.92] These results provide possible steps that rational controlling of particle size and concentration of catalysts can tune oxidation states for optimal catalytic HER activity. Electrodeposited Cobalt-sulfide is an interesting HER catalyst in that its synthesis is very facile (Figure 2.7 (g) - (i)).[2.93] Its low overpotential, high activity, long-term aqueous stability, and its taking the form of very thin films also offer promising features for the co-catalyst of a PEC cell as well as an HER catalyst.

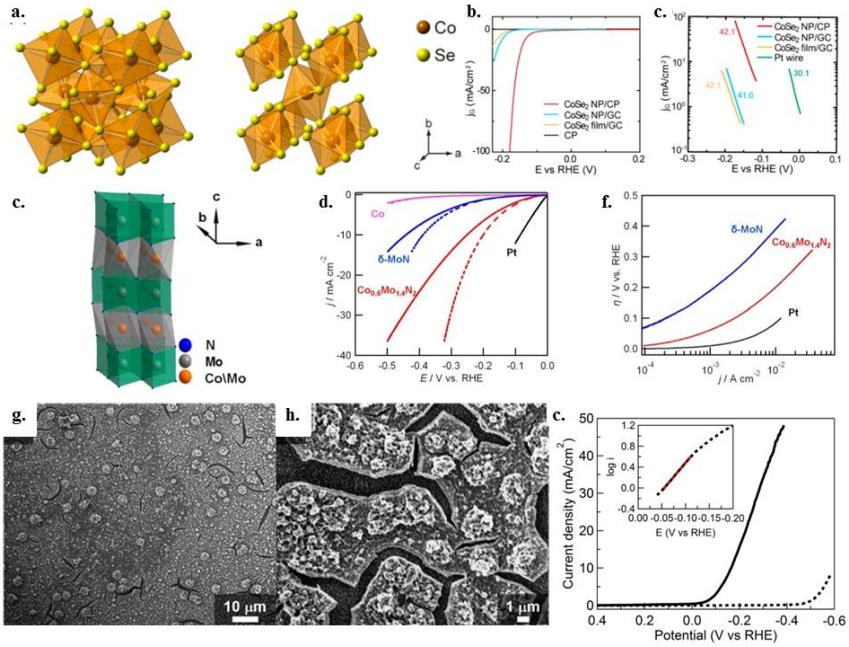

Figure 2.7. Fundamental properties of Cobalt based HER catalyst materials (a) Crystal structure of $CoSe_2$ in cubic pyrite-type phase (left) and orthorhombic macarsite-type phase (right), in which Co and Se are displayed in orange and yellow, respectively. (b) Polarization curves of $CoSe_2$ nanoparticle (NP)/carbon fiber paper (CP) electrode in 0.5 M H_2SO_4, along with $CoSe_2$ NP/glassy carbon (GC), $CoSe_2$ film/GC, and CP for comparison. (c) Corresponding Tafel plots in comparison with a Pt wire. (d) Four-layered crystal structure of $CoMoN_2$. (e) Polarization curves of Co, δ-MoN, $Co_{0.6}Mo_{1.4}N_2$ and Pt in H_2-saturated 0.1 M $HClO_4$ with (dashed line) and without (solid line) iR correction. (f) Corresponding Tafel plots. (g, h) Representative SEM images of the annealed Co-S film on FTO (i) Polarization curves of annealed Co–S/FTO (solid) with Tafel plot. (1.0 M potassium phosphate buffer of pH 7 water) Reprinted with permission (a), (b) and (c) from ref. 2.91 Copyright 2014 American Chemical Society, (d), (e) and (f) from ref. 2.92 2013 Copyright American Chemical Society and (g), (h) and (i) from ref. 2.93 2013 Copyright American Chemical Society.

Catalyst/Substrate (adhesive)	Loading method	Electrolyte	Activity			Ref. (Year)
			Tafel Slope (mV/dec)	TOFs (S^{-1})	Exchange current $-\log(j_0)$ (A/cm^2)	
MoS_2 NSs/GC (Nafion)	Mechanical activation	0.5M H_2SO_4	(68)	0.08(potential x)	4.41	[2.94](2013)
MoS_x/Ti-n^+p-Si	Electro deposition	1.0M $HClO_4$	(39)	N/A	N/A	[2.95](2012)
MoS_x/GC (2<x<3)	Wet-Chemical-Synthesis Drop casting	0.5M H_2SO_4	(50)	0.3(at 200mV)	N/A	[2.96](2012)
Mo_2C/CNT-Gr	Modified Urea-glass route	0.5M H_2SO_4	(58)	N/A	4.21	[2.97](2014)
Mo_2C/CNT (Nafion)	Carburization	0.1M $HClO_4$	(65.3±3.1)	N/A	4.85	[2.98](2013)
MoS_2/Mo/n^+p-Si	Sputtering & Sulphidization	1M $HClO_4$	112.23(103.84)	N/A	5.77	[2.99](2013)
Undoped MoS_x/Act-C-Paper	Electro deposition	1M $HClO_4$	(38.4)	N/A	5.97	[2.100](2013)
1T-MoS_2/GC	Electrochemical Exfoliation	0.5M H_2SO_4	43.5±2.5(40)	N/A	N/A	[2.88](2013)
MoS_3/GC	Drop or Spray casting	1M H_2SO_4	(41) (54)	N/A	7.70 6.20	[2.101](2012)
MoS_3-MWCNT/GC	Drop or Spray casting	1M H_2SO_4	(41) (42)	N/A	7.10 6.89	[2.101](2012)
MoS_x/GC (2<x<3)	Electro deposition	1M H_2SO_4	(40.5)	0.8(at 220mV)	6.89	[2.102](2011)
WS_2-NSs/GC	Electrochemical Exfoliation	0.5M H_2SO_4	60(55)	175(at 288mV)	4.70	[2.89](2013)
MoS_2-NPs/Au	PVD & Sulphidization	pH 0.24 H_2SO_4	(57.5±2.5)	0.02	6.70±0.19	[2.103](2007)
1T-MoS_2-NSs/Graphite	CVD	0.5M H_2SO_4	54(43)	N/A	N/A	[2.104](2013)
$[Mo_3S_4]^{4+}$/HO	Drop casting	0.5M	(120)	0.07	6.66	[2.105](2008)

PG (Nafion)		H_2SO_4				
MoS_2/RGO	Solvothermal Synthesis	0.5M H_2SO_4	(41)	N/A	N/A	[2.106](2011)
α-$MoS_{2.7}$/NPG	Chemical plating	0.5M H_2SO_4	(41)	N/A	N/A	[2.107](2014)
$[Mo_3S_{13}]^{2-}$/GP	Drop casting	0.5M H_2SO_4	(40)	3(at 200mV)	N/A	[2.87](2014)
MoO_3-MoS_2 NWs/FTO	HWCVD & Sulphidization	0.5M H_2SO_4	(55±5)	4(at 272mV)	N/A	[2.108](2011)
Mesoporous DG MoS_2/FTO	Electrodeposition & Sulphidization	0.5M H_2SO_4	(50)	N/A	6.16	[2.109](2012)
WC/Graphite (Nafion)	Carburization	100mM H_2SO_4 100mM Na_3PO_4	N/A	N/A	N/A	[2.90](2009)
Co-S/FTO	Electrodeposition	1.0M K_3PO_4	(93)	0.017(at 187 mV)	3.59	[2.93](2013)
$NiMoN_x$/C	Reducing precursor	0.1M $HClO_4$	(35.9)	N/A	0.24	[2.110](2012)
Li-MoS_2/CFP	Electrochemical exfoliation	0.5M H_2SO_4	(62)	0.1	0.167	[2.111](2014)
$CoSe_2$/CFP	Drop casting & Selenization	0.5M H_2SO_4	(42.1)	N/A	0.0049±0.0014	[2.91](2014)
$Co_{0.6}Mo_{1.4}N_2$/GC	Nitration & Drop casting	0.1M $HClO_4$	N/A	N/A	0.23	[2.92](2013)
$Ni_{74}Mo_{16}P_{10}$/Cu $Ni_{74}Mo_{16}P_{10}$/Cu $Ni_{86}Mo_{12}P_2$/Cu $Ni_{71}Mo_{27}P_2$/Cu $Ni_{73}P_{27}$/Cu $Ni_{89}Mo_{11}$/Cu $Ni_{50}Mo_{45}P_5$/Cu $Ni_{92}P_8$/Cu	Electro deposition (25°C, 1-step) (70°C, 1-step) (70°C, 3-step) (70°C, 3-step) (70°C, 2-step) (70°C, 2-step) (70°C, 3-step) (70°C, 3-step)	1M NaOH	(97) (103) (112) (89) (109) (180) (74) (57)	N/A	0.05 0.12 1.29 3.10 0.07 12.7 1.98 0.24	[2.84](1998)

*NS : Nano Sheet, *NP : Nano particle, *GC : Glassy Carbon, *Act-C-Paper : Activated C-paper, *α :

Amorphous, *NPG : Dealloyed nanoporous gold, *GP : Graphite paper, *HWCVD : Hot-wire chemical vapor deposition, *DG : Double Gyroid, *g- : Graphitic, *NG : N-Graphene, *CFP : Carbon Fiber Paper

Table 2.2. Selection of experimental values of Tafel slope, TOFs and exchange current for the hydrogen evolution on binary metals system. Loading method and electrolyte used are described.

Carbon based HER electrocatalysts

The design of the carbon-based catalysts can represent an important research direction in the search for non-precious, environmentally benign, and corrosion resistant catalysts. In particular, graphene possesses excellent transmittance and superior intrinsic carrier mobility,[2.112] thus there have been several attempts to use graphene as a catalyst. It has been reported that the reduced graphene oxide (rGO) containing catalytic active materials exhibited an improved activity in HERs as well as oxygen evolution reactions (OERs) or oxygen reduction reactions (ORRs).[2.113] However, in most cases, the role of carbon materials is limited to an electrical conducting substrate or a supporter that enhances the performance of other decorated active catalysts. Recently, new possibilities have been investigated that monolayer graphene acts as an electrocatalyst for efficient HER.[2.114] Uk Sim et al., reported that monolayer graphene acts as a catalyst for hydrogen evolution reaction on Si-electrode and boost their catalytic activity by plasma treatment in N_2-ambient.[2.114] Plasma treatment induces the abundant defects and the incorporation of nitrogen atom in graphene structure, which can act as catalytic sites on graphene. Monolayer graphene containing nitrogen impurities exhibits a remarkable increase in the exchange current density and leads to significant anodic shift of the onset current from an Si-electrode. The electro-catalytic activity of the carbon-based catalyst was much lower than other metal-based catalysts, but the HER activity of carbon catalyst has increased gradually. The J_0 of monolayer graphene is also comparable to that of the other non-noble metal catalyst, nanoparticulate MoS_2.[2.103, 2.114, 2.115] J_0 can be accurately

calculated by considering the number of active sites. For example, the J_0 of MoS_2 for the HERs is experimentally measured to be 1.3×10^{-7} to 3.1×10^{-7} $A/cm^2_{geometric}$.[2.103] Active sites of MoS_2 nanoparticle for HER are known to be edge sites of MoS_2 nanoparticle.[2.106] For the direct site-to-site comparison between MoS_2 nanoparticle and Pt catalyst, T. Jaramillo *et al*. have measured an exchange current per site of MoS_2 combined with STM analysis.[2.103] The exchange current per site is then multiplied by the site density of Pt for a fair comparison to the transition metal catalyst, resulting in the exchange current density of 7.9×10^{-6} A/cm^2. This value is still similar to exchange current density of monolayer graphene (2.7×10^{-6} A/cm^2). To sum up, while the representative carbon-based catalyst, graphene, has the catalytic activity for HER, the identification and quantification of the active sites of the single monolayer graphene should be further investigated for comparative study.

Recently, a metal-free carbon catalyst doped with nitrogen and phosphorous showed good activity for HER (Figure 2.8 (c) - (d)).[2.116] Co-activated N and P heteroatom, which is adjacent to C atom in the graphene matrix, could affect its valence orbital energy levels to enhance reactivity for HER. Graphitic-carbon nitride with nitrogen-doped graphene also shows enhanced HER activity with similar low overpotential and Tafel slope compared to some well-developed metallic catalysts. Through the density functional theory calculations, it is known that intrinsic chemical and electronic coupling of graphitic C_3N_4 and N-doped graphene synergistically promotes the proton adsorption and reduction kinetics. Table 2.3 summarizes a selection of experimental values of exchange current for the hydrogen evolution on carbon-based catalysts.

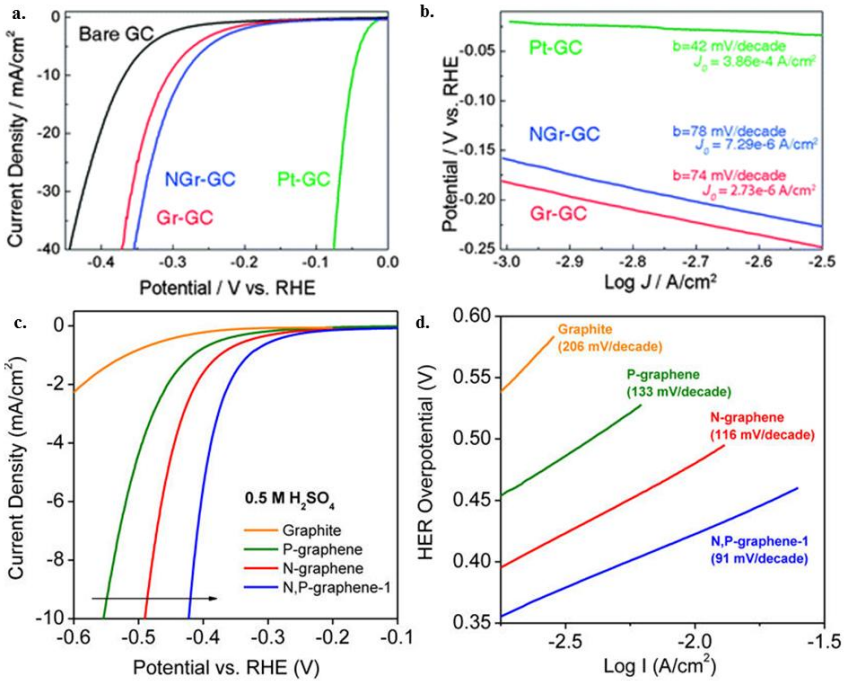

Figure 2.8. Electrochemical properties and chemical structure of graphene based electrodes (a) CV curve of GC, Gr on GC, NGr on GC, and Pt on GC from a rotating disk electrode system. (iR corrected) (b) Tafel plots were derived from (a) CV data. (c, d) HER polarization curves and the corresponding Tafel plots of N- and/or P-doped graphene electrocatalysts. Reprinted with permission (a), (b) from ref. 2.114 Copyright 2013 The Royal Society of Chemistry and (c), (d) from ref. 2.116 Copyright 2014 American Chemical Society.

Catalyst/Substrate (adhesive)	**Loading method**	**Electrolyte**	**Activity**			**Ref. (Year)**
			Tafel Slope (mV/dec)	**TOFs (S^{-1})**	**Exchange current –log(j_0) (A/cm^2)**	
Monolayer	CVD grown	1M HClO4	(75)	N/A	7.57	[2.114](20

graphene	graphene					13)
N doped Gr	Annealing mixed precursors	0.5M H_2SO_4 0.1M KOH	(116) (143)	N/A	7.15 9.93	[2.116](2014)
P doped Gr	Annealing mixed precursors	0.5M H_2SO_4 0.1M KOH	(133) (159)	N/A	8.05 10.79	[2.116](2014)
N,P doped Gr	Annealing mixed precursors	0.5M H_2SO_4 0.1M KOH	(91) (145)	N/A	6.62 9.40	[2.116](2014)
g-C_3N_4@NG/GC (Nafion)	Exfoliation & Polycondensation	0.5M H_2SO_4	(51.5)	N/A	6.46	[2.117](2014)

Table 2.3. Selection of experimental values of Tafel slope and exchange current for the hydrogen evolution on carbon based catalyst system. Loading method and electrolyte used are described.

Electrolyzer systems for water splitting reaction

These days, 96% of total hydrogen amount is produced through gas reforming and about 4% of is produced by water electrolysis. [2.6] However, gas reforming, which is a major hydrogen production method, has one critical disadvantage of CO_2 emission. To solve problem, hydrogen production by environmentally friendly means should be increased. Hydrogen production by the water splitting reaction is one such system with no carbon emissions. Development of electrolyzers has been made for low-cost and high-efficiency water splitting to generate hydrogen. Table 2.4 summarizes representative types of commercial electrolyzers which have been developed. [2.7]

Manufacturer	**Technology**	**Rated production(Nm^3/h)**	**Efficiency (%)**	**Location**
AccaGen	Alkaline	1-100	52.8-72.7	Switzerland
Avalence	Alkaline	0.4-4.6	65.2-70.8	USA
Erredue	Alkaline	0.6-21.3	59-69.8	Italy
Giner	PEM	3.7	65.5	USA

Statoil	Alkaline	10-500	82.3	Norway
Hydrogenics	Alkaline	10-60	65.5-68.1	Canada
Hydrogenics	PEM	1	49.2	Canada
H2 Logic	Alkaline	0.66-42.62	64.9-70.8	Denmark
Proton Onsite	PEM	0.265-30	48.5-61	USA
ELT	alkaline	3-330	76.9-82.3	Germany

Table 2.4. Manufacturers of electrolyzer

As shown in Figure 2.9 (a), the alkaline electrolyzer has two electrodes operating in a liquid alkaline electrolyte.[2.7] The alkaline electrolyzer is safe to use and its life span reaches up to 15 years.[2.8] In addition to this, it is quite efficient, having an efficiency of about 50~82%. Due to these advantages, the alkaline electrolyzer is being used commercially. The operating principle of an alkaline electrolyzer is shown in Figure 2.9 (a). The cell consists of two electrodes separated by a membrane. This assembly is immersed in a liquid solution of KOH (25~30 wt%) to maximize its ionic conductivity with an operating temperature of 65 ℃ to 100℃.[2.9] The Proton Exchange Membrane (PEM) electrolyzer is based on the proton conduction concept using a polymer membrane as an electrolyte and developed by General Electric in 1966.[2.5] In PEM electrolyzers, a thin polymeric membrane has a cross-linked structure, which is strong in an acidic solution due to the presence of functional groups of the sulfonic acid type. These groups are responsible for the proton conducting ability of the materials through an ion exchange mechanism.[2.10] The most commonly used membrane for PEM electrolyzer is Nafion. The operating principle of the PEM electrolyzer is shown in Figure 2.9 (b). In a solid oxide electrolyzer, water splitting reaction occurs at a high temperature of 600 ℃ ~ 900 ℃. Water splitting using the solid oxide electrolyzer is more efficient than that using the alkaline and the PEM electrolyzer.[2.5] The operating principle of the solid oxide electrolyzer is shown in Figure 2.9 (c).

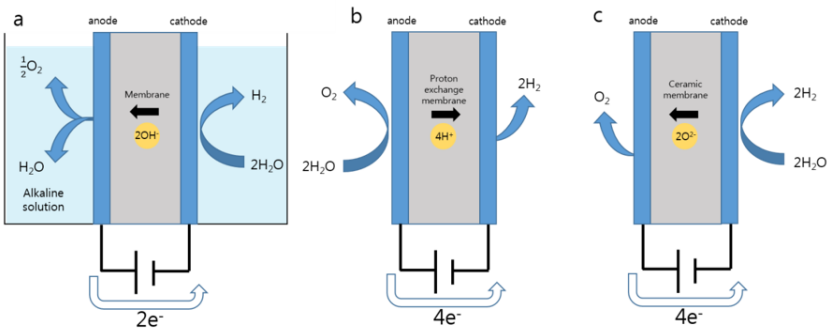

Figure 2.9. Various electrolyzer system for water splitting reaction. (a) Alkaline electrolyzer, (b) PEM electrolyzer, (c) Solid oxide electrolyzer

2.3 Oxygen evolution reaction (OER)

Water splitting and OER

As outlined above, splitting water to generate hydrogen and oxygen molecules is an environmentally friendly solar-to-energy conversion method. [2.2b, 2.120] The conversion of the solar source into the simplest energy form, hydrogen gas, can be realized by virtue of water splitting. [2.1] The concept of water splitting was originated from the naturally existing photosystem in plants. Thus it is essential to understand the biological system. In the photosystem, there are two separate subunits, photosystem I and photosystem II. In photosystem II, the water is oxidized into oxygen, which is catalyzed by Mn_4CaO_5 cluster.[2.121]

As shown in Figure 2.10, the electrons arisen from the water oxidation are then excited using visible light at two reaction centers, P700 and P680.[2.121-2.122] These electrons and surrounding hydrogen ions are incorporated with the $NADP^+$ (Nicotin amide adenine dinucleotide phosphate), and consequently reduced form of $NADP^+$, NADPH, are formed.[2.2-2.3] The reducing power NADPH is used for making glyceraldehyde 3-phosphate which is used as a

nutrient in the plant.[2.121f] Similar to the photosystem, artificial water splitting also can be categorized into two redox reactions. At the anode, water is oxidized into oxygen molecules, and at the cathode, the protons are reduced into hydrogen using the electrons from the anode.[2.123] This reaction can be summarized by water splitting equations (2.1) and (2.2).

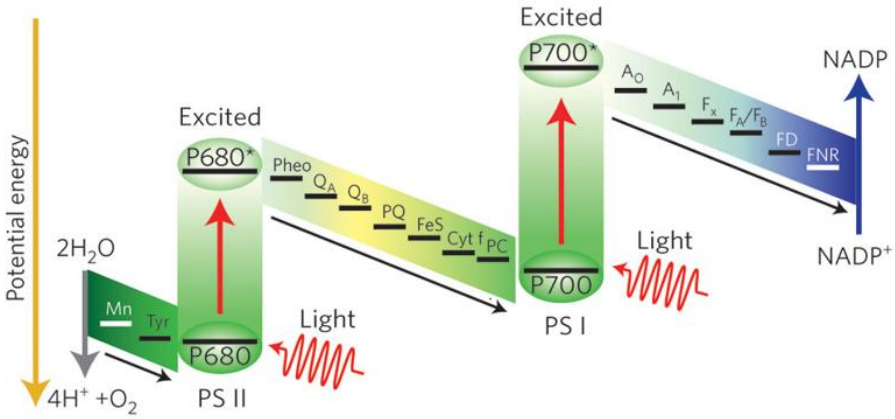

Figure 2.10. Schematic of water splitting in photosystem. Reprinted with permission from ref. 2.122.

The anode half reaction, the oxygen evolution reaction (OER) has been regarded as a major bottleneck in the overall water splitting process due to the slow transfer rate of four electrons and the high activation energy barrier for O-O bond formation. In this chapter, artificial water splitting system, specifically the OER process and OER catalysts will be discussed.

Regarding OER catalysts, most research is inspired by the photosystem II. Intensive research has focused on developing photo/electro catalysts for overall water splitting. [2.120d-g, 2.124] First, in case of photocatalysts, electron/hole pare is generated by light at the conduction/valence band of the catalysts, respectively, [2.120d-g] and used for hydrogen and oxygen production. [2.120e-h] Using

the photocatalysts, water can be converted into hydrogen and oxygen molecules with only visible lights without any additional voltage. [2.120e-h] Since Fujishima group used TiO_2 as photocatalysts for water splitting for the first time in 1970s, [2.124] many photocatalysts for cathodic and anodic reaction have been developed. [2.120e-h] However, even after using photocatalysts, the catalytic performance of the catalysts was not good enough due to the intrinsic kinetic barrier. [2.125] This phenomenon originates from the nature of the water splitting reaction that requires multi-step reactions which involve multiple electrons and holes. [2.123] To enhance its efficiency, much research has designed the combination of electrocatalysts and semiconductors for both anodic and cathodic reactions. Indeed, there have been numerous studies to find the electrocatalysts and incorporate them with the photoanode/photocathode materials to lower the activation energy and promote the efficiency of the water splitting reaction. [2.123a]

General description of Oxygen Evolution reaction (OER)

Generally, the mechanism for the OER at the surface of the metal oxides has been known as the following four electron involved reaction paths[2.125]:

$$H_2O\ (l) + * \rightarrow HO^* + H^+ + e^- \quad (2.14)$$

$$HO^* \rightarrow O^* + H^+ + e^- \quad (2.15)$$

$$O^* + H_2O\ (l) \rightarrow HOO^* + H^+ + e^- \quad (2.16)$$

$$HOO^* \rightarrow * + O_2(g) + H^+ + e^- \quad (2.17)$$

where * is the active sites for OER catalysis. Past research has suggested several theories for general description of the OER. [2.126] In 1984, the Rasiyah group proposed that when redox potential of the catalysis is close to the thermodynamic potential for OER, the catalysts could have high activity. [2.126a] The Trasatti group proposed that the strength of metal-oxygen bonds onto the surface can be a good descriptor for predicting the catalytic activity.[126b] The Otagawa group suggested that 3d electron numbers in the transition metal at

the bulk structures can be related to the activity. [2.127] Recently, Shao-horn Yang group found that e_g occupancy in surface transition metals can be related to the OER mechanism. [2.126d] They take some assumptions that e_g orbital at the surface of the catalyst can make the σ-bonding with the anion adsorbates onto the surface. [2.126d] Therefore, the occupancy of e_g orbital can affect on the binding of oxygen-containing intermediate species during the OER. [2.126d] Comparing the various perovskite materials which contain different e_g occupancy, they experimentally found that catalysts that have e_g value of 1.2 shows the highest catalytic activity. [2.126d] Norskov and Rossmeisl group theoretically understand the activity of the OER electrocatalysts using DFT calculations in case of metal oxide OER catalysts[2.125] They found the free energy of the rate liming step in the overall OER reaction and the overpotential value for the OER. These two values can be written as: [2.125]

$$G_{OER} = \max\,[\Delta G_1^{\circ}, \Delta G_2^{\circ}, \Delta G_3^{\circ}, \Delta G_4^{\circ}] \quad (2.18)$$

$$\eta\ (\text{overpotential}) = (\,G_{OER}/e\,) - 1.23 \quad (2.19)$$

They found that the difference between the binding energy of HOO* and OH* is nearly constant onto the various types of metal oxides surfaces. [2.125] This difference between two energy can be defined as the theoretically lowest overpotential for OER catalysis. [2.6] However, only a few catalysts can operate with this lowest overpotential. [2.6] Instead, they suggested that the difference between the binding energy of O* and OH* could be an origin for the overpotential for most of the OER electrocatalysts. Moreover, they found that this assumption could be applied to the experimental results studied in the previous reports well. [2.6] As briefly mentioned above, since the water oxidation reaction consists of multi-step reactions, identification of the change of current along with the applied potential offers a means of determining the Tafel slope of an electrochemical reaction and helps to reveal the detailed mechanism.[2.120a, 2.125, 2.128] From the Tafel analysis, not only comparison of catalytic activity, but basic analysis of the catalytic cycle is possible. For

example, the discharge of water molecules or hydroxyl ions to oxidize the active sites onto the surface of the catalysts results in Tafel slope value of 120 mV/dec. [2.128] Further chemical conversion into stable chemical species onto the active sites yields Tafel slope value of 60 mV/dec. [2.128]

Typically, electrochemical rate law with a single-step mechanism can be defined with a turnover-limiting electron transfer from the resting state, [2.128]

$$A \rightarrow B + e^- \tag{2.20}$$

Substituting the other key factors such as turnover velocity and surface concentration of active sites into the above relationship, the electrochemical rate law for a reaction is given as,

$$j = 4Fk°ET \exp(\beta\eta F/RT) \tag{2.21}$$

where F is faraday constant (96485.3 C/mol) and β is the transfer coefficient. This relationship will give a Tafel slope as $(\frac{\delta\eta}{\delta \log j})$, which can be simplified to 2.3 x RT/βF. In a single step, β is close to 0.5 (± 0.1) which gives a Tafel slope value around 120 mV/dec at 298K.

After verifying its major mechanism prior to current density activation, it is also necessary to evaluate the dependence of activity on pH and establish the dependence of the reaction rate on proton activity and buffer strength as:

$$j=k_0(a_{buffer})^n(a_{proton})^m\exp(\beta EF/RT) \tag{2.22}$$

where a_{buffer} is buffer activity, which depends on the buffer strength and a_{proton} is proton activity determined by pH dependence. To achieve the proton activity dependency of the mechanism, a partial differential equation was applied on the relationship of potential to pH, which is:

$$\left(\frac{\partial \mathrm{E}}{\partial \mathrm{pH}}\right)_j = -\left(\frac{\partial log j}{\partial pH}\right)_E \left(\frac{\partial E}{\partial log j}\right)_{pH} \tag{2.23}$$

Substituting the obtained experimental results of the Tafel slope and measured pH dependency, yields a reaction order in proton activity a_{proton}. While demonstrating the proton association during the mechanism, the number of electrons involved during OER, which is defined as the transfer coefficient (β),

has to be calculated. It can be written as:

$$\beta = \frac{2.3RT}{bF} \tag{2.24}$$

After substituting all constants, with b as the Tafel slope**,** it yields a reaction order in electron activity. Considering all of the protons and electrons involved during OER, the possible proposed pathway of each electrocatalyst as a water oxidizer can be explained. For instance, Nocera group successfully established the detailed water oxidation mechanism of newly developed Co-Pi and Ni-Bi catalysts, using electro-kinetic analysis, as described above.

Types of OER catalysts

Noble metal based OER electrocatalysts:

Since many factors that hinder the OER during water-electrolysis exist, many groups of scientist have focused on finding the most efficient catalysts which have superior catalytic activities. The first trial was done by the use of noble metal-based compounds as the catalysts. Typically, ruthenium (Ru),[2.129] iridium (Ir), and platinum (Pt)[2.126b] were chosen for investigating its catalytic activity under various conditions[2.130]. Due to its unique electronic structure such as the fully filled d-bands that gives no Fermi level interference, electrons have more freedom to alternate their chemical behaviors during the reaction. Therefore, noble metal-based catalysts have high catalytic activities compared to other types of catalysts. For example, IrO_x exhibits 1 mA/cm^2 of OER current with only 200mV of overpotential (1.43 V vs RHE) and Tafel slope value of 40 mV/dec. RuO_2 anodes reach 1 mA/cm^2 at the applied potential value of 1.36 V vs RHE and have Tafel slope of 40 mV/dec. [2.127] The Trasatti group demonstrated that an optimized metal-oxygen bond strength in RuO_2 and IrO_x resulted in their high OER catalytic activity. [2.126b] Moreover, the Norskov and Rossmeisl group theoretically explained the high activity of RuO_2 based on the difference between the binding energies of O* and OH* which are assumed to be the rate-limiting step in the overall water oxidation

process.[2.125] Using DFT calculations, RuO_2 exhibits the minimum difference among the various transition metal based OER catalyst, confirming their theoretical origin of high activity.[2.125] Noble metal-based OER catalysts has moderate stability.[2.131] their long-term stability and high catalytic activity, noble metal based OER electrocatalysts have been recognized as promising anode materials for overall water oxidation systems.[2.131]

However, serious problem does exist in using noble metal-based catalysts. The cost of the material itself is extremely high due to its scarcity (average prices are, Ru =$151.96/oz., Pt= $1035.62/oz. and Ir =$476.15/oz.). Thus, it is very hard to use these materials in large-scale energy supply. According to US department of energy (DOE), hydrogen production from water electrolysis is currently $2.50/kg. This price is still more expensive than electricity which is only $35/kWh. Therefore, noble metal catalysts which have high prices cannot be the next alternative in producing high-efficiency energy with lower price of the water electrolysis. Thus, an investigation for different types of catalyst materials had to be carefully considered.

Transition metal (Co, Ni, Cu, Fe) based OER electrocatalysts:

Precious metal oxides, such as RuO_2 and IrO_2, exhibit superb OER catalytic activity; however, their high price remains an unavoidable weakness. Therefore, the development of efficient, durable, and inexpensive alternative catalysts is needed. In this regard, research has focused on developing transition metal based OER electrocatalysts.[2.132] The Meyer group introduced copper based electro-catalysts which have high catalytic activities in alkali phosphate buffer condition.[2.133] They also reported the Cu-peptide molecular catalyst with a well-defined OER mechanism.[2.132d] They verified the oxidation state change of copper initially from Cu(II) to Cu(III) and the intermediate state of Cu(IV) occurs with the formation of peroxide. It showed a high stability during the measurement. In this result, they pointed out the important

key to oxidize water is either by the fluent transfer of oxygen atoms to water molecules or with intermolecular O-O coupling. The overpotential was about 0.52V at pH 11 which is relatively high value, but its impressive catalytic stability along with the high turnover frequency, $33s^{-1}$ exhibited a new path for transition metal based electrocatalysts for water oxidation. The Nocera group employed amorphous inorganic films containing Co atoms and phosphate anions, as shown in Figure 2.11. [2.123a] The films were prepared by electro-deposition of Co -Pi films onto ITO substrate using phosphate buffer with Co(II) ions. Interestingly, the Co -Pi catalyst is formed *in situ* and operates water oxidation with moderate overpotential value (~430 mV) in neutral water under ambient conditions. [2.123a] Moreover, the Co-Pi films have self-repairing characteristics that the films are continuously deposited on the ITO substrate during the OER. [2.131e] Similar with Co-Pi films, they also presented Ni-based amorphous films by electrodeposition method. [2.134] Instead of Co(II) ions and phosphate buffer, they used Ni(II) ions and borate buffer to make the films. Interestingly, the Ni-Bi catalyst is also formed *in situ* and catalyzes the water oxidation reaction under the overpotential value of ~620 mV at pH 9.2. [2.134]

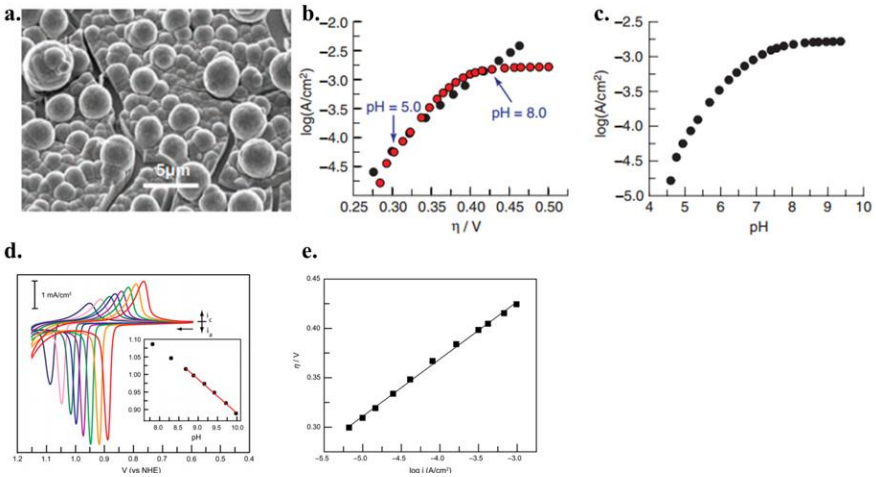

Figure 2.11. (a) SEM image (30° tilt) of the electrodeposited catalyst after $30C/cm^2$ were passed in 0.1 M KPi electrolyte at pH 7.0, containing 0.5 mM Co^{2+}.

(b) Tafel plot (black circles), $\eta = (V_{appl} - iR) - E$ (pH 7) (where V_{appl} is the applied potential), of a catalyst film on ITO in 0.1 M KPi electrolyte pH 7.0, corrected for the iR drop of the solution. pH data were converted into a Tafel plot (red circles), $h = (V_{appl} + 0.059\Delta pH - iR) - E(pH\ 7)$, assuming Nernstian behavior and correcting for the iR drop of the solution. The pH = 5 and pH = 8 data points are indicated by arrows. (c) Current density dependence on pH in 0.1 M KPi electrolyte. The potential was set at 1.24 V (versus NHE) with no iR compensation. (d) CVs scans of a Ni borate catalyst film at pH values of 7.82, 8.30, 8.68, 8.88, 9.16, 9.42, 9.72, and 9.98 in. going from left to right, respectively. The inset shows a linear fit for the 8.7–10.0 pH region, with a slope of 96 mV⁄pH unit. The CVs were taken at scan rates of 50 mV⁄s. (e) Tafel plot, $\eta = (V_{appl} - iR - E^0)$, of a Ni-$B_i$ catalyst film operated in 0.2 M B_i , pH 9.2 where η is the overpotential, iR accounts for the uncompensated solution resistance, and E^0 is the thermodynamic potential for water oxidation at this pH (0.69 V vs. NHE). The slope of the line is 58 mV⁄decade. Reprinted with permission (a), (b), (c) from ref. 2.123a Copyright 2008 American Association for the Advancement of Science and (d), (e) from ref. 2.134 Copyright 2010 Proceedings of the National Academy of Sciences

The Berlinguette group has recently developed another amorphous materials $Fe_{100-y-z}Co_yNi_zO_x$ films, using metal-organic deposition method. [2.127] This method can produce amorphous metal oxide films where metals are distributed homogeneously in the films. [2.127] Surprisingly, the catalytic ability of $Fe_{100-y-z}Co_yNi_zO_x$ films is comparable to that of IrO_x catalysts under basic condition. [2.127] Moreover, in addition to amorphous metal oxide films, the Hongjie Dai group synthesized the ultrathin, layered Ni-Fe-based double hydroxide plates onto mildly oxidized CNT, as shown in Figure 2.12 (a) – (d). [2.132a] This system is also found to be highly catalytically active which is comparable to conventional Ir-based electrocatalysts under basic conditions.

[2.132a] We have summarized Tafel slope, overpotential and onset potential values for oxygen evolution on various solid state OER electrocatalysts in Table 2.5.

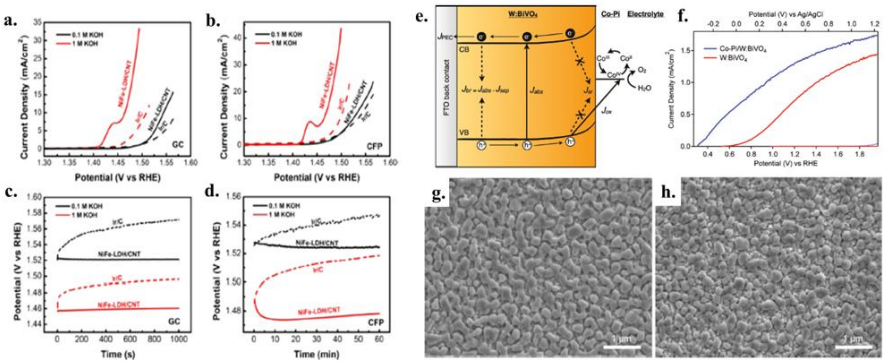

Figure 2.12. (a) iR-corrected polarization curves of NiFe-LDH/CNT hybrid and Ir/C catalyst on GC electrode in 0.1 and 1 M KOH, measured with a catalyst loading of 0.2 mg/cm^2 for both NiFe-LDH/CNT and Ir/C at a continuous electrode rotating speed of 1600 rpm. (b) iR-corrected polarization curves of NiFe-LDH/CNT hybrid and Ir/C catalysts on carbon fiber paper, measured with a catalyst loading of 0.25 mg/cm^2. (c) Chronopotentiometry curves of NiFe-LDH/CNT hybrid and Ir/C catalyst on GC electrode at a constant current density of 2.5 mA/cm^2. (d) Chronopotentiometry curves of NiFe-LDH/CNT hybrid and Ir/C catalyst on CFP at a constant current density of 5 mA/cm^2. (e) Energy diagram showing the kinetic processes active in the Co-Pi/W:$BiVO_4$ PEC photoanodes. (f) Current density-voltage (J-V) curves measured for a W:$BiVO_4$ photoanode before (red) and after (blue) photoassisted electrodeposition of Co-Pi under front-side illumination (solid line) and in the dark (dotted line). (g) Top-view SEM images of representative $BiVO_4$ photoanodes. (h) Top-view SEM images of representative W:$BiVO_4$ photoanodes. Both films were estimated from cross-sectional SEM to be ~300nm. Reprinted with permission (a), (b), (c), and (d)

from ref.2.132a Copyright 2013 American Chemical Society and (e), (f), (g), and (h) from ref. 2.132f Copyright 2011 American Chemical Society

In order to systemically understand and compare the catalytic abilities of transition metal oxide electrocatalysts, the Jaramillo group synthesized various Co, Fe, Ni based electrocatalysts, synthesized by electrodeposition. [2.132b] The overpotential values of the catalysts where current density of the catalysts reached 10 mA/cm^2 were measured for comparison. [2.132b] Under alkaline condition, it was observed that these catalysts can operate OER catalysis under moderate overpotential values between 350 mV and 430 mV. [2.132b]

Catalyst /Substrate	**Preparation Method**	**Electrolyte**	**Activity**			**Ref. (Year)**
			Tafel slope (mV/dec)	**Overpotential**	**Onset potential (V vs. RHE)**	
RuO_2	electrodeposition	0.1M $HCLO_4$(pH 1.3)	40	N/A	1.36	[2.143](2011)
IrO_2	thermal decomposition	1M H2SO4	40	N/A	1.44	[2.144](2009)
Ir/C	N/A	1M KOH	40	10 mA/cm^2@280 mV	N/A	[2.145](1981)
RuO_2	N/A	0.1M KOH	N/A	10 A/g@298 mV	N/A	[2.132a](2013)
IrO_2	N/A	0.1M KOH	N/A	10 A/g@288 mV	N/A	[2.132a](2013)
IrO_x	electrodeposition	1M NaOH	N/A	10 mA/cm^2@325	N/A	[2.132b](2013)

				mV		
hematite(Fe_2O_3)/FTO	Annealing of amor-FeOx	0.1M KOH	40	0.5 mA/cm^2@470 mV	1.62	[2.127](2013)
$LaNiO_3$ electrode	co-precipitation	1M NaOH	43	N/A	1.38	[2.126c](1983)
$LaCoO_3$ electrode	High-T solid-state reactions	1M NaOH	70	N/A	N/A	[2.126c](1983)
$LaMnO_3$ electrode	High-T solid-state reactions	1M NaOH	126	N/A	N/A	[2.126c](1983)
$SrVO_3$ electrode	High-T solid-state reactions	1M NaOH	235	N/A	N/A	[2.126c](1983)
$LaVO_3$ electrode	High-T solid-state reactions	1M NaOH	175	N/A	N/A	[2.126c](1983)
Co_3O_4 /metal	thermal decomposition	1M KOH	45	N/A	1.4	[2.146](1981)
Co_3O_4 /metal	electrophoterical depostion	1M KOH	41	100 mA/cm^2@494 mV	N/A	[2.147](2008)
$[(TGG^{4-})Cu^{II}-OH_2]^{2-}$/GC	Peptide-metal Self Assembly	0.25M phosphate buffer pH11	N/A	N/A	1.75	[2.132d](2013)
NiFe-LDH/CNT	Hummers's method, Solvothermal treatment	1M KOH	31	10 mA/cm^2@240 mV	N/A	[2.132a](2013)
NiFe-LDH/CNT	Hummers's method, Solvothermal treatment	0.1M KOH	35	10 mA/cm^2@300 mV	N/A	[2.132a](2013)
NiFe-LDH NP /GC	Hummers's method, Solvothermal treatment	1M KOH	N/A	5 mA/cm^2@290 mV	N/A	[2.132a](2013)

$Mn_3O_4/CoSe_2$	simple polyol reduction route	0.1M KOH	49	10 mA/cm^2@450 mV	N/A	[2.148](2012)
core-ring $NiCo_2O_4$ electrode	hydroxide decomposition method	1 M KOH	54	100 mA/cm^2@315 mV	N/A	[2.147](2008)
$NiCo_2O_4$ electrode	electrophoterical deposition	1M KOH	59	100 mA/cm^2@438 mV	N/A	[2.147](2008)
$NiCo_2O_4$ electrode	acetyl-acetonate sol-gel route	4M NaOH	N/A	100 mA/cm^2@300 mV	N/A	[2.149](2000)
$Mn_3(PO_4)_2 \cdot 3H_2O$ NP/FTO	Drop casting	0.5 M sodium phosphate electrolyte at pH 7	120	0.316 mA/cm^2@680 mV	N/A	[2.150](2014)
Mn_2O_3 NP/FTO	Drop casting	0.5 M sodium phosphate electrolyte at pH 7	120	0.08 mA/cm^2@680 mV	N/A	[2.150](2014)
$LiMnP_2O_7$/FTO	Drop casting	0.5 M sodium phosphate buffer (pH 7.0)	120	5 A/g@680 mV	N/A	[2.151](2014)
$Li_{1.5}MnP_2O_7$/FTO	Drop casting	0.5 M sodium phosphate buffer (pH 7.0)	120	4 A/g@680 mV	N/A	[2.151](2014)

$Li_{1.7}MnP_2O_7$/FTO	Drop casting	0.5 M sodium phosphate buffer (pH 7.0)	120	2.8 A/g@680 mV	N/A	[2.151](2014)
$Li_2MnP_2O_7$/FTO	Drop casting	0.5 M sodium phosphate buffer (pH 7.0)	120	2 A/g@680 mV	N/A	[2.151](2014)
amor-FeO_x/FTO	photochemical metal-organic deposition	0.1M KOH	40	0.5 mA/cm^2@400 mV	1.55	[2.127](2013)
amor-CoO_x/FTO	photochemical metal-organic deposition	0.1M KOH	42	N/A	1.44	[2.127](2013)
amor-NiO_x/FTO	photochemical metal-organic deposition	0.1M KOH	73	N/A	1.42	[2.127](2013)
amor-$FeCoO_x$/FTO	photochemical metal-organic deposition	0.1M KOH	33	0.5 mA/cm^2@250 mV	1.41	[2.127](2013)
amor-FeNiOx/FTO	photochemical metal-organic deposition	0.1M KOH	24	0.5 mA/cm^2@250 mV	1.44	[2.127](2013)
amor-$FeCoNiO_x$/FTO	photochemical metal-organic deposition	0.1M KOH	31	0.5 mA/cm^2@250 mV	1.42	[2.127](2013)
amor-CoP_i/FTO	electrodeposition	0.1M potassium phosphate electrolyte	60	N/A	1.51	[2.152](2010)

amor-NiB_i/FTO	electrodeposition	0.1M potassium borate pH 9.2	58	1 mA/cm^2@425 mV	1.53	[2.134](2010)
amor-MnO_x/FTO	electrodeposition	0.1M phophate buffer	76	0.5 mA/cm^2@565 mV or 1 mA/cm^2@590 mV	1.59	[2.137d](2012)
$Fe_{100}O_x$/FTO	photochemical metal-organic deposition	0.1 M KOH	40	0.5 mA/cm^2@380 mV, 1 mA/cm^2@410 mV	1.55	[2.153](2013)
$Fe_{36}Co_{64}O_x$/FTO	photochemical metal-organic deposition	0.1 M KOH	40	0.5 mA/cm^2@250 mV, 1 mA/cm^2@270 mV	1.43	[2.153](2013)
$Co_{100}O_x$/FTO	photochemical metal-organic deposition	0.1 M KOH	42	0.5 mA/cm^2@260 mV, 1 mA/cm^2@270 mV	1.44	[2.153](2013)
$Fe_{40}Ni_{60}$Ox/FTO	photochemical metal-organic deposition	0.1 M KOH	34	0.5 mA/cm^2@230 mV, 1 mA/cm^2@250 mV	1.42	[2.153](2013)
$Ni_{100}O_x$/FTO	photochemical metal-organic deposition	0.1 M KOH	73	0.5 mA/cm^2@250 mV, 1 mA/cm^2@280 mV	1.42	[2.153](2013)
$Co_{41}Ni_{59}O_x$/FTO	photochemical metal-organic deposition	0.1 M KOH	73	0.5 mA/cm^2@270 mV, 1 mA/cm^2@300 mV	1.42	[2.153](2013)

$Fe_{39}Co_{39}Ni_{22}O_x$/FTO	photochemical metal-organic deposition	0.1 M KOH	40	0.5 mA/cm^2@250 mV, 1 mA/cm^2@280 mV	1.42	[2.153](2013)
NiFe Oxide/GC	electrodeposition	1M KOH	N/A	5 mA/cm^2@420 mV	N/A	[2.132a](2013)
$Ni_{1-x}Cu_xCo_2O_4$/Ni	thermal decomposition	5M KOH	45~62	100 mA/cm^2@410 mV	N/A	[2.154](2001)
$NiCu_{2-y}Co_yO_4$/Ni	thermal decomposition	5M KOH	60~64	100 mA/cm^2@450 mV	N/A	[2.154](2001)
$NiFeO_x$/GC	electrodeposition	1M NaOH	N/A	10 mA/cm^2@351 mV	N/A	[2.132b](2013)
$CoFeO_x$/GC	electrodeposition	1M NaOH	N/A	10 mA/cm^2@362 mV	N/A	[2.132b](2013)
$NiCoO_x$/GC	electrodeposition	1M NaOH	N/A	10 mA/cm^2@377 mV	N/A	[2.132b](2013)
CoO_x/GC	electrodeposition	1M NaOH	N/A	10 mA/cm^2@392 mV	N/A	[2.132b](2013)
$NiLaO_x$/GC	electrodeposition	1M NaOH	N/A	10 mA/cm^2@410 mV	N/A	[2.132b](2013)
$NiCuO_x$/GC	electrodeposition	1M NaOH	N/A	10 mA/cm^2@412 mV	N/A	[2.132b](2013)
CoO_x/CoP_i/GC	electrodeposition	1M NaOH	N/A	10 mA/cm^2@423 mV	N/A	[2.132b](2013)
NiO_x/GC	electrodeposition	1M NaOH	N/A	10 mA/cm^2@424 mV	N/A	[2.132b](2013)
$NiCeO_x$/	Electrodeposition	1M	N/A	10	N/A	[2.132b](2013)

GC		NaOH		mA/cm^2@433 mV		

*LDH : Layered double hydroxide, *CNT : Carbon Nano Tube, *GC : Glassy Carbon

Table 2.5. Selection of experimental values of Tafel slope, overpotential and onset potential for oxygen evolution on various electrocatalysts and electrodes. Preparation Method and Electrolyte used are described.

As another route, much research has been devoted to the transition metal complexes which are comprised of transition metal and surrounding organic ligands.[2.132c, 2.132d] The organic ligands were used to systemically arrange the transition metals and stabilize the local structure and the valency state of the metals.[2.132c, 2.132d] Due to the high controllability of the organic ligands, a lot of transition metal complexes, including mononuclear, binuclear, and multinuclear complexes, were developed and their catalytic abilities were evaluated.[2.132c] Additionally, the complexes have been used as platforms for understanding the role of local structure of transition metal and surrounding ligands on OER catalysis.[2.132c] However, most of the complexes have difficulty in mass-production compared to transition metal-based oxide films because the synthesis of organic ligands and complexes is not facile.[2.132c] In this respect, ease of synthesis of surrounding organic ligands can be another breakthrough for commercializing the transition metal complexes for OER catalysis.

Additionally, in order to improve the efficiency of the photoelectrochemical (PEC) cell, amorphous transition metal oxides were incorporated with the photocatalysts.[2.132e-g] The Gratzel group employed photo-assisted electro-deposition methods in order to deposit Co-Pi OER catalyst onto α-Fe_2O_3.[2.132e] Using these photo-assisted electro-deposition approaches, Co-Pi[2.126d] films can be uniformly deposited onto α-Fe_2O_3.[2.132e] Due to their uniformity, Co-Pi/α-Fe_2O_3 PEC cells exhibit OER currents of ~ 3 mA/cm^2 at 1.23 V *vs*. RHE under AM 1.5 G.[2.132e] The Gamelin group also incorporated Co-Pi films onto the

well-known photoanode, W-doped $BiVO_4$.[2.132f] After Co-Pi films were deposited onto the photoanode, the onset potential of W doped BiVO4was largely shifted (~ 440 mV) toward the cathodic direction, indicating highly enhanced catalytic activity, as shown in Figure 2.12 (e) - (h).[2.132f] The enhanced catalytic ability of this system mainly results from the Co-Pi films which suppress electron-hole recombination in $BiVO_4$ effectively.[2.132f] Recently, the Wang group also performed similar studies using amorphous $NiFeO_x$ films which is developed by the Berlinguette group.[2.132g] They deposited the amorphous films onto hematite, and found that the a-$NiFeO_x$/hematite system can present very low onset potential of 0.62V vs RHE. [2.132g] Likewise, the transition metal-based OER catalysts have been incorporated with the photoanodes, and they dramatically have been enhancing the activity of photoanodes to realize the overall water splitting photoelectrochemical (PEC) cells. [2.132e-g] The Choi group from Purdue University also designed a simple and stable transition metal-based PEC system which is prepared with bismuth vanadate ($BiVO_4$) photoanode coupled with iron oxyhydroxide (FeOOH). [2.135] They primarily used $BiVO_4$, an n-type semiconductor which has adequate O_2 evolution band positioning at 2.4eV. However, its low stability showed a poor catalytic performance. This problem was overcome by the addition of an FeOOH layer with a photo-deposition method. The high stability of iron during water oxidation not only improved the catalytic stability, which maintained at 1.7 mA/cm^2 for 6 hours with only 2% of decay, but also enhanced its catalytic performance at~7.5 mA/cm^2 under AM 1.5G solar irradiation. This system suggested a new generation of hybrid catalyst for water splitting.

Manganese based OER electrocatalysts and Photosystem II in biological system

Photosystem II in biological system

As described in above section, in nature, there is a water oxidation complex (WOC) in photosystem II (PSII) comprised of the earth-abundant elements Mn and Ca.[2.121] The WOC in PSII, in the form of a cubical $CaMn_4O_5$ cluster, efficiently catalyzes water oxidation under neutral conditions with extremely low overpotential (~160 mV) and a high TOF number (~25,000 mmolO_2 mol^{-1}Mn s^{-1}).[2.121] The low overpotential value and high TOF number of WOC cannot be achieved with any artificially developed electrocatalyts.[2.121d] Recently, X-ray analysis of the PSII structure at a resolution of 1.9 Å provided detailed structural information about a cubical Mn_4CaO_5 cluster stabilized by a surrounding peptide ligand.[2.124] Four Mn atoms are oxo-bridged in asymmetric positions and undergo successive changes in oxidation state, taking part in a so-called Kok cycle, as shown in Figure 2.13.[2.121b, 2.121d, 2.121f] It was also suggested that O-O bond formation occurs at specific sites in the Mn_4CaO_5cluster.[2.121d, 2.121f]

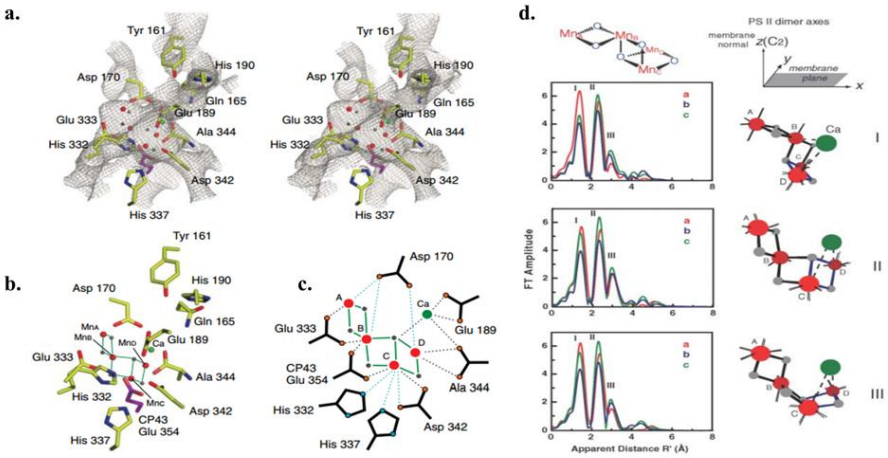

Figure 2.13. (a), (b), (c) Placement of model II for the Mn_4Ca cluster derived from polarized Mn EXAFS in relation to the putative ligands obtained from the 3.0 Å resolution x-ray crystal structure. The spheres represent Mn (red),

Ca (green), and the bridging oxygen ligand atoms (gray). The assignment of ligands is tentative because it is based on the electron density of the Mn_4Ca cluster, and its immediate environment may be altered by x-ray damage. (d) High-resolution structural models for the Mn_4Ca cluster in PSII from polarized EXAFS. The Mn_4Ca models I, II, and III are shown on the right. Reprinted with permission (a), (b), (c) and (d) from ref. 2.121b Copyright 2006 American Association for the Advancement of Science.

Bio-inspired Mn-based OER electrocatalysts

The unique capabilities of the cubical Mn_4CaO_5cluster have inspired the design of many synthetic catalysts for the OER.[2.136] Along with the biological system, manganese oxide compounds have been demonstrated as water splitting catalysts for several decades. Since manganese has the exclusive capability to change valence states easily and rapidly from lower to higher oxidation states (2^+ to 4^+ (or 7^+)), manganese based compounds have become one of the favorable catalyst candidates for water splitting applications. In this respect, research has been focused on the asymmetric geometry and mixed valent (III/IV) states of Mn atoms in the WOC. [2.136] For example, the geometry of oxo-bridged Mn atoms has been synthetically controlled by designed organic ligands. $[Mn_4O_4L_6]^+$(L =$(MeOPh)_2PO_2$) or $[Mn_4O_4L_6]^+$-Nafion system have been recently demonstrated as efficient water oxidation catalysts.[2.136a, 2.136b] The Agapie group has synthesized $[Mn_3CaO_4]^{6+}$ core structure which is almost identical to that of the WOC in nature by using a trinucleating ligand, as shown in Figure 14 (a). [2.136c] This was the first work that mimics the local Mn geometry of the WOC nearly perfect.[2.136c] Moreover, using the $[Mn_3CaO_4]^{6+}$core structure, they further synthesized $Mn_3M(\mu4\text{-}O)(\mu2\text{-}O)$(M = Ca^{2+}, Sr^{2+}, Na^+, Zn^{2+}, Y^{3+}) to understand the role of redox-inactive metals on water oxidation catalysis, as shown in Figure 2.14 (b) – (c).

[2.136d] By comparing their catalysts, they found than redox inactive metals (M) can modulate the redox potential of Mn atoms.[136d] From this result, they make the conclusion that Ca ions might change the redox potential of Mn atoms in the WOC, and consequently enhances the catalytic ability of the WOC. [2.136d] As another route, inspired by the WOC, various crystalline manganese oxide polymorphs and amorphous MnOx have been developed as water oxidation catalysts.[2.136e, 2.136f, 2.137] Demonstration of calcium manganese compounds, such as $CaMn_2O_4$-$4H_2O$, as an improved water oxidation catalyst also represents a bio-inspired effort to mimic the natural Mn_4CaO_5cluster. [2.136e] The Dismukes group mimicked the [Mn_4O_4] core units in the WOC by removing Li ions from $LiMn_2O_4$ Li-ion battery cathode material. [2.138] The Driess group developed amorphous MnO_x nanoparticles the local structure and valence state of the Mn atoms of which resemble with those of the WOC.[2.139] They oxidized inactive, crystalline MnO nanoparticles into active, amorphous MnO_x ($1 < x < 2$) using Ce(IV) oxidants. [2.139] Although they did not intend to mimic the Mn_4CaO_5 cluster, they found that high activity of their catalysts can be originated from the Mn structure and valence state which is similar with those of the Mn_4CaO_5 cluster. [2.137c, 2.137d] For example, The Dau group developed a new electrodeposition method which can present active MnO_x film. [2.137d] This new film shows much higher activity than conventionally electrodeposited films. Using EXAFS and XANES analysis, they found that the newly developed electrodeposited amorphous MnO_x films have mixed valency (III/IV) and disordered Mn geometry which are recognized as important properties of the WOC in nature. [2.137d] Similarly, The Jaramillo group found that the active manganese oxide catalysts have mixed valency state of Mn(III/IV). [2.137c]

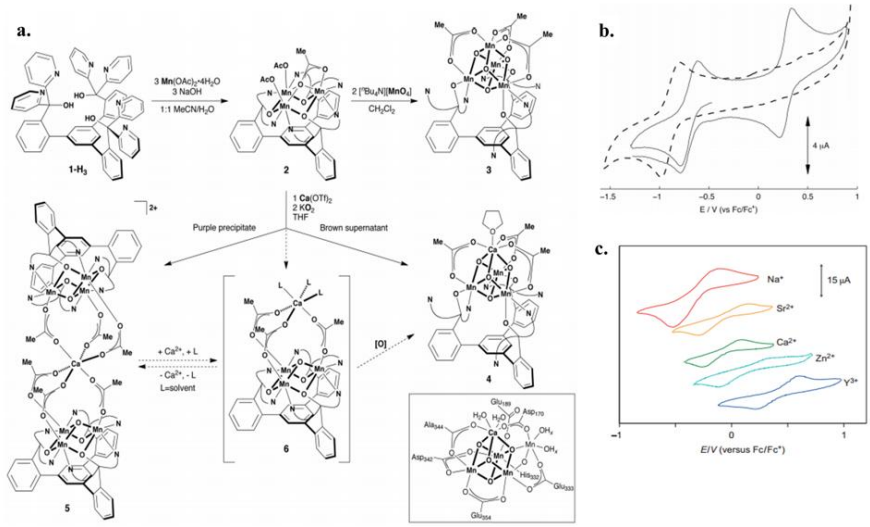

Figure 2.14. (a) Synthesis of bio-inspired Mn-based electrocatalyst. Curved lines in structures schematically represent 2-pyridyl groups. (Inset) A recent structure of the OEC from crystallographic studies is shown. OAc/AcO, acetoxy group; Me, methyl; Bu, butyl (b) Cyclic voltammograms of 3 in (a) (solid trace, DMA solution) and 4 in (a) (dashed trace, DMF solution) with 0.1 M n Bu_4NPF_6. Scan rates: 50 mV/s (3) and 100 mV/s (4). E/V, potential. (c) The redox potentials of the $[MMn_3O_2]$ complexes are correlated with the Lewis acidity of the redox-inactive metal(M : Na, Sr, Ca, Zn, Y). CVs of reported complexes in 0.1M NBu_4PF_6 10:1 CH_2Cl_2/DME (CV of $[1–Na]_2^{4+}$ in CH_2Cl_2) using a glassy carbon disc electrode at a scan rate of 100 mVs^{-1} Reprinted with permission (a) and (b) from ref. 2.136c Copyright 2011 American Association for the Advancement of Science and (c) from ref. 2.136d Copyright 2013 Nature Publishing Group.

Bottleneck in Mn based electrocatalysts in OER

While Manganese has very attractive characteristics for OER catalysts, it unfortunately has a problem to be used as an electrocatalyst in neutral pH. The

Nakamura group studied the relationship of manganese oxidation state in a wide range of pH(4-14).[2.140] As shown in Figure 2.15 (a), they defined that the activity degradation of manganese catalysts under neutral pH are related to the manganese charge disproportionation (CD) effect as:

$$2Mn^{3+} + 2H_2O \leftrightarrow Mn^{2+} + MnO_2 + 4H^+$$

Since the mechanism of OER starts from a low oxidation state, goes to a higher oxidation state, and goes back to a low oxidation state with generating proton and electrons, the intermediate state plays a key role to control the rate of OER. For manganese, Mn^{3+}, the trivalent state is the intermediate state. However, considering the electronic configuration, Mn (III) ($t_{2g}3e_g1$) accompanies strong Jahn-Teller distortion and tends to break the symmetry of the orbitals; thus, this state is not stable in symmetric octahedral structures. Due to the inherent instability of Mn^{3+} under neutral condition, the change of surface state does not follow the high efficiency catalytic routine. When the cycle reaches Mn^{3+} states, due to the CD effect, it goes back to Mn^{2+} or the partial change of Mn^{3+} to Mn^{4+} postpones the OER with instability of catalysts. Therefore, many different types of manganese oxide catalysts only performed high catalytic activities under strong alkaline condition (pH11~pH14), where CD does not occur.[2.137c] To prevent the CD effect of manganese electrocatalysts, many trials were applied. For example, the Nakamura group, which investigated CD effect in neutral pH, performed the ligand exchange method on MnO_2 nanoparticles with Poly-(allylamine hydrochloride) (PAH) to stabilize Mn^{3+} states by differentiating the structure of manganese cluster from symmetric to asymmetric, as shown in Figure 2.15 (b) – (c).[2.140]

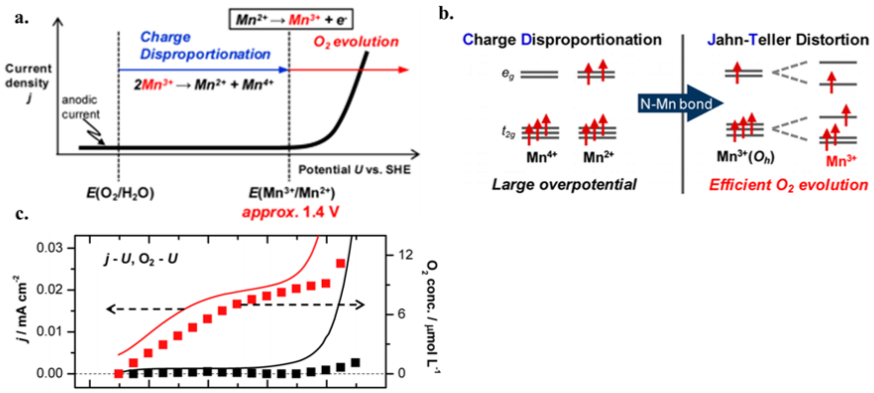

Figure 2.15. (a) Schematic illustration of a current density (j) vs potential (U) curve for a pristine δ-MnO_2 electrode under neutral pH conditions. The surface-associated intermediate Mn^{3+} species are rapidly consumed by charge disproportionation to form Mn^{2+} and Mn^{4+}, resulting in no net charges passing across the electrode. (b) Result of Charge Disproportionation and Jahn-Teller Distortion. (c) Current density (solid line) and dissolved O_2 concentration (filled squares) for PAH-MnO_2 and pristine δ-MnO_2 electrodes at pH 8. Solid red line and squares: PAHMnO_2; solid black line and squares: pristine δ-MnO_2. Reprinted with permission (a), (b) and (c) from ref. 2.140 Copyright 2012 American Chemical Society.

Mn valency and structure effect on water oxidation catalysis

Rigid and highly symmetric MnO_6 octahedrons in MnO_2 compounds hamper Jahn-Teller (J-T) distortion in the local coordination environment of Mn centers. As stated above, Mn^{2+} and Mn^{4+} cannot be easily oxidized or reduced to Mn^{3+}, which is an important intermediate step during oxygen evolution. [2.141] Conversely, Mn^{3+} containing Mn-oxide compounds, such as Mn_2O_3, cannot easily change valence state due to the high reorganizational energy associated with Mn^{3+} oxidation. [2.140-2.141] Similar phenomena can be found in the Ni(III)-

Bi catalysts.[2.134] Non-anodized Ni^{3+} -Bi catalysts have properties inferior (Tafel slope: 100 mV/dec) to those of their anodized counterparts because of the reorganization energy required to oxidize J-T distorted Ni^{3+} to non-distorted Ni^{4+}.[2.134] Therefore, the fundamental challenge is how to flexibly change the valence state of Mn atoms with ease and stabilize Mn^{3+} state in a crystal structure during oxygen evolution at neutral pH. Recently, the Navrotsky group introduced the concept of manganese mixed valence catalyst which has better OER during oxidation and reduction stage.[2.142] Because the change of the significant structure does not occur under closely balanced equilibrium of two mixed valence, it has more advantages for OER. They proved their theory with four different manganese compounds; CaMnO, Mn_2O_3, MnO_2 and Mn_3O_4. CaMnO had the highest catalytic activities and efficient electron transfer due to the existence of mixed valence (Mn^{3+} and Mn^{4+}).

2.4 Photoelectrochemical water splittng

Solar-to-hydrogen efficiency

In a solar water splitting system, the solar-to-hydrogen (STH) efficiency is defined as how much incident solar energy is converted to chemical energy in the form of H_2 and O_2. If the Faraday efficiencies for H_2 and O_2 evolution reactions are unity, we can calculate the STH efficiency (η) of a system from as:

$$\eta = \frac{J(1.23V)}{P_{in}} \tag{2.25}$$

where J is the externally measured photo-current density at short circuit condition from two electrode measurement, 1.23V is the useful thermodynamic potential in stored H_2 and O_2, and P_{in} is the power density of the illumination. For AM 1.5G illumination, P_{in} is 100 mW/cm^2. However, there are very few PEC materials and devices known to split water without external bias or sacrificial mediators. Therefore, it is useful to define conversion efficiency for water electrolysis half reaction to diagnose and benchmark a PEC materials for HER or OER.

For half reactions of water electrolysis, hypothetical thermodynamic efficiency of an individual photoanode for OER and photocathode for HER can be determined from J-V of each electrode from 3 electrode measurement, such that

$$\eta = \frac{J_{mp}V_{mp}}{P_{in}} \quad \text{and} \quad ff = \frac{I_{mp}V_{mp}}{I_{sc}V_{oc}}, \tag{2.26}$$

where V_{mp} and I_{mp} are the voltage and the current density at the maximum power point, and the fill factor (ff) is calculated using the open-circuit voltage (V_{oc}) and the short circuit current density (J_{sc}) in this half-reaction system. A three-electrode measurement consists of working, counter, and reference electrodes, and in this case, the polarization losses associated with driving the other half reaction for water electrolysis at the counter electrode is neglected. Therefore, individual photoanode and photocathode half reaction J-V data represent only the efficiency of each electrode for half-reaction. It must be

emphasized that this efficiency cannot be used to represent overall water splitting STH efficiency. In case of unassisted photoelectrolysis of water, a measurement must be used for a two-electrode configuration, consisting of a working and a counter electrode. For detailed discussion for PEC measurement and diagnosis methods, one should refer to the work of Turner *et al.* [2.161]

Semiconductor-electrolyte junction and requirement for water splitting

When a semiconductor is immersed into an aqueous solution with a redox couple having electrochemical potential of $E^o(A/A^-)$, where E^o is the Nernst potential of the redox couple, majority carriers (electrons for an n-type semiconductor or holes for a p-type semiconductor) will move between the semiconductor and the electrolyte until electrochemical potential, i.e., Fermi energy, is constant throughout the system. Because of this flow, an interfacial electric field forms and, therefore, the energy band of the semiconductor bends at the interface. For example, when an n-type semiconductor is immersed in an aqueous solution, electrons, a majority carrier, in an n-type semiconductor will be depleted at the semiconductor/electrolyte interface, building an electric field, as shown in Figure 2.16. Due to this built-in E-field, photo-excited holes in the semiconductor can be injected into the electrolyte, initiating a redox reaction. In case of a p-type semiconductor, the band bends downward, to drive photoexcited electrons to an electrolyte upon illumination. Note that in a PEC junction, the conduction and valence band edges at the semiconductor/electrolyte interface is usually fixed upon application of bias and/or illumination like the metal/semiconductor Schottky junction. Therefore, the barrier height, $q\phi_b$, is determined by the difference between the redox potential and electron affinity of a semiconductor.

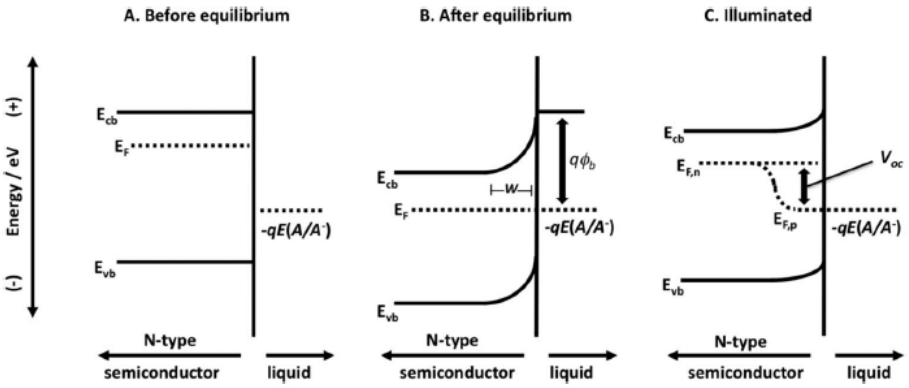

Figure 2.16. The band diagram of a semiconductor/liquid junction (A) before contact between a semiconductor and a liquid and (B) after equilibration in the dark and (C) in steady state illumination. In (B), W is the depletion width, $E_{F,n}$ and $E_{F,p}$ are the electron and hole quasi-Fermi level, respectively. The photovoltage under illumination is determined by $E_{F,n}$ and $-qE^o(A/A^-)$. Reprinted with permission from ref. 2.120a Copyright 2010 American Chemical Society.

Figure 2.17 shows the energetic (thermodynamic) requirements for efficient photoelectrolysis of water. Firstly, the material must have suitable bandgap for high efficiency. To split water, the bandgap of a semiconductor must be greater than 1.23 eV, the thermodynamic potential needed for water electrolysis. Moreover, one must consider additional energy to overcome the overpotential associated with HER and OER. To use large portion of solar spectrum for high efficiency, the bandgap of semiconductor must be less than ~ 3 eV. Hence, the suitable bandgap of semiconductor for water splitting is 1.6~2.4 eV, depending on overpotential.

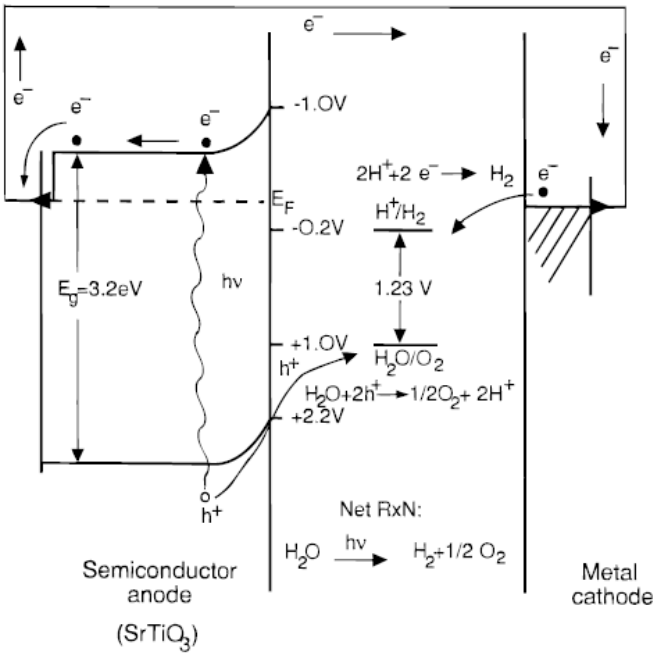

Figure 2.17. Energy level diagram for water splitting with a single junction semiconductor, e.g. $SrTiO_3$. Reprinted with permission from ref. 2.156 Copyright 1996 American Chemical Society.

Secondly, the semiconductor must have suitable band edge positions relative to the redox potentials for spontaneous carrier injection. For HER, a conduction band edge must be more negative than the H^+/H_2 redox potential and for OER, a valence band edge must be more positive than the O_2/H_2O redox potential. Therefore, the band edges of a semiconductor must straddle the water reduction and oxidation potentials for unassisted solar water splitting, as shown in Figure 2.17. The band edge position of various semiconductors relative to HER and OER potential are shown in Figure 2.18. As depicted in Figure 2.18, very few semiconductor materials satisfy this condition and they, unfortunately, have large bandgaps. Finally, a semiconductor must be stable in an aqueous solution for at least 10 years.

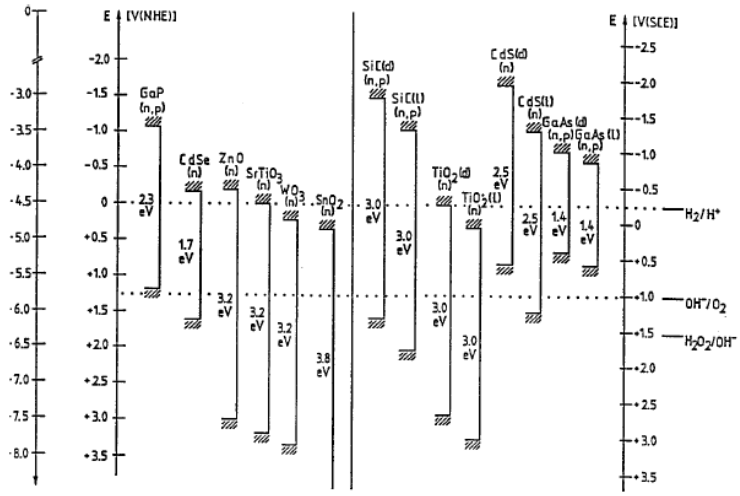

Figure 2.18. Position of energy band of various semiconductors in the dark (d) and in light (l) with respect to the electrochemical scale. Reprinted with permission from ref. 2.156 Copyright 1996 American Chemical Society.

A single-junction PEC device can be constructed with semiconductor working electrodes satisfying the requirements and a dark counter electrode, as shown in Figure 2.19 (a). In Figure 2.19 (a), an n-type semiconductor is used as a photoanode for OER, as an example. Under illumination, electron-hole pairs in semiconductor are generated by incident photon having larger energy than the bandgap of the semiconductor. Then, photogenerated holes are drifted and injected to oxidize water due to the internal electric field, and electrons move a dark counter electrode (normally Platinum electrode) to reduce water. According to recent theoretical work by Jaramillo et al. STH efficiency of a single-junction PEC cell can reach up to 11.2 % when a semiconductor with bandgap of 2.26 eV and appropriate co-catalysts (e.g., Pt for HER and RuO_2 for OER) are used. Unfortunately, as shown in Figure 18, very few materials show substantial STH efficiency due to bandgap limitation and/or band edge mismatch.[2.157]

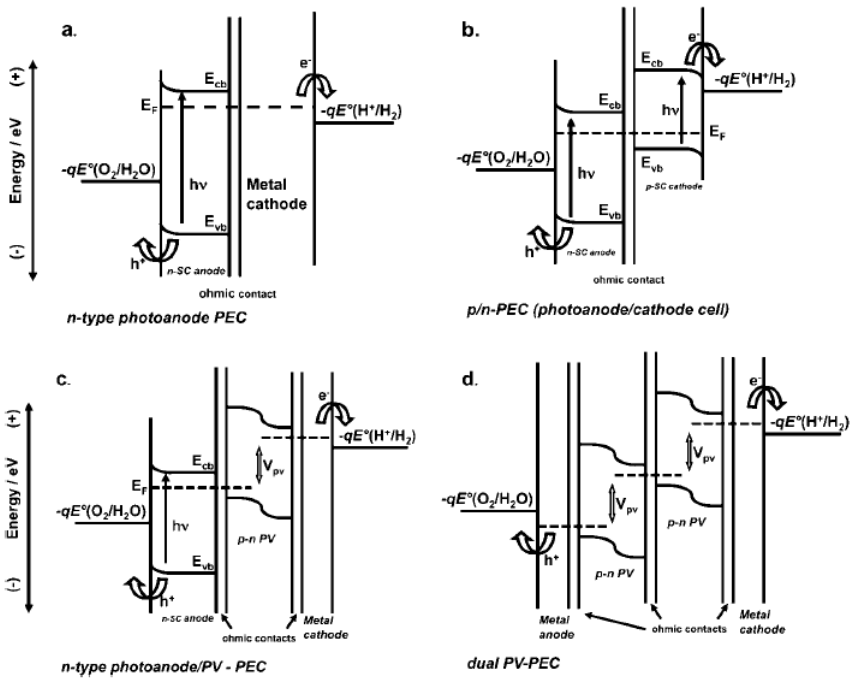

Figure 2.19. Energy diagrams for (a) a single junction photoanode (n-SC = n-type semiconductor) PEC with metal counter electrode (b) a PEC diode, or pn-PEC, with n-type and p-type photoelectrodes connected in tandem (c) n-type photoelectrode in series with a solar cell connected to a metal counter electrode (d) double junction tandem solar cell connected with OER and HER catalysts. Reprinted with permission from ref. 2.120a Copyright 2010 American Chemical Society.

In order to relax band edge and bandgap constraints, a tandem PEC cell, called photoelectrochemical diode or pn-PEC, is proposed. Figure 2.19 (b) shows a schematic of pn-PEC cell structures: an n-type semiconductor with the valence band edge more positive than O_2/H_2O redox potential and a p-type semiconductor with the conduction band edge more negative than H_2/H_2O redox potential, connected with ohmic contact. In this pn-PEC cell,

photogenerated holes in photoanode are transferred to water for OER and photogenerated electrons in photocathode are injected to water for HER under illumination. Majority carriers in each photoelectrode (electrons for n-type and holes for p-type semiconductors) will disappear at the ohmic junction by recombination. Therefore, the band edge constraint of a single-junction PEC cell is eliminated in a pn-PEC cell, and various combination of semiconductors can be used. More importantly, a pn-PEC cell can use semiconductors with different bandgaps to fully utilize solar spectrum for higher STH efficiency. For example, in Figure 2.19 (b), sunlight would strike an n-type semiconductor with high bandgap, so transmitted photons can be absorbed in a smaller bandgap p-type semiconductor. The STH efficiency of dual bandgap absorber with stacked structure can reach 22.8% with top and bottom material bandgaps of 1.84 eV and 1.23 eV, respectively. [2.157]

Another strategy to relax the band edge constraints is integrating a PV cell with a photoelectrode, as shown in Figure 2.19 (c). For example, in Figure 2.19 (c), a photoanode can oxidize water but cannot reduce water by itself since its conduction band edge is slightly positive to HER redox potential. However, by connecting with a pn-junction solar cell through ohmic contact, HER occurs at the pn-junction solar cell since it provides additional photovoltage. It should be noted that this configuration can also use semiconductors with two or more different bandgaps in tandem, and therefore can result in > 20% STH efficiency.

Finally, an integrated system of an electrolyzer on a PV cell can also be used to split water. In this device structure, as shown in Figure 2.19 (d), a PV cell with high photovoltage generates electron-hole pairs to drive water electrolysis at metal catalysts at the front and back surfaces. This devices are free of any band edge constraint, since the solid state semiconductor pn-junction is buried beneath the metal catalysts: the semiconductor/liquid junction responsible for the band edge pinning, no longer exists. Because of

this device characteristics, this cell is also called as a buried junction PEC cells. It should be noted that a solar cell for photoelectrolysis must have V_{oc} of 1.5 – 2.0 V in order to split water. Since it is very challenging to fabricate a solar cell with such high V_{oc} from a single junction, it is often required to form a tandem configuration or complex series connected solar cells to obtain high V_{oc}.

Semiconductor Materials for Photoelectrolysis

Photocathodes for hydrogen evolution

As stated in the previous section, in order to reduce water to H_2, a solar absorber must have a conduction band edge more negative than the hydrogen redox potential. In addition, for high efficiency, it must have suitable bandgap to generate sufficient HER under illumination. Typical materials in commercial photovoltaic industry, such as Si, III-V compound semiconductor, II-VI semiconductor including CdTe and CIGS ($CuIn_xGa_{(1-x)}Se_2$) and so on, satisfy those requirements for HER. Unfortunately, these materials are unstable in an aqueous solution. In the following sections, we introduce some of these materials for PEC H_2 production and provide recent advances for corrosion protection strategies.

Silicon:

Silicon is an attractive candidate for a photocathode: Si is earth-abundant, relatively stable under H_2-producing conditions, and has a suitable conduction band edge position for HER and bandgap for light absorption. In addition, the established Si PV industry can be leveraged for rapid deployment of a Si-based PEC system. However, Si suffers from high reflection of about 25% at the Si/water interface, and high overpotential for HER. In addition, indirect bandgap of Si requires a thick Si wafer to absorb most of sunlight, which leads to the fact that costly high-purity Si absorber is needed to collect

photoexcited carriers across the thick Si wafer.

Recent advances in nanotechnology provides promising routes toward overcoming these challenges, originating from nanostructure's excellent optical and electrical properties. For example, Oh *et al*. showed that a nanoporous *black* Si photocathode improves H_2 production rate more than 20% compared to polished Si, by suppressing optical reflection below 3% of the solar spectrum useful for Si by forming a density-graded layer, as shown in Figure 2.20 (a)-(c) .[2.158] In addition, the high surface area of nanostructures provides more surface reaction sites and hence reduces overpotential more than 60 mV for HER, as shown in Figure 2.20 (c). [2.158] Likewise, Si nano- and microwires decorated with inexpensive catalysts, such as Mo_3S_4 clusters, show hydrogen production rates comparable to Si with Pt co-catalysts, due to large catalysts loading on the high surface area structured Si.[2.159] In addition, the Lewis and Atwater groups at CalTech reported that Si microwire arrays grown by the vapor-liquid-solid (VLS) mechanisms have a similar H_2-producing performance compared to high-purity Si wafer, due to orthogonalization of light absorption in the length of the wire and charge collection in the diameter of the wire, as depicted in Figure 2.20 (e)-(g). [2.17] Furthermore, it is shown that a solid-state pn junction formed by diffusion can provide additional photovoltage for HER. Through these advances, currently, the current density for HER at reversible potential can reach over 10% STH with a high bandgap photoanode in tandem.

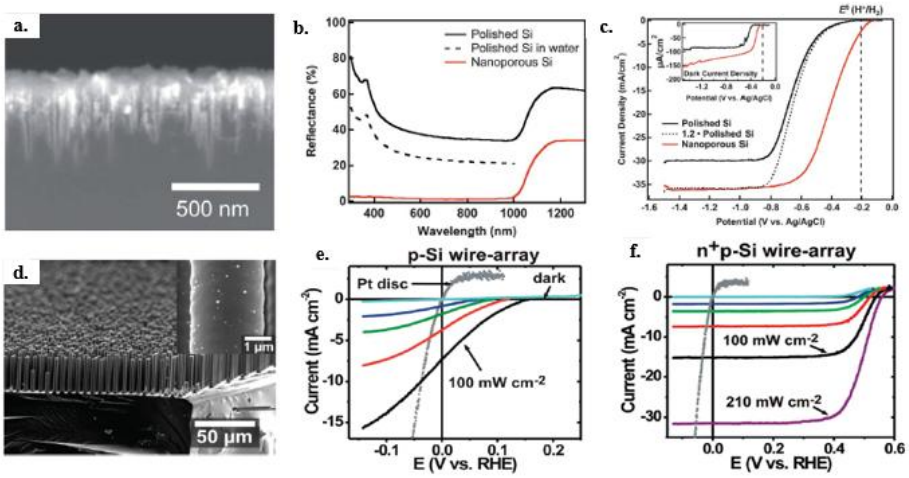

Figure 2.20. Examples of Si nano- and microstructures for PEC HER: (a) cross-sectional SEM image; (b) the total optical reflectance of polished and nanoporous Si in air measured with an integrated sphere; (c) PEC *j-V* curve of Si photocathodes for HER under simulated 1 sun illumination; (d) SEM image of the microwire-array electrodes with Pt particles; (e) PEC *j-E* curve for wire-array Pt/p-Si electrodes; (f) PEC *j-E* curve for Pt/n^+p-Si wire-array *J-E* data obtained in 0.5M H_2SO_4. Reprinted with permission (a), (b) and (c) from ref. 2.158 Copyright 2011The Royal Society of Chemistry and (d), (e) and (f) from ref. 2.17 Copyright 2011 American Chemical Society.

III-V semiconductors:

III-V semiconductor is one of promising materials for photocathode, because many of those have a suitable direct bandgap for light absorption and band edge position for hydrogen reduction. For example, InP has a bandgap of 1.35 eV that can absorb visible and near-infra-red spectrum. Heller and Vadimsky first introduced p-InP photocathode with Ru catalyst and achieved 12% hydrogen half reaction efficiency. Notably, Tuner *et al.* first developed a PEC for water spitting using p-$GaInP_2$ in 1998. [2.161] It has an ideal direct bandgap of

1.83 eV for photo-electrolysis, but its valence band edge is slightly negative to than the OER. To supply additional driving force for water splitting, p-$GaInP_2$ was grown monolithically on a GaAs PV cell. Schematic of the monolithic p-$GaInP_2$/pn-GaAs PEC cell is shown in Figure 2.21 (a). This cell shows STH efficiency of 12.8% under concentrated illumination for extended period of operation time, as shown in Figure 2.21 (b) and (c). [2.161] However, III-V semiconductors, including InP and p-$GaInP_2$, undergo reductive decomposition in water under H_2-producing condition. Recently, Javey *et al.* introduced thin pin-hole free TiO_2 protective coating on p-InP nanopillar structure made by RIE etching, as shown in Figure 2.21 (d). Figure 2.21 (e)-(f) show PEC *I-V* curve and stability test of the TiO_2 coated p-InP nanopillars for HER under simulated 1-sun illumination: nanopillars enhance photocurrents more than 20% and the TiO_2 coating on InP enhanced the stability over 4 hours.[2.162]

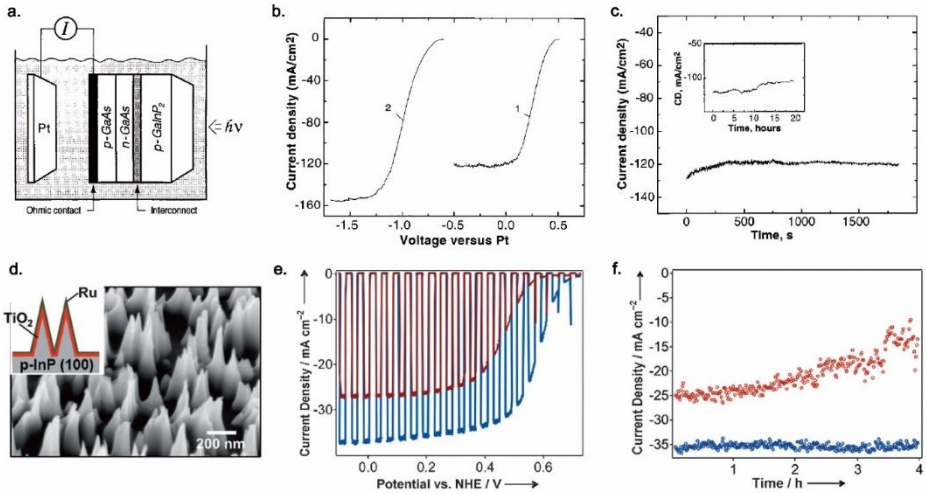

Figure 2.21. (a) Schematic of the p-$GaInP_2$ PEC/pn-GaAs PV device; (b) *j-V* characteristics for p-$GaInP_2$ on pn-GaAs cell (curve 1) and p-$GaInP_2$ (curve 2) photo-electrodes under white light illumination. (c) Long-term stability test of the PEC/PV device under short circuit condition. (d) SEM image of TiO_2 (3-5

nm thick) coated p-InP nanopillars (NPLs) photocathode with the Ru cocatalyst (thickness, ca. 2nm); (e) *J-E* curve of p-InP photocathode for planar (red trace) and NPL (blue) samples; (f) Long-term stability test of the photocurrent level of a p-InP/TiO_2/Ru phtocathode[2.162] Reprinted with permission (a), (b) and (c) from ref. 2.161 Copyright 1998 American Association for the Advancement of Science and (d), (e) and (f) from ref. 2.162 Copyright 2012 John Wiley & Sons.

CIGS and CZTS:

Cu(In,Ga)Se_2 (CIGS) and CZTS are well-known materials in thin film solar cells and an attractive candidate for a photocathode since it is possible to control their bandgap by modifying their In/Ga and S/Se composition ratio. However, CIGS and CZTS are also unstable in water and requires corrosion protection strategies. Recently, Domen *et al.* and coworker showed that CIGS with Pt particle is highly resistant to reductive decomposition and CdS layer enhances charge transfer kinetics by forming pn-junction. For example, Pt/CdS/CIGS photocathode had 59% incident photon-to-current conversion efficiency (IPCE) that was three times higher than Pt/CIGS. Moreover, they operated Pt/CIGS without degradation for 16 hours at the negative potential of -0.24 V versus RHE. [2.163] They also applied this structure to Cu_2ZnSnS_4 (CZTS). The onset potential of Pt/CdS/CZTS was 0.5 V higher than that of Pt/CZTS and The IPCE of Pt/CdS/CZTS was 16 times higher than Pt/CZTS. Additionally, with application of TiO_2 on CdS/CZTS, the IPCE of the electrode increased 5 times compared to that of Pt/CdS/CZTS. This Pt/TiO2/CdS/CZTS electrode achieved 1.2% STH efficiency.[2.164] In 2011, the same group designed a Pt/CdS/CZTS thin film photocathode with hollow-column morphology on Mo mesh. This surface morphology increased surface area of the CZTS and easier transfer of photo generated holes from the surface

to the Mo Substrate. This structure showed a very high photocurrent density under light irradiation. [2.165] In 2012, the Domen group also introduced $CuGa_3Se_5$ (CGSe) thin film with 1.8eV of bandgap to improve efficiency. They deposited ZnS on CGSe films for pn-junction, modified deposition condition for reducing anion vacancies and controlled the growth kinetics to enlarge the grain for enhanced charge transfer characteristic. Pt/ZnS/CGSe thin film photocathode reached 2.8% STH efficiency.[2.166]

Metal oxide:

Cu_2O is an attractive p-type oxide for hydrogen reduction. Because copper is abundant and Cu_2O can be processed by industrially proven low-cost methods. In addition, Cu_2O has a bandgap of 2eV and possesses favorable energy band edge position for HER. But Cu_2O has poor stability in aqueous solutions, because the redox potentials for the reduction and oxidation of monovalent copper oxide lie within bandgap: it reduces to Cu under cathodic bias. [2.167] In 2011, the Gratzel group designed a Cu_2O photocathode with protecting layer. Al-doped ZnO and TiO_2 were deposited on the Cu_2O electrode surface by atomic layer deposition (ALD), as shown in Figure 2.22 (a) and (b). Figure 2.22 (a) shows Al:ZnO/TiO_2/Cu_2O photocathode sturucture. Al:ZnO/TiO_2/Cu_2O photocathode with Pt particle makes photocurrent up to -7.6 mA/cm^2 at 0V versus RHE and did not show degradation of photocurrent during 1 hour of stability testing. Figure 2.22 (c) shows the photocurrent and stability of Al:ZnO/TiO_2/Cu_2O photocathode. [2.167] Recently, the same group shows that a Al:ZnO/TiO_2/Cu_2O photocathode with MoS_2 HER catalyst can produce photocurrent of -5.7 mA/cm^2 with good stability during 10 hours of continuous operation. [2.168]

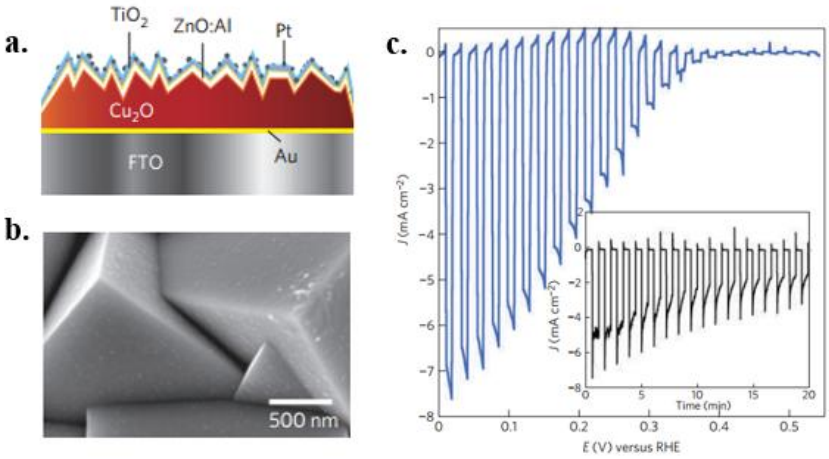

Figure 2.22. The surface-protected Cu_2O electrode. (a) Schematics of the electrode structure; (b) plan-view scanning electron micrograph (SEM) of the electrode with TiO_2/AZO/Cu_2O followed by electrodeposition of Pt nanoparticles. (c) The PEC *j-V* for the surface-protected electrode under chopped AM 1.5 light illumination. Reprinted with permission from ref. 2.167 Copyright 2011 Nature Publishing Group

Photoanode for water oxidation

An n-type semiconductor is used as a photoanode to oxidize water for OER. In order to drive OER in a photoanode, the materials must have a valence band edge position more positive than the redox potential of the water oxidation reaction. In addition, since OER competes with oxidation of a semiconductor itself, a photoanode must be stable in water oxidation condition. Because of this stability under oxidative environment, typical photoanode materials are metal-oxide semiconductors. However metal-oxide materials have poor minority carrier diffusion length that can cause poor oxygen evolution efficiency. In the following sections, we present an overview of some photoanodes and present seminal efforts to overcome their shortcomings.

Metal oxides:

Since the seminal work of Fujishima and Honda,[2.170] TiO_2 has been one of the most widely investigated PEC materials. However TiO_2-based PEC devices show poor STH efficiency due to large bandgap (~3 eV) and short minority carrier diffusion length (L=10~100nm).[2.171] Therefore, metal oxide semiconductors with smaller bandgap, such as WO_3 (bandgap ~ 2.7 eV), $BiVO_4$ (bandgap ~ 2.4 eV), and a-Fe_2O_3 (bandgap 2.1 eV) have received attention due to their ability to absorb visible light.[2.172, 2.173, 2.174] In addition, various approaches have been investigated to enhance charge transport in metal oxide semiconductors. For example, 1-dimensional metal oxide nanostructures have shown to greatly improve charge transport by orthogonalization. Figure 2.23 (a) and (b) show the difference of light absorption and carrier collection between planar metal oxide and 1-dimensional metal oxide nanostructures.[2.120] Other strategies to enhance charge separation include extrinsic doping to enhance carrier mobility and creation of electric field in a semiconductor. These new approaches are well-documented in recent reviews,[2.175- 2.177] but here we focus on some of recent results of $BiVO_4$ and α-Fe_2O_3.

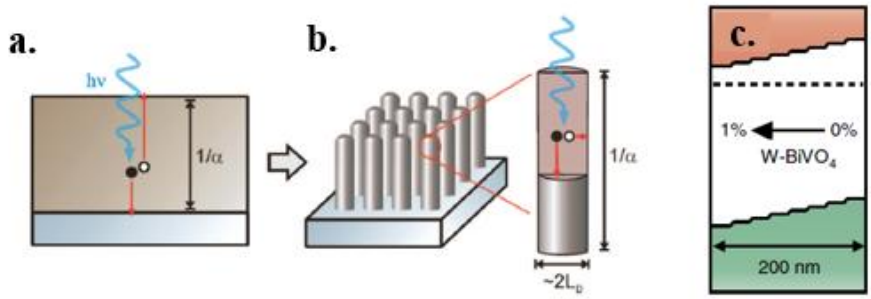

Figure 2.23. Strategies for carrier transport enhancement in semiconductors. (a) in a planar device, photogenerated carriers in bulk must diffuse the entire

thickness of the cell before collection; (b) in a 1-D structure, charges are collected via the diameter of the 1-D structures (c) Band diagram schematic of a semiconductor with gradient doping (e.g., W:$BiVO_4$). Reprinted with permission (a) and (b) from ref. 2.120a Copyright 2010 American Chemical Society and (c) from ref. 2.169 Copyright 2013 Nature Publishing Group.

$BiVO_4$ is a promising photoanode materials due to visible light response from bandgap of 2.4 eV, but shows poor IPCE due to charge recombination. Extrinsic doping with W, Mo, and other materials can increase carrier mobility and therefore enhance charge separation in the quasi-neutral region by increasing minority carrier diffusion length. [2.178-2.180, 2.131d] Gradient doping can further enhance charge separation by reducing charge recombination by creating electric field, as shown in Figure 2.23 (c). For example, Krol *et al.* reported that a 10-step gradient-doped W:$BiVO_4$ photoanode with Co-Pi catalyst generates a photocurrent density of 3.6 mA/cm^2 at 1.23V versus RHE under AM1.5 that represents a ~60% improvement over the W:$BiVO_4$ photoanode with homogeneous doping. Combination of this electrode with a 2-jn a-Si solar cell yield a water splitting cell with a ~4.9% STH efficiency. [2.169]

Nanostructures with characteristic length smaller than hole diffusion length can also effectively suppress bulk carrier recombination even without additional doping. In recent work by Choi *et al.*, nanoporous $BiVO_4$ shows a photocurrent density of ~3.3 mA/cm^2 at 0.6V versus RHE under sulfite oxidation condition, corresponding APCE of 70% at 420 nm with application of 0.6V versus RHE. In addition, the same group shows that that FeOOH catalyst reduces surface recombination and NiOOH catalyst enhanced water oxidation kinetics. A NiOOH/FeOOH/ $BiVO_4$ photoanodes reached high photocurrent of 2.8 mA/cm^2 at 0.6V versus RHE without degradation over 48 hours. [2.181]

Similar strategies have applied to hematite, α-Fe_2O_3, photoanodes which has 2.1eV bandgap and hole diffusion length of 2~4nm. Introducing dopants, such as Si and Pt, significantly increases carrier mobility and hence enhances PEC performance.[2.182-2.185] For instance, single crystalline, worm-like Pt-doped α-Fe_2O_3 by solution process and two-step annealing process showed remarkable performance of 4.32 mA/cm^2 that corresponds to 34% of the maximum theoretical limit expected for hematite. The IPCE values at short wave length (<400nm) were about 60~80%, which were unprecedented values for hematite photoanodes, as shown in Figure 2.24. [2.186]

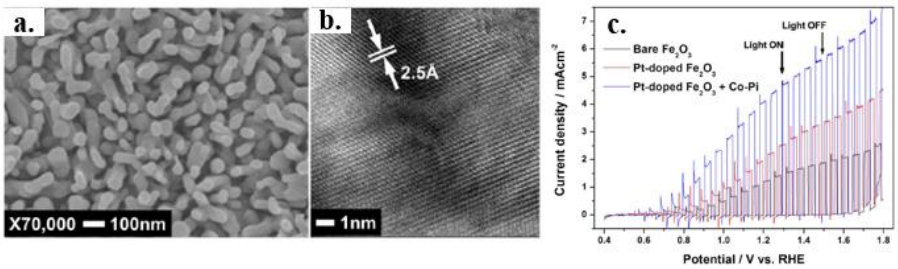

Figure 2.24. (a), (b) SEM and TEM images of a single-crystalline hematite (α-Fe_2O_3) photoanode with two-step annealing process at 550℃ and 800℃. (C) PEC *j-V* curves for OER with the hematite photoanode. Reprinted with permission from ref. 2.186 Copyright 2013 Nature Publishing Group.

Band-edge mismatching Semiconductors:

Since the valence band edge position of silicon is too negative to redox potential of OER, n-type silicon cannot oxidize water without external bias under illumination. Instead, silicon *can* produce O_2 by forming p^+n junction or metal-insulator-semiconductor (MIS) junction. These solid state junctions are buried beneath metal/electrolyte junction and therefore the band edge position of Si is no longer fixed. However, Si is easily oxidized under water oxidation

condition. Therefore, a Si photoanode with buried junctions has been focused on protecting the Si surface against oxidation and/or corrosion. In 2011, the Mclntyre group introduced the Si photoanode protected by ALD TiO_2 layer. A thin TiO_2 layer is very stable in oxidation condition and has low electron-tunneling resistance (< 0.006 Ω/cm^2 for p$^+$-Si). This ALD-TiO_2 Si photoanode with thin Ir catalyst layer forms MIS junction. It is capable of reaching much higher saturation current density (~10 mA/cm^2 at 0.4V versus NHE, 1M NaOH) and can operate under high oxidation condition(1.7 V versus NHE, 1M NaOH) without degradation over at least 24 hours. [2.187] More recently, Kenny et al. demonstrated that Ni nanoparticles, an earth abundant OER catalysts, can protect Si photoanodes against oxidation. A 2-nm Ni on Si with native SiO_2 forms MIS junction and shows a constant photocurrent density of 10 mA/cm^2 in 1M KOH during operation over 24 hours. This photoanode in 0.65M K-borate and 0.35M Li-borate solution was able to maintain a photocurrent of 10 mA/cm^2 for ~80 hours without degradation. [2.188]

Photovoltaic and electrolyzer

Instead of PEC devices, solar cells integrated with OER and HER catalysts can be used for unassisted solar H_2 production. In this case, the solar cell should generate a photovoltage of at least 1.23 V and 1.8 ~ 2.3 V for optimal STH efficiency. Bockris *et al.* first introduced a PV to split the water using a triple-junction amorphous silicon solar cell. This triple-junction a-Si PV cell was connected by a RuO_2 layer on a Ti substrate bottom cell as O_2 evolving catalyst and Pt particle on a-Si top cell as H_2 evolving catalyst, and achieved 5% STH efficiency under AM 1 radiation.[2.189] With advances in PV and catalysts technologies, Nocera *et al.* demonstrated water splitting cell based on an a-Si triple-junction solar cell with an earth-abundant catalyst. This cell consisted of triple-junction a-Si solar cell with Co-OEC as OER catalyst and NiMoZn as the HER catalyst. This device shows STH efficiencies of 4.7% for a wired

configuration.[2.190]

2. 5 Conclusion

Hydrogen production powered by solar power is still in its infancy terms of efficiency, durability and commercialization, but solar-driven fuel generation can be the most promising system for sustainable, secure, and plentiful energy supply. A PEC cell for water splitting has drawn much attention as a direct route to solar to hydrogen conversion energy. Development of HER and OER catalyst for the PEC cell has increased STH conversion efficiency, however, many attempts described herein to develop highly efficient catalysts have had limited success. The development of an earth-abundant catalyst that operates at neutral pH with a low overpotential is still a challenge. In PEC cells, negative effects from catalysts should be considered such as reflection by the overlaid catalyst, an unfavorable band structure, photocorrosion, and recombination sites at the interface. To design cost-effective and long-term stable catalysts and PEC with full solar absorbance, issues such as the optical properties, stability, band structure, and interfacial properties should be comprehensively considered.

Bibliography

2.1. A. Kudo, Y. Miseki, *Chemical Society Reviews* **2009**, *38*, 253-278.

2.2. aD. G. Nocera, *Daedalus* **2006**, *135*, 112-115; bN. S. Lewis, D. G. Nocera, *Proceedings of the National Academy of Sciences* **2006**, *103*, 15729-15735; cA. J. Esswein, D. G. Nocera, *Chemical reviews* **2007**, *107*, 4022-4047.

2.3. U. S. E. I. Administration., **2013**.

2.4. aP. M. Cox, R. A. Betts, C. D. Jones, S. A. Spall, I. J. Totterdell, *Nature* **2000**, *408*, 184-187; bJ. R. Petit, J. Jouzel, D. Raynaud, N. I. Barkov, J. M. Barnola, I. Basile, M. Bender, J. Chappellaz, M. Davis, G. Delaygue, M. Delmotte, V. M. Kotlyakov, M. Legrand, V. Y. Lipenkov, C. Lorius, L. Pepin, C. Ritz, E. Saltzman, M. Stievenard, *Nature* **1999**, *399*, 429-436; cJ. L. Sarmiento, C. Le Quéré, *Science* **1996**, *274*, 1346-1350; dS. Solomon, G.-K. Plattner, R. Knutti, P. Friedlingstein, *Proceedings of the National Academy of Sciences* **2009**, *106*, 1704-1709; eK. Caldeira, M. R. Rampino, *Geophysical Research Letters* **1991**, *18*, 987-990.

2.5. C. Ronneau, *Energie, pollution de l'air et developpement durable*, **2004**.

2.6. L. M. Gandia, G. Arzamedi, P. M. Diéguez, *Renewable Hydrogen Technologies: Production, Purification, Storage, Applications and Safety*, Newnes, **2013**.

2.7. A. Ursua, L. M. Gandia, P. Sanchis, *Proceedings of the IEEE* **2012**, *100*, 410-426.

2.8. aJ. Ivy, National Renewable Energy Lab., Golden, CO (US), **2004**; bA. Roy, Loughborough University **2006**.

2.9. R. J. Gilliam, J. W. Graydon, D. W. Kirk, S. J. Thorpe, *International Journal of Hydrogen Energy* **2007**, *32*, 359-364.

2.10. J. Larminie, A. Dicks, M. S. McDonald, *Fuel cell systems explained*,

Vol. 2, Wiley New York, **2003**.

2.11. H. Wolfschmidt, O. Paschos, U. Stimming, in *Fuel Cell Science*, John Wiley & Sons, Inc., **2010**, pp. 1-70.

2.12. B. E. Conway, G. Jerkiewicz, *Electrochimica Acta* **2000**, *45*, 4075-4083.

2.13. J. K. Nørskov, T. Bligaard, A. Logadottir, J. R. Kitchin, J. G. Chen, S. Pandelov, U. Stimming, *Journal of The Electrochemical Society* **2005**, *152*, J23-J26.

2.14 L. R. F. Allen J. Bard, *John Wiley & Sons, Inc.* **2001**, 864.

2.15. J. Tafel, *Z. phys. Chem* **1905**, *50*, 641.

2.16. B. E. Conway, B. V. Tilak, *Electrochimica Acta* **2002**, *47*, 3571-3594.

2.17. S. W. Boettcher, E. L. Warren, M. C. Putnam, E. A. Santori, D. Turner-Evans, M. D. Kelzenberg, M. G. Walter, J. R. McKone, B. S. Brunschwig, H. A. Atwater, N. S. Lewis, *Journal of the American Chemical Society* **2011**, *133*, 1216-1219.

2.18. J. R. McKone, E. L. Warren, M. J. Bierman, S. W. Boettcher, B. S. Brunschwig, N. S. Lewis, H. B. Gray, *Energy & Environmental Science* **2011**, *4*, 3573-3583.

2.19. C. Chen, Y. Kang, Z. Huo, Z. Zhu, W. Huang, H. L. Xin, J. D. Snyder, D. Li, J. A. Herron, M. Mavrikakis, M. Chi, K. L. More, Y. Li, N. M. Markovic, G. A. Somorjai, P. Yang, V. R. Stamenkovic, *Science* **2014**, *343*, 1339-1343.

2.20. V.I. Bystrov, L.I. Krishtalik, *Elektrokhimiya* **1967**, *3*, 1499.

2.21. V.I. Bystrov, L.I. Krishtalik, *Elektrokhimiya* **1967**, *3*, 1345.

2.22. A.B. Kilimnik, A.L. Rotinyan, *Elektrokhimiya* **1970**, *6*, 330.

2.23. K. Gossner, F. Mansfeld, *Z. Phys. Chem. Frankf. A.M.* **1968**, *58*, 24.

2.24. J. O. M. Bockris, I. A. Ammar, A. K. M. S. Huq, *The Journal of Physical Chemistry* **1957**, *61*, 879-886.

2.25. B. E. Conway, J. O. Bockris, apos, M., *The Journal of Chemical*

Physics **1957**, *26*, 532-541.

2.26. A. K. Vijh, *The Journal of Physical Chemistry* **1968**, *72*, 1148-1156.

2.27. R. J. Mannan, *Ph.D. Thesis, University of Pennsylvania* **1967**.

2.28. N. Pentland, J. O. M. Bockris, E. Sheldon, *Journal of The Electrochemical Society* **1957**, *104*, 182-194.

2.29. D. J. G. Ives, S. Swaroopa, *Journal of the Chemical Society (Resumed)* **1955**, 3489-3497.

2.30. U. V. Palm, V. E. Past, *Zh. Fiz. Khim.* **1964**, *38*, 773.

2.31. A.B. Kilimnik, A.L. Rotinyan, *Elektrokhimiya* **1969**, *5*, 1235.

2.32. T.T. Tenno, V.A. Slet, U.V. Palm, *Proceedings 2nd Symposium on Double Layer and Adsorption on Solid Electrodes, Tartu* **1970**, 361.

2.33. L.P. Bicelli, A. La Vecchia, M. Graziono, *Waddtech. Rp.* **1961**, 61-63.

2.34. A.L. Rotinyan, A.B. Kilimnik, E.D. Levin, *Proceedings 2nd Symposium on Double Layer and Adsorption on Solid Electrodes, Tartu* **1970**, 321.

2.35. J. O. M. Bockris, S. Srinivasan, *Electrochimica Acta* **1964**, *9*, 31-44.

2.36. Z. A. Lofa, W. Pao-Ming, *Zh. Fiz. Khim.* **1963**, *37*, 2300.

2.37. I.V. Kudryashov, E.S. Burmistrov, V.L. Kirlis, *Elektrokhimiya* **1970**, *5*, 737.

2.38. A.G. Pecherskaya, V.V. Stender, *Zh. Fiz. Khim.* **1950**, *24*, 856.

2.39. B. E. Wilde, F. G. Hodge, *Electrochimica Acta* **1969**, *14*, 619-627.

2.40. Kho Ngok Ba, Nguyen Dyk Vi, *Elektrokhimiya* **1968**, *4*, 990.

2.41. M. Magi, U. Palm, V. Past, *Uch. Zap. Tartu. Gos. Univ.* **1966**, *193*, 96.

2.42. S.Ya. Lanina, Z.A. Iofa, *Elektrokhimiya* **1969**, *5*, 359.

2.43. E. J. Kelly, *Journal of The Electrochemical Society* **1965**, *112*, 124-131.

2.44. U. Palm, M. Pärnoja, *Uch. Zap. Tartu. Gos. Univ.* **1970**, *265*, 34..

2.45. H.F. Fischer, H. Heiling, *Z. Elektrochem.* **1956**, *54*, 187.

2.46. A.M. Morozov, I.A. Bagotskaya, E.A. Preis, *Elektrokhimiya* **1969**, *5*, 40.

2.47. S. Raicheva, L. Andreeva, *C. R. Acad. Bulg. Sci.*, **1965**, *18*, 1023.

2.48. J. N. Butler, M. L. Meehan, *Transactions of the Faraday Society* **1966**, *62*, 3524-3534.

2.49. B. G. Dekker, M. Sluyters-Rehbach, J. H. Sluyters, *Journal of Electroanalytical Chemistry and Interfacial Electrochemistry* **1969**, *21*, 137-147.

2.50. B.N. Kabanov, A.N. Frumkin, *Zh. Fiz. Khim.* **1934**, *5*, 418.

2.51. Z.A. Iofa, K.P. Mikulin, *Zh. Fiz. Khim.* **1944**, *18*, 137.

2.52. J. O. M. Bockris, R. Parsons, *Transactions of the Faraday Society* **1949**, *45*, 916-928.

2.53. D. B. Matthews, *Ph. D. Thesis, University of Pennsylvania* **1965**.

2.54. J. N. Butler, A. C. Makrides, *Transactions of the Faraday Society* **1964**, *60*, 1664-1676.

2.55. A.L. Rotinyan, E.D. Levin, *Elektrokhimiya* **1970**, *6*, 328.

2.56. J. N. Butler, M. Dienst, *Journal of The Electrochemical Society* **1965**, *112*, 226-232.

2.57. A. T. Petrenko, *Elektrokhimiya* **1965**, *1*, 839.

2.58. I.V. Gamali, V.V. Stender, *Zh. Prikl. Khim.* **1962**, *35*, 127.

2.59. N.M. Kozhevnikova, A.L. Rotinyan, *Elektrokhimiya* **1965**, *1*, 664.

2.60. E.I. Mikhailova, Z.A. Iofa, *Elektrokhimiya* **1965**, *1*, 107.

2.61. A. K. M. S. Huq, A. J. Rosenberg, *Journal of The Electrochemical Society* **1964**, *111*, 270-278.

2.62. A. T. Kuhn, P. M. Wright, *Journal of Electroanalytical Chemistry and Interfacial Electrochemistry* **1970**, *27*, 319-323.

2.63. D.K. Avdeyev, G.V. Aleksandrov, *Y.V. Durdin, Proceedings 2nd Symposium on Double Layer and Adsorption on Solid Electrodes, Tartu* **1970,** 58.

2.64. H. Shiratori, *Denki Kagaku* **1961**, *29*, 765.

2.65. B. E. Conway, *Proceedings of the Royal Society of London. Series A. Mathematical and Physical Sciences* **1960**, *256*, 128-144.

2.66. A.G. Pecherskaya, V.V. Stender, *Zh. Fiz. Khim.* **1950**, *24*, 856.

2.67. K. Punning, V. Past, *Uch. Zap. Tartu. Gos. Univ.* **1969**, *265*, 34.

2.68. P. Rüetschi, B. D. Cahan, *Journal of The Electrochemical Society* **1957**, *104*, 406-413.

2.69. J. P. Hoare, S. Schuldiner, *The Journal of Chemical Physics* **1956**, *25*, 786-787.

2.70. D. Galizzioli, *Thesis, University of Milan* **1969**.

2.71. A. T. Petrenko, *Zh. Fiz. Khim.* **1962**, *36*, 1527.

2.72. N. T. Thomas, K. Nobe, *Journal of The Electrochemical Society* **1970**, *117*, 622-626.

2.73. N. Hackerman, C. D. Hall, *Journal of The Electrochemical Society* **1954**, *101*, 321-327.

2.74. O.L. Kabanova, A.N. Doronin, *Elektrokhimiya* **1970**, *6*, 222.

2.75. Ya.M. Kolotyrkin, L.A. Medvedeva, *Zh. Fiz. Khim* **1951**, *25*, 1365.

2.76. J. O. M. Bockris, R. Parsons, *Transactions of the Faraday Society* **1948**, *44*, 860-872.

2.77. A.L. Rotinyan, N.P. Fedotov, Li Un Sok, *Zh. Fiz. Khim.* **1957**, *31*, 1295.

2.78. V.L. Kheifets, B.S. Krastkov, A.L. Rotinyan, *Elektrokhimiya* **1970**, *6*, 916.

2.79. A. N. Frumkin, *Advances in Electrochemistry and Electrochemical Engineering* **1969**, *3*.

2.80. K. Gossner, *Z. Phys. Chem. Frankf. A.M.* **1963**, *36*, 392.

2.81. S. Schuldiner, *Journal of The Electrochemical Society* **1952**, *99*, 488-494.

2.82. S. Schuldiner, *Journal of The Electrochemical Society* **1954**, *101*,

426-432.

2.83. S. Schuldiner, *Journal of The Electrochemical Society* **1959**, *106*, 891-895.

2.84. R. K. Shervedani, A. Lasia, *Journal of The Electrochemical Society* **1998**, *145*, 2219-2225.

2.85. J. Choi, Y. Qu, M. Hoffmann, *Journal of Nanoparticle Research* **2012**, *14*, 1-12.

2.86. I. M. Kodintsev, S. Trasatti, *Electrochimica Acta* **1994**, *39*, 1803-1808.

2.87. J. Kibsgaard, T. F. Jaramillo, F. Besenbacher, *Nat Chem* **2014**, *6*, 248-253.

2.88. D. Voiry, M. Salehi, R. Silva, T. Fujita, M. Chen, T. Asefa, V. B. Shenoy, G. Eda, M. Chhowalla, *Nano Letters* **2013**, *13*, 6222-6227.

2.89. V. Damien, Y. Hisato, L. Junwen, S. Rafael, C. B. A. Diego, F. Takeshi, C. Mingwei, A. Tewodros, B. S. Vivek, E. Goki, C. Manish, *Nature Materials* **2013**, *12*, 850-855.

2.90. F. Harnisch, G. Sievers, U. Schröder, *Applied Catalysis B: Environmental* **2009**, *89*, 455-458.

2.91. D. Kong, H. Wang, Z. Lu, Y. Cui, *Journal of the American Chemical Society* **2014**, *136*, 4897-4900.

2.92. B. Cao, G. M. Veith, J. C. Neuefeind, R. R. Adzic, P. G. Khalifah, *Journal of the American Chemical Society* **2013**, *135*, 19186-19192.

2.93. Y. Sun, C. Liu, D. C. Grauer, J. Yano, J. R. Long, P. Yang, C. J. Chang, *Journal of the American Chemical Society* **2013**, *135*, 17699-17702.

2.94. Z. Wu, B. Fang, Z. Wang, C. Wang, Z. Liu, F. Liu, W. Wang, A. Alfantazi, D. Wang, D. P. Wilkinson, *ACS Catalysis* **2013**, *3*, 2101-2107.

2.95. B. Seger, A. B. Laursen, P. C. K. Vesborg, T. Pedersen, O. Hansen, S. Dahl, I. Chorkendorff, *Angewandte Chemie International Edition* **2012**, *51*, 9128-9131.

2.96. J. D. Benck, Z. Chen, L. Y. Kuritzky, A. J. Forman, T. F. Jaramillo, *ACS Catalysis* **2012**, *2*, 1916-1923.

2.97. D. H. Youn, S. Han, J. Y. Kim, J. Y. Kim, H. Park, S. H. Choi, J. S. Lee, *ACS Nano* **2014**, *8*, 5164-5173.

2.98. W. F. Chen, C. H. Wang, K. Sasaki, N. Marinkovic, W. Xu, J. T. Muckerman, Y. Zhu, R. R. Adzic, *Energy & Environmental Science* **2013**, *6*, 943-951.

2.99. A. B. Laursen, T. Pedersen, P. Malacrida, B. Seger, O. Hansen, P. C. K. Vesborg, I. Chorkendorff, *Physical Chemistry Chemical Physics* **2013**, *15*, 20000-20004.

2.100. A. B. Laursen, P. C. K. Vesborg, I. Chorkendorff, *Chemical Communications* **2013**, *49*, 4965-4967.

2.101. H. Vrubel, D. Merki, X. Hu, *Energy & Environmental Science* **2012**, *5*, 6136-6144.

2.102. D. Merki, S. Fierro, H. Vrubel, X. Hu, *Chemical Science* **2011**, *2*, 1262-1267.

2.103. T. F. Jaramillo, K. P. Jørgensen, J. Bonde, J. H. Nielsen, S. Horch, I. Chorkendorff, *Science* **2007**, *317*, 100-102.

2.104. M. A. Lukowski, A. S. Daniel, F. Meng, A. Forticaux, L. Li, S. Jin, *Journal of the American Chemical Society* **2013**, *135*, 10274-10277.

2.105. T. F. Jaramillo, J. Bonde, J. Zhang, B.-L. Ooi, K. Andersson, J. Ulstrup, I. Chorkendorff, *The Journal of Physical Chemistry C* **2008**, *112*, 17492-17498.

2.106. Y. Li, H. Wang, L. Xie, Y. Liang, G. Hong, H. Dai, *Journal of the American Chemical Society* **2011**, *133*, 7296-7299.

2.107. X. Ge, L. Chen, L. Zhang, Y. Wen, A. Hirata, M. Chen, *Advanced Materials* **2014**, *26*, 3100-3104.

2.108. Z. Chen, D. Cummins, B. N. Reinecke, E. Clark, M. K. Sunkara, T. F. Jaramillo, *Nano Letters* **2011**, *11*, 4168-4175.

2.109. J. Kibsgaard, Z. Chen, B. N. Reinecke, T. F. Jaramillo, *Nat Mater* **2012**, *11*, 963-969.

2.110. W.-F. Chen, K. Sasaki, C. Ma, A. I. Frenkel, N. Marinkovic, J. T. Muckerman, Y. Zhu, R. R. Adzic, *Angewandte Chemie International Edition* **2012**, *51*, 6131-6135.

2.111. H. Wang, Z. Lu, D. Kong, J. Sun, T. M. Hymel, Y. Cui, *ACS Nano* **2014**, *8*, 4940-4947.

2.112. K. Novoselov, A. K. Geim, S. Morozov, D. Jiang, M. K. I. Grigorieva, S. Dubonos, A. Firsov, *Nature* **2005**, *438*, 197-200.

2.113. aY. Liang, Y. Li, H. Wang, J. Zhou, J. Wang, T. Regier, H. Dai, *Nature Mater.* **2011**, *10*, 780-786; bJ.-D. Qiu, G.-C. Wang, R.-P. Liang, X.-H. Xia, H.-W. Yu, *J. Phys. Chem. C* **2011**, *115*, 15639-15645; cQ. Xiang, J. Yu, M. Jaroniec, *Chem. Soc. Rev.* **2012**, *41*, 782-796.

2.114. U. Sim, T.-Y. Yang, J. Moon, J. An, J. Hwang, J.-H. Seo, J. Lee, K. Y. Kim, J. Lee, S. Han, B. H. Hong, K. T. Nam, *Energy Environ. Sci.* **2013**, *6*, 3658-3664.

2.115. J. Kibsgaard, Z. Chen, B. N. Reinecke and T. F. Jaramillo, *Nat Mater*, **2012**, 11, 963-969.

2.116. Y. Zheng, Y. Jiao, L. H. Li, T. Xing, Y. Chen, M. Jaroniec, S. Z. Qiao, *ACS Nano* **2014**, *8*, 5290-5296.

2.117. Y. Zheng, Y. Jiao, Y. Zhu, L. H. Li, Y. Han, Y. Chen, A. Du, M. Jaroniec, S. Z. Qiao, *Nat Commun* **2014**, *5*.

2.118. A. J. Bard, L. R. Faulkner, *Electrochemical methods: fundamentals and applications, Vol. 2*, Wiley New York, **1980**.

2.119. H. E. Zittel, F. J. Miller, *Analytical Chemistry* **1965**, *37*, 200-203.

2.120. aM. G. Walter, E. L. Warren, J. R. McKone, S. W. Boettcher, Q. Mi, E. A. Santori, N. S. Lewis, *Chemical Reviews* **2010**, *110*, 6446-6473; bA. J. Bard, M. A. Fox, *Accounts of Chemical Research* **1995**, *28*, 141-145; cD. Gust, T. A. Moore, A. L. Moore, *Accounts of Chemical*

Research **2009**, *42*, 1890-1898; dJ. R. Swierk, T. E. Mallouk, *Chemical Society Reviews* **2013**, *42*, 2357-2387; eM. Gratzel, *Nature* **2001**, *414*, 338-344; fT. J. Meyer, *Accounts of Chemical Research* **1989**, *22*, 163-170; gJ. Barber, *Chemical Society Reviews* **2009**, *38*, 185-196; hT. A. Faunce, W. Lubitz, A. W. Rutherford, D. MacFarlane, G. F. Moore, P. Yang, D. G. Nocera, T. A. Moore, D. H. Gregory, S. Fukuzumi, K. B. Yoon, F. A. Armstrong, M. R. Wasielewski, S. Styring, *Energy & Environmental Science* **2013**, *6*, 695-698.

2.121. aB. Loll, J. Kern, W. Saenger, A. Zouni, J. Biesiadka, *Nature* **2005**, *438*, 1040-1044; bJ. Yano, J. Kern, K. Sauer, M. J. Latimer, Y. Pushkar, J. Biesiadka, B. Loll, W. Saenger, J. Messinger, A. Zouni, V. K. Yachandra, *Science* **2006**, *314*, 821-825; cK. N. Ferreira, T. M. Iverson, K. Maghlaoui, J. Barber, S. Iwata, *Science* **2004**, *303*, 1831-1838; dY. Umena, K. Kawakami, J.-R. Shen, N. Kamiya, *Nature* **2011**, *473*, 55-60; eT. A. Roelofs, W. Liang, M. J. Latimer, R. M. Cinco, A. Rompel, J. C. Andrews, K. Sauer, V. K. Yachandra, M. P. Klein, *Proceedings of the National Academy of Sciences* **1996**, *93*, 3335-3340; fH. Dau, L. Iuzzolino, J. Dittmer, *Biochimica et Biophysica Acta (BBA) - Bioenergetics* **2001**, *1503*, 24-39.

2.122. Y. Tachibana, L. Vayssieres, J. R. Durrant, *Nat Photon* **2012**, *6*, 511-518.

2.123. aM. W. Kanan, D. G. Nocera, *Science* **2008**, *321*, 1072-1075; bT. A. Betley, Q. Wu, T. Van Voorhis, D. G. Nocera, *Inorganic Chemistry* **2008**, *47*, 1849-1861.

2.124. A. Fujishima, K. Honda, *Nature* **1972**, *238*, 37-38.

2.125. I. C. Man, H.-Y. Su, F. Calle-Vallejo, H. A. Hansen, J. I. Martínez, N. G. Inoglu, J. Kitchin, T. F. Jaramillo, J. K. Nørskov, J. Rossmeisl, *ChemCatChem* **2011**, *3*, 1159-1165.

2.126. aP. Rasiyah, A. C. C. Tseung, *Journal of The Electrochemical Society*

1984, *131*, 803-808; bS. Trasatti, *Electrochimica Acta* **1984**, *29*, 1503-1512; cJ. O. Bockris, T. Otagawa, *The Journal of Physical Chemistry* **1983**, *87*, 2960-2971; dJ. Suntivich, K. J. May, H. A. Gasteiger, J. B. Goodenough, Y. Shao-Horn, *Science* **2011**, *334*, 1383-1385.

2.127. R. D. L. Smith, M. S. Prévot, R. D. Fagan, Z. Zhang, P. A. Sedach, M. K. J. Siu, S. Trudel, C. P. Berlinguette, *Science* **2013**, *340*, 60-63.

2.128. E. Gileadi, *Electrode Kinetics for Chemists, Chemical Engineers, and Materials Scientists*, wiley, **1993**.

2.129. S.-Y. Huang, P. Ganesan, W. S. Jung, N. Cadirov, B. N. Popov, *ECS Transactions* **2010**, *33*, 1979-1987.

2.130. Y. Matsumoto, E. Sato, *Materials Chemistry and Physics* **1986**, *14*, 397-426.

2.131. aW. J. Youngblood, S.-H. A. Lee, Y. Kobayashi, E. A. Hernandez-Pagan, P. G. Hoertz, T. A. Moore, A. L. Moore, D. Gust, T. E. Mallouk, *Journal of the American Chemical Society* **2009**, *131*, 926-927; bF. Liu, J. J. Concepcion, J. W. Jurss, T. Cardolaccia, J. L. Templeton, T. J. Meyer, *Inorganic Chemistry* **2008**, *47*, 1727-1752; cL. Duan, F. Bozoglian, S. Mandal, B. Stewart, T. Privalov, A. Llobet, L. Sun, *Nat Chem* **2012**, *4*, 418-423; dY. Zhao, J. R. Swierk, J. D. Megiatto, B. Sherman, W. J. Youngblood, D. Qin, D. M. Lentz, A. L. Moore, T. A. Moore, D. Gust, T. E. Mallouk, *Proceedings of the National Academy of Sciences* **2012**, *109*, 15612-15616; eM. W. Kanan, J. Yano, Y. Surendranath, M. Dincă, V. K. Yachandra, D. G. Nocera, *Journal of the American Chemical Society* **2010**, *132*, 13692-13701.

2.132. aM. Gong, Y. Li, H. Wang, Y. Liang, J. Z. Wu, J. Zhou, J. Wang, T. Regier, F. Wei, H. Dai, *Journal of the American Chemical Society* **2013**, *135*, 8452-8455; bC. C. L. McCrory, S. Jung, J. C. Peters, T. F. Jaramillo, *Journal of the American Chemical Society* **2013**, *135*,

16977-16987; cM. Yagi, M. Kaneko, *Chemical Reviews* **2000**, *101*, 21-36; dM.-T. Zhang, Z. Chen, P. Kang, T. J. Meyer, *Journal of the American Chemical Society* **2013**, *135*, 2048-2051; eD. K. Zhong, M. Cornuz, K. Sivula, M. Gratzel, D. R. Gamelin, *Energy & Environmental Science* **2011**, *4*, 1759-1764; fD. K. Zhong, S. Choi, D. R. Gamelin, *Journal of the American Chemical Society* **2011**, *133*, 18370-18377; gC. Du, X. Yang, M. T. Mayer, H. Hoyt, J. Xie, G. McMahon, G. Bischoping, D. Wang, *Angewandte Chemie International Edition* **2013**, *52*, 12692-12695.

2.133. Z. Chen, T. J. Meyer, *Angewandte Chemie International Edition* **2013**, *52*, 700-703.

2.134. M. Dincă, Y. Surendranath, D. G. Nocera, *Proceedings of the National Academy of Sciences* **2010**, *107*, 10337-10341.

2.135. J. A. Seabold, K.-S. Choi, *Journal of the American Chemical Society* **2012**, *134*, 2186-2192.

2.136. aR. K. Hocking, R. Brimblecombe, L.-Y. Chang, A. Singh, M. H. Cheah, C. Glover, W. H. Casey, L. Spiccia, *Nat Chem* **2011**, *3*, 461-466; bW. F. Ruettinger, D. M. Ho, G. C. Dismukes, *Inorganic Chemistry* **1999**, *38*, 1036-1037; cJ. S. Kanady, E. Y. Tsui, M. W. Day, T. Agapie, *Science* **2011**, *333*, 733-736; dE. Y. Tsui, R. Tran, J. Yano, T. Agapie, *Nat Chem* **2013**, *5*, 293-299; eM. M. Najafpour, T. Ehrenberg, M. Wiechen, P. Kurz, *Angewandte Chemie International Edition* **2010**, *49*, 2233-2237; fR. Brimblecombe, D. R. J. Kolling, A. M. Bond, G. C. Dismukes, G. F. Swiegers, L. Spiccia, *Inorganic Chemistry* **2009**, *48*, 7269-7279.

2.137. aM. Fekete, R. K. Hocking, S. L. Y. Chang, C. Italiano, A. F. Patti, F. Arena, L. Spiccia, *Energy & Environmental Science* **2013**, *6*, 2222-2232; bF. Jiao, H. Frei, *Chemical Communications* **2010**, *46*, 2920-2922; cY. Gorlin, T. F. Jaramillo, *Journal of the American Chemical*

Society **2010**, *132*, 13612-13614; dI. Zaharieva, P. Chernev, M. Risch, K. Klingan, M. Kohlhoff, A. Fischer, H. Dau, *Energy & Environmental Science* **2012**, *5*, 7081-7089.

2.138. D. M. Robinson, Y. B. Go, M. Greenblatt, G. C. Dismukes, *Journal of the American Chemical Society* **2010**, *132*, 11467-11469.

2.139. A. Indra, P. W. Menezes, I. Zaharieva, E. Baktash, J. Pfrommer, M. Schwarze, H. Dau, M. Driess, *Angewandte Chemie International Edition* **2013**, *52*, 13206-13210.

2.140. T. Takashima, K. Hashimoto, R. Nakamura, *Journal of the American Chemical Society* **2012**, *134*, 18153-18156.

2.141. D. M. Robinson, Y. B. Go, M. Mui, G. Gardner, Z. Zhang, D. Mastrogiovanni, E. Garfunkel, J. Li, M. Greenblatt, G. C. Dismukes, *Journal of the American Chemical Society* **2013**, *135*, 3494-3501.

2.142. N. Birkner, S. Nayeri, B. Pashaei, M. M. Najafpour, W. H. Casey, A. Navrotsky, *Proceedings of the National Academy of Sciences* **2013**, *110*, 8801-8806.

2.143. E. Tsuji, A. Imanishi, K.-i. Fukui, Y. Nakato, *Electrochimica Acta* **2011**, *56*, 2009-2016.

2.144. L. Ouattara, S. Fierro, O. Frey, M. Koudelka, C. Comninellis, *J Appl Electrochem* **2009**, *39*, 1361-1367.

2.145. S. Trasatti, *Electrodes of conductive metallic oxides*, Elsevier, Amsterdam 2.etc.., **1981**.

2.146. C. Iwakura, A. Honji, H. Tamura, *Electrochimica Acta* **1981**, *26*, 1319-1326.

2.147. B. Cui, H. Lin, J.-B. Li, X. Li, J. Yang, J. Tao, *Advanced Functional Materials* **2008**, *18*, 1440-1447.

2.148. M.-R. Gao, Y.-F. Xu, J. Jiang, Y.-R. Zheng, S.-H. Yu, *Journal of the American Chemical Society* **2012**, *134*, 2930-2933.

2.149. H. B. Suffredini, J. L. Cerne, F. C. Crnkovic, S. A. S. Machado, L. A.

Avaca, *International Journal of Hydrogen Energy* **2000**, *25*, 415-423.

2.150. K. Jin, J. Park, J. Lee, K. D. Yang, G. K. Pradhan, U. Sim, D. Jeong, H. L. Jang, S. Park, D. Kim, N.-E. Sung, S. H. Kim, S. Han, K. T. Nam, *Journal of the American Chemical Society* **2014**, *136*, 7435-7443.

2.151. J. Park, H. Kim, K. Jin, B. J. Lee, Y.-S. Park, H. Kim, I. Park, K. D. Yang, H.-Y. Jeong, J. Kim, K. T. Hong, H. W. Jang, K. Kang, K. T. Nam, *Journal of the American Chemical Society* **2014**, *136*, 4201-4211.

2.152. Y. Surendranath, M. W. Kanan, D. G. Nocera, *Journal of the American Chemical Society* **2010**, *132*, 16501-16509.

2.153. R. D. L. Smith, M. S. Prévot, R. D. Fagan, S. Trudel, C. P. Berlinguette, *Journal of the American Chemical Society* **2013**, *135*, 11580-11586.

2.154. A. C. Tavares, M. A. M. Cartaxo, M. I. da Silva Pereira, F. M. Costa, *J Solid State Electrochem* **2001**, *5*, 57-67.

2.155. Z. Chen, T. F. Jaramillo, T. G. Deutsch, A. Kleiman-Shwarsctein, A. J. Forman, N. Gaillard, R. Garland, K. Takanabe, C. Heske, M. Sunkara, *Journal of Materials Research* **2010**, *25*, 3-16.

2.156. A. J. Nozik, R. Memming, *The Journal of Physical Chemistry* **1996**, *100*, 13061-13078.

2.157. L. C. Seitz, Z. Chen, A. J. Forman, B. A. Pinaud, J. D. Benck, T. F. Jaramillo, *ChemSusChem* **2014**, *7*, 1372-1385.

2.158. J. Oh, T. G. Deutsch, H.-C. Yuan, H. M. Branz, *Energy & Environmental Science* **2011**, *4*, 1690-1694.

2.159. Y. Hou, B. L. Abrams, P. C. Vesborg, M. E. Björketun, K. Herbst, L. Bech, A. M. Setti, C. D. Damsgaard, T. Pedersen, O. Hansen, *Nature materials* **2011**, *10*, 434-438.

2.160. A. Heller, *Accounts of Chemical Research* **1981**, *14*, 154-162.

2.161. O. Khaselev, J. A. Turner, *Science* **1998**, *280*, 425-427.

2.162. M. H. Lee, K. Takei, J. Zhang, R. Kapadia, M. Zheng, Y. Z. Chen, J. Nah, T. S. Matthews, Y. L. Chueh, J. W. Ager, *Angewandte Chemie* **2012**, *124*, 10918-10922.

2.163. D. Yokoyama, T. Minegishi, K. Maeda, M. Katayama, J. Kubota, A. Yamada, M. Konagai, K. Domen, *Electrochemistry Communications* **2010**, *12*, 851-853.

2.164. D. Yokoyama, T. Minegishi, K. Jimbo, T. Hisatomi, G. Ma, M. Katayama, J. Kubota, H. Katagiri, K. Domen, *Applied physics express* **2010**, *3*, 101202.

2.165. G. Ma, T. Minegishi, D. Yokoyama, J. Kubota, K. Domen, *Chemical Physics Letters* **2011**, *501*, 619-622.

2.166. J. Kim, T. Minegishi, J. Kobota, K. Domen, *Energy Environ. Sci.* **2012**, *5*, 6368-6374.

2.167. A. Paracchino, V. Laporte, K. Sivula, M. Grätzel, E. Thimsen, *Nature Mater.* **2011**, *10*, 456-461.

2.168. C. G. Morales-Guio, S. D. Tilley, H. Vrubel, M. Grätzel, X. Hu, *Nature communications* **2014**, *5*, 3059.

2.169. F. F. Abdi, L. Han, A. H. Smets, M. Zeman, B. Dam, R. van de Krol, *Nature communications* **2013**, *4*, 2195.

2.170. A. Fujishima, *nature* **1972**, *238*, 37-38.

2.171. Q. Peng, B. Kalanyan, P. G. Hoertz, A. Miller, D. H. Kim, K. Hanson, L. Alibabaei, J. Liu, T. J. Meyer, G. N. Parsons, *Nano letters* **2013**, *13*, 1481-1488.

2.172. X. Liu, F. Wang, Q. Wang, *Physical Chemistry Chemical Physics* **2012**, *14*, 7894-7911.

2.173. J. Su, L. Guo, S. Yoriya, C. A. Grimes, *Crystal Growth & Design* **2009**, *10*, 856-861.

2.174. S. D. Tilley, M. Cornuz, K. Sivula, M. Grätzel, *Angewandte Chemie*

2010, *122*, 6549-6552.

2.175. C. Janáky, K. Rajeshwar, N. De Tacconi, W. Chanmanee, M. Huda, *Catalysis Today* **2013**, *199*, 53-64.

2.176. Y. Park, K. J. McDonald, K.-S. Choi, *Chemical Society Reviews* **2013**, *42*, 2321-2337.

2.177. K. Sivula, F. Le Formal, M. Grätzel, *ChemSusChem* **2011**, *4*, 432-449.

2.178. D. K. Zhong, S. Choi, D. R. Gamelin, *Journal of the American Chemical Society* **2011**, *133*, 18370-18377.

2.179. W. Luo, Z. Li, T. Yu, Z. Zou, *The Journal of Physical Chemistry C* **2012**, *116*, 5076-5081.

2.180. S. P. Berglund, A. J. Rettie, S. Hoang, C. B. Mullins, *Physical Chemistry Chemical Physics* **2012**, *14*, 7065-7075.

2.181. T. W. Kim, K.-S. Choi, *Science* **2014**, *343*, 990-994.

2.182. I. Cesar, A. Kay, J. A. Gonzalez Martinez, M. Grätzel, *Journal of the American Chemical Society* **2006**, *128*, 4582-4583.

2.183. Y.-S. Hu, A. Kleiman-Shwarsctein, A. J. Forman, D. Hazen, J.-N. Park, E. W. McFarland, *Chemistry of Materials* **2008**, *20*, 3803-3805.

2.184. A. Kleiman-Shwarsctein, Y.-S. Hu, A. J. Forman, G. D. Stucky, E. W. McFarland, *The Journal of Physical Chemistry C* **2008**, *112*, 15900-15907.

2.185. A. Kleiman-Shwarsctein, M. N. Huda, A. Walsh, Y. Yan, G. D. Stucky, Y.-S. Hu, M. M. Al-Jassim, E. W. McFarland, *Chemistry of Materials* **2009**, *22*, 510-517.

2.186. J. Y. Kim, G. Magesh, D. H. Youn, J.-W. Jang, J. Kubota, K. Domen, J. S. Lee, *Scientific reports* **2013**, *3*, 2681.

2.187. Y. W. Chen, J. D. Prange, S. Dühnen, Y. Park, M. Gunji, C. E. Chidsey, P. C. McIntyre, *Nature Mater.* **2011**, *10*, 539-544.

2.188. M. J. Kenney, M. Gong, Y. Li, J. Z. Wu, J. Feng, M. Lanza, H. Dai, *Science* **2013**, *342*, 836-840.

2.189. G. Lin, M. Kapur, R. Kainthla, J. M. Bockris, *Applied Physics Letters* **1989**, *55*, 386-387.

2.190. S. Y. Reece, J. A. Hamel, K. Sung, T. D. Jarvi, A. J. Esswein, J. J. Pijpers, D. G. Nocera, *Science* **2011**, *334*, 645-648.

Chapter 3. Experimental and Analysis

3.1 Synthesis of catalysts

Synthesis of graphene

A monolayer graphene was grown on Cu foil by chemical vapor deposition (CVD) and was transferred to SiO_2 surface. In the first step of graphene synthesis, a copper foil was put into a quartz reactor in CVD system and then, heated it up to 1000℃ with flowing H_2 at 70 mTorr. Additionally, the sample was annealed for 20 min without changing the condition. The gas mixture of H_2 and CH_4 was flowed with rates of 5 and 50 SCCM for 30 min under 8 Torr. Finally, the sample was rapidly cooled down to room temperature with flowing H_2. After growth, in order to remove graphene on one of the sides of Cu foil, graphene on Cu was placed into plasma chamber (SNTEK). The chamber pressure was pumped down to 50 mTorr, O_2 gas was introduced into the chamber by applying a radio-frequency (13.56 MHz) forward power of 100 W for 10 sec. In addition, to make vacancy sites and N-doping graphene on front side of Cu, low density N_2-plasma was produced by applying 10 W power. The N_2 flow rate was 20 SCCM and the working pressure of the chamber was 120 mTorr. Under these conditions, the plasma treatments were performed with various exposure times from 0 to 16 sec of N_2 plasma to test the electrochemical reaction of graphene surface. Finally, poly(methyl methacrylate) (PMMA) was spin-coated on the graphene and then, copper foil was removed in 0.1 M ammonium persulfate solution. After washing with deionized water, the graphene was transferred on Si substrate and then, PMMA was removed in acetone for 30 min.

Synthesis of graphene layers.

For the various stacked graphenes, the graphene with PMMA was floated on

deionized water and transferred onto another graphene layer on Cu and etched/rinsed again. The transfer and etching/rinsing procedures were consecutively performed for up to five layers of graphene. To synthesize the graphene with defects, the monolayer graphene on the back side of the copper was removed using oxygen plasma, and the graphene on the front side of the Cu was treated with argon plasma (10 W RF power, 4 s). The PMMA layer was coated onto this graphene, and the Cu foil was removed. Then, the treated graphene was transferred onto the silicon or used in the stacking process.

Synthesis of carbon-nanosheet

Carbon nanosheet was synthesized using polydopamine chemistry and detailed process was introduced to make active sites for hydrogen evolution reaction. SiO_2/Si target substrate was immersed in tris-(hydroxy-methyl) aminomethane solution (10 mM, pH 8.5) mixed with dopamine (2 mg). Then, polydopamine films were deposited on the surface of the target substrate. The thickness of the film could be controlled as a function of the immersion time. For carbonization, sample were then placed in a tube furnace for thermal treatment at elevated temperatures in a nitrogen atmosphere.

3.2 Electrode preparation

Preparation of Si photocathode

Boron-doped (p-type) single-crystal Si wafers (4 inch diameter, 500 μm thickness, doped to achieve a resistivity of 10~15 Ω·cm, oriented along the (100) plane) were purchased from Namkang Co. Ltd. The wafers were cut into 1 cm^2 pieces and successively cleaned in acetone, 2-propanol and deionized water for 10 min with sonication. To establish an Ohmic contact between copper wire and the unpolished back side of the Si wafer, a gallium-indium eutectic alloy (Ga:In = 75.5:24.5, Kojundo Chemical Laboratory Co. Ltd.) was incorporated, followed by a silver paste. Epoxy was used to insulate

and protect the back contact of Si, except for the intended illumination area (0.25 cm^2) on the front side of the Si. Graphene was transferred onto the Si surface from the Cu foil. PMMA was spin-coated onto the graphene, and the Cu foil was removed using an ammonium persulfate solution. After washing with deionized water, the graphene was transferred onto the Si substrate, and the PMMA was removed after soaking in acetone for 30 min.

Si Nanostructure Fabrication

Each of the Si nanostructures was fabricated by metal-catalyzed electroless etching method in 20 mL aqueous solution of $AgNO_3$ (0.679 g, 0.02 M) and HF (5 M) with the etching time of 10 min, 30min, 60 min, 120 min, 140 min, 160 min, 180 min, 200 min, 300min and 480 min. Excess Ag residues that could be contaminated during the electroless etching were completely washed by 70 % nitric acid solution for two hours.

3.3 Analysis methods of synthesized catalyst and electrode

Surface Characterization.

Raman spectra were measured at room temperature with a Renishaw spectrometer at 514 nm using an Ar laser. The spot diameter was ~ 2 μm, and a 50x objective lens was used. UPS spectra were recorded using a using a PHI 5000 Versa Probe (ULVAC-PHI) system. The surface morphologies of the graphene films were investigated using AFM (Park system, Xe-100). Images of the graphene layer were obtained via TEM (FEI-CM20) operated at 200 keV.

Scanning Electron Microscope Analysis

The surface morphology and wire length of nanostructured Si were analyzed by Field-Emission Scanning Electron Microscopy (SEM) using SUPRA 55VP model from Carl Zeiss. For cross-sectional view, samples were carefully cut

into two pieces with a diamond cutter. In order to avoid the surface charging, Pt was coated by the sputtering method for 200 sec (about 10 nm thickness) using the BAL-TEC/SCD 005 model prior to the SEM analysis.

Reflectance Measurement

Optical reflectance of Si surface was analyzed by UV/Vis/NIR spectrophotometer (Cary 5000, Agilent Technology) using Diffuse Reflectance Mode and Specular Reflectance Mode. Full scan range was 380 to 2300 nm and scan rate was 600 nm min-1. For comparison, the reflectance of planar Si and Si nanowire sample was measured.

3.4 Characterization method for catalytic activity

The electro-catalytic activity of a catalyst can be measured with cyclic voltammetry (CV) using a rotating disk electrode (RDE). An RDE is a convective electrode system to which the hydrodynamic equations and the convective-diffusion equation have been applied. Using a hydrodynamic working electrode system of RDE, methods involving convective mass transport of reactants and products can be studied. Representative parameters for RDE measurement are the rotating speed, the scan rate, and the applied potential range. To fabricate the working electrode, the catalyst can be loaded on a standard working electrode such as a glassy carbon electrode or a highly ordered pyrolytic graphite (HOPG) that are conductive and inert in an aqueous solution. To load the catalyst on the electrode, several loading methods such as catalyst ink are used. The catalyst powder mixed with a few wt% of Nafion or with a carbon black can be synthesized, loaded on the electrode, and stored at 100 ~ 110 ^{o}C for drying. Glassy carbon is a form of carbon which has been used as an indicator electrode and is a gas-impermeable, electrically conductive material which is highly resistant to chemical attack. In *J-E* curves of the RDE measurements, the current density

from the electrolysis of water increases exponentially after onset as the potential is swept from lower to higher cathodic potential. The measured potentials are corrected for the ohmic potential drop (iR) losses that originated from the resistance of the interface between the substrate and the electrolyte. To compare the onset potential for the HER in the RDE system, the potential to attain 0 mA/cm^2 or below -1 mA/cm^2 of HER current density is not usually chosen as the indicating potential because non-faradaic current or background current induced by solid electrodes are generated in the range of low applied potential. The non-faradaic current or background current may occur due to impurities in the electrolyte or may arise from the double-layer charging process. To compare the catalytic activity for HER, the potential to attain -5 mA/cm^2 of HER current density of bare electrode and of catalyst loaded electrode can be chosen as the onset potential for comparison.

Electrochemical measurements are performed in a three-electrode cell (the working electrode, the counter electrode, and the reference electrode) using an electrochemical analyzer. Pt electrode or HOPG electrode is used for counter electrode and Ag/AgCl/KCl electrode or Saturated Calomel electrode is used as the reference electrode. The reference electrode should be carefully calibrated with respect to the reversible hydrogen electrode (RHE) in an aqueous solution with high purity H_2 saturation at room temperature. The RHE is calibrated to between -0.197 V and -0.266 V vs. the Ag/AgCl/KCl reference electrode as the concentration of KCl varies in the electrode. Since the potential difference between Ag/AgCl and RHE is also dependent on electrolyte pH, temperature, etc, the potential should be carefully measured before each set of measurements and the measurement should be conducted at least several times for each condition.

Electrochemical measurements

Electrochemical measurements were performed in a three-electrode cell using

a electrochemical analyzer (CHI 760E, CH Instruments, Inc.). Pt foil or Pt wire was used for counter electrode and Ag/AgCl/3 M NaCl electrode was used as the reference electrode. The reference electrode was carefully calibrated with respect to RHE in an aqueous 1 M perchloric acid solution with high purity H_2 saturation at 25 ℃. The RHE was calibrated to between -0.201 V and -0.203 V vs. the Ag/AgCl reference electrode (Figure XX). For the electrochemical study, the Rotating Disk Electrode (RDE) system was purchased from PINE, Inc., and a glass carbon tip was used for the RDE measurements (dia. 5 mm). For comparison, 10 uL of Pt catalyst ink mixed with 5 wt% Nafion was loaded onto the GC and dried at 110oC. RDE measurements were performed at a differenct rotation speed (500 rpm, 1000 rpm, 1500 rpm, 2000 rpm, and 2500 rpm) and at a differenct scan rate (1 mV/sec, 10 mV/sec, 20 mV/sec, 50 mV/sec, and 100 mV/sec), respectively.

PEC measurements

A 300 W Xe lamp (Oriel) with a water filter was used as a light source with an Air Mass 1.5 Global glass filter (Newport Co., model #81094). During the photocurrent measurements, the light intensity was carefully maintained at 100 mW/cm2 using an optical power meter (Newport, Model 1916-R). PEC measurements were performed in a three-electrode cell using an electrochemical analyzer (CHI 760E, CH Instruments, Inc.). To minimize the hydrogen bubbles adhering to the planar Si surface, the electrolyte was stirred during the measurements without the introduction of an additional surfactant. Pt wire was used as the counter electrode, and an Ag/AgCl/3 M KCl electrode was used as the reference electrode. The reference electrode was carefully calibrated with respect to RHE at 25℃ in a 1 M perchloric acid aqueous solution saturated with high-purity H_2. The RHE was calibrated to -0.201 V vs. the Ag/AgCl reference electrode.

Electrochemical AC impedance spectroscopy measurement

Electrochemical AC impedance spectroscopy (EIS) was performed at 0 V vs. RHE under an illumination intensity of 100 mW/cm^2 with a frequency range of $1 \sim 10^6$ Hz and an amplitude of 5 mV in a three-electrode cell. From the Nyquist plot, an equivalent circuit was designed to analyze the EIS spectra.

Part I. Model Study of Carbon Platform:

From 2D monolayer graphene to pseudo-3D system of multi-layer graphene and graphene quantum sheets

Chapter 4. The Simplest Model: Monolayer Graphene

4.1 Introducation

Carbon-based catalysts have been attracting attention in renewable energy technologies due to the low cost and high stability, but their insufficient activity is still a challenging issue. Inspired by biomolecular system, we have designed enzyme-mimetic carbon-based catalyst for hydrogen evolution reaction (HER) and investigated the effect of each component with a systematic approach. As the simplest model carbon-based platform, 2D monolayer graphene is chosen as a HER catalyst. Graphene possesses excellent transmittance and superior intrinsic carrier mobility. For the first time, we have investigated new possibilities of monolayer graphene as the efficient HER catalyst. Here, we suggest monolayer graphene as a catalyst for solar-driven hydrogen evolution reaction on Si-photocathode and boost their catalytic activity by the plasma treatment in N_2-ambient. The plasma treatment induces abundant defects and the incorporation of nitrogen atom in graphene structure, which can act as catalytic sites on graphene. The monolayer graphene containing nitrogen impurities exhibits the remarkable increase in the exchange current density and leads to the significant anodic shift of the onset of photocurrent from Si-photocathode. Additionally, monolayer graphene shows the passivation effect that suppress the surface oxidation of Si, thus enabling the operation of Si-photocathode in neutral water. This study shows how graphene itself can be applied to photoelectrochemical system as a catalyst with high activity and chemical stability.

The discovery of efficient catalysts represents one of the most important and

challenging issues for the implementation of photoelectrochemical hydrogen production.[4.1] A critical requirement for outstanding catalysts in a photoelectrochemical cell (PEC) is not only the ability to boost the kinetics of a chemical reaction but also durability against electrochemical and photoinduced degradation.[4.2] Generally, precious metals, such as platinum, exhibit superior performance in these requirements; however, the unavoidable weakness of precious metals are the economic aspects because of the high-price.[4.1] Therefore, there has been an intense search for efficient, durable, and inexpensive alternative catalysts. [4.2, 4.3] Here, we demonstrate that monolayer graphene can catalyze the hydrogen evolution reaction (HER); thus, monolayer graphene can enhance the performance of silicon (Si) photocathodes through a significant decrease in the overpotential. The catalytic activity can be improved in N-doped and defect-abundant graphene that was prepared by treatment with N_2 plasma. Furthermore, surface passivation with a transparent monolayer graphene catalyst allows the Si photocathode to work efficiently and stably in neutral water by suppressing oxidation.

A PEC is the most promising system to sustainably produce hydrogen fuel; a PEC requires semiconductor photoelectrodes that generate electron-hole pairs with absorbed photons and stimulate charge transfer to a semiconductor/aqueous interface.[4.1] To improve the kinetics of charge transfer, heterogeneous catalysts are added to the surface of a semiconductor. [4.4] Many attempts to develop the highly efficient catalyst have had limited success; the development of an earth-abundant catalyst that operates at pH 7 with a low overpotential is still a challenge. [4.2, 4.5] In PEC, negative effects from catalysts should be considered: 1) reflection by the overlaid catalyst, 2) an unfavorable band structure such as a Schottky barrier 3) photocorrosion, and 4) recombination sites at the interface.[4.6, 4.7] Therefore, to design catalysts for photoelectrochemical water splitting, the optical properties, stability and

interfacial issues must be comprehensively considered.

The design of carbon-based catalysts can represent an important research direction in the search for non-precious, environmentally benign, and corrosion resistant catalysts. Especially, graphene possesses excellent transmittancy and superior intrinsic carrier mobility, [4.8] thus there have been several attempts to use graphene as a catalyst. It has been reported that reduced graphene oxide (rGO) containing catalytic active materials exhibited improved activity in HERs, oxygen evolution reactions (OERs), and oxygen reduction reactions (ORRs).[4.9-4.11] However, in most cases, the role of carbon materials is limited to an electrical conducting substrate or a supporter that enhances the performance of other decorated active catalysts. In this study, we investigated new possibilities for monolayer graphene as an electrocatalyst for efficient HER and found that nitrogen doping and defects achieved through treatment with N_2 plasma improved the catalytic activity. To the best of our knowledge, there is no prior report of the application of monolayer graphene to hydrogen production.

As a proof of concept, the Si photocathode was employed to investigate the catalytic activity of graphene and the effect of nitrogen doping in photoelectrochemical HER. Si is the most promising photocathode material due to the small band gap of 1.12 eV, and precise controllability, [4.12] however, cannot durably operate in aqueous electrolyte because of surface oxidation. [4.13] Therefore, passivation of Si surface is essential for the durable operation of the Si photocathode in neutral water.[4.13] Monolayer graphene on Si acts as a passivation layer against surface oxidation without attenuating the photon incidence.

4.2 Results and Discussion

Monolayer graphene (Gr) was grown on Cu foil through chemical vapor deposition (CVD) and was transferred to p-type Si wafer. To evaluate the

photocathodic behavior of Gr loaded on a Si (Gr-Si) electrode, a current density measurement was performed as the potential was swept from 0.4 V to -1.0 V vs. Reversible Hydrogen Electrode (RHE) in a three electrode cell. A light source of a 300 W Xe lamp illuminated the Si photoelectrode with a light intensity of 100 mW/cm^2 with an Air Mass 1.5 Global condition filter in an aqueous 1 M perchloric acid solution (pH 0).

In measurements of the photoelectrochemical performance, Gr exhibited catalytic activity for HER. As shown in Figure 4.1a, the current density of the bare Si increased gradually from -0.2 V vs. RHE and saturated at approximately -32 mA/cm^2 below -1.0 V, vs. RHE, as a potential was negatively applied. Interestingly, in the measurement of Gr-Si, the overall current density-potential (*J-E*) curve shifted by approximately 0.2 V toward the positive potential. The onset potential is defined as the potential at the photocurrent density of -1 mA/cm^2. The onset potential of Gr-Si is 0.01 V vs. RHE, and this potential is a positive shift by 0.18 V compared to that of bare Si (-0.17 V vs. RHE). Figure 1b also shows dark current densities of heavily arsenic doped n$^+$ type Si electrodes. In the dark condition, the positive shift in 0.14 V of the onset potential (-0.49 V vs. RHE for Gr-Si) also shows higher activity for HER compared to that of the bare Si (-0.63 V vs. RHE). This result indicates that monolayer Gr acts as an effective catalyst for HERs on the Si photocathode.

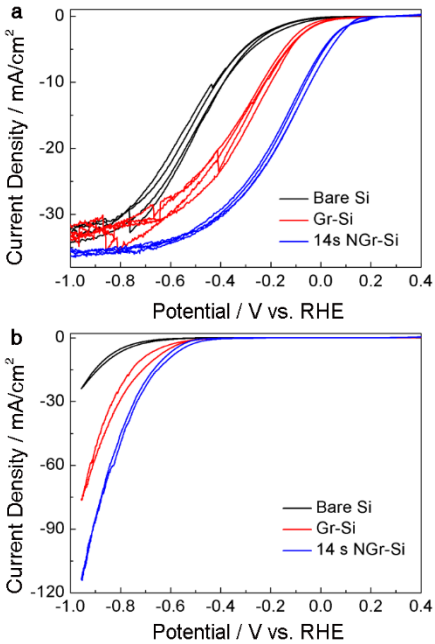

Figure 4.1. Cyclic Voltammetry (CV) of graphene (Gr) and N_2-plasma-treated Gr (NGr) on a Si electrode. (a) Photocurrent density-voltage (*J-E*) curves for the lightly boron doped p-Si electrode deposited with Gr and NGr. The durations of the plasma treatment on Gr were introduced with high purity N_2 gas for 14 sec, which is called 14 s NGr-Si. (b) Polarization curves of Gr, and NGr on heavily arsenic doped n^+ type Si electrodes under dark condition. Each CV was performed at a scan rate of 0.05 V/s. [4.24]

To investigate the electrocatalytic activity of Gr, we measured cyclic voltammetry (CV) without illumination with a rotating disk electrode (RDE). To fabricate the working electrode, Gr was transferred to a glassy carbon (GC) tip that is inert in aqueous solution. As shown in Figure 4.2a, in *J-E* curves of the RDE measurements, the current density from the electrolysis of water exponentially increased after the onset as the potential was swept from 0 V to -0.5 V. To compare the onset potential for the HER in the RDE system, the potential to attain -5 mA/cm^2 of HER current density was measured for bare

GC and for Gr-GC. The potential to attain -5 mA/cm^2 of HER current density is -0.33 V for the bare GC. Similar to the behavior of the photocurrent response for the Gr-Si electrode, a positive shift in the overall J-E curve was also observed for Gr-loaded GC (Gr-GC). The onset potential for Gr-GC was -0.28 V vs. RHE; this onset potential is shifted positive by 50 mV compared to that for the bare GC. This result means that the Gr monolayer has electrocatalytic activity for HER regardless of substrate materials.

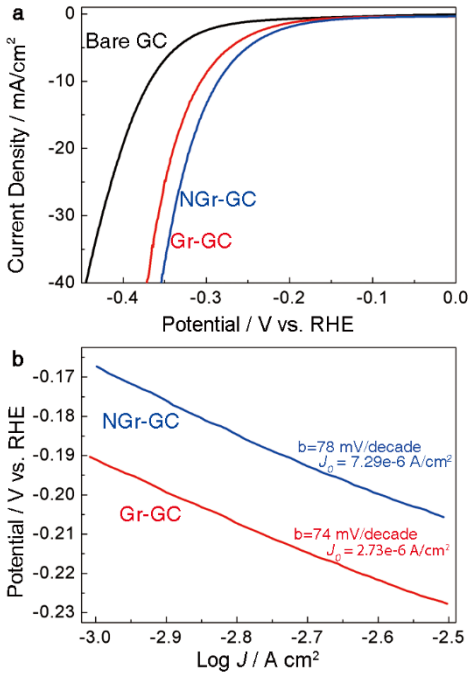

Figure 4.2. Electrochemical activity of Gr on Glassy Carbon (GC) electrode. (a) CV curve of GC, Gr on GC, and NGr on GC from rotating disk electrode system. CV data were corrected by iR compensation. (b) Tafel plots derived from (a) CV data. The 'b' in the inset (mV/decade) and J_0 (A/cm^2) indicate a Tafel slope and an exchange current density, respectively. [4.24]

To quantitatively gain more insight into the catalytic activity of Gr, the *J-E*

curves in Figure 4.2a were converted into a plot of the potential as a function of the logarithm of *J*; this plot is called a Tafel plot. The measured potentials were corrected for the ohmic potential drop (iR) losses that originated from the resistance of the interface between the substrate and the electrolyte. Analyzing the impedance spectroscopy revealed that the resistances of the bare GC and Gr-GC are 7.1 and 7.2 ohm, respectively (Figure 4.6). The Tafel plot provides two parameters to estimate the electrocatalytic activity: the Tafel slope and the exchange current density. The Tafel slope is defined to be a measure of the potential increase required to increase the resulting current by 1 order of magnitude.[4.14] The bare GC showed a Tafel slope of 85 mV/decade, and Gr-GC exhibited a 9 mV/decade lower Tafel slope (74 mV/decade) than that of bare GC.

The Tafel slope is an inherent property of the catalyst that is determined by the rate-limiting step for HER. Mechanistically, for the HER in acidic solution, the following possible reaction steps have been suggested: [4.15]

$H_3O^+ + e^- \rightarrow H_{ads} + H_2O$ (1)

$H_{ads} + H_3O^+ + e^- \rightarrow H_2 + H_2O$ (2)

$H_{ads} + H_{ads} \rightarrow H_2$ (3)

where H_{ads} is the adsorbed H. (1) is a discharge step (the Volmer reaction), (2) is a desorption step (the Heyrovsky reaction), and (3) is a recombination step (the Tafel reaction). The value of the Tafel slope also relates to the adsorbed hydrogen coverage (θ_H) on the surface of electrode. If the recombination of adsorbed hydrogen (the Tafel reaction) is the rate-determining step for the HER and if the coverage is very high ($\theta_H \approx 1$), the measured Tafel slope is 30 mV/decade. However, if the electrochemical desorption step (the Heyrovsky reaction) is the rate-determining step, a Tafel slope of 40 ~ 118 mV/decade is measured and is dependent of the value of θ_H (0 ~ 1).[4.16] The observed Tafel slope of ~80 mV/decade in the current work indicates that the kinetics of the HER on bare GC and Gr-GC electrodes is determined by the Heyrovsky

reaction because θ_H has an intermediate value.

The exchange current density (J_0) is defined to be the current density at zero overpotential. The catalytic effect originates from improving the rate of charge transfer at the interface between the electrode and electrolyte or from lowering the activation energy barrier for a chemical reaction; these catalytic effects are represented by J_0. From the Tafel plot, J_0 can be obtained by extrapolating the plot in Figure 4.2b and extracting the current density at 0 V vs. RHE. The Gr-GC electrode showed an enhanced J_0 of 2.73×10^{-6} A/cm^2, which is higher than the J_0 value for bare GC (1.63×10^{-6} A/cm^2) (Figure 4.7). The higher J_0 indicates that electron transfer or the adsorption/desorption of protons at the electrode/electrolyte can occur more easily with a lower kinetic barrier. From the Tafel analysis, the HER catalytic activity of the monolayer Gr catalyst is identified from the increase in J_0.

The catalytic activity of Gr can be further enhanced by generating more active sites. We expected that treatment with N_2 plasma would induce nitrogen doping and abundant defects in graphitic carbon structure and that these doping and defect sites could be catalytic sites for the HER. In a previous study, Dai's group showed that introducing nitrogen dopants and defect sites in a CNT-Gr composite facilitated an improvement in electrocatalytic activity for ORR.[4.17] The surface of the as-grown Gr on Cu foil was modified with a N_2 plasma in a reactive ion etcher (RIE), and the catalytic activities of the N_2-plasma-treated Gr (NGr) were measured for various durations of the plasma treatment.

The N_2-plasma treatment improved the catalytic activity of Gr. We optimized the duration of the plasma treatment, and obtained the best-performing Gr at the duration of 14 sec (Figures 4.1a and 4.8). As shown in Figure 4.1a, an additional positive shift of the onset potential was observed for NGr under illumination. The onset potential for NGr-Si was 0.12 V vs. RHE, and this onset potential was enhanced by more than 0.11 V compared to that

for Gr-Si. In comparison to bare Si with the onset of -0.17 V vs. RHE, the onset potential is shifted positively by 0.29 V. The more significant enhancement by Gr and NGr is detected at a current density of -10 mA/cm^2. To obtain -10 mA/cm^2 of photocurrent, potentials of -0.42 V, -0.21 V, and -0.04 V vs. RHE are needed for bare Si, Gr-Si, and NGr-Si, respectively. The potential for -10 mA/cm^2 is shifted to the anodic direction by 0.38 V for NGr-Si compared with bare Si. The cathodic current from NGr-Si rose rapidly at potentials more negative than the onset potential and at current densities less than -5 mA/cm^2. In the dark condition, NGr-Si also showed the positive shift in 50 mV (-0.44 V vs. RHE) compared to the Gr-Si (Figure 4.1b), which resulted in the photovoltage of 0.56 V by depositing NGr on bare Si (Table 4.1). For comparison, we also performed photoelectrochemical measurements with electroless-deposited Pt catalysts on Si. Although NGr-Si electrode shows lower increase of the potential for HER at -10 mA/cm^2 than that of the electrode decorated with the optimized Pt nanoparticle, the onset potential of 0.12 V vs. RHE and the positive shift of 0.29 V compared that of the bare Si are larger than that of any other reported data with a carbon-based catalyst for HERs. [4.18]

An additional positive shift in the onset potential by NGr was also observed in the RDE measurements. The potential to attain current density of -5 mA/cm^2 is -0.26 V vs. RHE; this value is 70 mV larger than that of the bare GC (-0.33 V vs. RHE) and is 20 mV larger than that of the Gr-GC (-0.28 V vs. RHE). The improvement in the catalytic activity with NGr was also confirmed by the comparison of J_0 in the Tafel plot (Figure 4.2b). The resulting exchange current density on NGr-GC is 7.29×10^{-6} A/cm^2, which is a higher value than that measured on Gr-GC and is a comparable value to that of J_0 for HERs on transition metals, such as Ni or Cu.[19] The tendency of J_0 to increase on Gr and NGr agrees with the tendency of the overpotential for the onset current to decrease. The Tafel slope of 79 mV/decade measured for NGr-Gc

also closely matches that measured for bare GC and Gr-GC.

In Figure 4.3, we describe the changes in chemical states of Gr after N_2 plasma treatments of various durations. AFM images for the surface of NGr with N_2 treatment for 14 sec show that plenty of defects and edges were generated in the Gr, while that of monolayer Gr was smooth (Figure 4.10). In the Raman spectra (Figure 4.3a), the generation of defects and edges by the N_2 treatment is also identified. In the Raman spectra of pristine Gr, the D peak is due to the breathing modes of six-atom rings, which comes from transverse optical phonons around *K* or *K′* point in the first Brillouin zone. It involves an intervalley double resonance process. The absence of a significant D peak is evidence of the good crystallization of the single Gr layer. Normally, the D peak is negligibly weak in pristine Gr, but the peak exists still ~ 2% of the G peak. However, after the plasma treatment, the D intensity significantly increased and the D′ at ~1620 cm^{-1} was activated by intravalley double resonance process, i.e., connecting two points belong to the same cone around *K* or *K′*. Moreover, the D + G combination mode at ~2950 cm^{-1} requires defects for its activation. [4.20] Thus, these changes in the Raman spectra indicate the formation of abundant edge and defective sites in NGr.

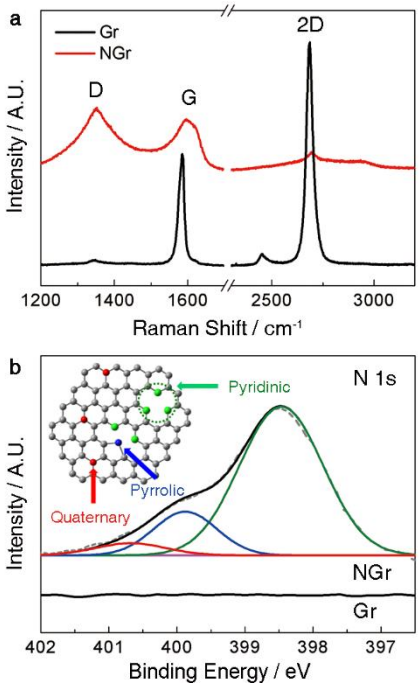

Figure 4.3. (a) Raman spectra and (b) high resolution XPS spectra of N 1s peak of Gr and NGr. The N 1s peak is separated into N1 (398.5 eV), N2 (399.9 eV), and N3 (401 eV) which are labeled by green, blue, and red lines. An inset image in (b) represents schematic of NGr. The gray, green, blue, and red spheres indicate the carbon, pyridinic nitrogen, pyrrolic nitrogen, and quaternary nitrogen atoms, respectively. [4.24]

Additionally, the spectral features of monolayered Gr are observed in the Raman spectra. Before the plasma treatment, the G to 2D intensity ratio of ~0.5 and a symmetric 2D band are found at ~1580 cm^{-1} and at ~2670 cm^{-1}. [4.21] These features are caused by the G band from the in-plane vibrational mode and the 2D band from double resonance scattering, respectively. [4.22, 4.23] Thus, they can be observed when Gr is successfully formed in a single-layer.

The plasma treatment induces not only the formation of many defect sites but also nitrogen doping in Gr. The chemical states of the nitrogen dopant

were identified from the high resolution N 1s spectra from XPS (Figure 4.3b and 4.11). No obvious distinct nitrogen peak was observed for Gr, whereas nitrogen peaks for NGr were observed at pyridinic (398.5 eV), pyrrolic (399.9 eV), and a small number of quaternary nitrogen (401 eV) sites with a concentration of ~ 2.2 at.%. Inset in Figure 3b shows a schematic diagram of the bonding configurations for nitrogen in NGr.

The passivation effect of Gr was also investigated. CV of Si photocathodes was measured during 300 cycles with a scan rate of 0.05 V/s (Total operation time of each electrodes is about 20,000 sec) in pH 0 and pH 6.8. As shown in Figure 4.4a and 4.4b, CV curves of all electrodes shifted negatively vs. RHE as the CV cycle increased, but bare Si showed the largest negative shift even in much lower cycles. As a key parameter determining the passivation performance of Gr and NGr against the surface oxidation of Si, the changes in onset potentials were measured (Figure 4.12). At pH 0, the Gr-Si and NGr-Si electrodes showed only shifts in the onset potential of 0.1 V and 0.035 V, respectively, while the onset potential of the bare Si electrode shifted negatively by 0.38 V within 100 cycles (Figure 4.12). At pH 6.8, both the Gr-Si and NGr-Si electrodes showed the negative shift of less than 0.24 V in the onset potential, whereas the onset potential of the bare Si sharply decreased and saturated at a value of approximately -1.1 V vs. RHE within only 30 cycles. With increasing pH, the degradation of the Si photocathode is accelerated because of the elevated oxidation from the increase in OH^-,[4.13] but Gr and NGr suppress the oxidation of the Si surface even at neutral pH solution.

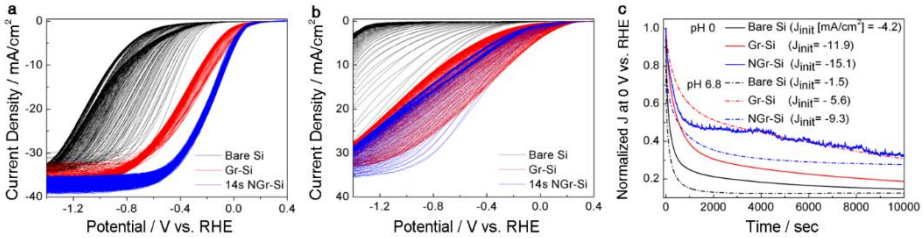

Figure 4.4. The stability test of bare Si, Gr-Si, and NGr-Si photocathodes. CV of Si photocathodes during 300 cycles with a scan rate of 0.05 V/s in (a) pH 0 and (b) pH 6.8. Polarization curves of each photoelectrodes shifted negatively vs. RHE as the CV operation increased. (c) Chronoamperometry operation of Si photocathodes. The change of normalized photocurrent density (J/J_{init}) at 0 V vs. RHE of each photoelectrodes with increasing the operation time in pH 0 (solid line) and pH 6.8 (dash-dotted line), respectively. J_{init} is the initial current density in the chronoamperometry operation. [4.24]

A chronoamperometray test of the bare Si, Gr-Si, and NGr-Si was also performed at 0 V vs. RHE (Figure 4.13) and the current densities normalized by their initial values were displayed as a function of time in Figure 4.4c. Gr-Si and NGr-Si also showed the suppressed degradation of the performance in the photocurrent density compared to that of the bare Si at both pH 0 and pH 6.8 condition. The performance of the bare Si completely failed only after 1000 sec (Figure 4.4c and 4.13) at pH 6.8. The NGr-Si electrode maintained more than 30 % of the normalized current and -4.8 mA/cm^2 (pH 0) even at 10,000 sec. Thus, from the change of the onset potential and current density at 0 V vs. RHE, Gr and NGr suppresses the degradation of the photoelectrochemical performance by the oxidation of Si surface.

To confirm the passivation effect of Gr and NGr on the Si surface, the surface state of Si was investigated before and after the chronoamperometry test at 0 V vs. RHE for 10 000 s (Figure 4.17). XPS spectra of bare Si, Gr–Si, and NGr–Si were obtained in the Si $2p_{3/2}$ region. The Si peak can be assigned

at 99.3 eV, and the SiO_2 peak can be assigned at 103.3 eV.26 From XPS spectra of bare Si, the peak of Si–O increases after the chronoamperometry test. In the case of Gr–Si and NGr–Si samples, after the long-term test, there is only a slight increase in the Si–O peak. These results indicate that graphene suppresses the oxidation of the Si surface during photoelectrolysis.

To further enhance the electro-catalytic activity of Gr, Pt nanoparticles were electrodeposited onto the NGr–Si (Pt–NGr–Si). We also expected that the passivation effect of Gr to suppress the Si oxidation during the photoelectrolysis could make the synergistic advantage with other catalysts. As a proof of concept, Pt was chosen to investigate those effects. The catalytic activity of Pt–NGr–Si was significantly enhanced compared to that of NGr–Si as shown in Figure 4.1a. From a CV measurement, the onset of Pt–NGr–Si is 0.35 V vs. RHE at -1 mA/cm^2, and the potential to reach -10 mA/ cm^2 is 0.25 V vs. RHE. The STH conversion efficiency is increased to 3.05%. As expected, the long-term stability was also achieved by combining Pt and Gr as demonstrated in Figure S10 and S11. The chronoamperometry test showed that Pt–NGr–Si maintained the stable current density of -4.7 mA/ cm^2 and -4.0 mA/cm^2, respectively, at pH 3.8 and 6.8 even after 8000 s.

4.3 Conclusion

We have presented the N-doped monolayer graphene catalyst that enhanced the PEC performance of a Si-photocathode. The onset potential for photocurrent from the Si was significantly shifted toward the anodic direction without a change in the saturation current density. NGr has excellent catalytic activity for photoelectrochemical HER on the Si photocathode and is the passivation layer that maintains higher onset potential and current density even at neutral pH. Our approach in this study exploits a strategy to develop metal-free carbon-based catalysts with high efficiency and durability for solar-driven hydrogen fuel production.

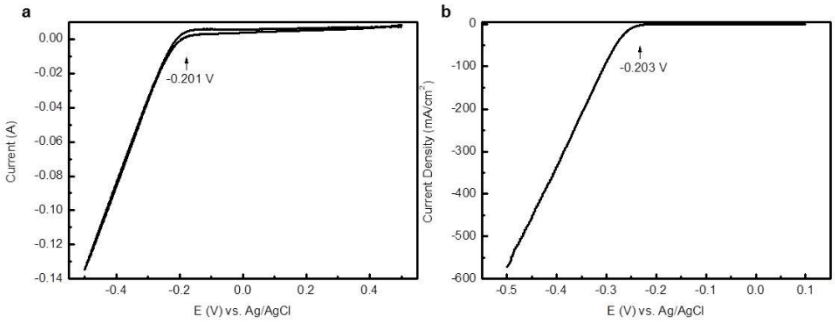

Figure. 4.5. Calibration respect to RHE. Current vs. the applied potential respect to Ag/AgCl reference electrode with using (a) Pt foil for Si PEC cell experiment and (b) Pt wire as the counter electrode for RDE experiment. [4.24]

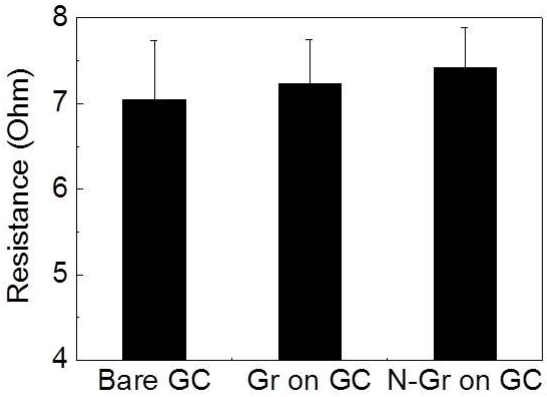

Figure 4.6. Resistance of bare Glassy Carbon (GC), Gr on GC, and NGr on GC. Impedance spectroscopy analysis revealed that the resistances of the bare GC, Gr-GC, NGr-GC are 7.1 ohm, 7.2 ohm, and 7.4 ohm respectively. Resistances were measured using iR compensation mode in the electrochemical analyzer. [4.24]

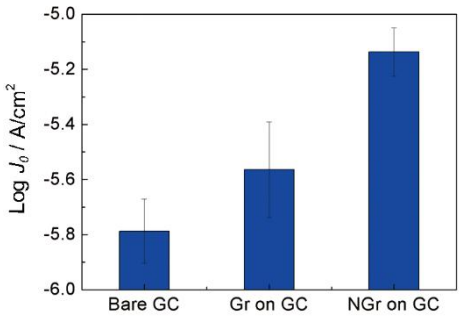

Figure 4.7. The logarithm of the exchange current densities calculated by extrapolation to the x-axis. Compared to the bare GC, Gr and NGr catalysts show the high activity for the HER. [4.24]

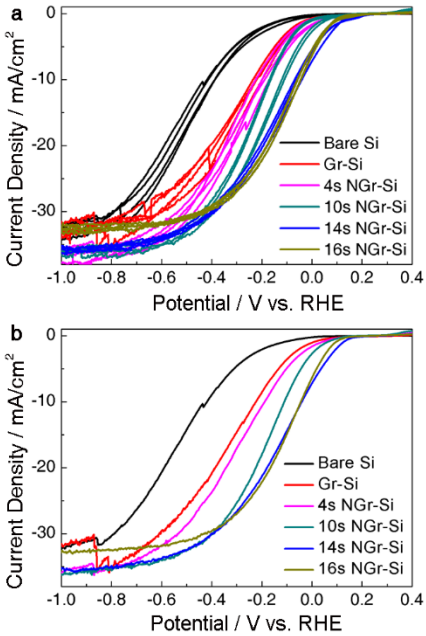

Figure 4.8. Photoelectrochemical performance of NGr-Si photocathode with variation of the amount of Pt solution. (a) Polarization curves of NGr on Si electrode. Each cyclic voltammetry was performed during 4 cycles at a scan rate of 0.05 V/s. The durations of the plasma treatment on Gr were introduced with high purity N_2 gas for 4 sec, 10 sec, 14 sec, and 16 sec. For comparison, cyclic voltammogram of Gr without plasma treatment on Si electrode is presented. (b) Representative data from polarization curves of NGr on Si electrode of (a).[4.24]

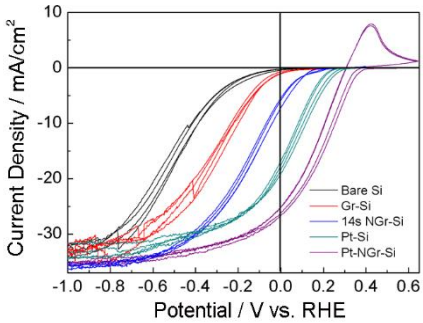

Figure 4.9. Cyclic Voltammetry (CV) of bare Si, Gr-Si, NGr-Si, Pt-Si, and Pt-NGr-Si electrodes. *J-E* curves for the lightly boron doped p-Si electrode deposited with Gr, NGr, Pt, and Pt on NGr. The durations of the plasma treatment on Gr were introduced with high purity N_2 gas for 14 sec, which is called 14 s NGr-Si. In case of Pt-Si and Pt-NGr-Si electrodes, Pt nanoparticles were deposited on bare Si and NGr-Si by the electroless deposition method, respectively. A drop of 0.2 mM H_2PtCl_6 (aq.) in 0.5 M HF was dropped on the Si surface for 10 sec. Each CV was performed at a scan rate of 0.05 V/s. [4.24]

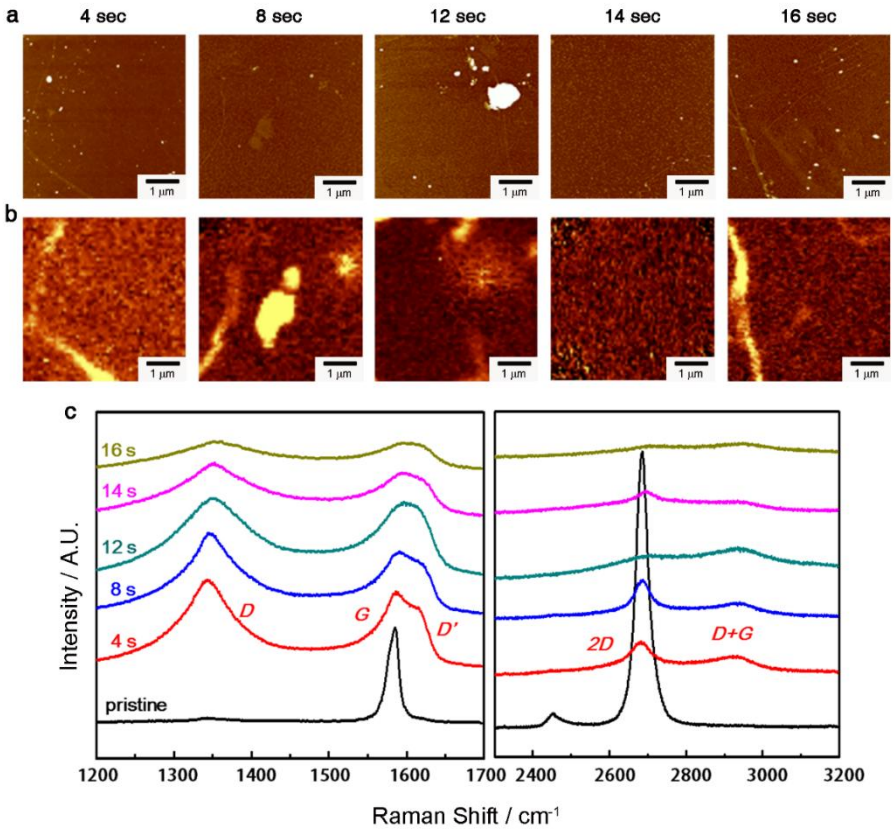

Figure 4.10. Surface morphology of monolayer Gr and NGrs. (a) AFM images and (b) Raman characterization of a pristine Gr sample as a function of the exposure time to N_2 plasma and the each image was taken the same area measured by AFM. Numbers on each figure indicate the exposure time. All figures have a size of 6.5 × 6.5μm^2 (c) Raman spectra of the samples. Numbers on the left side of the left figure indicate the exposure time. Raman peaks are indexed accordingly. [4.24]

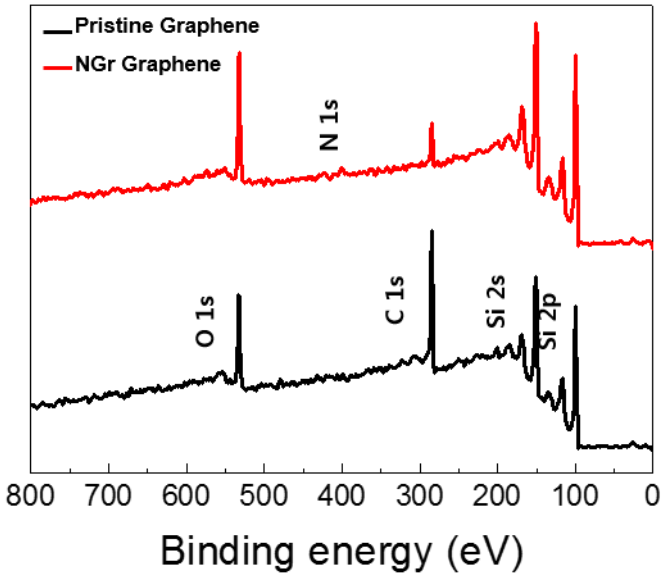

Figure 4.11. XPS spectra of Gr and NGr. The C 1s is 76.78 atomic weight % (at. %) for Gr and 57.17 at. % for NGr, N 1s is 0.00 at. % for Gr and 2.20 at. % for NGr, and O 1s is 23.22 at. % for Gr and 40.63 at. % for NGr, respectively.

4.24

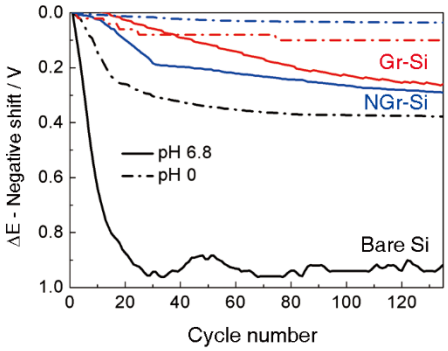

Figure 4.12. The change of onset potential of bare Si (black line), Gr-Si (red line), and NGr-Si (blue line) electrodes. The onset potential measured from the first CV sweep was a standard, and the difference between the measured onset potential during the CV cycles and the value of the first sweep was investigated; this difference is defined as ΔE – negative shift. The onset potential was measured with increasing the number of cyclic voltammetry in 1M $HClO_4$ (pH 0, dash dot line) and 0.4 M NaH_2PO_4 and 0.6 M Na_2HPO_4 (pH 6.8, solid line) electrolytes, respectively. [4.24]

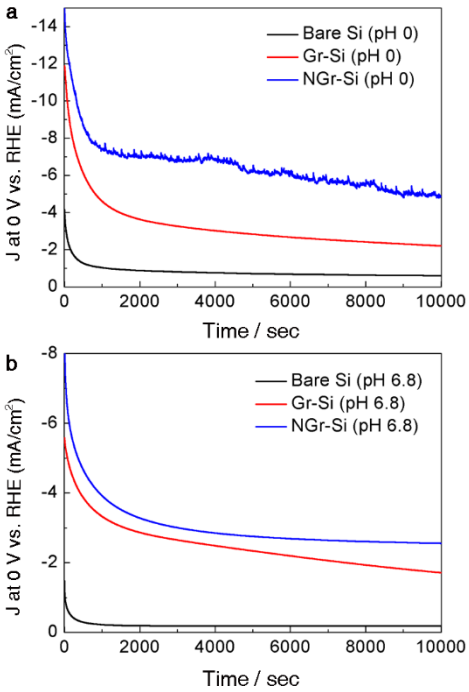

Figure 4.13. The change of photocurrent density at 0 V vs. RHE of bare Si (black line), Gr-Si (red line), and NGr-Si (blue line) electrodes with increasing the operation time in (a) pH 0 (1M $HClO_4$) and (b) pH 6.8 (0.6 M NaH_2PO_4 and 0.4 M Na_2HPO_4), respectively. At pH 0, NGr-Si electrode shows a spiky plot during a chronoamperometry operation because hydrogen bubbles stick to hydrophobic surfaces until sudden bursts occur.[4.24]

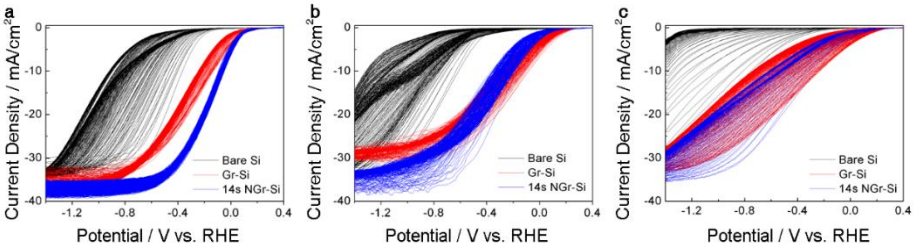

Figure 4.14. The stability test of bare Si, Gr-Si, and NGr-Si photocathodes. CV of Si photocathodes during 300 cycles with a scan rate of 0.05 V/s in (a) pH 0, (b) pH 3.8, and (c) pH 6.8. Polarization curves of each photoelectrodes shifted negatively vs. RHE as the CV operation increased. [4.24]

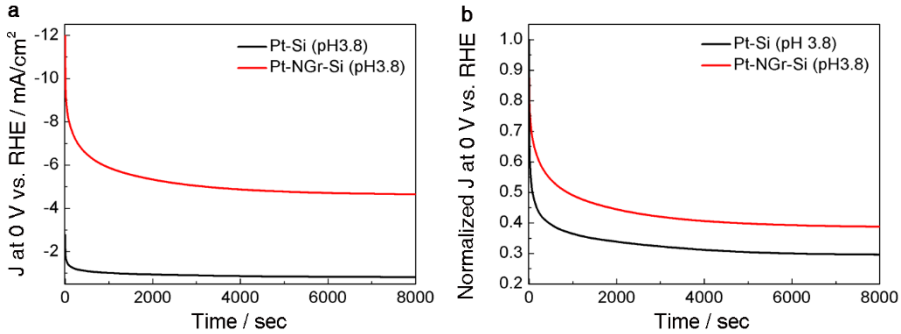

Figure 4.15. Chronoamperometry operation of Pt-Si and Pt-NGr-Si photocathodes at pH 3.8. (a) The change of photocurrent density at 0 V vs. RHE of Pt-Si (black line) and Pt-NGr-Si (red line) electrodes with increasing the operation time at pH 3.8. (b) The change of normalized photocurrent density (J/ J_{init}) at 0 V vs. RHE of each photoelectrodes with increasing the operation time at pH 3.8. J_{init} is the initial current density in the chronoamperometry operation. [4.24]

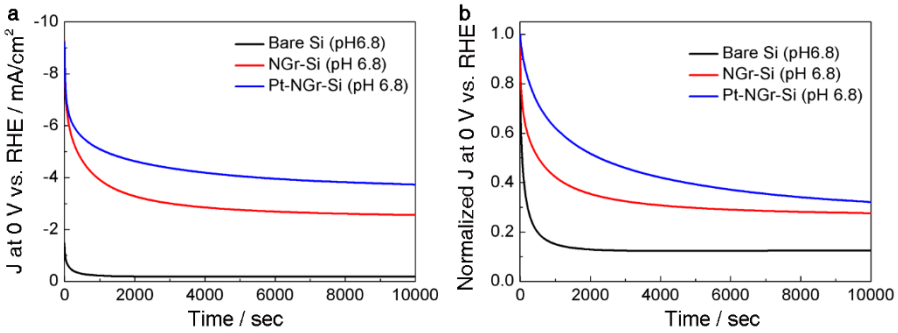

Figure 4.16. Chronoamperometry operation of bare Si, NGr-Si, and Pt-NGr-Si photocathodes at pH 6.8. (a) The change of photocurrent density at 0 V vs. RHE of bare Si (black line), NGr-Si (red line), and Pt-NGr-Si (blue line) electrodes with increasing the operation time at pH 3.8. (b) The change of normalized photocurrent density (J/ J_{init}) at 0 V vs. RHE of each photoelectrodes with increasing the operation time at pH 6.8. [4.24]

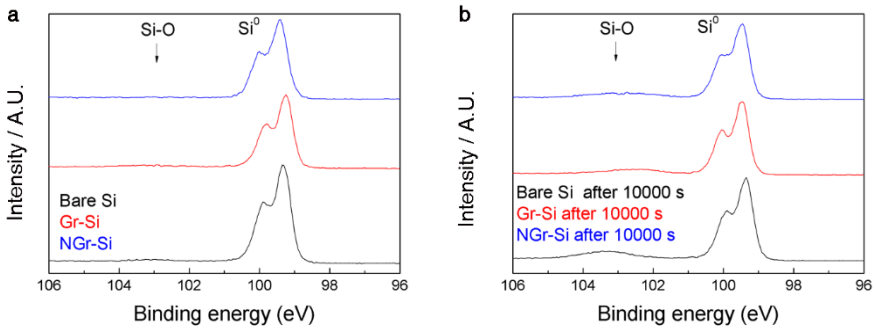

Figure 4.17. High resolution XPS spectra of Si 2p region of bare Si, Gr-Si, and NGr-Si electrodes. (a) XPS spectra of each samples before long-term CV operation and (b) after long-term CV operation for 10000 sec at pH 6.8. Narrow-scan data of the Si 2p region were collected using pass energy of 40 eV and 0.05 eV/step. [4.24]

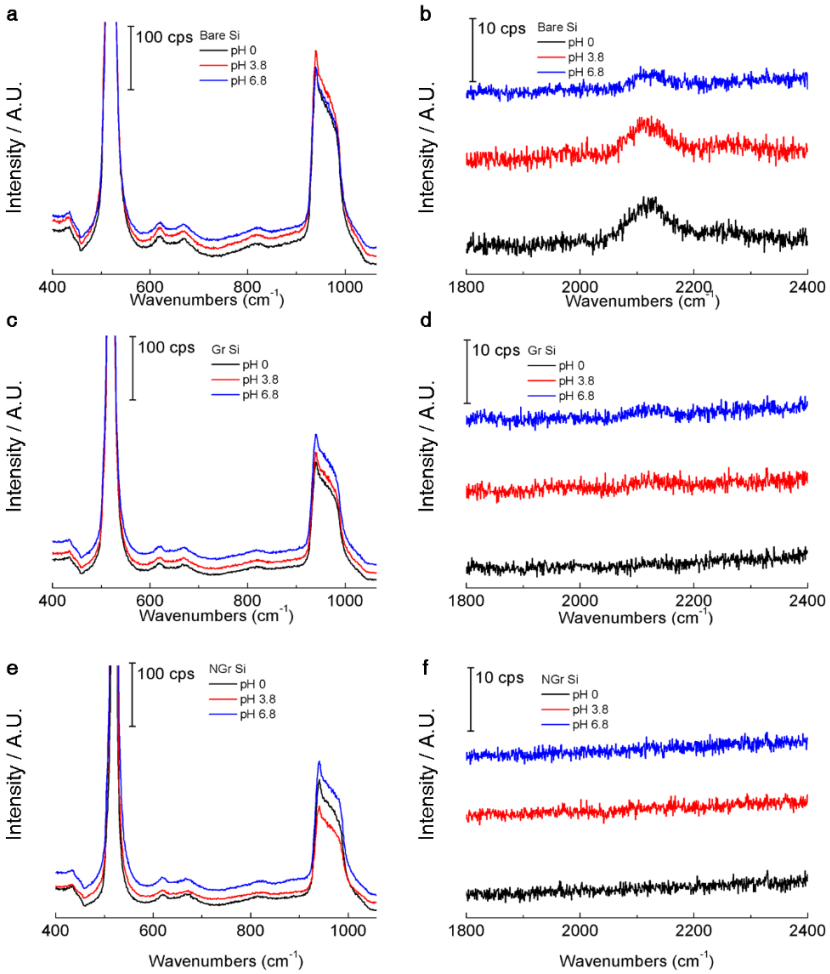

Figure 4.18. *In situ* Raman spectra of bare Si, Gr-Si, and NGr-Si at each pH solution. Raman spectra of each electrodes (a, c, e) in the low frequency region and (b, d, f) in the high frequency region. According to a useful pH range, each electrolyte was selected as 1M $HClO_4$ (pH 0), 0.2 M potassium hydrogen phthalate with 0.5 M K_2SO_4 buffered with KOH (pH 3.8), and 0.6 M monosodium phosphate and 0.4 M disodium phosphate (pH 6.8).[4.24]

Condition	Electrode	Onset potential [E (V) at -1 mA/cm^{-2}]	E (V) at -5 mA/cm^{-2}	E (V) at -10 mA/cm^{-2}
Under illumination (p type Si)	Bare Si	-0.17	-0.29	-0.42
	Gr--Si	0.01	-0.13	-0.21
	14s NGr-Si	0.12	0.02	-0.04
	Pt-Si	0.24	0.16	0.11
	Pt-NGr-Si	0.35	0.29	0.25
Under dark condition (n^+ type Si)	Bare Si	-0.63	-0.78	-0.85
	Gr-Si	-0.49	-0.61	-0.69
	14s NGr-Si	-0.44	-0.55	-0.62
Photovoltage*	Bare Si	0.46		
	Gr-Si	0.50		
	14s NGr-Si	0.56		
RDE (GC) under dark condition	Bare GC	-0.24	-0.33	-0.37
	Gr-GC	-0.18	-0.28	-0.31
	14s NGr-GC	-0.16	-0.26	-0.29

* The photovoltage is defined as the difference between the onset potential under the dark and illumination condition. This value was calculated from the consideration of the following reference; Y. W. Chen, J. D. Prange, S. Dühnen, Y. Park, M. Gunji, C. E. Chidsey and P. C. McIntyre, *Nature Mater.*, 2011, **10**, 539-544.

Table 4.1. Summary of the experimental data for Si and Glassy Carbon (GC) electrodes.

Bibliography

4.1. A. Heller, E. Aharon-Shalom, W. A. Bonner and B. Miller, *J. Am. Chem. Soc.*, 1982, **104**, 6942-6948.

4.2. Y. Hou, B. L. Abrams, P. C. K. Vesborg, M. E. Björketun, K. Herbst, L. Bech, A. M. Setti, C. D. Damsgaard, T. Pedersen, O. Hansen, J. Rossmeisl, S. Dahl, J. K. Nørskov and I. Chorkendorff, *Nature Mater.*, 2011, **10**, 434-438.

4.3. S. Y. Reece, J. A. Hamel, K. Sung, T. D. Jarvi, A. J. Esswein, J. J. H. Pijpers and D. G. Nocera, *Science*, 2011, **334**, 645-648.

4.4. A. Kudo and Y. Miseki, *Chem. Soc. Rev.*, 2009, **38**, 253-278.

4.5. Y. W. Chen, J. D. Prange, S. Dühnen, Y. Park, M. Gunji, C. E. Chidsey and P. C. McIntyre, *Nature Mater.*, 2011, **10**, 539-544.

4.6. R. N. Dominey, N. S. Lewis, J. A. Bruce, D. C. Bookbinder and M. S. Wrighton, *J. Am. Chem. Soc.*, 1982, **104**, 467-482.

4.7. U. Sim, H.-Y. Jeong, T.-Y. Yang and K. T. Nam, *J. Mater. Chem. A*, 2013, **1**, 5414-5422.

4.8. K. Novoselov, A. K. Geim, S. Morozov, D. Jiang, M. K. I. Grigorieva, S. Dubonos and A. Firsov, *Nature*, 2005, **438**, 197-200.

4.9. Y. Liang, Y. Li, H. Wang, J. Zhou, J. Wang, T. Regier and H. Dai, *Nature Mater.*, 2011, **10**, 780-786.

4.10. J.-D. Qiu, G.-C. Wang, R.-P. Liang, X.-H. Xia and H.-W. Yu, *J. Phys. Chem. C*, 2011, **115**, 15639-15645.

4.11. Q. Xiang, J. Yu and M. Jaroniec, *Chem. Soc. Rev.*, 2012, **41**, 782-796.

4.12. M. G. Walter, E. L. Warren, J. R. McKone, S. W. Boettcher, Q. Mi, E. A. Santori and N. S. Lewis, *Chem. Rev.*, 2010, **110**, 6446-6473.

4.13. F.-M. Liu, B. Ren, J.-W. Yan, B.-W. Mao and Z.-Q. Tian, *J. Electrochem. Soc.*, 2002, **149**, G95-G99.

4.14. A. J. Bard and L. R. Faulkner, *Electrochemical methods: fundamentals and applications*, Wiley New York, 1980.

4.15. Y. Li, H. Wang, L. Xie, Y. Liang, G. Hong and H. Dai, *J. Am. Chem. Soc.*, 2011, **133**, 7296-7299.

4.16. B. Conway and B. Tilak, *Electrochim. acta*, 2002, **47**, 3571-3594.

4.17. Y. Li, W. Zhou, H. Wang, L. Xie, Y. Liang, F. Wei, J.-C. Idrobo, S. J. Pennycook and H. Dai, *Nature Nanotech.*, 2012, **7**, 394-400.

4.18. Z. Huang, P. Zhong, C. Wang, X. Zhang and C. Zhang, *ACS Appl. Mater. Interfaces*, 2013, **5**, 1961-1966.

4.19. S. Trasatti, *J. Electroanal. Chem. Interfacial Electrochem.*, 1972, **39**, 163-184.

4.20. F. Tuinstra and J. L. Koenig, *J. Chem. Phys.*, 1970, **53**, 1126.

4.21. A. Ferrari and J. Robertson, *Phys. Rev. B*, 2001, **64**, 075414.

4.22. C. Casiraghi, S. Pisana, K. S. Novoselov, A. K. Geim and A. C. Ferrari, *Appl. Phys. Lett.*, 2007, **91**, 233108.

4.23. X. Li, W. Cai, J. An, S. Kim, J. Nah, D. Yang, R. Piner, A. Velamakanni, I. Jung, E. Tutuc, S. K. Banerjee, L. Colombo and R. S. Ruoff, *Science*, 2009, **324**, 1312-1314.

4.24. U. Sim, T.-Y. Yang, J. Moon, J. An, J. Hwang, J.-H. Seo, J. Lee, K. Y. Kim, J. Lee, S. Han, B. H. Hong and K. T. Nam, *Energy & Environ. Sci.*, 2013, **6**, 3658-3664.

Chapter 5 Layer Dependency of Graphene Catalysts

As an intermediate stage of extension from the single 2D platform to a complicate 3D structure, we have transferred graphene layer-by-layer as a well-defined model of the pseudo-3D system and investigated the layer dependence of catalytic activity. Comprehensive electrochemical analysis shows that there is an optimized structure of stacked graphene for the best catalytic activity and the highest charge transfer rate.

5.1 Introduction

The realization of cost-effective hydrogen production by water splitting requires photoelectrochemical (PEC) cells decorated with highly efficient co-catalysts.[5.1-5.4] In the race to replace noble-metal catalysts, carbon-based nanomaterials have emerged as a promising candidate for the hydrogen evolution reaction (HER). [5.5] For the first time, we investigated the use of monolayer graphene as an electrocatalyst for efficient HER, and a Si substrate was employed as a photocathode to develop a proof of concept for the HER catalytic activity.[5.6] We prepared mono-, double-, tri-, and multilayer graphene on p-Si photocathodes and investigated the layer dependence of the catalytic activity for HER. A comprehensive electrochemical analysis proved that a hetero-junction between the Si semiconductor, graphene layers, and electrolyte played a pivotal role in determining the catalytic activity and PEC performance. Because of the junction effect, the best PEC activity with the highest charge-transfer rate among graphene catalysts for HER reported to date was the plasma-treated double-layer graphene.

Because of their low cost and high stability, carbon-based nanomaterials have attracted considerable attention as catalytic materials for a variety of

chemical reactions, such as HER,[5.7] oxygen evolution reaction,[5.8] oxygen reduction reaction.[5.9] N and P heteroatoms adjacent to C atoms in the graphene matrix can affect these catalysts' valence orbital energy levels, thereby enhancing their reactivity toward HER.[5.5] Graphitic-carbon nitride combined with nitrogen-doped graphene also exhibits enhanced HER activity with properties similar to those of well-established metallic catalysts.[10] Reduced graphene oxide-containing catalytic active materials have exhibited improved activity in oxygen-reduction reactions and oxygen-evolution reactions in addition to HER.[5.9, 5.11-5.13] In most cases, however, the role of carbon materials is limited to an electrically conductive substrate or to promote the activity of other decorated catalysts.[5.9, 5.11, 5.12]

Graphene, a flat monolayer of carbon atoms, continues to attract extensive interest because of its outstanding electronic and structural properties, which make it a promising candidate for touch-screen displays,[5.14] photonics and optoelectronics,[5.15] and energy storage systems.[5.16, 5.17] In our previous reports, the graphene-silicon electrode was found to be effective for HER because of its superior transmittance, oxidation barriers, and abundant reaction sites for electron transfer.[5.6, 5.18, 5.19] In another study, we introduced a nitrogen plasma treatment to the graphene to increase the active sites, including defects and doping sites for HER, and proposed nitrogen-doped graphene quantum sheets (N-GQSs) and silicon nanowires to further improve the efficiency via both the orthogonalization of the incident light absorption and charge carrier collection. The combination of optimized Si nanowires and N-GQSs showed an applied bias photon-to-current efficiency (ABPE) of 2.29%. This finding led us to believe that the introduction of graphene and N-GQSs as high-performance, low-cost electrodes with superior cycle stability constitutes an important breakthrough for HER and future energy-storage systems.

Recently, multilayer graphenes with various structures were introduced to alter the physical and chemical properties of catalysts and active electrode

materials. However, the mechanism is still not understood, and studies modeling the interaction between the bulky carbon and the Si substrate are needed. Graphene is an interesting material because its number of layers can be defined, it can be used to tune the band gap of a material,[5.20] and it has striking characteristics, such as its electric field,[5.21, 5.22] chemical functionality,[5.23] and optical properties.[5.14] Yeom's group reported that the photovoltaic response of graphene/Si depends directly on the number of graphene layers and that the power-conversion efficiencies of devices with mono- and double-layer graphenes are higher than those of devices with tri- and tetralayer graphenes.[5.20] Moreover, the mobility of monolayer graphene decreases with increasing temperature because of surface polar phonon scattering, while the mobility of double- and trilayer graphenes is higher because scattering is screened by the additional graphene layers.[5.24] Lee's group calculated the interaction between graphene and H-passivated Si(100) and found that the change in the band gap was negligible for monolayer graphene.[5.25] The electronic properties of double-layer graphene on Si(100) changed significantly because of the asymmetry of the carbon sites, which caused band-gap widening as high as 108 meV.

There have been intense efforts to study the electrochemical behavior of graphene, graphene multilayers, and graphene derivatives. Monolayer and double-layer graphene on multilayer graphite have improved the electron transfer kinetics for the ferricyanide reduction compared with those on bare basal-plane or multilayer graphite substrates, and defects in the monolayer graphene exert minimal influence on the voltammetric response.[5.26] In contrast, Dale *et al.* reported that monolayer graphene possesses slow electrochemical kinetics in terms of heterogeneous electron transfer (HET) compared with the multilayered structure of quasi-graphene because of monolayer graphene's low degree of edge-plane coverage.[5.27] The electrochemical properties of multilayer graphene transferred onto an

insulating polyethylene terephthalate substrate were also investigated with regard to its HET properties and diversity of redox mediators. Its electrochemical behavior was similar to that of basal-plane graphite with a low density of edge-plane defect sites.[5.28] The electrochemical properties of monolayer or multilayer graphene have mostly been investigated in terms of HET and have been compared with those of the heterogeneous graphitic surfaces, such as the edge-plane sites or the basal plane. The electrochemical behavior of monolayer graphene-coated n-type Si(111) photoanodes was also investigated not as a catalyst but mainly as a passivation layer formed by oxidation in an aqueous solution.[5.29] Unfortunately, studies on the PEC responses specifically attributable to the number of graphene layers on electronic structures in a heterojunction system are lacking.

Here, we elucidate the mechanism of the PEC response for HER at the interface between graphene and the Si substrate. Graphene was selectively controlled layer-by-layer via an advanced graphene transfer-technique that we developed. We also introduced plasma treatment onto the various layered graphenes to generate more active sites. The graphene was synthesized via chemical vapor deposition (CVD), and the graphene layers were prepared by layer-by-layer transfer whereby each graphene layer was randomly oriented. The work function of the plasma-treated double-layer graphene on the Si electrode unexpectedly showed the smallest value and induced the strongest band bending for enhanced HER, which is consistent with the results of a Mott-Schottky analysis at the interface between the graphene/Si and the electrolyte. Moreover, the PEC performance exhibits an enhanced ABPE of 0.32%, which is 64 times higher than that of bare Si and is the highest value recorded for carbon-based catalysts on planar p-Si photocathodes.

5. 2 Results and discussion

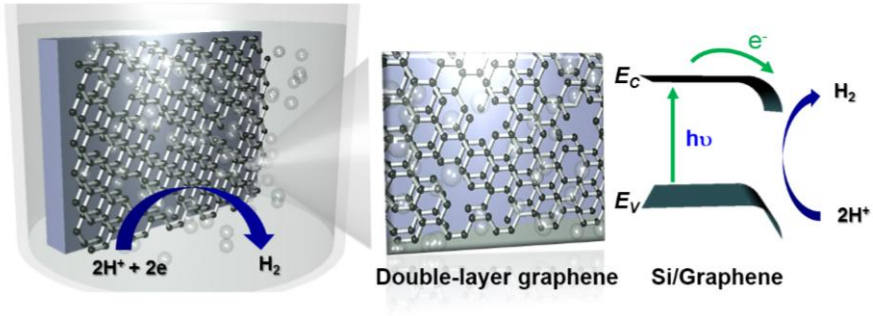

Figure 5.1. Schematic of double-layer graphene on p-silicon photocathode. Minor carriers (electrons) are generated when silicon absorbs photons, which drift to the photocathode/electrolyte interface, where $2H^+$ is reduced to H_2. Plasma-treated double-layer graphene acts as an electrocatalyst for hydrogen production as well as induces surface modification of the photocathode leading to change energy band diagram of photocathode. E_{CB} and E_{VB} indicate conduction band maximum and valance band minimum of graphene/Si photocathode. The photogenerated electron can be easily moved to the conduction band edge of graphene/Si, and the strong band bending accelerates hydrogen production.

Figure 5.1 shows HER catalyzed by double-layer graphene on p-type Si in an acidic solution under irradiation. Photons absorbed by the silicon wafer generate minority carriers (electrons), which drift to the graphene on the semiconductor/electrolyte interface and reduce $2H^+$ to H_2. The double-layer graphene plays a key role not only as an electrocatalyst for HER but also in tuning the surface work function of the photocathode to facilitate hydrogen gas generation. The atomic force microscope (AFM) images in Figures 5.1a-d show the gradual increase of surface roughness, wrinkles, and folded regions

with higher numbers of layers. The inset shows the height profile of each graphene layer: the thickness of monolayer graphene was less than 1 nm, double-layer graphene was approximately 1.5 nm, trilayer graphene was less than 3 nm, and the multilayer (4 layer) graphene was approximately 4 nm because of wrinkles and folded areas. To study the interfacial structure between the graphene and Si electrode, focused ion beam milling was used to prepare the transmission electron microscopy (TEM) specimens. The cross-sectional TEM images show that mono-, double-, tri-, and multilayer graphenes transfer well onto the Si electrode; a partially folded area is shown in Figures 5.2e-h. The typical real-space TEM images of the various graphenes show largely clean and flat layers. Each inset represents the fast Fourier transform (FFT) of each image. The six spots with the same intensity in the inset of Figure 5.2i exhibit the classic pattern of monolayer graphene. The two sets of hexagonal patterns in double-layer graphene are rotated relative to each other by ~23.5°. From the diffraction spots, we can confirm that the upper and lower graphene are stacked with the rotation angle. [5.23] The three sets of patterns in the trilayer graphene and the four sets in the multilayer graphene also indicate that each graphene layer was transferred with some rotation. To verify the graphene layers, Raman spectroscopy was conducted on each graphene specimen at room temperature with a Renishaw spectrometer at 514 nm. The two strongest features are the G peak at 1590 cm^{-1} and 2D peak at 2700 cm^{-1}, which originate from the in-plane vibrational E_{2g} phonon and the second order of zone-boundary phonons, respectively. [5.30] With the transfer of each graphene layer, the intensities of both the G- and 2D-band peaks increase, and the 2D peaks become slightly blueshifted relative to the 2D peak in monolayer graphene. However, the intensity ratio of the G peak to the 2D peak (I_G/I_{2D}) ratios does not change significantly. We observed a D peak at 1350 cm^{-1} in the several-layer graphene specimens, which indicates the presence of defects, most likely introduced by the

randomly oriented hexagonal lattices of the upper and lower layers, unlike in the structure of graphite. Therefore, the typical properties of each graphene layer remain unchanged, even after stacking. In contrast, the optical transmittance of each graphene specimen is reduced by approximately 2.3% for each additional layer, which reduces the transmittance of multilayer graphene (4 layers) to 90% transmittance at 550 nm. The superior transmittance of graphene substantially enhanced the amount of incident light reaching the photocathode.

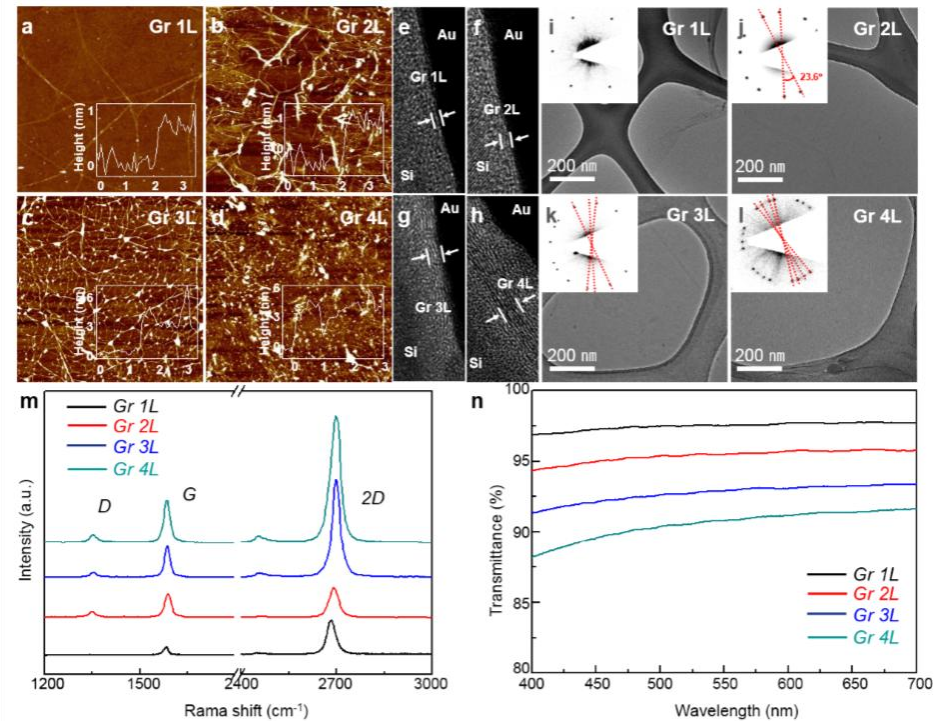

Figure 5.2. Surface characterization of graphene with number of layer. (a)-(d), Atomic force microscopy (AFM) images of graphene with different number of layer: mono-layer graphene (Gr 1L), double-layer graphene (Gr 2L), tri-layer graphene (Gr 3L), multi-layer graphene (Gr 4L). Each inset

shows the height profile. (e)-(h), Cross-sectional TEM images of graphene with different number of layer on Si electrode and (i)-(l), top-view TEM images of graphene with different number of layer on holly carbon grid. Each inset shows the selective area electron diffraction (SAED) of each image. The hexagonal patterns in double-, tri-, and multi-layer graphene show that graphene layers are misoriented when the graphene is transferred and stacked. (m), Raman spectra of graphene with different number of layer. (n), Transmittance of graphene specimens on polyethylene terephthalate substrate.

The PEC performance of graphene/Si electrodes for hydrogen production is strongly dependent on the number of graphene layers. To evaluate the photocathodic behavior of the graphene/Si electrodes, the current density was measured as the potential was swept from 0.3 V to -0.8 V vs. RHE in a three-electrode cell. As shown in Figure 5.3a, the current density of the bare planar Si increases gradually from -0.2 V vs. RHE and becomes saturated at the limiting current density of approximately -31 mA/cm^2 at a specific applied potential. Measurement of the monolayer graphene on planar Si shows that the potential required to attain a current density of -5 mA/cm^2 is 180 mV more positive than that of bare planar Si. When graphene layers are added on the electrode, up to five layers in total, all samples show positive shifts of the overall current density-potential (*J-E*) photoresponse curve. Interestingly, the *J-E* curve of double-layer graphene shows the largest positive shift. The potential at -5 mA/cm^2 is -0.04 V vs. RHE, indicating a positive shift of 230 mV compared with bare Si (-0.27 V vs. RHE). Thereafter, the potential at -5 mA/cm^2 decreases with additional graphene layers (Figure 5.3b). To compare the incident photon-to-current conversion efficiency, the applied bias photon-to-current efficiency (ABPE) is calculated from the *J-E* response using the following relation: [5.31]

$$ABPE = [j_{ph}\ (mA/cm^2) \times (V_{redox} - V_{bias})\ (V) / P_{in}\ (mW/cm^2)]_{AM\ 1.5\ G} \times 100\ (\%) \quad (1)$$

where j_{ph} is the photocurrent density obtained under an applied bias V_{bias}, V_{redox} is the redox potential for hydrogen production (0 V), V_{bias} is the externally applied bias potential that is often necessary to achieve reasonable photocurrents, and P_{in} is the intensity of the incident light for the AM 1.5 G condition (100 mW/cm^2). Figure 5.8 summarizes the ABPE data of various catalysts on p-type planar Si photocathodes. As shown in Figure 5.8, the ABPE of monolayer graphene/Si is 0.04%. When the double-layer graphene is deposited on the Si, the ABPE is 0.05%, which is 10 times higher than that of bare Si and 1.25 times higher than that of monolayer graphene on Si (Figure 5.8). Both the double-layer and monolayer graphenes can act as effective HER catalysts on the Si photocathode. However, the transfer of additional graphene layers gradually decreases the ABPE. Therefore, the number of graphene layers significantly affects the PEC performance and influences the intensity of the incident light. As shown in Figure 5.2a, the limiting current density decreases from 31.1 mA/cm^2 to 24.9 mA/cm^2 as the number of graphene layers increases. A decrease in the current density of approximately 97.7% with each graphene layer corresponds well with the intrinsic optical transmittance of the graphene layer (Figure 1n), which also decreases by approximately 97.7% for each layer (Figure 5.9). Therefore, the decrease in the limiting current density can be attributed to the hindrance of light absorption.

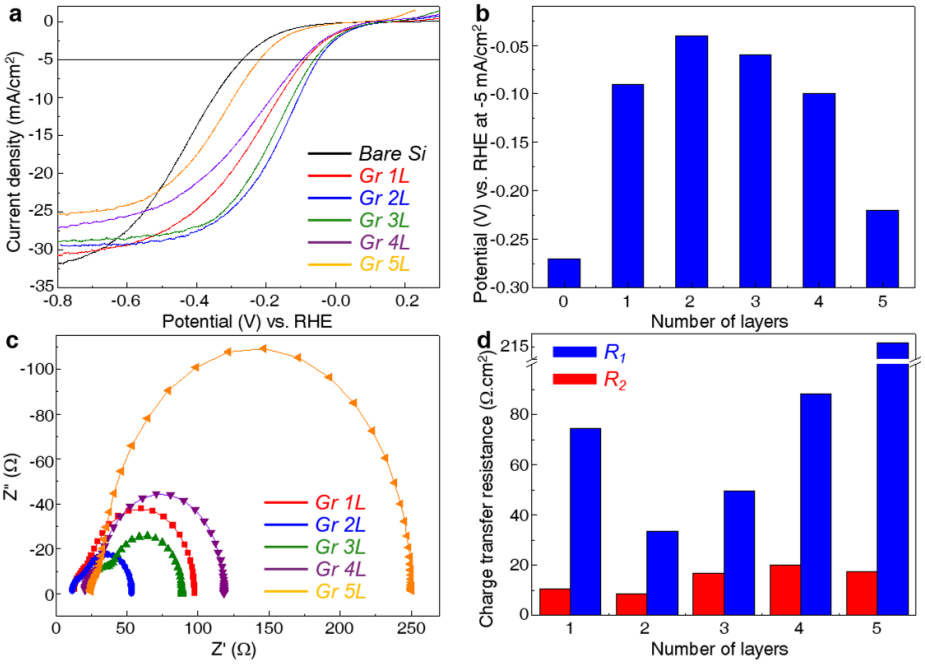

Figure 5.3. Photoelectrochemical response of graphene on silicon. (a), Photocurrent density-potential (*J-E*) curves of multiple layers of graphene on lightly boron-doped planar p-Si. (b), Potential vs. RHE at -5 mA/cm^2 depending on the number of graphene layers. (c), Nyquist plot for graphene/Si electrode at 0 V vs. RHE under illumination condition. (d), Charge transfer resistance depending on the number of graphene layers. R_1 is the charge transfer resistance of the electrical double layer at interface between electrode and electrolyte and R_2 is the charge transfer resistance of the depletion layer in graphene/Si.

To investigate the origin of the change in the catalytic activity by varying the number of graphene layers, electrochemical impedance measurements were performed. Figure 5.3c shows a Nyquist plot representing a typical impedance result. Compared with the bare Si (not shown here), each graphene/Si

electrode shows a much smaller semicircle, which corresponds to lower charge-transfer resistance. The graphene/Si electrodes show two semicircles, corresponding to two different charge-transfer resistances: R_1 and R_2. In the equivalent circuit, $R_{overall}$ is the overall series resistance of the circuit. R_1 is the charge-transfer resistance and C_1 is the capacitance phase element of the electrical double layer at the interface between the electrode and electrolyte. R_2 is the charge-transfer resistance and C_2 is the capacitance phase element of the depletion layer in graphene/Si. The charge transfer across the electrical double layer at the semiconductor/electrolyte interface is dominant in the low-frequency region, while that in the depletion layer of the semiconductor dominates in the high-frequency region.[5.32, 5.33] In the case of the double-layer graphene/Si electrodes, both semicircles are smaller than those of the other graphene/Si systems, and thus, the values of both R_1 and R_2, i.e., the overall charge-transfer resistance, for the double-layer graphene/Si electrode are the lowest of all the graphene/Si electrodes, as shown in Figure 5.3d and Table 5.1. The charge-transfer resistance is related to a kinetic barrier energy for the faradaic reactions across the electrical double layer.[5.32] The charge-transfer resistance is also inversely proportional to the exchange current for the faradaic reaction, as described by the Butler-Volmer equation.[5.33] A graphene/Si system with a lower charge-transfer resistance promotes the faradaic reaction, which is related to relatively low R_1 value, thus enhancing HER (through faradaic reactions) with a lower overpotential. The smaller semicircle in the high-frequency range (related to R_2) indicates that the charge-transfer resistance of the semiconductor depletion layer in the graphene/Si is also lower than that of the bare Si. This depletion layer resistance is also correlated with a higher photocurrent response because of the increased band bending in the depletion layer.[5.34, 5.35]

To study the band bending effect of the graphene layers on the Si electrode in an aqueous electrolyte, capacitance measurements were performed as the

potential was swept from 0.6 V to -0.3 V vs. RHE in a three-electrode cell without illumination as shown in Figure 5.4a. The flat-band potential of the bare Si and graphene/Si electrodes were calculated from the capacitance results using the Mott-Schottky relation: [5.36]

$$1/C_{sc}^2 = 2(E - E_{fb} - kT/e)/(e\varepsilon\varepsilon_0 N) \quad (2)$$

where C_{sc} is the capacitance of the space charge region, ε is the dielectric constant of the semiconductor, ε_0 is the permittivity of free space, N is the donor density (i.e., the hole acceptor concentration for a p-type semiconductor), E is the applied potential, and E_{fb} is the flat-band potential. Figure 5.3a shows the typical Mott-Schottky plots for a p-type silicon semiconductor. The donor density was calculated from the slope, and the E_{fb} was determined by extrapolation to a capacitance of zero. The monolayer graphene/Si electrode exhibited an E_{fb} of 0.20 V vs. RHE, whereas the E_{fb} of the bare planar Si was 0.001 V vs. RHE, as shown in Figure 5.3b. The applied potential and E_{fb} determine the magnitude of band bending in the semiconductor (E_b) according to the equation: $E_b = E - E_{fb}$. [5.37] As E_{fb} increases positively, the absolute value of E_b increases because the applied potential, E is always negative for proton reduction at the cathode. Higher band bending at the electrode/electrolyte interface promotes faster charge separation of generated electrons and holes. [5.34] The higher E_{fb} of the graphene/Si electrode relative to that of the bare planar Si appears to have increased the extent of band bending at the depletion region of the semiconductor near the solid/solution interface because of the relationship between E_b and E_{fb}. Furthermore, in the case of double-layer graphene/Si, E_{fb} increased to 0.26 V vs. RHE, corresponding to the highest band bending among the multilayered graphene/Si electrode systems. Meanwhile, the doping densities of bare Si and graphene/Si are also calculated from the Mott-Schottky relationship. Using Eq. (2), the bare Si is calculated to have a donor

density of 4.46×10^{15} /cm^3, whereas the graphene/Si electrodes have an average donor density of 5.74×10^{15} /cm^3. Interestingly, transferring additional graphene layers has little influence on the value of the slope. To gain more insight into the effect of the number of graphene layers, we also measured (1) the cyclic voltammetry (CV) scan-rate dependence to confirm the capacitance of the electrical double layer at the solid/solution interface and (2) the UV photoelectron spectroscopy (UPS) characterization to investigate the origin of the change in the depletion region of graphene/Si.

The capacitance of the electrical double layer at the solid/solution interface was evaluated by measuring the *J-E* response of the graphene/Si electrode at various scan rates, as shown in Figure 5.4c. The capacitance of the double layer is estimated from the slope of the plot of J_C, which is the current at the potential with a net current density of 0 μA/cm^2, as a function of the scan rate (Figure 5.3d). The capacitance of monolayer graphene is 81.6 μF/cm^2, and that of the double-layer graphene is 106.9 μF/cm^2, both of which are higher than those of bare Si (10 μF/cm^2) and a compact flat electrode (10~20 μF/cm^2). [5.38] The slope is also proportional to the exchange current density, which is directly related to the catalytically active surface area. [5.39, 5.40] The graphene layer, therefore, only has an electrochemical catalytic surface area, which may provide the intrinsic active sites for the HER. Moreover, compared with the monolayer graphene, the double-layer graphene has an electrochemical surface area that is 1.31-times larger and, therefore, more active surface areas for HER are generated in the double-layer graphene.

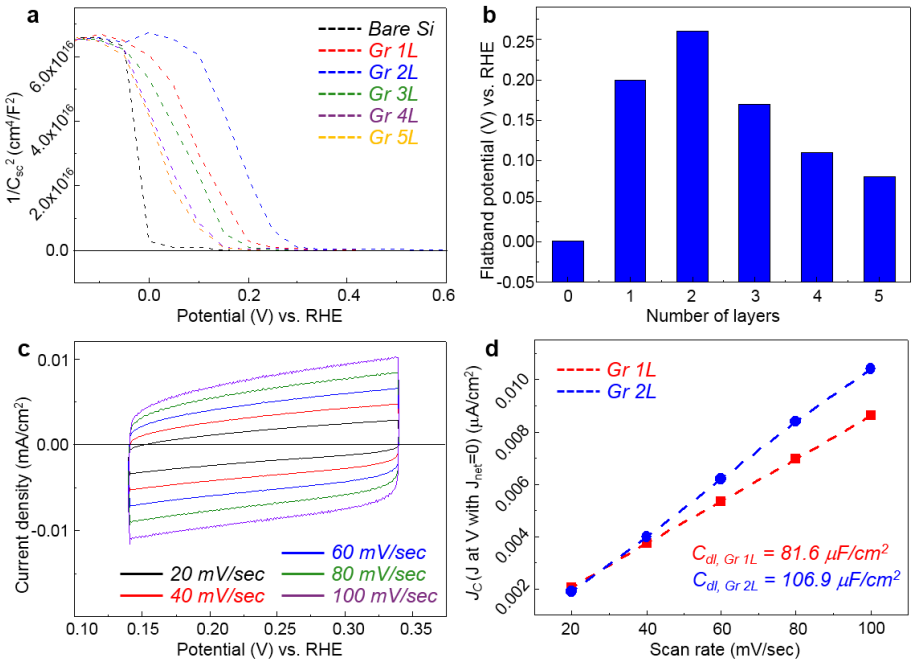

Figure 5.4. Electrochemical response of graphene on silicon under dark condition. (a), Mott-Schottky plots of bare Si and graphene on Si from capacitance measurement as a function of potential vs. RHE under dark condition. C_{sc} is the capacitance of the space charge region. (b), Flatband potential of graphene depending on the number of graphene layers. (c), The current to potential result of monolayer graphene on Si electrode at different scan rates. (d), The capacitance current (J_C) of mono- and double-layer graphene at J_{net}= 0 mA/ depending on scan rates. The slope of the J_C to scan rates plot is the capacitance of the double layer (C_{dl}).

UPS He I (21.2 eV) was investigated to study the effect of the energy band structure on hydrogen production. Figure 5.4a shows the onset of the secondary cut-off of the photoemission electron spectra of Si and graphene/Si electrodes. The work function (Φ) was calculated as follows: [5.20]

$$\Phi = h\nu - | E_{cut\text{-}off} - E_F | \quad (3)$$

where E_F is the Fermi level energy and $E_{cut\text{-}off}$ is the secondary cut-off energy. The work function of the bare Si substrate, approximately 4.61 ± 0.02 eV, is decreased by the addition of graphene layers. These changes are depicted as $\Delta\Phi_{Gr}$ in Figure 5.4b. The $\Delta\Phi_{Gr}$ is -0.2 eV for monolayer graphene, -0.36 eV for double-layer graphene, -0.26 eV for trilayer graphene, and -0.025 eV for multilayer graphene (4 layers). This result indicates that the work function of graphene/Si electrodes can be controlled by the addition of graphene layers, which also changes energy band structure of the photoelectrode. Interestingly, the double-layer graphene on Si shows the smallest work function. Based on the work function values measured by UPS, the schematic energy-band diagrams of bare Si and graphene/Si are depicted in Figure 5.4c to easily describe the interface energetics between the photocathode and electrolyte. In the energy band diagram of Si, the difference of E_F and the H^+/H_2 redox potential is the maximum attainable photovoltage (V_{OS}), which is also the maximum amount of band-bending at the bare Si/electrolyte interfaces. At the graphene/electrolyte interface in the graphene/Si systems, as shown in Figure 5.4c, the smaller work function indicates that the conduction band edge is strongly bended to H^+/H_2 redox potential. As a result, the smallest work function, which is attributed to the double-layer graphene/Si, enables the strongest band bending in the depletion region, leadingly to the most obvious positive shift of the onset potential in the PEC response, as shown in Figure 5.2a. The schematic depiction of the work function is also well supported by the result of the flat-band potential from the Mott-Schottky plot, as shown in Figure 5.3a. The double-layer graphene/Si heterostructure shows the Schottky

contact, which produces an electron path for proton reduction at the electrode/electrolyte interface.[5.20] Double-layer graphene has been reported to cause band gap opening, which may affect the work function of the graphene/Si system.[5.21] The present results show that the surface modification with layered graphene changes the band bending of the Si surface and affects the kinetics of hydrogen production.

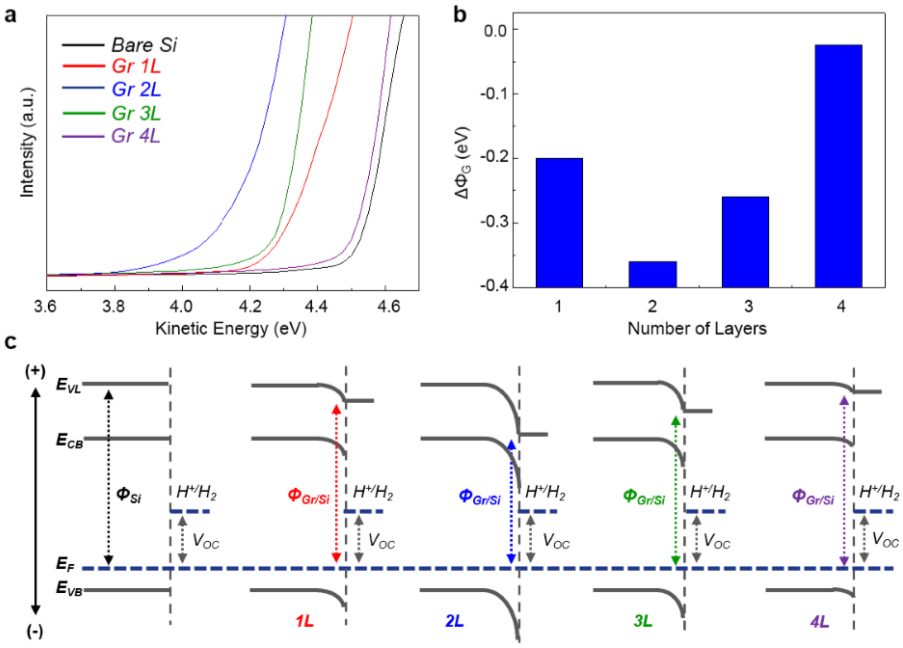

Figure 5.5. Work function and energy band diagrams of different number of graphene layer/Si. (a), Ultraviolet photoelectron spectroscopy (UPS) spectra of mono-, double-, tri-, and multi-layer graphene on Si electrode. (b), Work function difference ($\Delta\Phi_G$) between graphene and Si with different number of graphene layers. (c), Schematic energy band diagrams of bare Si and graphene/Si on the basis of the work function values measured by UPS. E_{VL}, E_{CB}, E_{VB}, E_F, and Φ_{si} represent vacuum level, conduction band edge, valence

band edge, fermi level, and work function of silicon electrode. The difference in E_F and H^+/H_2 is the maximum attainable photovoltage (V_{OC}).

To further enhance the HER properties of the graphene catalyst, plasma treatment is introduced to the pristine graphene layer. Plasma treatment can easily tune the intrinsic properties of graphene and produce large quantities of defects/edges.[5.6] Graphene on Cu foil was exposed to argon plasma (10 W RF power) for 4 seconds under 120 mTorr. This treatment was repeated for each layer in the stacking process mentioned above to obtain plasma-treated multilayer graphene. Figure 5.11 shows the AFM images of plasma-treated graphene, and the surface roughness clearly increases as the number of layers increases because of the formation of wrinkles, ripples, and folded areas. After exposure to argon plasma, the intensity of the D peak, which is related to structural defects at the edges of graphene, is significantly higher, and the intensities of the G and 2D peaks increase together (Figure 5.11e).[5.41] The plasma-treated graphene also shows a decrease in optical transmittance with each layer (approximately 2.15%/layer), but each layer shows higher transmittance than that of untreated graphene layers (Figure 5.11f). As shown in Figure 5a and S6, plasma-treated graphene exhibits an additional positive shift of the overall *J-E* curve under illumination. In the case of the plasma-treated double-layer graphene, the PEC performance has an ABPE of 0.32%, which is 64 times higher than that of bare p-type Si, which is the highest value recorded for carbon-based catalysts on planar p-Si photocathodes (Figure 5.8). The E_{fb} of double-layer graphene also increases up to 0.30 V vs. RHE, which is higher than that of the pristine double-layer graphene (0.26 V vs. RHE). To study the origin of the enhanced photoresponse and electrochemical performance of the plasma-treated graphene, UPS measurements were performed. The work functions of Si and the plasma-treated graphene/Si are shown in Figure 5.5d. Interestingly, the work functions of the plasma-treated

graphene/Si electrodes are much smaller than those of the untreated graphene/Si electrodes. The plasma-treated graphene contains a large quantity of defects and edges, which enables protons in the electrolyte to easily adsorb onto active sites. [5.42] Aqueous protons have been reported to easily adsorb onto the atomic defect sites of graphene because of a low kinetic energy barrier. [5.43] Another previous study also indicated that graphene with adsorbed protium atoms (or protons in the electrolyte) exhibits an upward shift of E_F (i.e., a smaller E_F) because adsorbed protium atoms alter the electronegativity within the graphene and the less-electronegative protium atoms behave similar to electron donors. [5.44] Specifically, the plasma-treated double-layer graphene/Si shows the lowest work function ($\Delta\Phi_{Gr}$= -1.0 eV). The results indicate that surface modification with graphene changes the band bending of the Si surface and enhances the kinetics of hydrogen production. In this study, based on the PEC results and the electrochemical analysis, generating defects in the graphene structure via plasma treatment effectively improves the catalytic activity of graphene layers on Si.

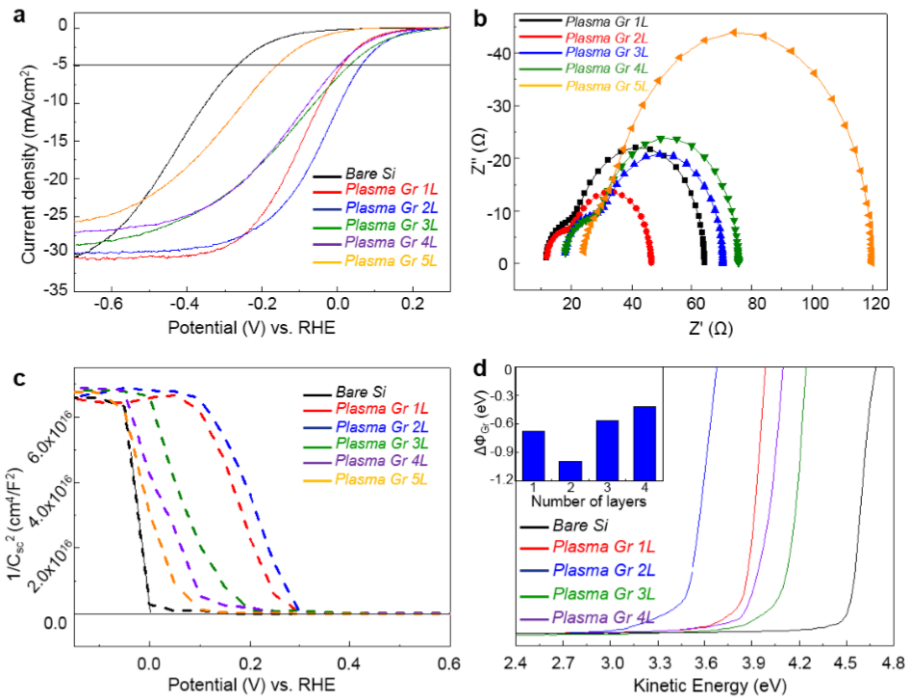

Figure 5.6. Electrochemical response of Ar plasma-treated graphene on silicon. (a), *J-E* curves of plasma-treated multiple layers of graphene on planar p-Si. (b), Nyquist plot for plasma-treated graphene/Si electrode at 0 V vs. RHE under dark condition. (c), Mott-Schottky plots of plasma-treated graphene on Si from capacitance measurement. (d), UPS spectra of the plasma-treated graphene layer/Si electrode. Inset shows $\Delta\Phi_G$ between plasma-treated graphene and Si surface with different number of graphene layers.

5.3 Conclusion

In conclusion, we designed heterostructures with mono-, double-, and multilayers of graphene on Si to obtain enhanced PEC performance, and we investigated the layer dependence of HER catalysis. Double-layer graphene significantly increased the photon-to-current conversion efficiency. Moreover, the plasma-treated double-layer graphene had a large number of defects and active sites, which further promoted the PEC performance up to an ABPE of 0.32%. Based on the in-depth electrochemical analysis, the low charge-transfer resistance of double-layer graphene/Si gives rise to a high photocurrent response for HER. The junction effect in the double-layer graphene/Si system also induced the strongest bending of the conduction band edge, thereby improving the likelihood that the photogenerated electrons would participate in the hydrogen-production reaction. We believe that our study provides a new and important approach to develop metal-free carbon-based catalysts for PEC hydrogen production.

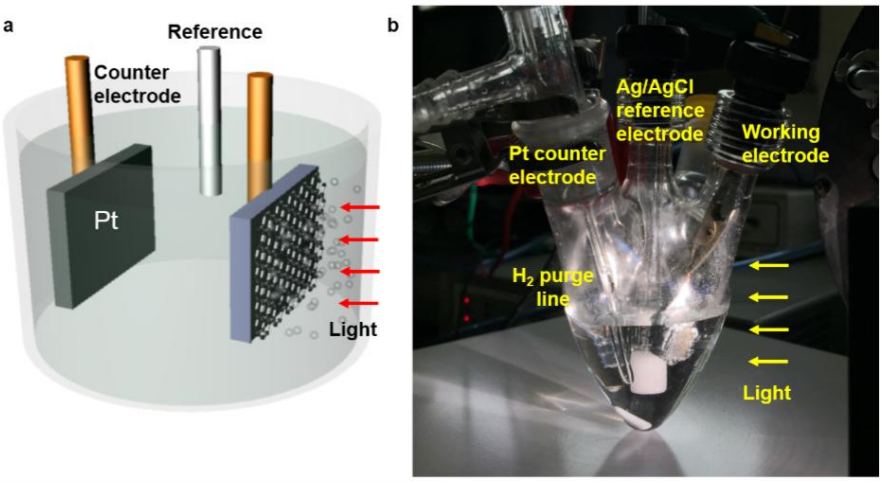

Figure 5.7. Schematic illustration and photograph images of hydrogen evolution reaction on graphene/Si Photocathode.

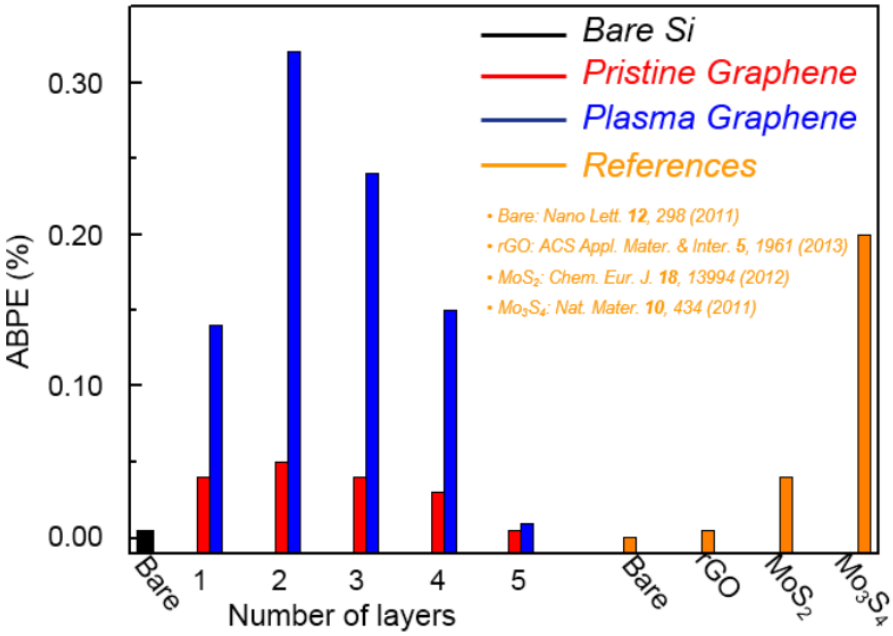

Figure 5.8. Photoelectrochemical performance of catalysts on p-Si. ABPE indicates the applied bias photon-to-current efficiency. 'Bare' indicates the performance of the bare electrode without deposition of catalyst.

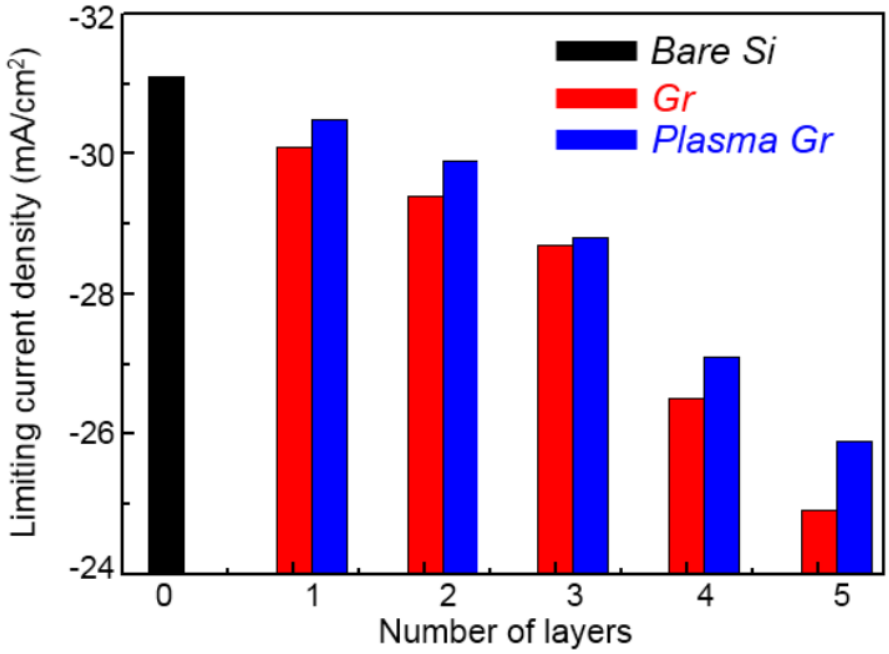

Figure 5.9. Photoelectrochemical response of graphene on silicon. Limiting current density (Saturation current density) from photocurrent density-potential (*J*-*E*) curves of different number of graphene layers on lightly boron-doped planar p-Si electrode.

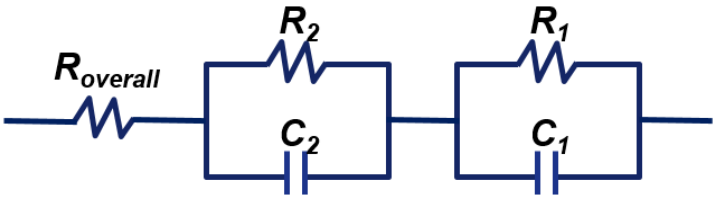

Figure 5.10. Equivalent circuit to analyze the electrochemical impedance spectroscopy data. $R_{overall}$ is the overall series resistance of the circuit, R_1 is the charge transfer resistance of the double layer at interface between electrode and electrolyte, C_1 is the capacitance phase element of the double layer at interface between electrode and electrolyte, R_2 is the charge transfer resistance of the depletion layer in graphene/Si and C_2 is the capacitance phase element of the depletion layer in graphene/Si.

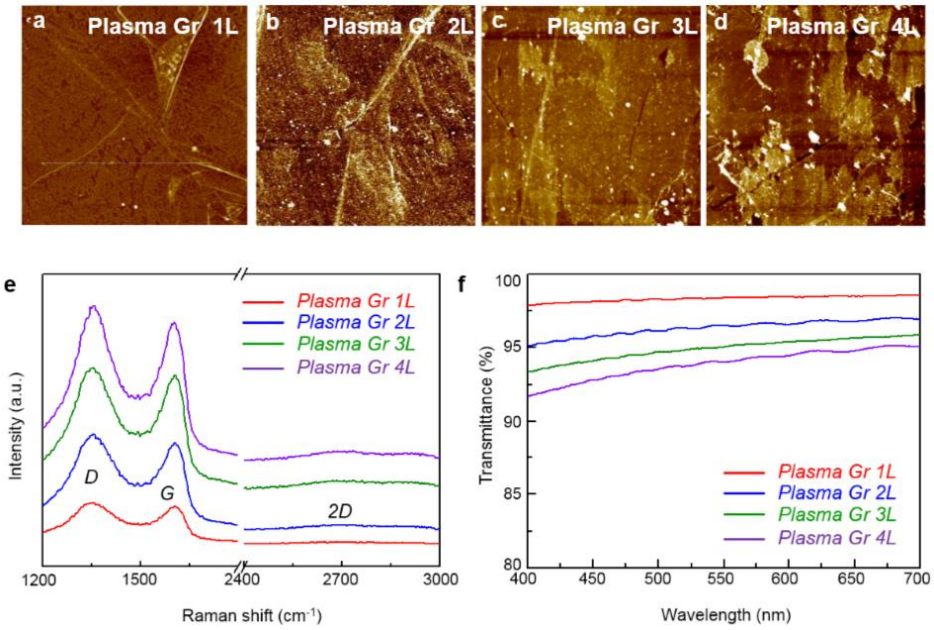

Figure 5.11. Surface characterization of the different number of plasma-treated graphene layers. (a)-(d), Atomic force microscopy (AFM) images of different number of plasma-treated graphene layers. (e), Raman spectra of plasma-treated. (f), Transmittance of plasma-treated graphene specimens on polyethylene terephthalate substrate.

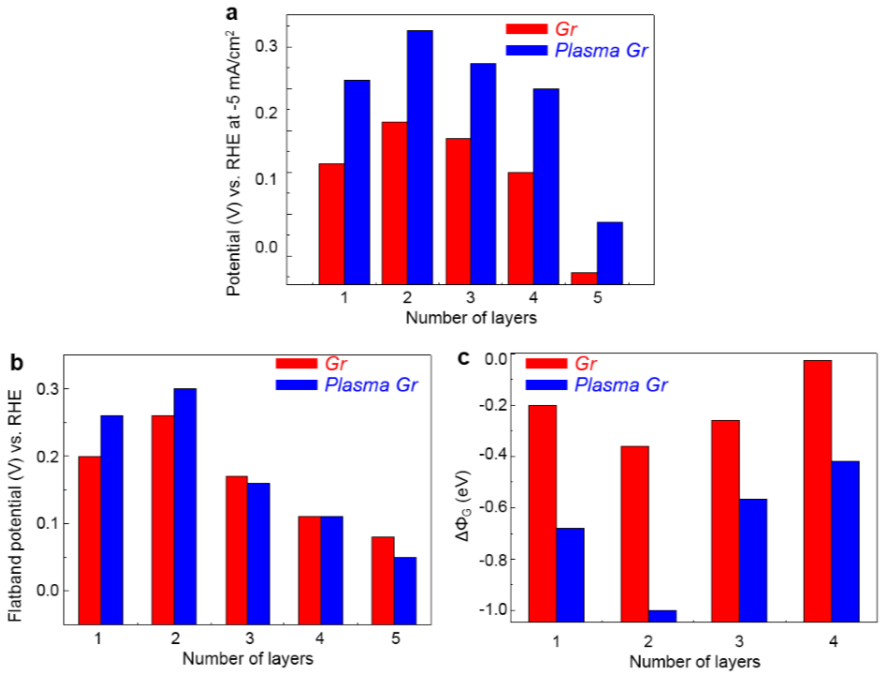

Figure 5.12. Comparison of electrochemical data between pristine graphene and plasma-treated graphene. (a), Potential vs. RHE at -5 mA/cm^2 of different number of graphene layers. (b), Flatband potential of pristine graphene and plasma-treated graphene. (c), Work function difference between graphene and the Si.

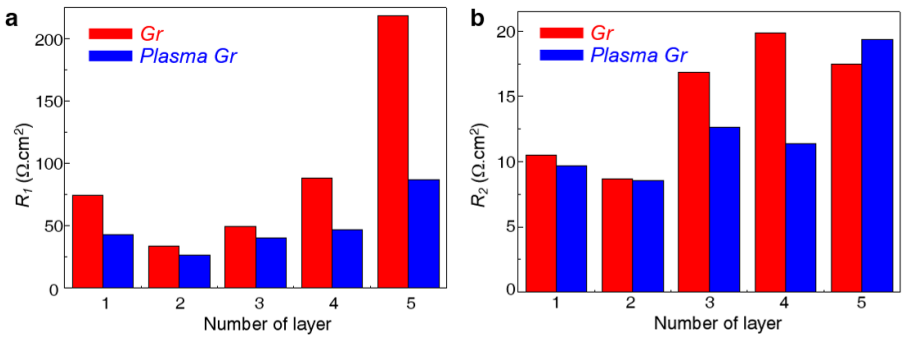

Figure 5.13. Comparison of electrochemical data between pristine graphene and plasma-treated graphene. Charge transfer resistance of different number of graphene layers. (a), R_1 is the charge transfer resistance of the electrical double layer at interface between electrode and electrolyte. (b), R_2 is the charge transfer resistance of the depletion layer in graphene/Si.

Sample	$R_{overall}$ ($\Omega.cm^2$)	R_2 ($\Omega.cm^2$)	C_2 ($\mu F/cm^2$)	R_1 ($\Omega.cm^2$)	C_1 ($\mu F/cm^2$)
Bare Si	11.65	3083	2.081E-06	-	-
Pristine Gr 1L	12.76	10.51	1.49E-06	74.39	3.439E-06
Pristine Gr 2L	11.61	8.672	2.043E-06	33.34	7.68E-06
Pristine Gr 3L	22.33	16.86	5.081E-07	49.49	3.14E-06
Pristine Gr 4L	20.32	19.906	1.54E-06	88.26	3.918E-06
Pristine Gr 5L	24.36	17.461	2.93E-06	218.3	4.377E-06
Plasma Gr 1L	11.63	9.700	2.38E-06	43.03	1.002E-05
Plasma Gr 2L	11.74	8.588	2.057E-06	26.11	1.16E-05
Plasma Gr 3L	17.66	12.64	1.17E-06	40.15	6.638E-06
Plasma Gr 4L	17.58	11.38	1.13E-06	46.58	6.081E-06
Plasma Gr 5L	23.71	19.372	1.360E-06	86.74	2.44E-06

Table 5.1. Results obtained from the fitting of the EIS data.

Bibliography

5.1. M. G. Walter, E. L. Warren, J. R. McKone, S. W. Boettcher, Q. Mi, E. A. Santori and N. S. Lewis, *Chem. Rev.*, 2010, **110**, 6446-6473.

5.2. Y. Hou, B. L. Abrams, P. C. K. Vesborg, M. E. Björketun, K. Herbst, L. Bech, A. M. Setti, C. D. Damsgaard, T. Pedersen, O. Hansen, J. Rossmeisl, S. Dahl, J. K. Nørskov and I. Chorkendorff, *Nat. Mater.*, 2011, **10**, 434-438.

5.3. Y. Kim, D. Shin, W. J. Chang, H. L. Jang, C. W. Lee, H.-E. Lee and K. T. Nam, *Adv.Func. Mater.*, 2015, **25**, 2369-2377.

5.4. K. Jin, J. Park, J. Lee, K. D. Yang, G. K. Pradhan, U. Sim, D. Jeong, H. L. Jang, S. Park, D. Kim, N.-E. Sung, S. H. Kim, S. Han and K. T. Nam, *J. Am. Chem. Soc.*, 2014, **136**, 7435-7443.

5.5. Y. Zheng, Y. Jiao, L. H. Li, T. Xing, Y. Chen, M. Jaroniec and S. Z. Qiao, *ACS Nano*, 2014, **8**, 5290-5296.

5.6. U. Sim, T.-Y. Yang, J. Moon, J. An, J. Hwang, J.-H. Seo, J. Lee, K. Y. Kim, J. Lee, S. Han, B. H. Hong and K. T. Nam, *Energy & Environ. Sci.*, 2013, **6**, 3658-3664.

5.7. Y. Li, H. Wang, L. Xie, Y. Liang, G. Hong and H. Dai, *J. Am. Chem. Soc.*, 2011, **133**, 7296-7299.

5.8. J. Tian, Q. Liu, A. M. Asiri, K. A. Alamry and X. Sun, *ChemSusChem*, 2014, **7**, 2125-2130.

5.9. Y. Liang, Y. Li, H. Wang, J. Zhou, J. Wang, T. Regier and H. Dai, *Nat. Mater.*, 2011, **10**, 780-786.

5.10. Y. Zheng, Y. Jiao, Y. Zhu, L. H. Li, Y. Han, Y. Chen, A. Du, M. Jaroniec and S. Z. Qiao, *Nat. Comm.*, 2014, **5**:3783.

5.11. J.-D. Qiu, G.-C. Wang, R.-P. Liang, X.-H. Xia and H.-W. Yu, *J. Phys. Chem. C*, 2011, **115**, 15639-15645.

5.12. Q. Xiang, J. Yu and M. Jaroniec, *Chem. Soc. Rev.*, 2012, **41**, 782-796.

5.13. Z. Huang, P. Zhong, C. Wang, X. Zhang and C. Zhang, *ACS Appl. Mater. & Inter.*, 2013, **5**, 1961-1966.

5.14. S. Bae, H. Kim, Y. Lee, X. Xu, J.-S. Park, Y. Zheng, J. Balakrishnan, T. Lei, H. Ri Kim, Y. I. Song, Y.-J. Kim, K. S. Kim, B. Ozyilmaz, J.-H. Ahn, B. H. Hong and S. Iijima, *Nat. Nanotech.*, 2010, **5**, 574-578.

5.15. F. Bonaccorso, Z. Sun, T. Hasan and A. C. Ferrari, *Nat. Photon.*, 2010, **4**, 611-622.

5.16. S. Ryu, M. Y. Han, J. Maultzsch, T. F. Heinz, P. Kim, M. L. Steigerwald and L. E. Brus, *Nano Lett.*, 2008, **8**, 4597-4602.

5.17. B. Xie, C. Yang, Z. Zhang, P. Zou, Z. Lin, G. Shi, Q. Yang, F. Kang and C.-P. Wong, *ACS Nano*, 2015, **9**, 5636-5645.

5.18. U. Sim, J. Moon, J. An, J. H. Kang, S. E. Jerng, J. Moon, S.-P. Cho, B. H. Hong and K. T. Nam, *Energy & Environ. Sci.*, 2015, **8**, 1329-1338.

5.19. U. Sim, K. Jin, S. Oh, D. Jeong, J. Moon, J. Oh and K. T. Nam, *Handbook of Clean Energy Systems*, John Wiley & Sons, Ltd, 2015, **5**, 1-42

5.20. K. Ihm, J. T. Lim, K.-J. Lee, J. W. Kwon, T.-H. Kang, S. Chung, S. Bae, J. H. Kim, B. H. Hong and G. Y. Yeom, *Appl. Phys. Lett.*, 2010, **97**, 032113.

5.21. Y. Zhang, T.-T. Tang, C. Girit, Z. Hao, M. C. Martin, A. Zettl, M. F. Crommie, Y. R. Shen and F. Wang, *Nature*, 2009, **459**, 820-823.

5.22. C. H. Lui, Z. Li, K. F. Mak, E. Cappelluti and T. F. Heinz, *Nat. Phys.*, 2011, **7**, 944-947.

5.23. K. Muhammad Farooq, I. Muhammad Zahir, I. Muhammad Waqas and E. Jonghwa, *Sci. Tech. Adv. Mater.*, 2014, **15**, 055004.

5.24. W. Zhu, V. Perebeinos, M. Freitag and P. Avouris, *Phys. Rev. B*, 2009, **80**, 235402.

5.25. X. Dang, H. Dong, L. Wang, Y. Zhao, Z. Guo, T. Hou, Y. Li and S.-T. Lee, *ACS Nano*, 2015, **9**, 8562-8568.

5.26. A. T. Valota, I. A. Kinloch, K. S. Novoselov, C. Casiraghi, A. Eckmann, E. W. Hill and R. A. W. Dryfe, *ACS Nano*, 2011, **5**, 8809-8815.

5.27. D. A. C. Brownson, S. A. Varey, F. Hussain, S. J. Haigh and C. E. Banks, *Nanoscale*, 2014, **6**, 1607-1621.

5.28. A. Ambrosi and M. Pumera, *J. Phys. Chem. C*, 2013, **117**, 2053-2058.

5.29. A. C. Nielander, M. J. Bierman, N. Petrone, N. C. Strandwitz, S. Ardo, F. Yang, J. Hone and N. S. Lewis, *J. Am. Chem. Soc.*, 2013, **135**, 17246-17249.

5.30. A. C. Ferrari, J. C. Meyer, V. Scardaci, C. Casiraghi, M. Lazzeri, F. Mauri, S. Piscanec, D. Jiang, K. S. Novoselov, S. Roth and A. K. Geim, *Phys. Rev. Lett.*, 2006, **97**, 187401.

5.31. Z. Chen, T. F. Jaramillo, T. G. Deutsch, A. Kleiman-Shwarsctein, A. J. Forman, N. Gaillard, R. Garland, K. Takanabe, C. Heske, M. Sunkara, E. W. McFarland, K. Domen, E. L. Miller, J. A. Turner and H. N. Dinh, *J. Mater. Res.*, 2010, **25**, 3-16.

5.32. D. Merki, H. Vrubel, L. Rovelli, S. Fierro and X. Hu, Chemical *Science*, 2012, **3**, 2515-2525.

5.33. L. R. F. Allen J. Bard, *Electrochemical Methods: Fundamentals and Applications*, John Wiley & Sons, Inc., 2001, **864**.

5.34. N. S. Lewis, *J. Electrochem. Soc.*, 1984, **131**, 2496-2503.

5.35. T. Lopes, L. Andrade, H. A. Ribeiro and A. Mendes, *Inter. J. Hydro. Energy*, 2010, **35**, 11601-11608.

5.36. A. W. Bott, *Current Separations*, 1998, **17**, 87-91.

5.37. K. Gelderman, L. Lee and S. W. Donne, *J. Chem. Edu.*, 2007, **84**, 685.

5.38. J. P. Randin and E. Yeager, *J. Electrochem. Soc.*, 1971, **118**, 711-714.

5.39. D. Kong, H. Wang, Z. Lu and Y. Cui, *J. Am. Chem. Soc.*, 2014, **136**, 4897-4900.

5.40. S. Trasatti and O. A. Petrii, *J. Electroanal. Chem.*, 1992, **327**, 353-376.

5.41. K. Dong Chul, J. Dae-Young, C. Hyun-Jong, W. YunSung, S. Jai Kwang and S. Sunae, *Nanotechnology*, 2009, **20**, 375703.

5.42. S. Yadav, Z. Zhu and C. V. Singh, *Inter. J. Hydro. Energy*, 2014, **39**, 4981-4995.

5.43. J. L. Achtyl, R. R. Unocic, L. Xu, Y. Cai, M. Raju, W. Zhang, R. L. Sacci, I. V. Vlassiouk, P. F. Fulvio, P. Ganesh, D. J. Wesolowski, S. Dai, A. C. T. van Duin, M. Neurock and F. M. Geiger, *Nat. Comm.*, 2015, **6**:6539.

5.44. B. Eren, T. Glatzel, M. Kisiel, W. Fu, R. Pawlak, U. Gysin, C. Nef, L. Marot, M. Calame, C. Schönenberger and E. Meyer, *Appl. Phys. Lett.*, 2013, **102**, 071602.

Chapter 6 Nanostructral Dependence of Photoelectrode

Controlling a surface structure of the light-absorbing photoelectrode and the deposition with the co-catalyst represent a significant step toward enhancing the hydrogen production.

6.1 Introduction

The development of efficient and cheap photoelectrodes for water splitting is one of the fundamental challenges in hydrogen production.[6.1-6.3]. Despite the fascinating advances in controlling the nanostructure interface and advances in the discoveries of material compositions[6.4, 6.5], kinetic issues regarding the high overpotential are still one of the most difficult issues that need to be solved. Here, we demonstrate that controlling the nanostructure can make another significant contribution to lower the overpotential. In the present work, the 250 mV decrease in overpotential by the silicon (Si) nanostructuring is close to the lowering effect achievable by the well-known platinum (Pt) catalysts. Furthermore, current density at reversible potential vs. reversible hydrogen electrode (RHE) is about 43 fold enhancement compared to the planar Si substrate.

Considering the thermodynamic potential, a single component semiconductor that possesses higher band gap than 1.23V can generate hydrogen and oxygen gas from water simultaneously as long as its conduction and valence band are in their proper positions[6.6, 6.7]. Successful examples include Ti, Nb, Ta based compounds, oxynitride, oxysulfide, and sulfide photocatalysts[6.8, 6.9]. However, overall water splitting by one single component semiconductor is usually limited by the kinetic overpotential[6.10]. Therefore, only half of the reaction such as water oxidation or proton reduction reaction occurs instead of both side evolutions. This leaves the other half of the

reaction to be possible with the use of sacrificial alcohol for reduction, and silver or sulfide ions as oxidation[6.8]. However, the maximum solar-to-fuel conversion efficiency still does not exceed the range of 5%[6.8]. Because of such inherent weakness of one-component-approaches, many developments have been made in photoelectrochemicals cell that have cathode and anode separately and is easily implementable in terms of tunability and efficiency. The detailed advances have been well presented in recent comprehensive reviews[6.11]. Among the many issues in photoelectrochemical hydrogen production, one of the most fundamental questions is the effect of nanostructuring in photoelectrodes. In an effort to address such a challenge, we precisely controlled the nanostructure of single crystal Si and studied its photoelectrochemical behaviors.

Silicon is one of the most abundant elements in the earth's crust. In addition, its compatibility with already developed processes and precise controllability makes Si a propitious element for the development of water splitting platforms[12]. Both the reduction in reflection and the increment in the absorption of solar energy can be achieved through surface engineering. With doping control and band tuning, Si can be used both as a photocathode and a photoanode for photochemical water splitting[6.13, 6.14]. However, the formation of native oxide on Si surface lowers its photoelectrochemical performance and Si is not stable at oxidative potentials in an aqueous electrolyte[6.15]. Moreover, the small band bending between valence band edge and redox level of electrolyte limits its photovoltaic performance compared to Si/non-aqueous solvent system[6.16]. Therefore, under the visible light irradiation, the application of an external potential is needed and the use of catalysts seems necessary for an efficient operation.

The deposition of catalysts on the electrode can enhance the photoelectrochemical performance. Examples include pure metals (Pt, Pd, Ni, etc.)[16], metal composites/alloys (Ni-Mo, Ni-Co, Ni-Mo-Cd, etc.) [6.17],

compounds such as nonmetallic elements (RuO_2, Sr_xNbO_3, Mo_3S_4, etc.)[6.8, 6.18, 6.19], and molecular catalysts[6.20]. For example, Pt nanoparticles can enhance the onset potential by about 0.42 V for p-type Si nanowire/aqueous electrolyte solution[6.21]. To overcome the economical issues, nonprecious metal catalysts and catalysts that are abundant in nature such as Mo_3S_4, Ni, Mo, and Ni-Mo have been interfaced with Si pillar structures which exhibit a high current density at a reversible potential vs RHE[6.13, 6.17]. However, when deposited with catalysts, the saturation current density significantly decreases due to the light scattering by catalysts on Si surface.

Controlling the structure of Si represents another important direction for improving the photoelectrochemical property. A porous structure can enhance the current density of the Si photoelectrode through the increase of effective reaction sites between the Si semiconductor and the liquid electrolyte junction[6.22]. A nanowire or pillared structure can increase the efficiency due to the orthogonalization of the direction of incident light absorption and charge carrier collection[6.23]. However, it has also been reported that the increase of junction area between the Si semiconductor/liquid electrolyte decreases the onset potential which results in a lower efficiency of cell performance[6.24]. Thus, it is not clear what nanostructure of Si photocathode is most efficient for the hydrogen evolution.

Recent experimental results suggest the nanostructuring enhances the photoelectrochemical performance, but still there is a gap between theoretical understanding and actual observation[6.22, 6.24]. Additionally, an inconsistency exists among the presented data about how much and why overpotential and current change. The fundamental question is whether the nanostructuring of photoelectrodes truly generates positive effects or not. To address this ongoing challenge, we studied the photoelectrochemical responses from various nanostructured Si photocathodes that were controlled by metal-catalyzed electroless etching.

6.2 Results and Discussion

Various nanostructures of boron doped p-type (100) Si substrates were fabricated by metal assisted chemical etching process[6.25]. Briefly summarizing, normal doped Si substrates were immersed in aqueous solution of 0.02 M silver nitrate ($AgNO_3$) and 5 M hydrofluoric acid (HF). Continuous Si oxidation by the galvanic reduction of Ag ions and following dissolution of Si oxide by HF resulted in directional etching of Si substrates. Depending on the etching time, different Si nanostructures were observed as characterized by SEM. The variation of etching time was set at 10 min, 20 min, 30 min, 60 min, 120 min, 140 min, 160 min, 180 min, 200 min, 300 min, and 480 min. Full images of all datasets are shown in Figure 6.5 and representative images are selected for Figure 6.1. When etching time was shorter than 120 min, a porous nanostructure was observed as shown in Figure 6.1a. A transition from porous to nanowire structure occurred when etched for 120 min. Both the porous structure and the nanowire structure co-existed at 120 min of etching as shown in Figure 6.1b. After this stage, it was observed that the length of nanowires increased as the etching time got longer as shown in Figure 6.1c and 6.1d.

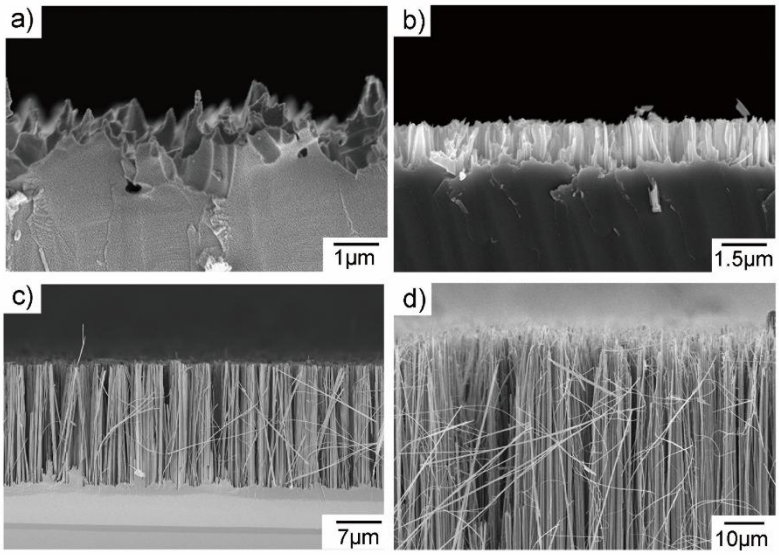

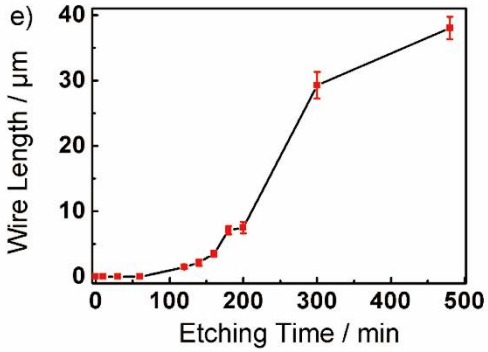

Figure 6.1. Nanostructure of Si surface and the related formation kinetics. (a)-(d) SEM images of cross-sectional views of p-type (100) Si wafers etched in 5M HF and 0.02 M $AgNO_3$ solution at different etching times and (e) the formation kinetics of Si nanowire made by metal-catalyzed electroless method. Each of the etching time is (a) 30 min, (b) 120 min, (c) 300 min, and (d) 480 min.[6.54]

To control Si nanostructure by metal-catalyzed electroless etching, the formation mechanism was investigated. The length of nanowire was plotted in the variation of the etching time (Figure 6.1e). The increasing rate of nanowire length is relatively low at the beginning stage of etching time and grows rapidly between 120 min and 300 min. After 300 min of etching, the growth rate saturated. To understand the observed s-shaped kinetics, we compared the result with the formation kinetics in Si nanowire explained by Peng *et al*, who pioneered the field of the metal-catalyzed electroless etching method[6.25]. The overall shape looks similar to the conventional nucleation and growth model that can be fit by the Avrami equation[6.26]. To understand the slow reaction at the beginning stage, we monitored how the etching of Ag particles started on Si substrate using SEM. From many samples, linear or crooked traces were observed as shown in Figure 6.6a. These phenomena seem to be the results of initial etching where Ag particles started to form. These etched tracks may suggest the evidence of Ag particles' movements. Initially, the high driving force of the galvanic reaction caused the nucleation of many small Ag particles followed by the growth on Si and then the Ag particles diffused on the surface before the vertical penetration. The crooked trace is the direct evidence of lateral movements of Ag particles (Figure 6.6a). It is likely that after certain incubation time, Si surface starts to make porous structures. As etching time increases, a pit which is generated by Ag particle grows deeper and wider by the etching of pore wall. Remaining parts except for the etched pores on Si surface begin to transform porous into nanowire shown in Figure 6.1b. At the middle stage, the nanowire length increases much faster than at the early stage of reaction. After 300 min of etching time, however, the increasing rate of nanowire length decreases due to the large quantity of Ag residue on Si surface. Presumably, a large amount of Ag residue interrupts further galvanic displacement reaction because it is difficult for Ag^+ ion to be transported to the bottom of the pit. This is supported by the

fact that 5 μm of Si nanowire usually forms about eightfold thicker than the Ag residues on Si surface[6.25]. Another possibility is that excess Ag residue film prevents a flow of HF solution into the Si surface. Thus, understanding the behaviors of the Ag nanoparticles is a key in interpreting the sigmoidal formation kinetics.

The photoelectrochemical performance of Si electrodes for hydrogen evolution is strongly dependent on their nanostructures. Visible light from 300 W Xe lamp was illuminated onto the substrate with the light intensity of 100 mW cm^{-2} using Air Mass 1.5 Global condition glass filter. To evaluate the photo-cathodic behavior, the current density (*J*) was measured as the potential (*E*) was swept from 0.4 V to -1.0 V with 4 cycles for statistical reliability and long-term stability as shown in Figure 6.2. For comparison, photoelectrochemical performance of Si structure was also measured as a function of light intensity as shown in Figure 6.7. As the potential of Si working electrode was negatively applied, the magnitude of the current density increased and saturated at the specific value of the applied potential, called a limiting current density or a saturation current density. Moreover, planar Si surface shows a spiky plot at a highly negative potential because hydrogen bubbles stick to hydrophobic surfaces until sudden bursts occur. The photoelectrochemical behavior observed here with nanostructured Si also follows a typical pattern for normal doped p-type Si electrode. Figure 6.2b shows dark current densities of representative Si electrodes. The dark current density of the nanostructured electrodes increases compared to the planar Si. As shown in Figure 6.2c, the average limiting current density of the planar Si is about -34.1 mA cm^{-2} and keeps increasing until the length of nanowire reaches 1.5 μm as the surface becomes more nanostructured. The nanostructured Si has an increased surface area compared to the planar structure. The reflectance of the illumination can be reduced in the nanostructured Si surface. While the surface of planar Si reflects about a

quarter of the incident light[6.22], photon absorption increases in the nanostructured surface due to low reflectance. It is reported that the nanostructure has the effect of light trapping[6.27, 6.28]. The trapped light can enhance the current level for hydrogen production when the length of Si wire is optimized with a strong broadband optical absorption[6.29]. The nanowire structure also has the advantage of orthogonalization of the light absorption and the charge-carrier collection. Thus, the minority carrier generated by the incident light can move to the lateral side of each nanowire and participate in hydrogen generation more quickly than the planar structure does.

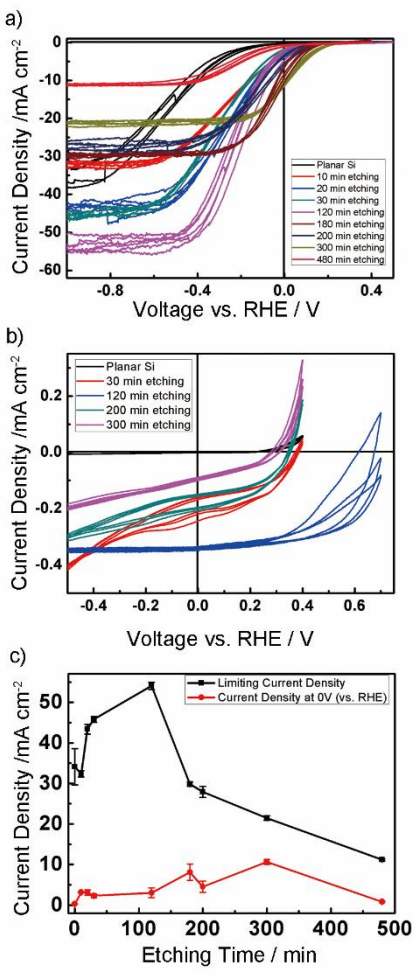

Figure 6.2. Photoelectrochemical performance of Si nanostructure. (a) Polarization curve of various Si electrodes. Different structures are made at different etching times. (b) Dark current densities of Si electrodes. (c) Plot of the current density as a function of the length of Si nanowires. The black squares indicate the limiting current density and the red circles indicate the current density at reversible potential (0 V) vs. RHE. [6.54]

More striking is the fact that the current density of nanoporous Si is 54.1 mA cm^{-2} and the current level of nanoporous structure is 1.58 times higher than that of the planar structure. The fabrication methods of Si wire by other groups are slightly different from our group. Si wire made by vapor-liquid-solid growth method was the ratio of 1.4 and the nanoporous Si by gold assisted electroless etching was the ratio of 1.2[6.13, 6.22]. According to the ASTM International standard G173-03, however, 1 sun (Air Mass 1.5 global condition) of solar irradiation which provides 2.7 x 10^{17} photons cm^{-2} [6.30]. This means that single crystal Si solar cell with a ~1.1eV of band gap energy cannot exceed theoretical maximum 43.6 mA cm^{-2} assuming that all absorbed photons are converted into electron-hole charge carries[6.31]. In our experiment, the observed current density of 54.1 mA cm^{-2} is much larger than the theoretical upper limit of current density. In addition to the effect of increased effective area and the reduced reflectance of the incident light, the increased current density might be attributed to IR absorption by light trapping associated with the surface states on the nanowire or sub-band gap absorption by production of impurity states[6.29, 6.32]. In order to study this effect, we measured the absorption spectrum of planar surface and nanostructured surface of Si using UV/Vis/NIR spectroscopy. We minimized the effect of scattering loss by the surface using both diffuse reflectance mode and specular reflectance mode. In case of the diffuse reflectance mode, we can measure the reflectance of the nanostructured Si exactly by using the integrated sphere. In

case of the specular reflectance mode, the reflectance of the planar Si can be measured more exactly as shown in Figure 6.8. Figure 6.3a shows the summation of specular reflectance and diffuse reflectance mode from Figure 6.8. As shown in Figure 6.3a and 6.3b, the reflectance and transmittance of both Si increase sharply near 1010 nm. Nanostructured Si has about 4 % higher reflectance and about 20 % lower transmittance than those of planar Si in the IR region. Using the simple relation that absorbance equals 1-reflectance - transmittance, absorbance is plotted as shown in Figure 6.3c. In the nanostructured Si, about 20 % of absorption in the range of about 1200 nm and 2300 nm is observed. The additional IR absorption of incident light might produce the increased current density compared to the current density of the planar bulk Si. In order to compare the band gap energy of both structures, we plotted absorption spectrum as a funtion of band gap energy using following model equation[6.33];

$$\boldsymbol{\alpha} \propto \frac{(\boldsymbol{h\nu}-\boldsymbol{E_g})^2}{\boldsymbol{h\nu}} \qquad (6.1)$$

where, α is the absorption coefficient, h is the Planck`s constant, v is the frequency, and E_g is the band gap energy. This simplified equation gives information that band gap energy is the the intercept of the straight lines with the x-axis of the plot of $(\alpha h\nu)^{1/2}$ as a function of energy ($h\nu$). To derive α from a measured absorbance, we compared four absorption spectrum models[6.32, 6.34, 6.35] as shown in Figure 6.9 and selected the most accurate model among absorption models. The model equation is as follows[6.35];

$$\boldsymbol{\alpha} = -\frac{\boldsymbol{1}}{\boldsymbol{d}}\boldsymbol{\ln}\left(\frac{\boldsymbol{T}}{(\boldsymbol{1}-\boldsymbol{R})^2}\right) \qquad (6.2)$$

where R is the reflectance, T is the transmittance, d is the optical path length. Using this model equation, we plotted $(\alpha h\nu)^{1/2}$ as a function of energy ($h\nu$) and confirmed that Si nanowire absorbs incident light more than that of planar Si below band gap absorption as shown in Figure 6.3d. (Full spectral range is shown in Figure 6.9d). The increased absorption shows the sub-

bandgap photon absorption mediated by defect states of nanostructured Si even though it is extremely difficult to separate and collect the photocarriers which are excited by sub-bandgap photons before they recombine[6.29]. To clarify the sub-bandgap photon absorption, multiple analysis tools can be applied. For example, spectroscopic ellipsometry is used to characterize charge trapping defect states[6.36]. X-ray absorption fine structure spectroscopy can be used to measure the chemical state of each atom in silicon[6.37]. The exact mechanism of photocarrier excited by sub-bangap photon is still under study.

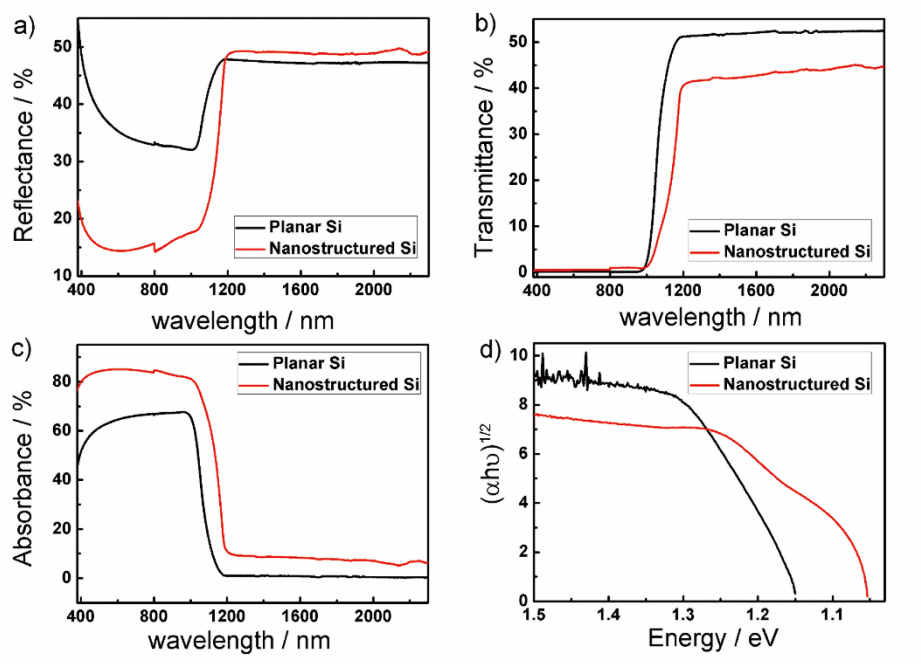

Figure 6.3. Optical spectra of planar Si surface and Si nanowire surface. (a) Reflectance, (b) transmittance, (c) absorbance of planar and nanostructured Si. (d) Plot of $(\alpha h\nu)^{1/2}$ vs. $h\nu$ for planar Si and Si nanowire. Other model calculations are listed in supporting information. Black line indicates planar Si and red line indicates Si nanowire.[6.54]

As shown in Figure 6.2c, however, the limiting current density decreases as the length of Si nanowire increases after hitting the highest current level at 1.5 μm in nanowire length. The limiting current densities of the 7.1 μm ~ 38.0 μm Si nanowire are lower than the untreated Si. A possible explanation about the decrease is that long nanowires have some Si surface traps or defect sites. Another possibility is the increase of charge carrier recombination as the nanowire become longer. As pointed by Foley *et al* recently, a longer nanowire possesses an enlarged depletion region that gives more chance of recombination[6.38]. The long nanowire provides a high probability of carrier recombination due to the enlarged depletion region. However, the quantitative analysis on the recombination and defect is hard to be completed in the current manuscript. It is still ongoing challenge to understand the recombination mechanism and defect density in nanostructured silicon. Recent study done by J. Oh *et al* has shown that there are two competing charge recombination processes (surface recombination and Auger recombination) in nanostructured silicon solar cells[6.39]. J. Oh *et al.*, have quantitatively shown that Auger recombination limits the photogenerated charge collection and cell efficiency of nanostructured Si solar cells and suggested that Auger recombination can be suppressed by controlling light and shallow doping and tuning surface area. We are still under investigation to decouple the contribution of each parameter based on J. Oh`s work. To sum up, in Si nanowire photocathodes, positive effects such as the increased surfaced area, the light trapping, the reduced light reflection, and the orthogonalization of light and carrier collection seem to compete with the negative effects such as the increased surface defects, the enlarged depletion region, and charge recombination processes.

We have also investigated how overpotentials are modified by nanostructuring. A nanostructure makes a positive shift of the overall

polarization curve as shown in Figure 6.2a. Like the behavior of limiting current density depending on the nanowire length, there is an optimum condition where the degree of shift is in its maximum level. Interestingly, these conditions are different from the point where the maximum saturation current point was observed. When the length of nanowire is 29.3 μm, the shift to the positive potential was the largest. Figure 2a clearly shows that the applied voltage required for -10 mA cm^{-2} shifts from -0.40 V to 0.02 V in the case of 29.3 μm nanowire. To measure the overpotential for the photoelectrochemical cell quantitatively, we introduced the onset potential (V_{os}) which is defined as a voltage where the photocurrent density exceeds the dark current density. It is also called a photovoltage. Considering the charge-carrier generation, recombination, and the transport throughout a semiconductor, a simplified model equation for the onset potential at a semiconductor/electrolyte junction is as follows[6.40];

$$\boldsymbol{V_{os} \cong \frac{kT}{q} ln \frac{J_{ph}L_N}{qN_cD_N} + \frac{1}{q}E_g - V_p = \frac{kT}{q} ln \frac{J_{ph}L_N N_A}{qD_N n_i^2} = \frac{kT}{q} ln \frac{J_{ph}}{J_0}} \qquad (6.3)$$

where, N_c is the density of states in the conduction band, J_{ph} is the photocurrent density by illumination, L_N is the minority carrier diffusion length, k is the Boltzmann constant, T is the temperature, q is the charge of an electron, D_N is the diffusion coefficient of electron, qV_p is the difference between the Fermi level energy and valence band energy of Si, and J_0 is the saturation current density. The onset potential for nanostructured electrodes is between from 0.23 V to 0.38 V compared to the current density of 0.13 V for planar Si, which are shown in Table 6.1. Full datasets are shown in supplementary Table 6.2 and representative data are selected for Table 6.1. Previously, the increase of the overpotential has been observed by others in search of ways to develop Si nanostructures[6.24]. In contrast, the decrease of the overpotential has been reported recently[6.21, 6.22]. These contradicting performance of Si nanostructures may seem elusive. The previous reports have shown either the increase or the decrease of the overpotential. Therefore,

our demonstration could provide helpful information to understand how the structures affect the shift of the overpotential. The theoretical studies by Atwater and Lewis can explain very well the decrease of the onset potential in Si nanostructure[11]. By introducing the roughness factor, the onset potential equation can be modified as follows[6.24];

$$\boldsymbol{V_{os,nanostructure} = \frac{kT}{q} ln \frac{J_{ph}}{\gamma J_0}} \qquad (6.4)$$

where γ is the roughness factor, i.e. the ratio of the actual junction area to the surface of Si working electrode. The flux of charge carriers in the electrode is constant at the fixed light intensity (J_{ph}), but the flux of minority carrier through the electrode-electrolyte junction (J_0) depends on the junction area. The minority carrier flux through the junction decreases proportionally to the increase of the junction area. The large junction area in nanostructured electrode results in the decreases of the flux of minority carrier through the junction from J_0 to J_0/γ. Thus, the decrease of minority carrier flux lowers the quasi-Fermi level splitting which determines the onset potential. According to the theory by equation (4), about 10 fold of increase of γ can reduce the onset potential by 60 mV. The onset potential, however, increases in both the nanoporous and nanowire structure in our experiment. Recently, J. Oh *et al* proposed that the surface area and the increased reaction sites can lower the overpotential[6.22]. Ilwhan Oh *et al*. also observed the shift of J-E curve in the case of Si nanowire[21]. From many repeated experiments in ours, we excluded the possible activity of unwashed silver residues from electroless etching. We think that our observation can be an example of nano-enhanced electrochemical reactions that have been observed in many systems. Although recent experimental and theoretical studies showed that the chemical overpotential can be lowered by a longer residence time of the reactant and the confinement effect in nanostructure as well as the increased collision frequency between reactant molecules and nanostructured surface[6.41, 6.42]. Although there may be other factors responsible for the enhancement such as

the different surface state or the stress of nanowires[6.43], it seems clear that the geometry makes a significant contribution to the enhancement. The exact mechanism of the enhancement and the molecular simulation is still under study.

Consequently, the decreased overpotential and the increased current density have contributed to the enhanced thermodynamic efficiency of solar-to-hydrogen (STH) conversion in the photoelectrochemical cell. The relationship between the conversion efficiency in the half reaction and the other variables can be explained by the equation below[6.11];

$$\textbf{STH Conversion Efficiency}(\%) = \frac{V_{os} \times J_{sc} \times FF}{P_{in}} \times 100 = \frac{V_{max} \times J_{max}}{P_{in}} \times 100 \quad (6.5)$$

where, J_{sc} is the current density at the reversible potential vs. RHE, FF is the fill factor, P_{in} is the input power of light (P_{in} is 100 mW cm^{-2} in this study), V_{max} is the voltage at the maximum of power, and J_{max} is the current at the maximum of power. The J_{sc} is also plotted in Figure 6.2c. Among them, the 29.3 µm Si nanowires reached J_{sc} of -10.65 mA cm^{-2}. Especially, the J_{sc} from our group is about 43 times higher than that of the untreated Si, which is the highest value among the ever reported values under the same condition. Combined with the onset potential data, we calculated the STH conversion efficiency of the Si photoelectrodes with and without the deposition of the catalyst on their surface. For the clear structural function relationship, we deposited Pt nanoparticles on the planar Si substrate and the nanowires. Pt nanoparticles were made by electroless deposition method. A drop of 1 mM H_2PtCl_6 (aq) in 0.5 M HF was dropped on the Si surface for 2 min. The SEM images of the Si nanowire with the Pt particles are shown in Figure 6.4a and 6.4b. From the photoelectrochemical measurements, the STH conversion efficiency of five representative Si electrodes and releated parameters are selected in Table 6.1 and Figure 6.10. Especially, STH conversion efficiency of Si electrodes with the Pt catalyst increased from 0.03 % to 0.69 % for the

planar Si, 0.12 % to 1.19 % for the 1.5 μm nanowire, and 0.48 % to 1.20 % for the 29.3 μm nanowire as shown in Table 6.1. Although Si electrodes without Pt catalyst show lower conversion efficiencies than that of electrodes decorated with the Pt catalyst, the efficiency of 29.3 μm Si nanowire (0.48%) without depositing any catalyst has reached up to about 70 % of the efficiency of planar Si decorated with Pt (0.69 %) as shown in Figure S6. The current density of 8 mA cm^{-2} without bias at the cathode and the anode can reach approximately the efficiency of 10% in the STH energy conversion and this efficiency can be applied for the commercial photoelectrochemical cell[6.44]. This enhanced STH conversion efficiency by only controlling the structure of surface provides the possibility of highly efficient overall water splitting combined with catalyst decoration.

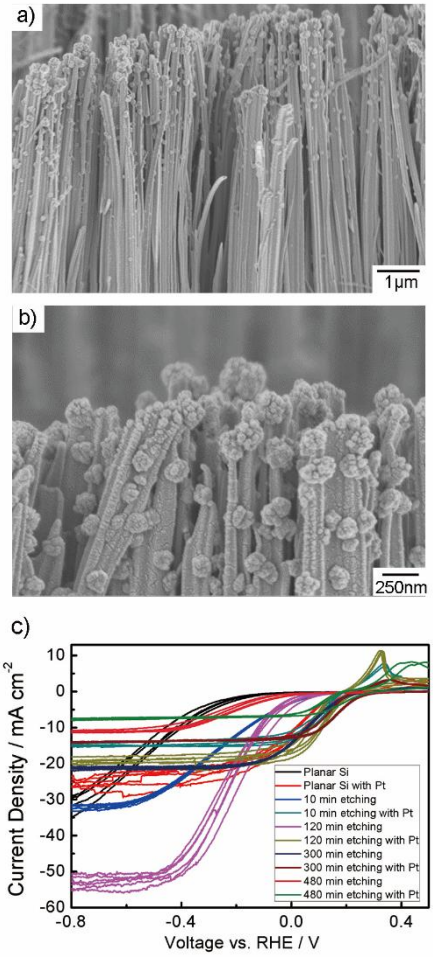

Figure 6.4. Si photoelectrodes decorated with Pt nanoparticle. (a)-(b) SEM images of cross-sectional views of Si nanowire with Pt nanoparticle and (c) Polarization curves of planar Si, porous Si (10 min etching), porous/1.5 μm Si nanowire (120 min etching), 29.3 μm Si nanowire (300 min etching), and 38.0 μm Si nanowire (480 min etching) electrodes decorated with Pt nanoparticle.
6.54

6.3 Conclusion

The nanostructure optimization enhanced the electrochemical performance of the Si photocathode for the hydrogen evolution. The 1.58 fold increase of saturation current and the achieved 250 mV decrease of the overpotential improved the efficiency for the solar-to-hydrogen conversion by the visible light. Without any catalyst, the Si nanowire photocathode produced -10.65 mA cm^{-2} which corresponds to the approximately 0.05 μmole s^{-1} hydrogen production at reversible potential vs. RHE. Therefore, the solar-to-hydrogen conversion efficiency of the optimized Si nanowire by only controlling surface without depositing any catalyst has reached up to about 70 % of the efficiency of planar Si decorated with Pt catalyst. We expect that our work provides a key guideline in designing the optimal Si nanostructure for an improved hydrogen production.

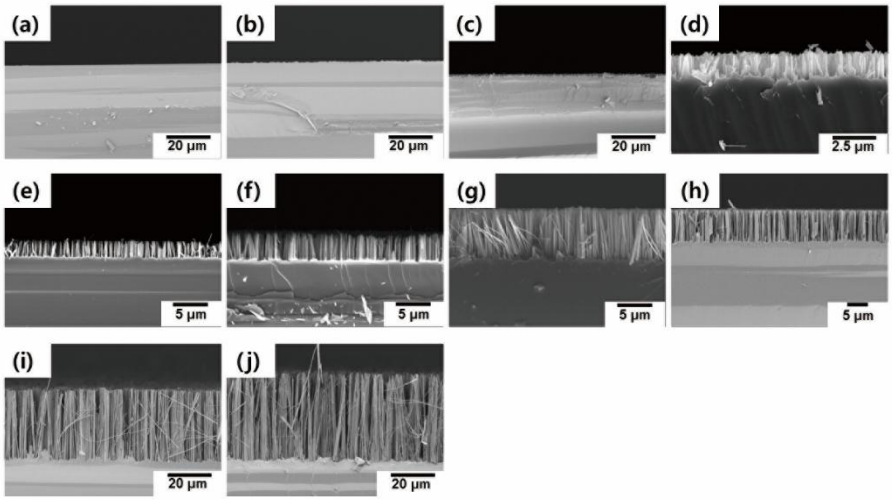

Figure 6.5. SEM images of cross-sectional views of p-type (100) Si wafers etched in 5M HF and 0.02 M $AgNO_3$ solution at different etching times. Each of the etching time is (a) 10 min, (b) 30 min, (c) 60 min, (d) 120 min, (e) 140 min, (f) 160 min, (g) 180 min, (h) 200 min, (i) 300 min, and (j) 480 min. [6.54]

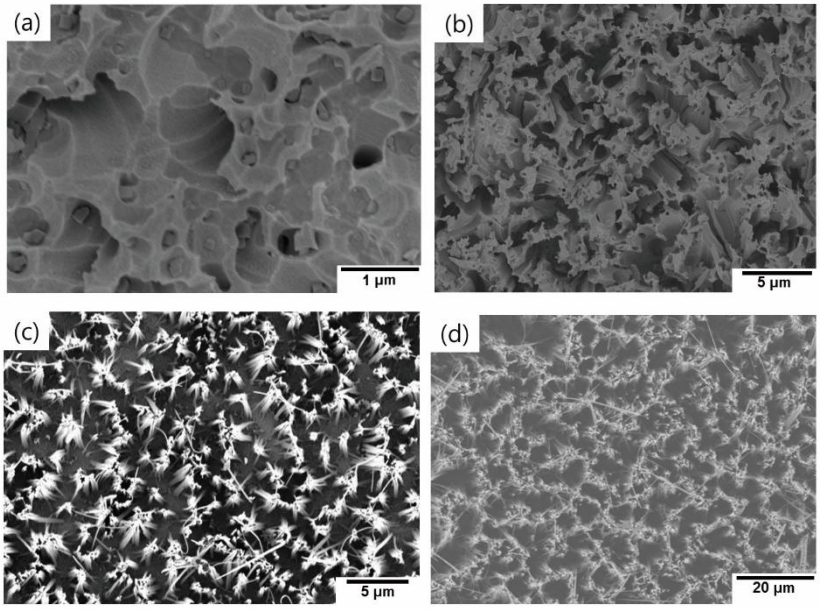

Figure 6.6. SEM images of top views of p-type (100) Si wafers etched in 5M HF and 0.02 M $AgNO_3$ solution at different etching times. Each of the etching time is (a) 30 min, (b) 120 min, (c) 300 min, (d) 480 min. (a)-(b) porous, and (c)-(d) nanowire structure are observed.[6.54]

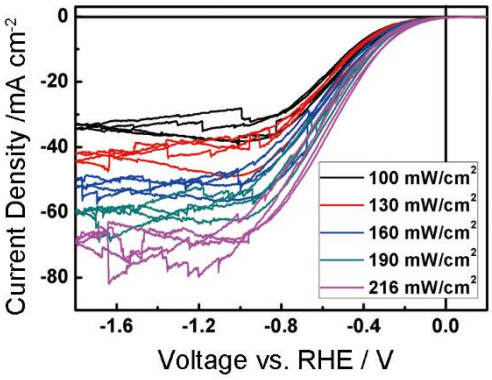

Figure 6.7. Photoelectrochemical performance of planar Si structure as a function of light intensity. Black: 100mW cm^{-2}, red: 130 mW cm^{-2}, blue:160 mW cm^{-2}, dark green:190 mW cm^{-2}, pink: 216 mW cm^{-2}. [6.54]

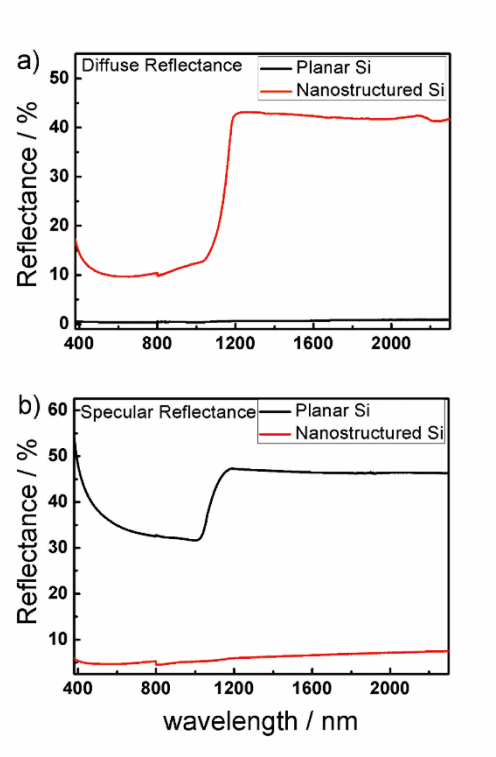

Figure 6.8. Optical reflectance of planar Si surface and Si nanowire surface. (a) Diffuse reflectance mode and (b) specular reflectance mode. Black line indicates planar Si and red line indicates Si nanowire. [6.54]

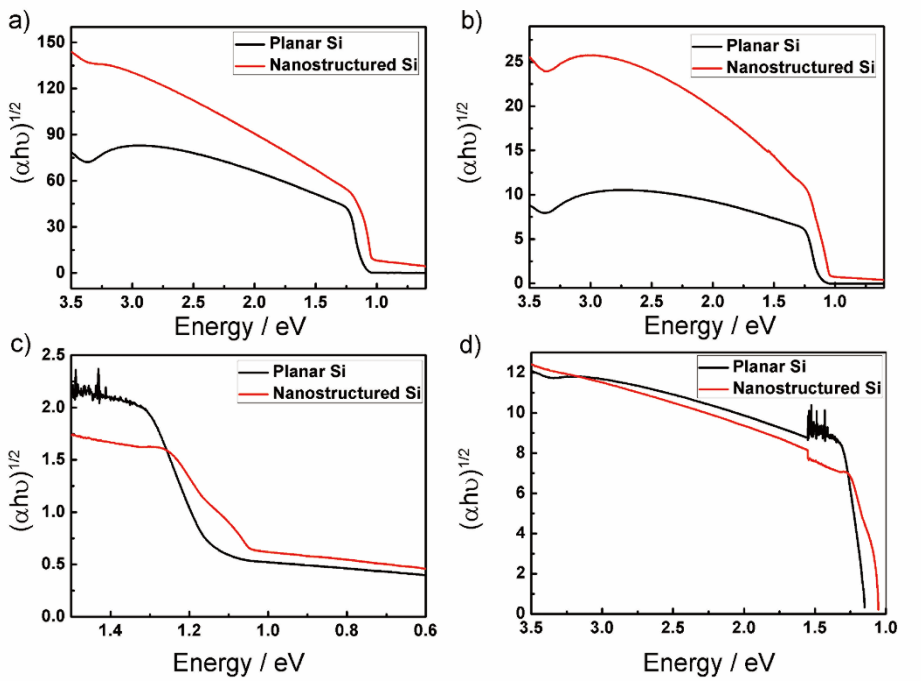

Figure 6.9. Plot of $(\alpha h\nu)^{1/2}$ vs. hυ for planar Si and Si nanowire from various absorption spectrum models[6.44-6.46]. Each model is based on the following assumption; (a) $\alpha = A = 1 - R - T$, (b) $\alpha = -1/d \times \ln(R+T)$, (c) $\alpha = 2 - \log(\%T)$, and (d) $\alpha = -1/d \times \ln(T/(1-R)^2)$. α is the absorption coefficient, *hv* is the photon energy, *v* is the frequency, h is the Planck`s constant, A is the absorbance, R is the reflectance, T is the transmittance, and d is the optical path length. [6.54]

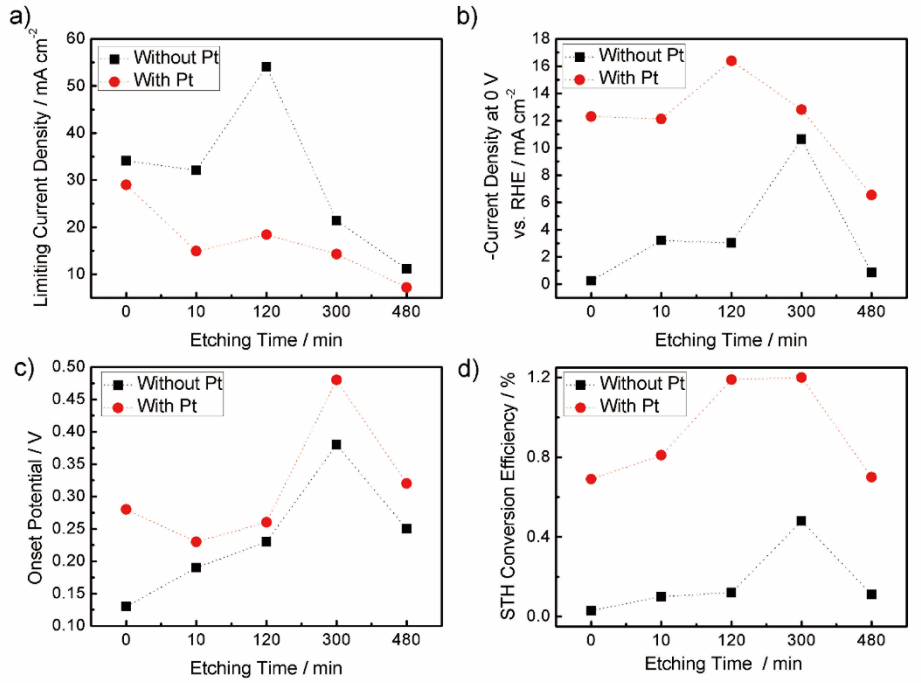

Figure 6.10. The photoelectrochemical performance of p-type Si based photoelectrodes without Pt and with Pt catalyst on Si surface as a function of etching time. (a) Limiting current density, (b) current density at 0 V vs. RHE, (c) onset potential, and (d) solar-to-hydrogen (STH) conversion efficiency. [6.54]

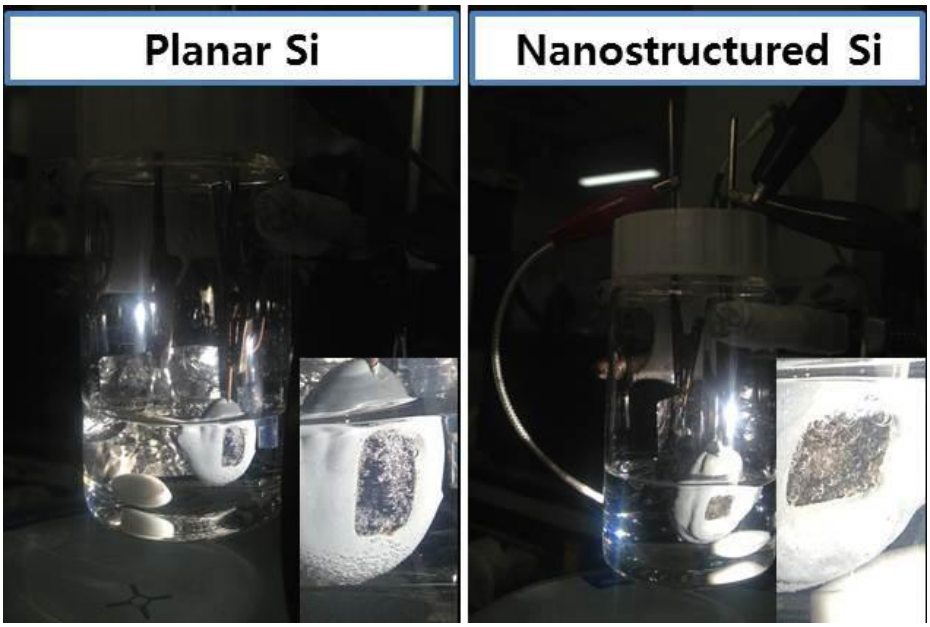

Figure 6.11. Photographs taken during CV measurement for planar Si (left) and nanostructured Si (right). Inset images are the enlarged photographs of illumination area. [6.54]

Structure	Limiting current density [mA cm^{-2}]	Current density at 0 V vs. RHE [mA cm^{-2}]	Onset potential [V]	Solar-to-Hydrogen Conversion Efficiency [%]
Planar Si	-34.1	-0.25	0.13	0.03
Planar Si with Pt	-29.0	-12.3	0.28	0.69
Porous Si (10 min etching)	-32.1	-3.21	0.19	0.10
Porous Si with Pt (10 min etching)	-14.9	-12.13	0.23	0.81
Porous & 1.5 μm Nanowire (120 min etching)	-54.1	-3.02	0.23	0.12
Porous & 1.5 μm Nanowire with Pt (120 min etching)	-18.4	-16.4	0.26	1.19
29.3 μm Si Nanowire (300 min etching)	-21.4	-10.65	0.38	0.48
29.3 μm Si Nanowire with Pt (300 min etching)	-14.3	-12.81	0.48	1.20
38.0 μm Si Nanowire (480 min etching)	-11.1	-0.86	0.25	0.11
38.0 μm Si Nanowire with Pt (480 min etching)	-7.2	-6.54	0.32	0.70

Table 6.1. The photoelectrochemical performance of p-type Si based photoelectrodes.

Structure	Limiting current density [mA cm^{-2}]	Current density at 0 V vs. RHE [mA cm^{-2}]	Onset potential [V]	Solar-to-Hydrogen Conversion Efficiency [%]	Ref.
Planar Si	-34.1	-0.25	0.13	0.03	This study
Planar Si with Pt	-29.0	-12.3	0.28	0.69	
Porous Si[a)] (10 min etching)	-32.1	-3.21	0.19	0.10	
Porous Si with Pt [a)] (10 min etching)	-14.9	-12.13	0.23	0.81	
Porous Si [a)] (20 min etching)	-43.4	-3.07	0.31	0.12	
Porous Si [a)] (30 min etching)	-45.8	-2.29	0.28	0.08	
Porous & 1.5 μm Nanowire[a)] (120 min etching)	-54.1	-3.02	0.23	0.12	
Porous & 1.5 μm Nanowire with Pt [a)] (120 min etching)	-18.4	-16.4	0.26	1.19	
7.1 μm Si Nanowire[a)] (180 min etching)	-29.9	-8.08	0.32	0.31	
7.5 μm Si Nanowire[a)] (200 min etching)	-27.9	-4.51	0.31	0.18	
29.3 μm Si Nanowire[a)] (300 min etching)	-21.4	-10.65	0.38	0.48	
29.3 μm Si Nanowire[a)] with Pt	-14.3	-12.81	0.48	1.20	

(300 min etching)					
38.0 μm Si Nanowire[a)] (480 min etching)	-11.1	-0.86	0.25	0.11	
38.0 μm Si Nanowire with Pt [a)] (480 min etching)	-7.2	-6.54	0.32	0.70	
Planar Si	-11.8	N/A	N/A	N/A	47
Planar Si with Mo_3S_4 catalyst	-10.5	-9	N/A	N/A	
Si Microwire[b)]	-16.5	-0.4	N/A	N/A	
Microwire with Mo_3S_4 catalyst[b)]	-14	-10	N/A	N/A	
Planar Si	-30	N/A	N/A	N/A	48
Nanoporous Si[a)]	-36	N/A	N/A	N/A	
Planar Si	N/A	~0[c)]	~0.1[c)]	N/A	49
Planar with Pt	-29	-27[c)]	~0[c)]	N/A	
Si Nanowire[a)]	-27	~0[c)]	0.33	N/A	
Nanowire with Pt[a)]	-18	-17[c)]	0.42	N/A	
Planar Si	N/A	0.82	0.255	0.03	50
Planar with Pt	N/A	21.8	0.230	1.1	
Si Microwire[b)]	N/A	0.005	0.034	0	
Microwire with Pt[b)]	N/A	11.7	0.265	1.0	
Planar Si	N/A	0.28	0.232	~0.02[c)]	51
Si Wire[b)]	N/A	1.43	0.389	~0.14[c)]	
Planar Si with Pt[b)]	N/A	23	0.30	2.1	52
Wire with Pt[b)]	N/A	7.3	0.16	0.21	

[a)]Wire fabricated by the metal-catalyzed electroless etching method; [b)]Wire grown by the vapor-liquid-solid method; [c)]Values were measured and extrapolated by our group referring to the figures and data from other papers.

Table 6.2. Summary of the photoelectrochemical performance of p-type Si based photoelectrode. Performance of reported Si electrode for water splitting was compared with our study. The successful performances of our data are highlighted in gray. N/A indicates that there was a difficulty in estimating the values due to the lack of availability of full data set in the report.

Bibliography

6.1. M. Gratzel, *Nature*, 2001, **414**, 338-344.

6.2. J. A. Turner, *Science*, 2004, **305**, 972-974.

6.3. N. S. Lewis and D. G. Nocera, *Proc. Natl. Acad. Sci. U. S. A.*, 2006, **103**, 15729-15735.

6.4. C. Zhen, G. Liu and H.-M. Cheng, *Nanoscale*, 2012, **4**, 3871-3874.

6.5. P. A. Mangrulkar, V. Polshettiwar, N. K. Labhsetwar, R. S. Varma and S. S. Rayalu, *Nanoscale*, 2012, **4**, 5202-5209.

6.6. F. Akira and H. Kenichi, *Nature*, 1972, **238**, 37.

6.7. K. Maeda and K. Domen, *J. Phys. Chem. Lett.*, 2010, **1**, 2655-2661.

6.8. A. Kudo and Y. Miseki, *Chem. Soc. Rev.*, 2009, **38**, 253-278.

6.9. N. K. Allam, A. J. Poncheri and M. A. El-Sayed, *ACS Nano*, 2011, **5**, 5056-5066.

6.10. H. J. Yun, H. Lee, N. D. Kim, D. M. Lee, S. Yu and J. Yi, *ACS Nano*, 2011, **5**, 4084-4090.

6.11. M. G. Walter, E. L. Warren, J. R. McKone, S. W. Boettcher, Q. Mi, E. A. Santori and N. S. Lewis, *Chem. Rev.*, 2010, **110**, 6446-6473.

6.12. Y.-C. Lin, Y. Chen, A. Shailos and Y. Huang, *Nano Lett.*, 2010, **10**, 2281-2287.

6.13. Y. D. Hou, B. L. Abrams, P. C. K. Vesborg, M. E. Bjorketun, K. Herbst, L. Bech, A. M. Setti, C. D. Damsgaard, T. Pedersen, O. Hansen, J. Rossmeisl, S. Dahl, J. K. Norskov and I. Chorkendorff, *Nat. Mater.*, 2011, **10**, 434-438.

6.14. Y. W. Chen, J. D. Prange, S. Duhnen, Y. Park, M. Gunji, C. E. D. Chidsey and P. C. McIntyre, *Nat. Mater.*, 2011, **10**, 539-544.

6.15. M. Matsumura and S. Roy Morrison, *J.Eelectroanal. Chem. Interfacial electrochem.*, 1983, **147**, 157-166.

6.16. S. W. Boettcher, E. L. Warren, M. C. Putnam, E. A. Santori, D.

Turner-Evans, M. D. Kelzenberg, M. G. Walter, J. R. McKone, B. S. Brunschwig, H. A. Atwater and N. S. Lewis, *J. Am. Chem. Soc.*, 2011, **133**, 1216-1219.

6.17. J. R. McKone, E. L. Warren, M. J. Bierman, S. W. Boettcher, B. S. Brunschwig, N. S. Lewis and H. B. Gray, *Energy Environ. Sci.*, 2011, **4**, 3573-3583.

6.18. B. Marsen, B. Cole and E. L. Miller, *Sol. Energy Mater. Sol. Cells*, 2008, **92**, 1054-1058.

6.19. M. W. Kanan, Y. Surendranath and D. G. Nocera, *Chem. Soc. Rev.*, 2009, **38**, 109-114.

6.20. T. R. Cook, D. K. Dogutan, S. Y. Reece, Y. Surendranath, T. S. Teets and D. G. Nocera, *Chem. Rev.*, 2010, **110**, 6474-6502.

6.21. I. Oh, J. Kye and S. Hwang, *Nano Lett.*, 2012, **12**, 298-302.

6.22. J. Oh, T. G. Deutsch, H. C. Yuan and H. M. Branz, *Energy Environ. Sci.*, 2011, **4**, 1690-1694.

6.23. B. M. Kayes, H. A. Atwater and N. S. Lewis, *J. Appl. Phys*, 2005, **97**, 114302.

6.24. J. R. Maiolo, H. A. Atwater and N. S. Lewis, *J. Phys. Chem. C*, 2008, **112**, 6194-6201.

6.25. K. Q. Peng, H. Fang, J. J. Hu, Y. Wu, J. Zhu, Y. J. Yan and S. Lee, *Chem. Eur. J.*, 2006, **12**, 7942-7947.

6.26. M. Avrami, *J.Chem. Phys.*, 1939, **7**, 1103-1112.

6.27. E. Garnett and P. Yang, *Nano Lett.*, 2010, **10**, 1082-1087.

6.28. C. Battaglia, C.-M. Hsu, K. Söderström, J. Escarré, F.-J. Haug, M. Charrière, M. Boccard, M. Despeisse, D. T. L. Alexander, M. Cantoni, Y. Cui and C. Ballif, *ACS Nano*, 2012, **6**, 2790-2797.

6.29. L. Tsakalakos, J. Balch, J. Fronheiser, M.-Y. Shih, S. F. LeBoeuf, M. Pietrzykowski, P. J. Codella, B. A. Korevaar, O. V. Sulima, J. Rand, A. Davuluru and U. Rapol, *J. Nanophotonics*, 2007, **1**, 013552.

6.30. ASTM International Standards Worldwide, http://www.astm.org/Standards/G173.htm

6.31. F. Meillaud, A. Shah, C. Droz, E. Vallat-Sauvain and C. Miazza, *Sol. Energy Mater. Sol. Cells*, 2006, **90**, 2952-2959.

6.32. C. Wu, C. H. Crouch, L. Zhao, J. E. Carey, R. Younkin, J. A. Levinson, E. Mazur, R. M. Farrell, P. Gothoskar and A. Karger, *Appl. Phys. Lett.*, 2001, **78**, 1850-1852.

6.33. E. Rosencher and B. Vinter, *Optoelectronics*, Cambridge University Press, Cambridge, UK, **2002**.

6.34. J. D. J. Ingle and S. R. Crouch, *Spectrochemical Analysis*, Prentice Hall, NJ, USA, **1988**.

6.35. S. Koynov, M. S. Brandt and M. Stutzmann, *J. Appl. Phys*, 2011, **110**, 043537.

6.36. J. Price, P. S. Lysaght, S. C. Song, Hong-Jyh Li and A. C. Diebold, *Appl. Phys. Lett.*, 2007, **91**, 061925-061927

6.37. B.K. Newman, J.T. Sullivan, M.T. Winkler, M.J. Sher, M.A. Marcus, S. Fakra, M.J. Smith, S. Gradecak, E. Mazur and T. Buonassisi, *24th European Photovoltaic Solar Energy Conference*, 21-25 september 2009, Hamburg, Germany.

6.38. J. M. Foley, M. J. Price, J. I. Feldblyum and S. Maldonado, *Energy Environ. Sci.*, 2012, **5**, 5203-5220.

6.39. J. Oh, H.-C. Yuan and H. M. Branz, *Nat. Nanotech.*, 2012, **7**, 743-438.

6.40. N. S. Lewis, *J. Electrochem. Soc.*, 1984, **131**, 2496-2503.

6.41. J. H. Bae, J.-H. Han and T. D. Chung, *Phys. Chem. Chem. Phys.*, 2012, **14**, 448-463.

6.42. Y. Nakano, S. Iwamoto, I. Yoshinaga and J. W. Evans, *Chem. Eng. Sci.*, 1987, **42**, 1577-1583.

6.43. R. N. Sajjad and K. Alam, *J. Appl. Phys*, 2009, **105**, 044307-6.

6.44. Z. B. Chen, T. F. Jaramillo, T. G. Deutsch, A. Kleiman-Shwarsctein, A.

J. Forman, N. Gaillard, R. Garland, K. Takanabe, C. Heske, M. Sunkara, E. W. McFarland, K. Domen, E. L. Miller, J. A. Turner and H. N. Dinh, *J. Mater. Res.*, 2010, **25**, 3-16.

6.45. C. Wu, C. H. Crouch, L. Zhao, J. E. Carey, R. Younkin, J. A. Levinson, E. Mazur, R. M. Farrell, P. Gothoskar and A. Karger *Appl. Phys. Lett.*, 2001, **78** 1850-1851.

6.46 J. D. J. Ingle and S. R. Crouch *Spectrochemical Analysis*, Prentice Hall, NJ, USA, 1988.

6.47 S. Koynov, M. S. Brandt and M. Stutzmann *J. Appl. Phys.*, 2011, **110,** 043537.

6.48 Y. D. Hou, B. L. Abrams, P. C. K. Vesborg, M. E. Bjorketun, K. Herbst, L. Bech, A. M. Setti, C. D. Damsgaard, T. Pedersen, O. Hansen, K. Rossmeisl, S. Dahl, J. K. Norskov and I. Chorkendorff, *Nat. Mater.* 2011, **10,** 434-441.

6.49 J. Oh, T. G. Deutsch, H. C. Yuan and H. M. Branz, *Energy Environ. Sci.*, 2011, **4**, 1690-1694.

6.50 I. Oh, J. Kye and S. Hwang, *Nano Lett.*, 2012, **12**, 298-302.

6.51 J. R. McKone, E. L. Warren, M. J. Bierman, S. W. Boettcher, B. S. Brunschwig, N. S. Lewis and H. B. Gray, *Energy Environ. Sci.*, 2011, **4**, 3573-3583.

6.52 J. R. Maiolo, B. M. Kayes, M. A. Filler, M. C. Putnam, M. D. Kelzenberg, H. A. Atwater and N. S. Lewis, *J. Am. Chem. Soc.*, 2007, **129,** 12346-12352.

6.53 S. W. Boettcher, E. L. Warren, M. C. Putnam, E. A. Santori, D. Turner-Evans, M. D. Kelzenberg, M. G. Walter, J. R. McKone, B. S. Brunschwig, H. A. Atwater and N. S. Lewis, *J. Am. Chem. Soc.*, 2011, **133**, 1216-1219

6.54 U. Sim, H.-Y. Jeong, T.-Y. Yang and K. T. Nam, *Journal of Materials Chemistry A*, 2013, **1**, 5414-5422.

Chapter 7 Graphene Quantum Sheets Catalyst and Structural Optimization of Its Catalyst and Photoelectrode

7.1 Introduction

The development of sustainable energy sources is an urgent issue because of the current level of energy consumption.[7.1] Renewable and sustainable energy sources must be developed because present energy sources have several disadvantages such as CO_2 emission and limited deposits of fossil fuels.[7.2] Photoelectrochemical hydrogen production using solar energy represents an important and environmentally friendly technology with no carbon emissions.[7.3] The development of efficient and cheap photoelectrodes for water splitting is one of the fundamental challenges in hydrogen production.[7.4] Despite the intriguing advances in controlling the nanostructural interface and newly discovered material compositions for photoelectrodes, sluggish kinetic issues associated with a high overpotential remain some of the most difficult issues that need to be resolved.[7.5, 7.6] Intense research into efficient, durable, and inexpensive hydrogen evolution reaction (HER) catalysts has been undertaken to solve the kinetic problem.[7.7-7.10] In general, precious metals such as platinum exhibit superior performance HER catalysts; however, the unavoidable weakness of precious metals is their high cost.[7.11] A critical requirement for producing outstanding catalysts in a photoelectrochemical cell is not only the ability to boost the kinetics of electrochemical reaction but also the ability to resist electrochemical and photoinduced degradation. Herein, we demonstrate that the combination of controlling a nanostructure of the photoelectrode and using a carbon-based hydrogen evolution catalyst represents a significant step toward enhancing the applied bias photon-to-current efficiency (ABPE). In the present work, a 430 mV decrease in

overpotential was achieved using graphene quantum sheets on a silicon nanowire, which exhibited an enhancing effect comparable to that of platinum catalysts. Furthermore, the current density at the reversible potential vs. a reversible hydrogen electrode (RHE) exhibited a 101 fold enhancement relative to the current density achieved with planar silicon substrates.

The thermodynamic potential of water splitting is 1.23 V, which is observed by subtracting the reduction reaction and oxidation reaction in the photoelectrochemical reaction of water. At the anode, the oxidation reaction in the electrolysis of water is:

$$O_2 + 4e^- + 4H^+ \leftrightarrow 2H_2O,\ E_{anodic} = 1.23\ V - 0.059(pH)\ V\ (vs.\ NHE) \quad (7.1)$$

whereas the reduction reaction at the cathode is:

$$4e^- + 4H^+ \leftrightarrow 2H_2, \qquad E_{cathodic} = 0\ V - 0.059(pH)\ V\ (vs.\ NHE) \quad (7.2)$$

where, NHE is the normal hydrogen electrode and the standard potential is dependent on pH ($E_{half} = E - 0.059(pH)$ vs NHE). Kinetically, however, when a voltage of 1.23 V is applied, electrolysis is difficult to induce, which results in no current flow. In this situation, a higher potential, which is referred to as the overpotential, η, is needed to drive the reaction at a certain rate. Moreover, if a current i_c flows at the cathode, a current i_a of the same magnitude must flow at the anode to complete the circuit, which requires the overpotential at both electrodes. The overpotentials at the cathode and anode are denoted as η_c and η_a, respectively. Therefore, the total applied potential, E_{appl}, is

$$E_{appl} = 1.23\ V + \eta_c + \eta_a \quad (7.3)$$

A higher overpotential requires a higher total applied voltage. Using an electrocatalyst for water splitting can reduce the overpotential required for the electrolysis of water.

In an effort to reduce the overpotential for the water splitting reaction, various catalysts have been deposited onto photoelectrode materials. Previously reported HER catalysts include pure metals, metal

composites/alloys, compounds such as nonmetallic elements, and molecular catalysts.[7.4, 7.5, 7.12-7.16] Among metal-based catalysts, Pt, Pd, and Ru are near the top of the volcano plot, exhibiting high catalytic activity toward the HER.[7.7] For example, Pt nanoparticles on p-type Si nanowires in aqueous electrolyte solutions can enhance the onset potential by approximately 0.42 V.[7.17] In view of economic issues, recent progress has been concentrated on the incorporation of metal nanoparticles into earth-abundant elements rather than on the use of noble metals alone.[7.11] Nonprecious metal catalysts and catalysts that are abundant in nature have also exhibited high activity toward the HER. Binary structures such as MoS_2, Mo_2N, Mo_2C, and Ni_2P and bimetallic compounds such as Co-Mo-N and Ni-Mo have been suggested as catalysts with high HER activity.[7.12, 7.18-7.21] However, the rigorous and precise tuning of the composition of $A_xB_yM_z$ compounds, controlling the active sites in catalysts for the HER, and nanostructuring make optimization of the properties of catalysts for the HER difficult. Moreover, when deposited with catalysts, the saturation current density and the current density at a reversible potential vs. RHE significantly decrease because of light scattering by catalysts on the surface of the photoelectrodes.

To solve the problems associated with previously developed catalysts, carbon-based catalysts may represent an important research direction in the search for low-cost, environmentally friendly, and corrosion-resistant catalysts. Among carbon-based catalysts, graphene, in particular, possesses excellent transmittance and superior intrinsic carrier mobility; thus, several attempts have been made to use graphene as a catalyst.[7.22] Co-activated N and P heteroatoms adjacent to C atoms in the graphene matrix can affect such catalysts' valence orbital energy levels and thereby enhance their reactivity toward the HER.[7.23] Graphitic-carbon nitride combined nitrogen-doped graphene also exhibits enhanced HER activity, with HER properties similar to those of well-established metallic catalysts.[7.24] Reduced graphene oxide

containing catalytic active materials has exhibited improved activity in oxygen reduction reactions and oxygen evolution reactions as well as in the HER.[7.25-7.28] However, in most cases, the role of carbon materials is limited to an electrically conducting substrate or a supporter that increases the HER activity of other decorated active catalysts. Recently, we suggested that monolayer graphene deposited onto a planar Si electrode acts as an efficient HER electrocatalyst and that N_2 plasma treatment enhances its catalytic activity.[7.29] In this study, we further investigated N_2-plasma-treated graphene quantum sheets deposited on the Si nanowire photocathodes as efficient HER electrocatalyst.

Controlling the surface structure of Si represents another important approach to improving photoelectrochemical performance. Si, one of the most abundant elements in the Earth's crust, can be used both as a photocathode and a photoanode for photochemical water splitting because its bandgap (1.12 eV) allows for the absorption of a significant portion of the solar spectrum.[7.30, 7.31] However, the small band bending between the conduction band edge and H^+/H_2 redox level of aqueous electrolytes limits the photoelectrochemical performance of Si relative to that of Si/non-aqueous solvent systems.[7.5] The application of an external potential or the use of catalysts is necessary for efficient operation under solar irradiation. To overcome this problem, a porous structure or a nanostructure can increase the current density of Si photoelectrodes by increasing the number of effective reaction sites between the Si semiconductor and the liquid electrolyte junction as well as reducing the reflection of incident light.[7.6, 7. 32] A nanowire structure can increase the efficiency due to the orthogonalization of the direction of incident light absorption and charge carrier collection.[33] Therefore, the combination of an optimized Si nanowire photocathode and a graphene quantum sheet catalyst can boost the catalytic activity toward the photoelectrochemical HER.

7.2 Results and Discussion

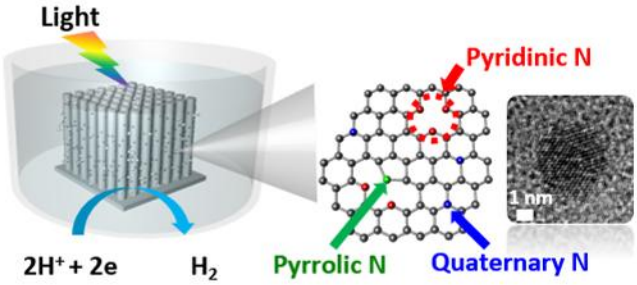

Figure 7.1. Schematic of N-doped graphene quantum sheets (N-GQSs) decorated on a Si nanowire (SiNW) photocathode electrode. Photons absorbed by the SiNWs generate minority carriers (electrons), which drift to the semiconductor/electrolyte interface, where $2H^+$ is reduced to H_2; the N-GQSs serve as electrocatalysts for hydrogen production. The gray, green, blue, and red spheres in the schematic of N-GQSs represent the carbon, pyrrolic nitrogen, quaternary nitrogen, and pyridinic nitrogen atoms, respectively. The average diameter of the N-GQSs is 5 nm, as determined from a TEM image.[7.50]

Measurements of photoelectrochemical performance show that N-doped graphene quantum sheets (N-GQSs) on Si photoelectrode exhibit catalytic HER activity. Figure 7.1 shows a schematic of hydrogen production on N-GQSs on Si nanowire arrays (SiNWs) in an acid solution under irradiation. Photons absorbed by the SiNWs generate minority carriers (electrons), which drift to the semiconductor/electrolyte interface where $2H^+$ is reduced to H_2; the N-GQSs serve as electrocatalysts for hydrogen production. In the schematic of the N-GQSs, gray, green, blue, and red spheres represent carbon, pyrrolic nitrogen, quaternary nitrogen, and pyridinic nitrogen atoms, respectively, based on high resolution X-ray photoelectron spectrum (XPS)

measurements. From Transmission electron microscopy (TEM) image and a size-distribution histogram indicate that the average diameter of the N-GQSs was 5 nm (Figure 7.7). N-GQSs were transferred to p-type silicon nanowires via drop-casting. The N-GQSs were converted from monolayer graphene on Cu foil using nitrogen plasma. After exposure to nitrogen plasma, the nano-sized GQSs were distributed on the Cu foil and were subsequently characterized by atomic force microscopy (AFM); the strong D peak of the sheets, which is related to the structural defects at the edges of graphene, was identified in the Raman spectrum. In addition, the doping of the GQSs with ~2.9% nitrogen was indicated by the N 1s XPS of the structures, and the UV-vis absorption spectrum of the N-GQSs revealed an absorption band with a peak at 275 nm, as shown in Figure 7.7. The well-aligned SiNW arrays serve as an anti-reflector that enhances light absorption in the structure and increases the overall surface area; the N-GQSs act as electrocatalysts for hydrogen evolution.

Top-view and cross-sectional scanning electron microscope (SEM) images of the N-GQSs on SiNWs are shown in Figures 7.2a and 7.2b. The SiNWs exhibited an average diameter of ~400 nm, and lengths of up to ~5 μm. To determine the crystallinity, orientation, and morphology of the N-GQSs on SiNWs, TEM analyses were performed. The selected area electron diffraction pattern, with an incident beam axis of [1-10] (Figure 7.9), indicated that a single-crystalline SiNW was well aligned along the [001] direction; the thickness fringes, brightness and dark line pattern indicate that the SiNW was etched as a column with angled edges, as shown in Figure 7.2c. Moreover, the N-GQSs, which measured approximately 7 nm in diameter, were uniformly placed on the SiNWs, as indicated by dark-field TEM imaging (Figure 7.2c); moreover, the formation of the N-GQSs was verified by high-resolution TEM (HRTEM). The HRTEM image shows Moiré pattern created by the superposition of the mismatched crystalline lattices of the N-GQSs and

SiNWs, as shown in Figure 7.2d. The lattice plane spacing of p-Si was observed to be 3.1 Å, which corresponds to the silicon (100) plane (JCPDS, No. 24-1402). The Moiré pattern (6.2 Å) indicates mixed translational and rotational geometry. The corresponding spacing of the fringes was calculated as follows:[7.34]

$$a_m = (a_{GQS} \times a_{Si}) / \sqrt{a_{GQS}^2 + a_{Si}^2 - 2a_{GQS}a_{Si}\cos(\alpha_{GQS} - \alpha_{Si})} \quad (7.4)$$

where a_m is the *d*-spacing of the Moiré pattern, a_{GQS} is the *d*-spacing of the N-GQS, and a_{si} is the *d*-spacing of Si. On the basis of Eq. (7.4), the placement of an N-GQS on a SiNW with a 20 degree tilt was verified by the relation between the Moiré fringe spacing and the Si lattice plane.

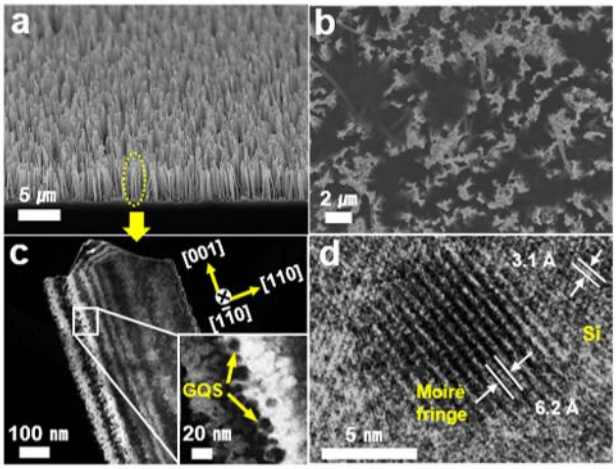

Figure 7.2. SEM images of SiNW arrays on p-silicon substrate obtained by metal assisted chemical etching method. (a) Cross-section and (b) top-view. (c) Dark-field TEM images of N-GQSs on p-SiNWs. (d) High-resolution TEM image shows Moiré pattern created by N-GQS in silicon lattices.[7.50]

To investigate the dependence of Si photoelectrode on its nanostructure, Si substrates of various nanostructures were fabricated by silver metal-assisted

chemical etching.[7.35] Normal boron-doped p-type (100) Si substrates were immersed in an aqueous solution of 0.015 M silver nitrate and 5 M hydrofluoric acid. Continuous Si oxidation by the galvanic reduction of Ag^+ ions and the ensuing dissolution of silicon oxide by HF resulted in the [100] directional etching of the Si substrates. The etching time was varied among 20 min, 30 min, 120 min, and 180 min. Depending on the etching time, different Si nanostructures were observed as characterized by SEM (Figure 7.11). When the etching time was shorter than 120 min, a porous nanostructure was observed. The transition of the surface structure from a porous to a nanowire structure occurred when the Si substrates were etched for 120 min. After this stage, the length of the nanowires was observed to increase with increasing etching time. Representative images of the SiNWs are shown in Figures 7.2a and 7.2b.

For the evaluation of the photocathodic behavior of the nanostructured Si electrodes, the current density was measured as the potential was swept from 0.4 V to -1.0 V vs. RHE in a three-electrode cell. A 300 W Xe lamp illuminated the Si photoelectrode with a light intensity of 100 mW/cm^2 through an Air Mass 1.5 Global filter in an aqueous 1 M perchloric ($HClO_4$) acid solution (pH 0). Because the applied potential of the Si working electrode was negative (cathodic), the magnitude of the current density increased and saturated at a specific value of the applied potential. The current density at the saturation point is called the limiting current density or the saturation current density. As shown in Figure 7.3a and Figure 7.10, the current density of the planar Si continued to increase until the length of the nanowires reached 5 μm as the surface became increasingly nanostructured. The limiting current density of bare planar Si was approximately -33 mA/cm^2. The surface area of the nanostructured Si substrate was greater than that of the planar structure. The reflectance of incident light could be reduced by the nanostructured Si surface. Although the surface of planar Si reflects approximately one quarter

of incident light, photon absorption is enhanced at the nanostructured surface because of its low reflectance. Nanostructured silicon wires have been reported to exhibit a light trapping effect,[7.36] which can enhance the current level for hydrogen production when the length of the Si nanowires is optimized to exhibit strong broadband optical absorption.[7.37] The nanowire structure also has the advantage of inducing the orthogonalization of light absorption and charge-carrier collection.[7.33] Thus, the minority carriers generated by incident solar light can move to the lateral side of each nanowire and participate in the hydrogen evolution reaction more quickly than in the planar structure. To calculate the photovoltage of the Si photoelectrode, the dark current density was also measured. The photovoltage is defined as the difference between the onset potential under the dark and illuminated conditions. Figure 3b shows the dark current densities of representative Si electrodes. The dark current density of the nanostructured electrodes was also greater than that of the planar Si substrate. The nanostructured photoelectrode (0.59 V of photovoltage) exhibited a positive shift in photovoltage of 0.13 V relative to that of the planar Si electrode (0.46 V of photovoltage) as shown in Table 7.1.

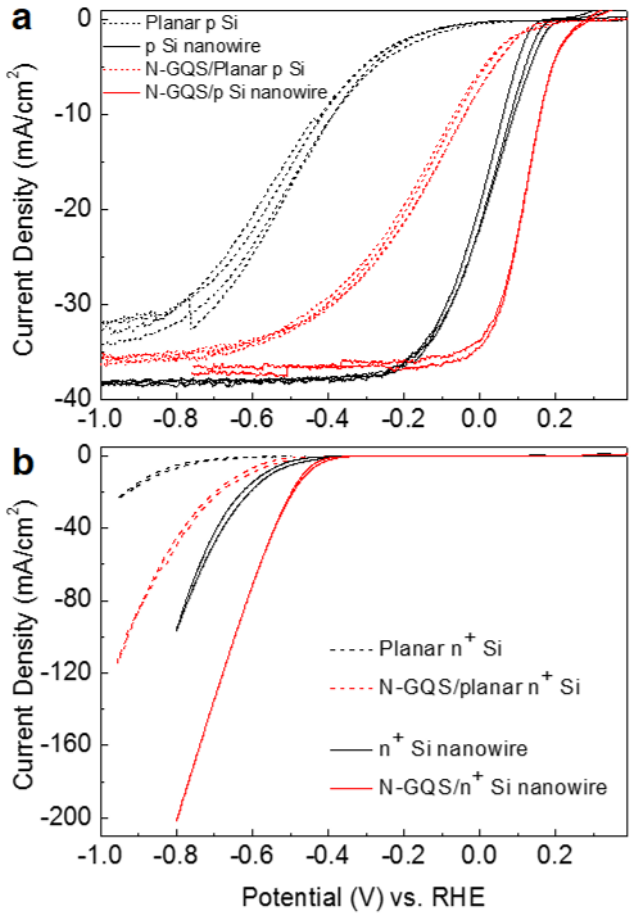

Figure 7.3. Cyclic voltammograms of N-doped graphene quantum sheets (N-GQSs) on silicon photocathodes. (a) Photocurrent density-potential (*J-E*) curves for a lightly boron-doped planar p-Si electrode and Si nanowire deposited with N-GQSs. The Si nanowire was fabricated using a metal-catalyzed electroless method. (b) Polarization curves of N-GQS on heavily arsenic-doped n^+-type Si electrodes under dark conditions. [7.50]

In measurements of the photoelectro-catalytic performance, N-GQSs on SiNWs exhibited catalytic activity toward the HER. As shown in Figure 7.3a,

the current density of the N-GQSs/planar Si structure increased gradually from -0.2 V vs. RHE and was saturated at approximately -35 mA/cm^2 below -0.8 V vs. RHE at negative applied potentials. This current density is higher than that of planar Si without N-GQSs. Interestingly, measurements of the N-GQSs/planar Si structure showed that the overall current density-potential (*J-E*) curve was shifted by approximately 0.2 V toward positive potentials compared to that of planar Si without N-GQSs. The onset potential is defined as the potential at a photocurrent density of -1 mA/cm^2. The onset potential of N-GQSs/planar Si was 0.13 V vs. RHE, representing a positive shift of 0.30 V compared to the onset potential of bare Si (-0.17 V vs. RHE). Figure 7.3b also shows the dark current densities of the heavily arsenic-doped n$^+$-type Si electrodes. In the dark condition, the positive shift in the onset potential of 0.21 V (-0.44 V vs. RHE for N-GQSs/planar Si) also shows higher than that of planar Si (-0.63 V vs. RHE for planar Si).

When incorporated into the nanostructured photoelectrode system, the N-GQSs exhibited much higher catalytic activity than that of the planar photoelectrode system. The onset potential of the N-GQSs/Si nanowire electrode was 0.26 V vs. RHE, which is 0.09 V higher than that of the Si nanowire without a catalyst (0.17 V vs. RHE). Both the increased onset potential and the current density at the reversible potential (0 V vs. RHE) showed an enhanced ABPE of 2.29%, which is greater than that of the bare Si nanowire system (0.91%). ABPE is the applied bias photon-to-current efficiency: [7.38]

$$\text{ABPE} = [j_{ph}\ (\text{mA/cm}^2) \times (V_{redox} - V_b)\ (\text{V}) / P_{in}\ (\text{mW/cm}^2)]_{\text{AM 1.5 G}} \times 100\ (\%)$$

where, j_{ph} is the photocurrent density obtained under an applied bias V_b, V_{redox} is the redox potential for hydrogen production (0 V), V_{bias} is the externally applied bias potential that is often necessary to achieve reasonable photocurrents, and P_{light} is the intensity of the incident light for AM 1.5 G condition (~100 mW/cm^2).The enhanced photocatalytic performance indicates

a synergistic effect between the N-GQSs and Si nanowire structures; moreover, the N-GQSs act as effective HER catalysts on the Si photocathode. Compared to previously reported carbon-based catalysts on Si system, the N-GQSs/Si nanowire system exhibits a higher ABPE.

To investigate the electrocatalytic activity of the N-GQSs, we measured cyclic voltammetry using a rotating disk electrode (RDE) system. To fabricate the working electrode, an N-GQSs solution was transferred to a glassy carbon (GC) tip that was inert in an aqueous solution. As shown in Figure 7.4a, in the *J-E* curves obtained by the RDE measurements, the current density associated with the water splitting reaction exponentially increased after the onset point as the potential was swept from 0.1 V to -0.45 V. For comparison with the potential for the HER in the RDE system, the potential required to attain -5 mA/cm^2 of HER current density was measured for graphene monolayer/GC, N-GQSs/GC, and Pt/GC systems. Also for comparison, the RDE of a graphene monolayer without plasma treatment was measured. The potential required to attain -5 mA/cm^2 of HER current density was -0.32 V vs. RHE for the graphene monolayer without plasma treatment. The potential for the N-GQSs/GC electrode at -5 mA/cm^2 was -0.22 V vs. RHE; this potential was positively (anodically) shifted by 100 mV relative to that for the monolayer graphene. This result indicates that the N-GQSs and monolayer graphene exhibit electrocatalytic activity toward the HER.

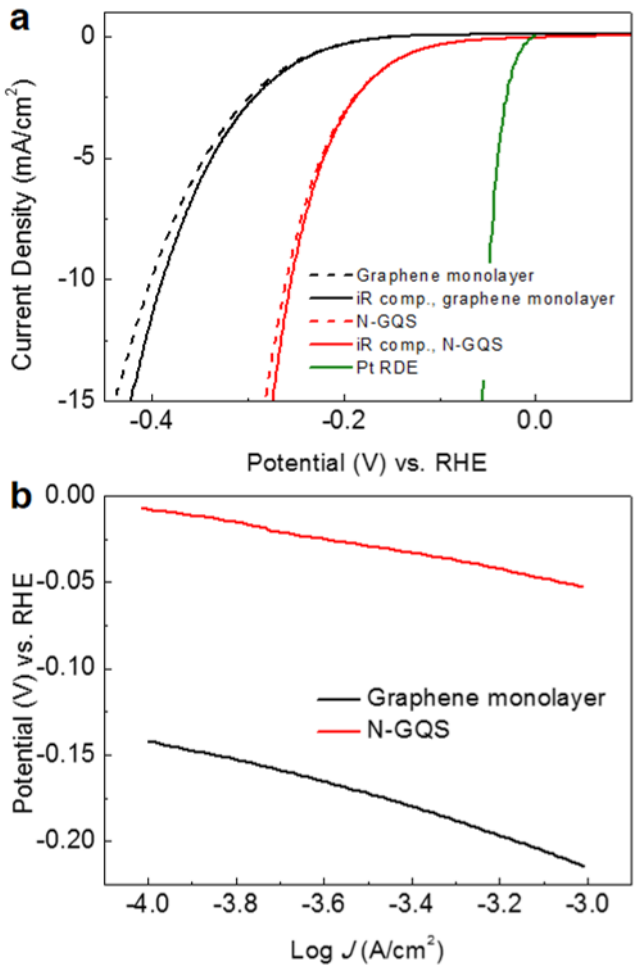

Figure 7.4. Electrochemical activity of graphene monolayer and N-GQSs on glassy carbon (GC) electrodes in a rotating disk electrode system. (a) Cyclic voltammograms (CV) of a graphene monolayer on GC, N-GQSs on GC, Pt/C on GC. CV data obtained compensating for ohmic drop (iR) losses are also plotted (dashed curves). (b) Tafel plots derived from the CV data in (a). [7.50]

To gain further quantitative insight into the catalytic activity of the N-GQSs, the *J-E* curves in Figure 7.4a were converted into plots of the potential as a function of the logarithm of *J*. This potential-log *J* plot is called a Tafel plot.

The measured potentials were corrected for the iR losses that originated from the resistance of the interface between the electrode and the electrolyte. Analysis of the impedance spectra revealed that the resistances of the graphene monolayer and N-GQSs/GC were 7.5 and 8.0 Ω, respectively. The Tafel plot provides two parameters for estimating the electrocatalytic activity: the Tafel slope and the exchange current density. The Tafel slope is defined to be a measure of the potential increase required to increase the resulting current by one order of magnitude. The graphene monolayer exhibited a Tafel slope of 75 mV/decade, and the N-GQSs/GC exhibited a slope of 45 mV/decade, 30 mV lower than that of the graphene monolayer. For comparison with a well-known catalyst, Pt particles were deposited onto GC and the electro-catalytic activity of the resulting electrode was measured. The applied potential required to obtain -5 mA/cm^2 was -0.04 V vs. RHE, which represents a positive shift of 0.18 V relative to that of the N-GQSs/GC electrode. The Tafel slope of Pt-GC was 42 mV/decade, which is similar to that of the N-GQSs/GC. For previously reported carbon-based catalysts, the potential required to attain -5 mA/cm^2 was -0.5 V vs. RHE for N-doped graphene and -0.3 V vs. RHE for graphitic C_3N_4, respectively. [7.23, 7.24] The Tafel slope was reported to be 116 mV/decade for N-doped graphene and 51.5 mV/decade for graphitic C_3N_4 when deposited as a mixture with Nafion or carbon black on GC, respectively.

The Tafel slope provides an indication of which reaction steps are possible in the HER among the following: [7.39]

$H_3O^+ + e^- \rightarrow H_{ads} + H_2O$	Volmer reaction	(7.5)
$H_{ads} + H_3O^+ + e^- \rightarrow H_2 + H_2O$	Heyrovsky reaction	(7.6)
$H_{ads} + H_{ads} \rightarrow H_2$	Tafel reaction	(7.7)

where H_{ads} is adsorbed H, (7.5) is a discharge step, (7.6) is a desorption step, and (7.7) is a recombination step. Considering the adsorbed hydrogen coverage (θ_H) on the surface of an electrode, if the recombination of adsorbed

hydrogen (the Tafel reaction) is the rate-determining step for the HER and if the coverage is very high ($\theta_H \approx 1$), the measured Tafel slope will be 30 mV/decade. However, if the electrochemical desorption step (the Heyrovsky reaction) is the rate-determining step, a Tafel slope of 40-118 mV/decade is measured and is dependent of the value of θ_H (0-1).[7.40] The observed Tafel slope of 45 mV/decade in the present work indicates that the kinetics of the HER on the graphene monolayer/GC and N-GQS/GC electrodes is determined by the Heyrovsky reaction.

The exchange current density (J_0) of the N-GQSs catalyst was also analyzed. During hydrogen evolution, the current I can be described the following equation:[7.7]

$$I=-e(r^{+}-r^{-}) \qquad (7.8)$$

where $r^{+}-r^{-}$ is the net rate of the electron transfer between the oxidation ($4e^{-} + 4H^{+} \leftarrow 2H_2$) and the reduction ($4e^{-} + 4H^{+} \rightarrow 2H_2$) from Eq. (7.2). The exchange current is the sum of the forward and backward rates when Eq. (7.2) is in equilibrium. The ability of a given material to catalyze the HER is usually measured by J_0, which is the rate of hydrogen evolution per surface area at the electrode potential when the reaction is at equilibrium. The J_0 is also defined as the current density at zero overpotential. The catalytic effect originates from improvement of the rate of charge transfer at the interface between the electrode and electrolyte or from a decrease in the activation energy barrier for a chemical reaction; these catalytic effects are represented by J_0. A high value of J_0 indicates that electron transfer or the adsorption/desorption of protons at the electrode/electrolyte can occur more easily, with a lower kinetic barrier. The value of J_0 can be obtained by extrapolating the Tafel plot in Figure 4b and extracting the current density at 0 V vs. RHE. The N-GQSs/GC electrode exhibited an enhanced J_0 of 7.1×10^{-5} A/cm^2, which was 26.3 times greater than the J_0 of monolayer graphene on GC (2.7×10^{-6} A/cm^2). The J_0 of the N-GQSs was also compared with that of

other carbon-based catalysts (Table S3). The reported carbon-based catalysts exhibited a lower J_0 than that of our N-GQSs electrode. In addition, a metal-free carbon catalyst doped with nitrogen and phosphorous exhibited a J_0 of 2.4 × 10^{-7} A/cm^2 and a graphitic C_3N_4 catalyst with nitrogen-doped graphene exhibited 3.5×10^{-6} A/cm^2 of J_0.[7.23, 7.24]

Figure 7.5 summarizes the experimental data for the Si and GC electrodes. As shown in Figure 5b, our N-GQSs catalyst exhibited a lower Tafel slope and a higher J_0 compared to those of other reported carbon-based HER catalysts. Moreover, considering its role as a co-catalyst on the photoelectrode, the N-GQSs/Si nanowire system exhibited better photoelectrochemical performance in terms of ABPE and onset potential than any other reported catalyst/photoelectrode system (Figure 7.5a). Using only a non-metal carbon-based catalyst without incorporating a noble catalyst, the ABPE was increased to 2.29% by the combination of the nanostructured photoelectrode and N-GQSs catalyst. The good HER activity of the N-GQSs electrode is attributed to abundant defects introduced by the plasma treatment and to the incorporation of nitrogen atoms, which can act as catalytic sites, into the graphene structure. Previous report revealed that N doping on graphene could significantly improve the HER by providing additional active sites.[7.23] The N-graphene model also shows a negative Gibbs free energy for hydrogen evolution (ΔG) with the improved capability to adsorb hydrogen, which stimulates H adsorption (the lowest step) to be enhanced. The effect of the hydrogen adsorption on various N defects in graphene was also reported using first-principles electronic-structure calculation.[7.41] The nitrogen peak for our N-GQSs is classified into pyridinic, pyrrolic, and a small number of quaternary nitrogen sites with a concentration of 2.7 at% (Figure 7.7 e). In conjunction with the discussion above, N-sites in GQSs might provide a moderate binding energy between the catalyst and hydrogen adsorbed for HER by lowering the ΔG effectively. Their binding energy to hydrogen in

neither too strong nor weak, which might give the good catalytic behavior for HER.

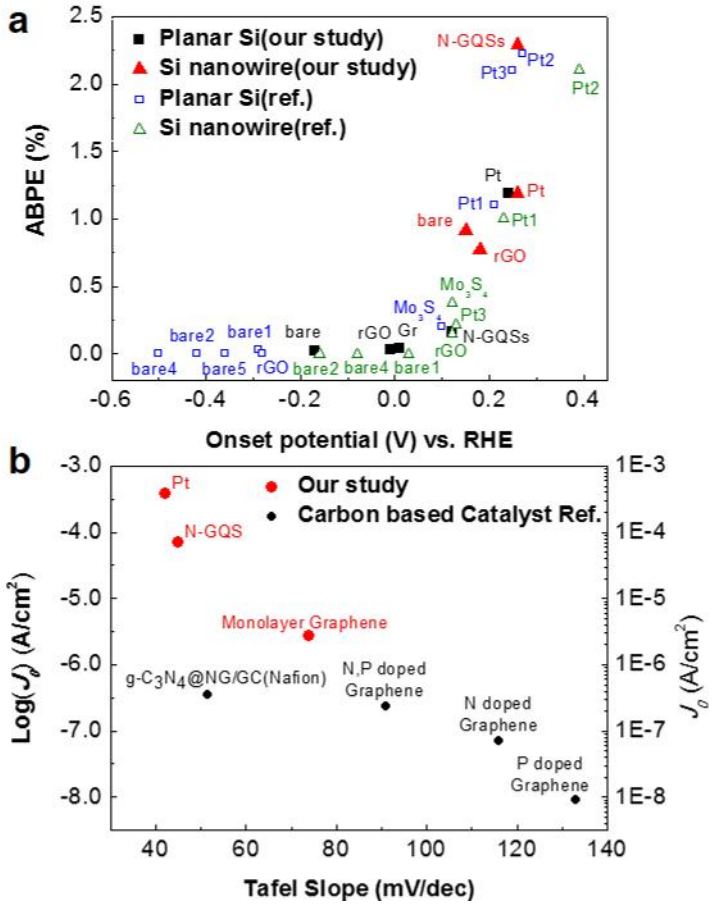

Figure 7.5. Summary of the experimental data for Si and glassy carbon (GC) electrodes. (a) The photoelectrochemical performance of p-type Si-based photoelectrodes. 'Onset potential' and 'ABPE' indicate the potential at -1 mA/cm^2 vs. RHE and the applied bias photon-to-current efficiency, respectively; 'bare' indicates the performance of the bare electrode without deposited catalyst. (b) Electrochemical performance of N-GQSs on GC electrode and other HER catalysts determined using rotating disk electrode

system. J_0 indicates that the exchange current density. References can be found in the Tables 7.2 and 7.3. [7.50]

To further study the electrochemical performance of the N-GQSs/Si electrode, capacitance, impedance, and transient photoresponse measurements were performed, the results of which are shown in Figure 7.6. Capacitance measurements of the N-GQSs/Si nanowire and bare Si nanowire electrodes were performed as the potential was swept from 0.6 V to -0.5 V vs. RHE in a three-electrode cell without illumination. On the basis of the capacitance results, the flat band potential of the Si nanowire and N-GQSs/Si nanowire electrodes were calculated using the Mott-Schottky relation: [7.42]

$$1/C_{sc}^2 = 2(E - E_{fb} - kT/e)/(e\varepsilon\varepsilon_0 N) \qquad (7.9)$$

where C_{sc} is the capacitance of the space charge region, ε is the dielectric constant of the semiconductor, ε_0 is the permittivity of free space, N is the donor density (electron donor concentration for an n-type semiconductor or hole acceptor concentration for a p-type semiconductor), E is the applied potential, and E_{fb} is the flat band potential. Figure 6a shows the typical Mott-Schottky plots for a p-type silicon semiconductor. The donor density was calculated from the slope, and the E_{fb} was determined by extrapolation to a capacitance of zero. On the basis of these relations, the N-GQSs/Si nanowire electrode exhibited an E_{fb} of 0.13 V vs. RHE, whereas the E_{fb} of the bare Si nanowires was 0.02 V vs. RHE, as shown in Figure 7.6a. According to the equation: $E_b = E - E_{fb}$, the applied potential determines the magnitude of band bending (E_b) in the semiconductor and E_{fb}. [7.43] As E_{fb} increases positively, the absolute value of E_b increases because the applied potential, E is always negative under the cathodic reaction for proton reduction. Higher band bending at the interface between the electrode and electrolyte promotes faster charge separation of generated electrons and holes. [7.44] The possibility of

charge recombination or surface trapping at sub-band gap energy levels may also be diminished. The higher E_{fb} of the N-GQSs/SiNW electrode relative to that of the bare SiNW electrode appears to have augmented the extent of band bending at the depletion region of the semiconductor near the solid/solution interface because of the relationship between E_b and E_{fb}. Moreover, the doping density of bare SiNW and N-GQSs/SiNW is also calculated from Mott-Schottky relationship. Using the Eq. (9), the bare SiNW shows the donor density of 4.46×10^{15} /cm^3, which corresponds to the resistivity of $10^0 \sim 10^1$ ohm×cm for boron doped p-Si. [7.45] The N-GQSs/SiNW electrodes shows the donor density of 5.74×10^{15} /cm^3, From the donor density results, N-GQSs deposited on SiNW showed slight increase of the donor density, which might change the electrochemical property at the semiconductor/liquid interface. Zheng *et al.* reported that N dopant adjacent to C atom in a graphene matrix act as an electron acceptor through the analysis of the natural bond orbital population. [7.23] Likewise, N dopant on GQSs might also act as an active catalytic site for HER. To clarify the relationship between the amount of the N dopant on GQSs and the donor density calculated from Mott-Schottky plot, additional in-depth analysis such as density functional theory calculation will be investigated.

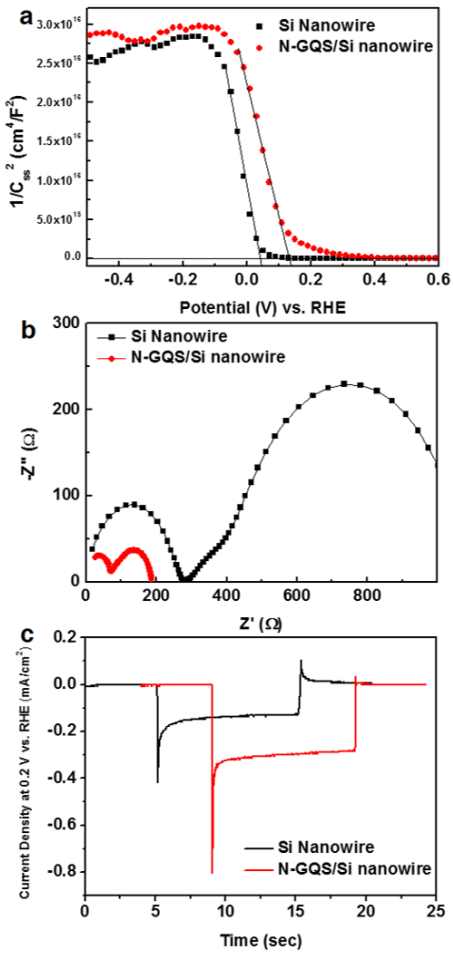

Figure 7.6. Comparison of the electrochemical activity of Si nanowire and N-GQSs on Si nanowire. (a) Mott-Schottky plots from capacitance measurement as a function of potential vs. RHE under dark condition. (b) Nyquist plot for Si nanowire and N-GQSs on Si nanowire at 0 V vs. RHE under dark condition. (c) The transient curve of the photocurrent from Si nanowire and N-GQSs on Si nanowire when the light was turned on and turned off at 0 V vs. RHE.[7.50]

Impedance measurements were also performed to study the enhanced electrochemical properties of the N-GQSs/SiNW system. Under an

illumination intensity of 100 mW/cm^2 with a frequency of 10^3-1 Hz and an amplitude of 5 mV in a three electrode system, electrochemical impedance spectroscopy was performed at 0 V vs. RHE. Figure 7.6b shows a Nyquist plot representing a typical impedance result. In Figure 7.6b, the N-GQSs/SiNW electrode shows two semicircles that are smaller than those exhibited by the Si nanowire electrode. On the basis of the results gathered from these two semicircles, two capacitance elements can be assigned: the capacitance of the charge depletion layer in the semiconductor and the capacitance of the double layer at the semiconductor/electrolyte interface. In the high-frequency region, the charge transfer process in the depletion layer of the semiconductor dominates, whereas charge transfer across the double layer at the semiconductor/electrolyte interface is dominant in the low-frequency region. [7.46] In the case of the N-GQSs/SiNW electrodes, the two semicircles indicating charge transfer processes in the double layers at the solid/solution interface and in the depletion region of the semiconductor are smaller than those of the bare SiNWs. The smaller semicircle in the low frequency range indicates that a kinetic barrier energy for the faradaic reactions across the double layer in the N-GQSs/SiNW is lower than that of the bare SiNWs. Thus, N-GQSs promote the proton reduction by reducing the charge transfer resistance in the double layer. From the result of smaller semicircle in the high frequency range, the charge transfer resistance of the depletion layer in the N-GQSs/SiNW is also lower than that of the bare SiNW, which might be correlated with the slightly higher doping density and flat band potential obtained from the Mott-Schottky plot compared to that of the bare SiNW. The lower charge transfer resistance is also associated with the higher photocurrent response at the zero potential vs. RHE. N-GQSs might also contribute to the rapid charge transfer by enhancing the number of photogenerated carriers to participate in the HER. In addition, N-GQSs/SiNW electrode shows more enhanced onset potential and current density than that

of the N-GQSs/GC electrode (Table 7.1), which indicates that an additional junction effect between N-GQSs and Si electrode might operate. To study the synergetic junction effect, the change of the band bending between the conduction band edge and H^+/H_2 redox level of the electrolyte will be further investigated.

Transient photoresponse measurements were also performed to determine the factors enhancing the photoelectrochemical performance of the N-GQSs/SiNW electrodes; the results are shown in Figure 6c. The transient behavior of the N-GQSs/SiNW and bare Si nanowire electrodes was measured at 0.2 V vs. RHE using a chopped illumination system. Figure 7.6c shows the transient behavior of the N-GQSs/Si and bare Si electrodes without a catalyst. The light was turned on and turned off after 10 sec while the potential was maintained at 0.2 V vs. RHE. At the moment of the light was turned on, the current density reached a peak, which is referred to as the initial photocurrent density (J_{in}). The J_{in} values of the N-GQSs/Si nanowire and bare Si nanowire electrodes were -0.80 mA/cm^2 and -0.42 mA/cm^2, respectively. The current density then saturated, and the saturated photocurrent density (J_{st}) under illumination was -0.30 mA/cm^2 for the N-GQSs/Si nanowire electrode and -0.13 mA/cm^2 for the bare Si nanowire electrode. At the moment the light was turned off, the current density again showed an oscillating plot, and the current density at the peaks was designated as J_{off}. The J_{off} values of the N-GQSs/Si nanowire and Si nanowire electrodes were is -0.02 mA/cm^2 and -0.12 mA/cm^2, respectively. The high $J_{st}/J_{in,\text{ N-GQSs}}$ ratio of 0.375 and small J_{off} of the N-GQS/Si nanowire electrode suggest that fewer carriers were trapped and that less recombination occurred at the surface state of the electrode surface, in comparison with those of the surface state of the bare Si nanowire sample ($J_{st}/J_{in,\text{ bare}}$ = 0.309). Together, the capacitance and impedance results indicate that the N-GQSs/Si nanowire electrode can contribute to charge separation by inducing favorable band bending and boosting the charge

transfer rate, which enhance the electrode's HER performance. To summarize, the results obtained from the capacitance, impedance, and transient photoresponse measurements indicate that the N-GQSs/SiNW electrode enhances the HER activity by reducing the possibility of charge recombination and lowering the kinetic barriers for the HER at the interface between the Si semiconductor and electrolyte solution.

7.3 Conclusion

We fabricated N-doped graphene quantum sheets (N-GQSs) as a catalyst for the solar-driven hydrogen evolution reaction on Si nanowire photocathodes. The onset potential for the Si nanowire photocurrent was significantly shifted toward the anodic direction without a change in the saturation current density. N-GQSs exhibited excellent catalytic activity for the photoelectrochemical HER on Si nanowire photocathodes. The results showed that the N-GQSs electrodes exhibited a ABPE of 2.29%, which is higher than that of any other carbon-based photoelectrochemical HER catalysts reported to date. Our approach in this study involved a strategy for developing metal-free carbon-based catalysts with high efficiency for solar-driven hydrogen fuel production.

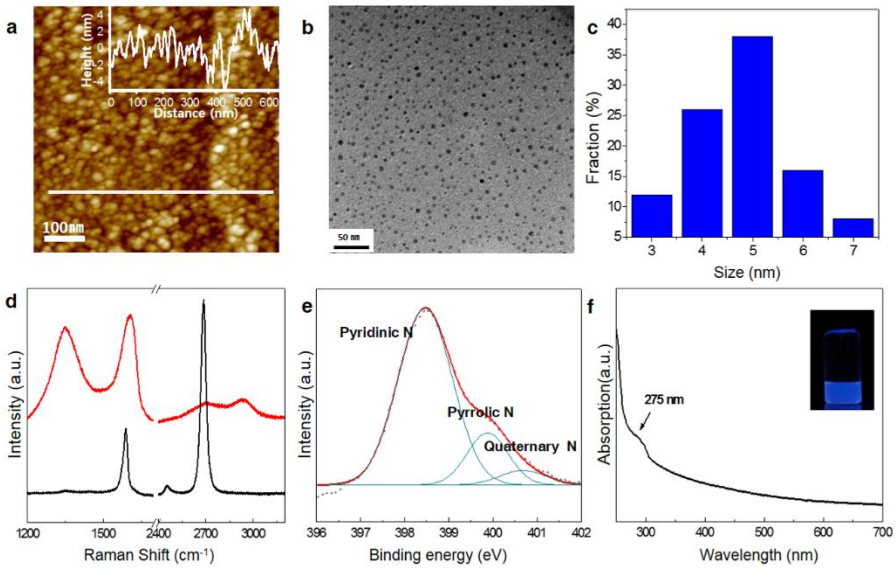

Figure 7.7. (a) AFM image of nitrogen plasma treated GQSs on Cu foil. Scan size, 600 x 600 nm^2. (b) TEM image of N-GQSs. (c) Histogram showing the size distribution of N-GQSs. (d) Raman spectra of graphene (black) and N-GQSs (red) and (e) detailed N 1s XPS spectra of N-GQSs. (f) UV-vis absorption of the N-GQSs in dichloromethane. The inset shows a photograph of the N-GQSs solution under 365 nm wavelength UV lamp.[7.50]

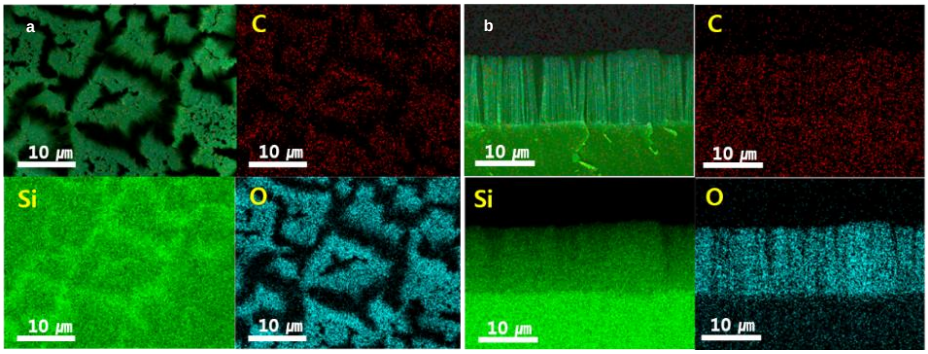

Figure 7.8. SEM mapping images of N-GQSs decorated on Si nanowires. (a,b) Colour images of all displayed with three elements; C (red), Si (green), and O (blue). [7.50]

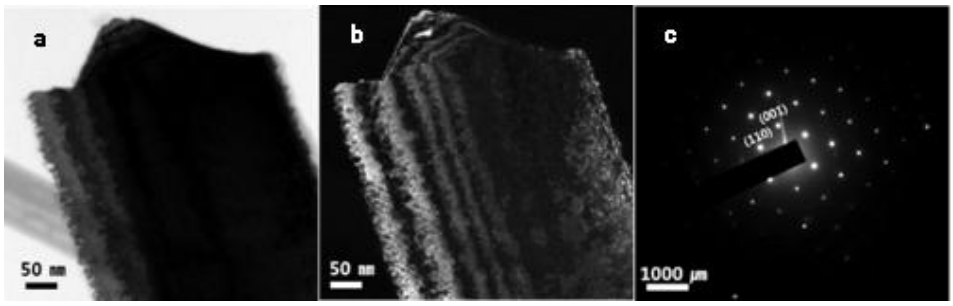

Figure 7.9. (a) Bright-field and (b) dark-filed TEM images of N-GQSs dispersed on p-SiNWs. (c) Selected area diffraction patterns (SAED) gives p-SiNWs are well etched toward [001] direction. GQS pattern is hardly observed due to the strong silicon lattice. [7.50]

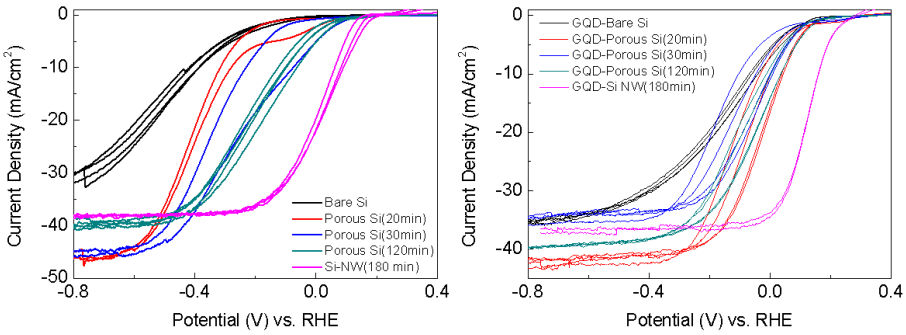

Figure 7.10. Photoelectrochemical performance of Si photocathode (a) Polarization curves of various Si electrodes without depositing any catalyst. Si nanowire were made by metal-catalyzed electroless method. Each of the etching time is 20 min, 30 min, 120 min, and 180 min. Each cyclic voltammetry was performed during 2 or 4 cycles at a scan rate of 5 mV/s. (b) Polarization curves of various Si electrodes deposited with N-GQSs catalyst.

7.50

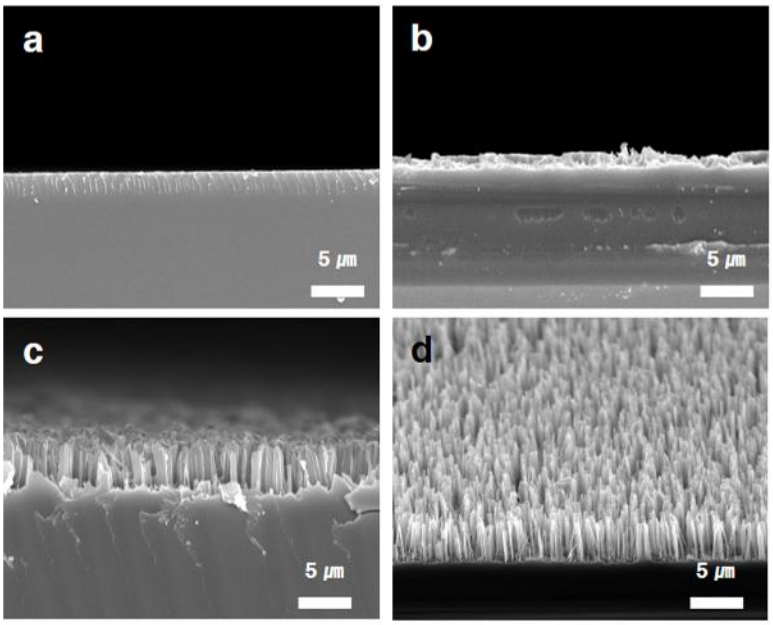

Figure 7.11. SEM images of cross-sectional views of p-type (100) Si wafers etched in 5 M HF and 0.015 M $AgNO_3$ solution at different etching times. The etching times are (a) 20 min, (b) 30 min, (c) 120 min, and (d) 180 min. [7.50]

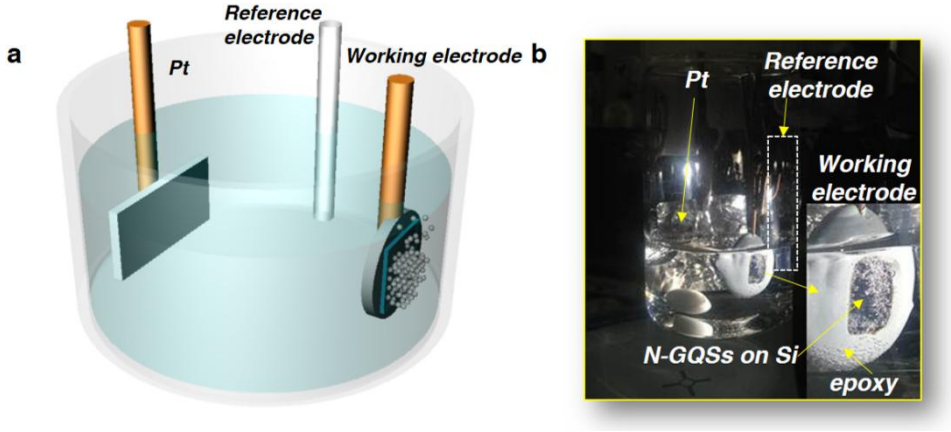

Figure 7.12. (a) Schematic illustration and (b) photograph images of hydrogen evolution reaction on N-GQSs/Si photocathode. [7.50]

Condition	**Electrode**	**Onset potential [E (V) at -1 mA/cm^2]**	**E (V) at -5 mA/cm^2**	**E (V) at -10 mA/cm^2**	**Current density at reversible potential vs. RHE [mA/cm^2 at 0 V vs. RHE]**	**ABPE$^{\#}$ (%)**
Under illumination (p type Si)	Planar Si	-0.17	-0.29	-0.42	0.34	0.02
	Si NW	0.17	0.12	0.09	21.61	0.91
	N-GQSs/ planar Si	0.13	0.03	-0.04	6.78	0.16
	N-GQSs/ Si NW	0.26	0.19	0.16	34.49	2.29
Under dark condition (n^+ type Si)	Planar Si	-0.63	-0.78	-0.85		
	Si NW	-0.42	-0.51	-0.56		
	N-GQSs/ planar Si	-0.44	-0.55	-0.62		
	N-GQSs/ Si NW	-0.37	-0.42	-0.45		
Photovoltage*	Planar Si	0.46				
	Si NW	0.59				
	N-GQSs/ planar Si	0.57				
	N-GQSs/ Si NW	0.63				
RDE analysis	Graphene/ GC	-0.20	-0.32	-0.37		
	N-GQSs/ GC	-0.11	-0.22	-0.25		

	Pt/GC	-0.02	-0.04	-0.05		

* The photovoltage is defined as the difference between the onset potential under the dark and illumination condition.

ABPE is the applied bias photon-to-current efficiency.

Table 7.1. Summary of the experimental data of Si and Glassy Carbon (GC) electrodes.

Catalyst	Synthesis and Loading method	Electrolyte	Activity			Ref. (Year)
			Onset Potential vs. RHE (V)	ABPE (%)	E (V) at -5 mA/cm^2	
Planar Si (our study)						
without catalyst (bare)		1M $HClO_4$	-0.17	0.02	-0.42	
Graphene (Gr)	CVD grown graphene & transfer	1M $HClO_4$	0.01	0.04	-0.21	
N-doped graphene quantum sheets (N-GQSs)	CVD grown graphene, plasma treatment, GQSs solution & drop casting	1M $HClO_4$	0.12	0.16	-0.04	
Pt	Nanoparticle by metal catalyzed electroless method	1M $HClO_4$	0.24	1.19	0.11	
Reduced graphene oxide (rGO)	Hummers` method & drop casting	1M $HClO_4$	-0.01	0.03	-0.20	
Si nanowire(our study)						
bare		1M $HClO_4$	0.15	0.91	0.13	
rGO	Hummers`	1M $HClO_4$	0.18	0.77	0.13	

	method & drop casting					
N-GQSs	CVD grown graphene, plasma treatment, GQSs solution & drop casting	1M $HClO_4$	0.26	2.29	0.19	
Pt	Nanoparticle by metal catalyzed electroless method	1M $HClO_4$	0.26	1.19	0.19	
Planar Si(Ref.)						
bare[1]		0.2 M potassium hydrogen phthalate (KHP) with 0.5 M K_2SO_4, buffered to pH 4.5 using KOH.	-0.29*	0.03	-0.423*	[7.12](2011)
Pt[1]	Nanoparticle by metal catalyzed electroless method		0.21*	1.1	0.15*	
rGO	Hummers` method & drop casting	H_2SO_4 solution containing 0.5 M K_2SO_4 (pH = 1.8)	-0.28*	~0*	-0.49*	[7.28](2013)
bare[2]		H_2SO_4 and	-0.42*	~0*	-0.55*	[7.17](20

Pt[2]	Nanoparticle by metal catalyzed electroless method	0.5 M K_2SO_4 (pH 1)	0.27*	~2.22*	0.2*	12)
Pt[3]	Nanoparticle by metal catalyzed electroless method	0.5 M aq. K_2SO_4 adjusted to pH ~ 2 using H_2SO_4	0.25*	2.1	0.2*	[7.49](2011)
bare[4]		1M $HClO_4$	-0.5*	~0*	-0.07*	[7.30](2011)
Mo_3S_4	Molecular cluster synthesis & drop casting		0.1*	~0.2*	0.04*	
bare[5]		0.5M H_2SO_4	-0.36*	~0*	-0.54*	[7.32](2011)
Si nanowire(Ref.)						
bare[1]		0.2 M KHP with 0.5 M K_2SO_4, buffered to pH 4.5 using KOH.	0.03	0	N/A	[7.12](2011)
Pt[1]	Nanoparticle by metal catalyzed electroless method		0.23*	1	0.16*	
bare[2]	Nanoparticle by metal catalyzed electroless method	H_2SO_4 and 0.5 M K_2SO_4 (pH 1)	~-0.16*	~0*	~-0.3*	[7.17](2012)
Pt[2]			~0.39*	~2.1*	~0.33*	
Pt[3]	Nanoparticle by metal	0.5 M aq. K_2SO_4	0.13*	0.21	0.04*	[7.49](2011)

	catalyzed electroless method	adjusted to pH ~ 2 using H_2SO_4				
bare[4]		1M $HClO_4$	-0.08*	~0*	-0.22*	[7.30](2011)
Mo_3S_4	Molecular cluster synthesis & drop casting		0.12*	~0.38*	0.08*	
rGO	Hummers` method & drop casting	H_2SO_4 solution containing 0.5 M K_2SO_4 (pH = 1.8)	0.12*	0.15*	-0.04*	[7.28](2013)

*: Values were measured and extrapolated by our group referring to the figures and data from the references.

The onset potential is defined as the potential at a photocurrent density of -1 mA/cm^2.

Table 7.2. Summary of the photoelectrochemical data of various catalysts on p-type Si electrodes.

Catalyst/Substrate (adhesive)	Loading method	Electrolyte	Activity			Ref. (Year)
			Tafel Slope (mV/dec)	Exchange current J_0 (A/cm^2)	Exchange current log(J_0) (A/cm^2)	
Our Study						
Monolayer Graphene	CVD grown graphene	1M $HClO_4$	74	2.7E-6	-5.57	
N-GQSs	CVD grown graphene and plasma treatment	1M $HClO_4$	45	7.1E-5	-4.15	
Pt	Annealing from mixed precursors	1M $HClO_4$	42	3.86E-4	-3.41	
Carbon based catalyst (Ref.)						
N doped Graphene	Annealing from mixed precursors	**0.5M H_2SO_4**	116	7.04E-8	-7.15	[7.23](2014)
P doped Graphene	Annealing from mixed precursors	0.5M H_2SO_4	133	8.97E-9	-8.05	[7.23](2014)
N, P doped Graphene	Annealing from mixed precursors	0.5M H_2SO_4	91	2.4E-7	-6.62	[7.23](2014)
graphitic-C_3N_4@N-graphene/glass	Exfoliation & Polycondensation	0.5M H_2SO_4	51.5	3.5E-7	-6.46	[7.24](2014)

y carbon (Nafion)						

Table 7.3 Summary of the electrochemical data of RDE system for various catalysts on GC electrodes.

Bibliography

7.1 J. A. Turner, *Science*, 2004, **305**, 972-974.

7.2. N. S. Lewis and D. G. Nocera, *Proceedings of the National Academy of Sciences*, 2006, **103**, 15729-15735.

7.3. M. G. Walter, E. L. Warren, J. R. McKone, S. W. Boettcher, Q. Mi, E. A. Santori and N. S. Lewis, *Chemical Reviews*, 2010, **110**, 6446-6473.

7.4. T. R. Cook, D. K. Dogutan, S. Y. Reece, Y. Surendranath, T. S. Teets and D. G. Nocera, *Chemical Reviews*, 2010, **110**, 6474-6502.

7.5. S. W. Boettcher, E. L. Warren, M. C. Putnam, E. A. Santori, D. Turner-Evans, M. D. Kelzenberg, M. G. Walter, J. R. McKone, B. S. Brunschwig, H. A. Atwater and N. S. Lewis, *Journal of the American Chemical Society*, 2011, **133**, 1216-1219.

7.6. U. Sim, H.-Y. Jeong, T.-Y. Yang and K. T. Nam, *Journal of Materials Chemistry A*, 2013, **1**, 5414-5422.

7.7. J. K. Nørskov, T. Bligaard, A. Logadottir, J. R. Kitchin, J. G. Chen, S. Pandelov and U. Stimming, *Journal of The Electrochemical Society*, 2005, **152**, J23-J26.

7.8. T. F. Jaramillo, J. Bonde, J. Zhang, B.-L. Ooi, K. Andersson, J. Ulstrup and I. Chorkendorff, *The Journal of Physical Chemistry C*, 2008, **112**, 17492-17498.

7.9. Y. Hou, A. B. Laursen, J. Zhang, G. Zhang, Y. Zhu, X. Wang, S. Dahl and I. Chorkendorff, *Angewandte Chemie International Edition*, 2013, **52**, 3621-3625.

7.10. Y. Yan, B. Xia, Z. Xu and X. Wang, *ACS Catalysis*, 2014, **4**, 1693-1705.

7.11. C. Chen, Y. Kang, Z. Huo, Z. Zhu, W. Huang, H. L. Xin, J. D. Snyder, D. Li, J. A. Herron, M. Mavrikakis, M. Chi, K. L. More, Y. Li, N. M. Markovic, G. A. Somorjai, P. Yang and V. R. Stamenkovic,

Science, 2014, **343**, 1339-1343.

7.12. J. R. McKone, E. L. Warren, M. J. Bierman, S. W. Boettcher, B. S. Brunschwig, N. S. Lewis and H. B. Gray, *Energy & Environmental Science*, 2011, **4**, 3573-3583.

7.13. B. Marsen, B. Cole and E. L. Miller, *Solar Energy Materials and Solar Cells*, 2008, **92**, 1054-1058.

7.14. M. W. Kanan, Y. Surendranath and D. G. Nocera, *Chemical Society Reviews*, 2009, **38**, 109-114.

7.15. A. Kudo and Y. Miseki, *Chemical Society Reviews*, 2009, **38**, 253-278.

7.16. J. Ran, J. Zhang, J. Yu, M. Jaroniec and S. Z. Qiao, *Chemical Society Reviews*, 2014, **43**, 7787-7812.

7.17. I. Oh, J. Kye and S. Hwang, *Nano Letters*, 2011, **12**, 298-302.

7.18. D. H. Youn, S. Han, J. Y. Kim, J. Y. Kim, H. Park, S. H. Choi and J. S. Lee, *ACS Nano*, 2014, **8**, 5164-5173.

7.19. R. K. Shervedani and A. Lasia, *Journal of The Electrochemical Society*, 1998, **145**, 2219-2225.

7.20. B. Cao, G. M. Veith, J. C. Neuefeind, R. R. Adzic and P. G. Khalifah, *Journal of the American Chemical Society*, 2013, **135**, 19186-19192.

7.21. S. Chen, J. Duan, Y. Tang, B. Jin and S. Zhang Qiao, *Nano Energy*, 2015, **11**, 11-18.

7.22. K. S. Novoselov, A. K. Geim, S. V. Morozov, D. Jiang, M. I. Katsnelson, I. V. Grigorieva, S. V. Dubonos and A. A. Firsov, *Nature*, 2005, **438**, 197-200.

7.23. Y. Zheng, Y. Jiao, L. H. Li, T. Xing, Y. Chen, M. Jaroniec and S. Z. Qiao, *ACS Nano*, 2014, **8**, 5290-5296.

7.24. Y. Zheng, Y. Jiao, Y. Zhu, L. H. Li, Y. Han, Y. Chen, A. Du, M. Jaroniec and S. Z. Qiao, *Nature Communication*, 2014, **5**.

7.25. Y. Liang, Y. Li, H. Wang, J. Zhou, J. Wang, T. Regier and H. Dai,

Nat Mater, 2011, **10**, 780-786.

7.26. J.-D. Qiu, G.-C. Wang, R.-P. Liang, X.-H. Xia and H.-W. Yu, *The Journal of Physical Chemistry C*, 2011, **115**, 15639-15645.

7.27. Q. Xiang, J. Yu and M. Jaroniec, *Chemical Society Reviews*, 2012, **41**, 782-796.

7.28. Z. Huang, P. Zhong, C. Wang, X. Zhang and C. Zhang, *ACS Applied Materials & Interfaces*, 2013, **5**, 1961-1966.

7.29. U. Sim, T.-Y. Yang, J. Moon, J. An, J. Hwang, J.-H. Seo, J. Lee, K. Y. Kim, J. Lee, S. Han, B. H. Hong and K. T. Nam, *Energy & Environmental Science*, 2013, **6**, 3658-3664.

7.30. Y. Hou, B. L. Abrams, P. C. K. Vesborg, M. E. Björketun, K. Herbst, L. Bech, A. M. Setti, C. D. Damsgaard, T. Pedersen, O. Hansen, J. Rossmeisl, S. Dahl, J. K. Nørskov and I. Chorkendorff, *Nat Mater*, 2011, **10**, 434-438.

7.31. Y. W. Chen, J. D. Prange, S. Dühnen, Y. Park, M. Gunji, C. E. D. Chidsey and P. C. McIntyre, *Nat Mater*, 2011, **10**, 539-544.

7.32. J. Oh, T. G. Deutsch, H.-C. Yuan and H. M. Branz, *Energy & Environmental Science*, 2011, **4**, 1690-1694.

7.33. B. M. Kayes, H. A. Atwater and N. S. Lewis, *Journal of Applied Physics*, 2005, **97**.

7.34. D. B. Williams, Carter, C. Barry, *Transmission Electron Microscopy*, Springer, 2009.

7.35. K. Peng, H. Fang, J. Hu, Y. Wu, J. Zhu, Y. Yan and S. Lee, *Chemistry – A European Journal*, 2006, **12**, 7942-7947.

7.36. E. Garnett and P. Yang, *Nano Letters*, 2010, **10**, 1082-1087.

7.37. L. Tsakalakos, J. Balch, J. Fronheiser, M.-Y. Shih, S. F. LeBoeuf, M. Pietrzykowski, P. J. Codella, B. A. Korevaar, O. V. Sulima, J. Rand, A. Davuluru and U. Rapol, *Nanophotonics*, 2007, **1**, 013552-013552-013510.

7.38. Z. Chen, T. F. Jaramillo, T. G. Deutsch, A. Kleiman-Shwarsctein, A. J. Forman, N. Gaillard, R. Garland, K. Takanabe, C. Heske, M. Sunkara, E. W. McFarland, K. Domen, E. L. Miller, J. A. Turner and H. N. Dinh, *Journal of Materials Research*, 2010, **25**, 3-16.

7.39. L. R. F. Allen J. Bard, John Wiley & Sons, Inc., 2001, **864**.

7.40. B. E. Conway and G. Jerkiewicz, *Electrochimica Acta*, 2000, **45**, 4075-4083.

7.41. Y. Fujimoto and S. Saito, *Journal of Applied Physics*, 2014, **115**, 153701-1-153701-5.

7.42. A. W. Bott, *Current Separations*, 1998, **17**, 87-91.

7.43. K. Gelderman, L. Lee and S. W. Donne, *Journal of Chemical Education*, 2007, **84**, 685.

7.44. N. S. Lewis, *Journal of The Electrochemical Society*, 1984, **131**, 2496-2503.

7.45. R. E. Hummel, *Electronic Properties of Materials*, Springer, 4th edn., 2011.

7.46. D. Merki, H. Vrubel, L. Rovelli, S. Fierro and X. Hu, *Chemical Science*, 2012, **3**, 2515-2525.

7.47. T. Lopes, L. Andrade, H. A. Ribeiro and A. Mendes, *International Journal of Hydrogen Energy*, 2010, **35**, 11601-11608.

7.48. J. Moon, J. An, U. Sim, S.-P. Cho, J. H. Kang, C. Chung, J.-H. Seo, J. Lee, K. T. Nam and B. H. Hong, *Advanced Materials*, 2014, **26**, 3501-3505.

7.49. S. W. Boettcher, E. L. Warren, M. C. Putnam, E. A. Santori, D. Turner-Evans, M. D. Kelzenberg, M. G. Walter, J. R. McKone, B. S. Brunschwig, H. A. Atwater and N. S. Lewis, *Journal of the American Chemical Society*, 2011, **133**, 1216-1219.

7.50. U. Sim, J. Moon, J. An, J. H. Kang, S. E. Jerng, J. Moon, S.-P. Cho, B. H. Hong and K. T. Nam, *Energy & Environ. Sci.*, 2015, **8**, 1329-

1338.

Part II. Model Study of Metal Active Sites: Synthetic bioinspired carbon-based catalyst

Chapter 8 Syntehtic Bioinpsired Carbon-based Catalyst

8.1. Introduction

Hydrogen energy has been drawing much attention in renewable energy technologies.[8.1] Especially, hydrogen production by water splitting reaction has been widely studied as environmental and sustainable energy source.[8.2, 8.3] Realization of cost-effective hydrogen production by water splitting requires electrolysis or photoelectrochemical cells decorated with highly efficient co-catalysts. In the race to replace previous noble metal catalyst, the design of carbon-based catalysts can represent an important research direction in the search for non-precious, environmentally benign, and corrosion resistant catalysts. Recently, we investigated graphene quantum sheets as an electrocatalyst for efficient HER and found that nitrogen doping and defects achieved through treatment with N_2 plasma improved the catalytic activity.[8.6] Nevertheless, previous carbon-based catalysts still have several disadvantages during synthesis. The bottleneck associated with previous carbon-based catalysts lies in the complicated and inefficient synthesis with multiple transfer process. For example, representative carbon based catalyst, CVD graphene as starting materials requires very delicate fabrication condition and high cost. Graphene-based materials also require multiple gas source with precise constrol of pressure, temperature, and quenching rate, and multiple transfer process after synthesis. In order to produce more efficient catalyst for HER, we should investigate the candidates which can be easily synthesized with inexpensive starting materials. Here, inspired by biomolecular system, we suggest biomimetic carbon-based nanosheet as a new hydrogen evolution catalyst for photoelectrochemical cell system inspired by biomolecular system. Source of carbon nanosheet can be polydopamine, which are adhesive

proteins secreted by marine mussels. Moreover, through a variety of chemical doping process, active sites for hydrogen evolution reaction in carbon nanosheet can be generated and these active sites can boost their catalytic activity with controllability. This significant enhancement achieved in this study emphasizes the new possibilities for the application of bioinspired materials as the hydrogen evolution reaction catalyst as well as molecular precursor approach.

8.2 Results and Discussion

Synthesis of carbon nanosheet from polydopamine was referred to the literature method and modified detail process to make active sites for hydrogen evolution reaction. SiO_2/Si target substrate was immersed in tris-(hydroxy-methyl) aminomethane solution (10 mM, pH 8.5) mixed with dopamine (2 mg). Then, polydopamine films were deposited on the surface of the target substrate. The thickness of the film could be controlled as a function of the immersion time. For carbonization, sample were then placed in a tube furnace for thermal treatment at elevated temperatures in a nitrogen atmosphere.

The observation of natural phenomena can be breakthrough for discovery of novel materials and pathway of innovative technology. Among the many biomimetic researches, surface coating process using by polydopamine which motivated by mussel adhesives proteins (MAPs) is suitable examples of this discovery.[8.23] Mussel can adhere to virtually all types of surfaces by secreting adhesives protein. Figure 8.1 (a) shows mussel attached to rock surface by secreting adhesive proteins (MAPs). MAPs are composed to several amino acids, which are abundant in 3,4-dihydroxy-L-phenylalanine (DOPA) and lysine as shown in Figure 8.1 (b). By oxidative polymerization leading to bulk solidification, DOPA and other catechol compound can covalently (or noncovalently) attached to diverse surface. Polydopamine has similar

structure with naturally occurring melanin (eumelanin) that incorporates many functional groups such as catechol, hydroxyl, amine and imine (Figure 8.1 (c)). Polydopamine film was obtained according to below procedure as shown in Figure 8.1 (d). First, Dopamine as monomer is added into an alkaline solution and oxidized with oxygen as oxidant without any complicated reactant or harsh condition. Oxidized dopamine immediately turns into quinone form which can be oligomer, and finally coated on substrate with dense polymer film. This hetero-aromatic polymer film can be controllably coated on several substrates in the thickness range of a few tens of nanometer depending on the immersion time. For the preparation of the N-doped carbon nanosheet, polydopamine coated substrate is pyrolyzed in tube furnace under H_2 and Ar atmosphere.

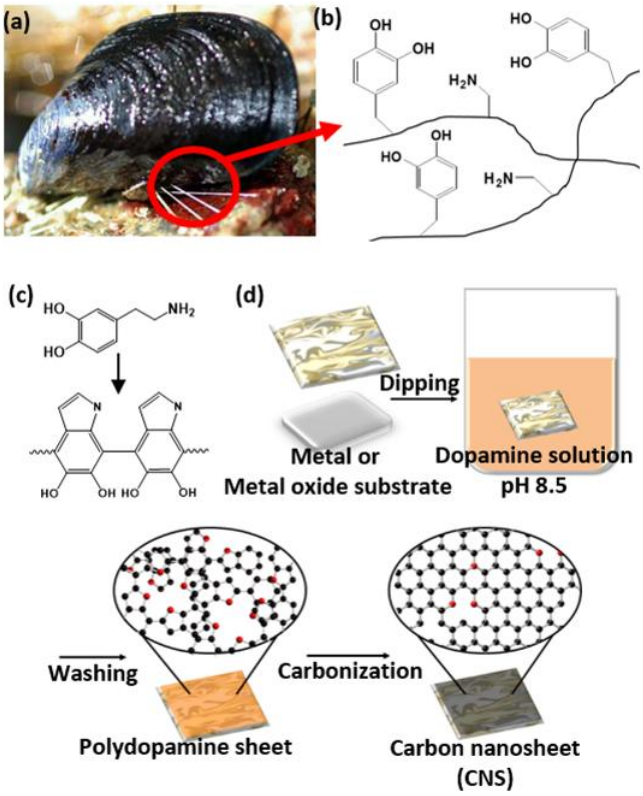

Figure 8.1. Schematic of a structure of polydopmaine and a synthetic process of carbon nanosheets. (a) Photograph of a marine mussel secreting adhesives protein. (b) Structural proposal of mussel adhesives protein (MAPs). (c) Schematic illustration of polydopamine as MAPs analogues by polymerization. (d) Schematic illustration of the synthetic process for carbon nanosheet from polydopamine

After carbonization of polydopamine film, the D peak (disordered carbon) was significantly increased in Raman spectra, the generation of defects and edges by the H_2/Ar treatment during annealing is also identified (Figure 8.2 (a)). The intensity ratio of D peak (1380 cm^{-1})/G peak (1600 cm^{-1}) (I_D/I_G ratio) indicates the extent of the carbonization, which is the extent of crystallization of sp2 phase.[8.22] Carbon nanosheet shows 0.97 of I_D/I_G ratio with both sharp peaks, while pristine polydopamine sample shows 0.69 of I_D/I_G ratio. This D-

to-G Peak intensity ratio (I_D/I_G) of carbon nanosheet indicated that polydopamine film successfully transforms into graphitic structure, which is similar with chemical structure of graphene.[8.24] Chemical structural analysis of polydopamine and carbon nanosheet is performed by measurement of X-ray photoelectron spectroscopy (Figure 8.2 (a)-(f)). The peak of C 1s, N 1s and O 1s, obtained on the polydopamine film were shown in Figure 8.2 (c) and 8.2 (e). Primary N (401.7 eV), secondary N (399.6 eV) and tertiary/aromatic N (398.2 eV) in N S1 spectrum of polydopamine indicate that nitrogen-to carbon ratio is ~11%. N S1 originated from polydopamine is dominated with secondary amine at 399.6 eV, and include low amount of tertiary or aromatic amine. Also, a large amount of hydroxyl functional group can be measure in C 1s. These functional groups such as hydroxyl, primary amine, and other dangling bonds have low stability in annealing condition. These unstable functional groups are converted to more stable conformation (secondary N or tertiary/aromatic N) or detached from polymer matrix. In case of carbon nanosheet, low oxygen contents and high aromatic amine were measured at N 1s and C 1s, it means that polydopamine is reduced and transformed into graphitic structure during heat treatment. As a result of thermal reduction, nitrogen-to-carbon ratio is ~6% in N_1 spectrum of carbon nanosheet.

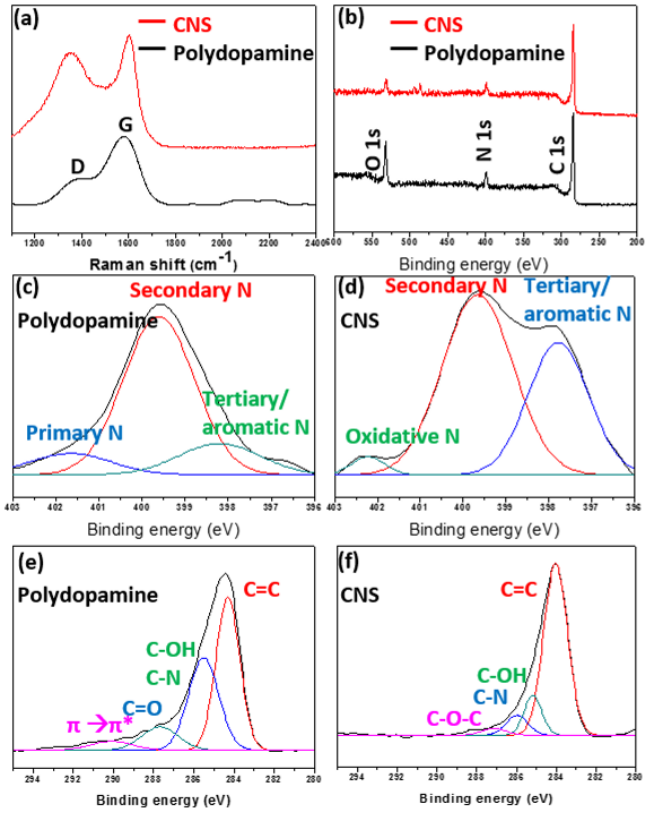

Figure 8.2. Surface characterization of the polydopamine and the carbon nanosheets (a) Raman spectra and (b) XPS spectra of polydopamine and carbon nanosheet. (c)-(d) High-resolution N1 peak of polydopamine and carbon nanosheet

To investigate surface analysis, AFM measurement is conducted. AFM images of polydopamine film shows 28 nm thickness and low RMS of nm on SiO_2/Si substrate, which is substantially uniform coating behavior (Figure 8.3 (a)). After carbonization, AFM images for the surface of carbon nanosheet show that the thickness of carbon nanosheet is approximately 10 nm with a relative smooth surface (Figure 8.3 (b)). Plenty of carbon aggregations are also shown on the sheet during annealing process (white islands in the image).

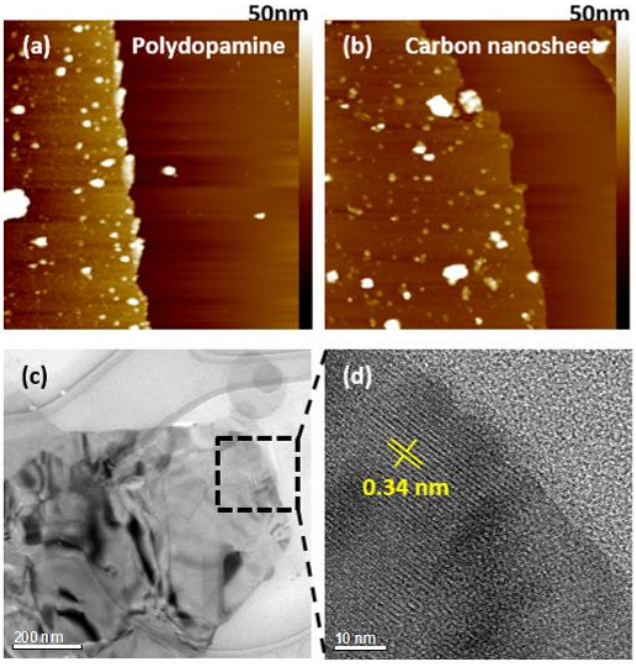

Figure 8.3. AFM images of (a) polydopamine, (b) carbon nanosheet. (c) and (d) TEM image of carbon nanosheet from pyrolysis of polydopamine.

For further characterization of atomic structure, TEM is measured (Figure 8.3 (c) and (d)). The sample was prepared by conventional CVD graphene transfer method on TEM grid. Figure 8.3 (a) shows TEM images of carbonized polydopamine nanosheet which was annealed at 800 ℃ for 1h in a heating rate of 10 ℃. The magnified image shows that carbonized film had clear atomic lattice structure and its layer distance was approximately 0.34 nm, which is distance between graphite stacking layers (Figure 8.3 (d)).[8.25]

To evaluate the photocathodic behavior of carbon nanosheet loaded on a p-type Si electrode (CNS-Si), a current density was measured as the potential was swept from 0.4 V to -1.0 V vs. Reversible Hydrogen Electrode (RHE) using cyclic voltammetry. As shown in Figure 8.1 (a), the current density of the bare Si increases gradually from -0.2 V vs. RHE and is saturated at

approximately -35 mA/cm^2 below -1.0 V, vs. RHE, as a potential is negatively applied. Interestingly, in the measurement of CNS-Si, the overall current density-potential (*J*-*E*) curve is shifted by approximately 0.2 V toward the positive potential. The onset potential (V_{os}) is defined as the potential at the photocurrent density of -1 mA/cm^2. As shown in Figure 8.4 (a), V_{os} is 0.21 V vs. RHE, and this V_{os} is a positive shift by 0.38 V compared to that of bare Si (-0.17 V vs. RHE). To our knowledge, the value of 0.29 V is the best among the extent of shifts by carbon-based catalysts. This result showed solar-to-hydrogen conversion efficiency of 0.59 %. Although reduced graphene oxide and carbon nanotube have been applied to silicon photoelectrodes as catalysts, the performances of these catalysts are not comparable to those of precious metal catalysts. [8.26] Additionally, for previously reported carbon-based catalysts, the insufficient activity remain unsolved. Our result showing the increase of V_{os} indicates that carbon nanosheet acts as an effective catalyst for HERs on the Si photocathode.

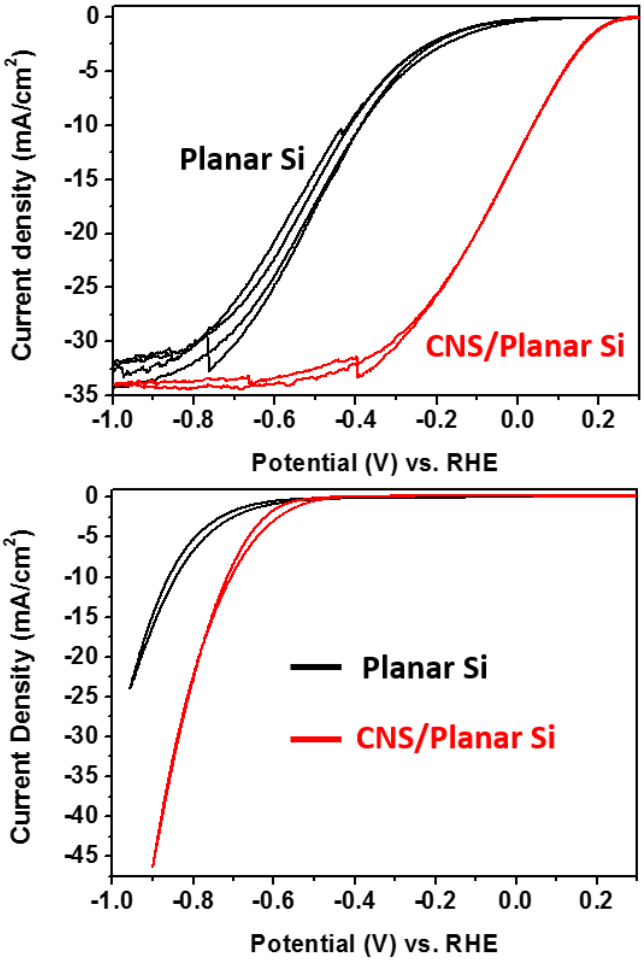

Figure 8.4. Cyclic Voltammetry (CV) of bare Si and carbon nanosheet (CNS) on a Si electrode. (a) Photocurrent density-potential (*J-E*) curves for the lightly boron doped p-Si electrode deposited with CNS and without any catalysts, respectively. (b) Polarization curves of bare and CNS on heavily arsenic doped n^+ type Si electrodes under dark condition. Each CV was performed at a scan rate of 0.05 V/sec.

To investigate the electrocatalytic activity of CNS, we measured cyclic voltammetry (CV) without illumination with a rotating disk electrode system (RDE). To fabricate the working electrode, CNS was transferred to a glassy

carbon tip that is inert in aqueous solution. An additional positive shift in the onset potential by CNS is also observed in the RDE measurements. As shown in Figure 8.5 (a), the potential to attain current density of -5 mA/cm^2 is -0.25 V vs. RHE; this value is 80 mV larger than that of the bare glassy carbon (-0.33 V vs. RHE). For comparison, representative carbon based catalyst, RDE of pristine graphene was also measured and carbon nanosheet shows 30 mV larger than that of the graphene material (-0.28 V vs. RHE, not shown here), which shows the catalytic activity of CNS is slightly better than that of monolayer graphene.[8.6]

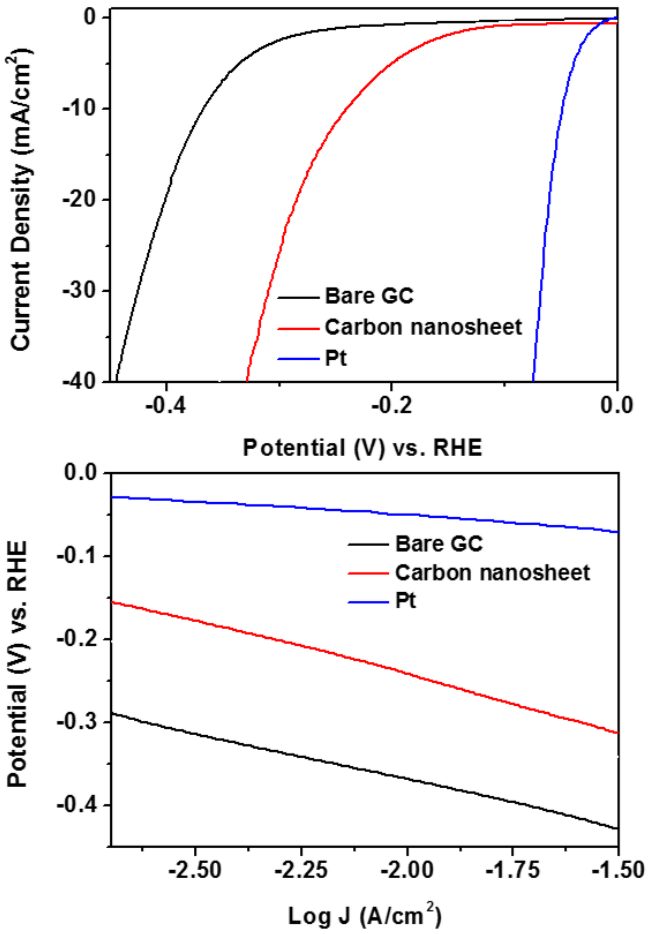

Figure 8.5. Electrochemical activity of carbon nanosheet (CNS) on Glassy Carbon (GC) electrode from rotating disk electrode system. (a) CV curve of bare, CNS, and Pt/C on GC. (b) Tafel plots were derived from (a) CV data.

The *J-E* curves in Figure 8.5 (a) is converted into a plot of the potential as a function of the logarithm of *J*, to quantitatively gain more insight into the catalytic activity of CNS. This plot is called a Tafel plot. The measured potentials are corrected for the ohmic potential drop losses that originated from the resistance of the interface between the substrate and the electrolyte. Analysing the impedance spectroscopy reveals that the resistances of the bare glassy carbon (GC) and CNS on GC are 13.0 and 13.2 ohm, respectively. The Tafel plot provides two parameters to estimate the electrocatalytic activity: the Tafel slope and the exchange current density. The Tafel slope is defined to be a measure of the potential increase required to increase the resulting current by 1 order of magnitude. [8.27] The bare GC shows a Tafel slope of 85 mV/decade, and CNS-GC exhibited a 7 mV/decade lower Tafel slope (78 mV/decade) than that of bare GC. For the comparison with the well-known catalyst, Pt particles were deposited on GC and the electro-catalytic activity was analysed. The applied potential to obtain -5 mA/cm^2 is -0.04 V vs. RHE, which is shifted positively by 0.24 V compared to that of CNS-GC. The Tafel slope of Pt-GC is 42 mV/decade, which is a 32 mV/decade lower than that of CNS-GC. The Tafel slope is an inherent property of the catalyst that is determined by the rate-limiting step for HER. Mechanistically, for the HER in acidic solution, the following possible reaction steps have been suggested: [8.28]

$$H_3O^+ + e^- \rightarrow H_{ads} + H_2O \qquad (8.1)$$

$$H_{ads} + H_3O^+ + e^- \rightarrow H_2 + H_2O \qquad (8.2)$$

$$H_{ads} + H_{ads} \rightarrow H_2 \qquad (8.3)$$

where H_{ads} is the adsorbed hydrogen atom. (8.1) is a discharge step (the Volmer reaction), (8.2) is a desorption step (the Heyrovsky reaction), and (8.3)

is a recombination step (the Tafel reaction). The value of the Tafel slope also relates to the adsorbed hydrogen coverage (θ_H) on the surface of electrode. If the recombination of adsorbed hydrogen (the Tafel reaction) is the rate-determining step for the HER and if the coverage is very high ($\theta_H \approx 1$), the measured Tafel slope is 30 mV/decade. However, if the electrochemical desorption step (the Heyrovsky reaction) is the rate-determining step, a Tafel slope of 118 ~ 40 mV/decade is measured and is dependent of the value of θH (0 ~ 1).[8.17] The observed Tafel slope of ~80 mV/decade in the current work indicates that the kinetics of the HER on bare GC and CNS-GC electrodes is determined by the Heyrovsky reaction because θ_H has an intermediate value. Specifically, HER using catalyst (Cat.) can be described as follows:[8.29]

Cat. + H^+ + e^- → H-Cat.,	Volmer reaction	(8.4)
2(H-Cat.) → H_2 + 2Cat.,	Tafel reaction	(8.5)
H-Cat. + H^+ + e^- → H_2 + Cat.,	Heyrovsky reaction	(8.6)

In the Volmer-Heyrovsky mechanism, the proton from the electrolyte solution is discharged on the catalyst surface to form an adsorbed hydrogen atom. This step is followed by combination with another proton and electron to form molecular hydrogen.

The improvement in the catalytic activity with CNS is also confirmed by the comparison of exchange current density in the Tafel plot. HER activity of the catalyst can be characterized by representative parameters; the exchange current density and the bond energy of hydrogen adsorbed to the catalyst. During hydrogen evolution, a current I can be described as:[8.30]

$$I = -e(r+ - r-) \qquad (8.7)$$

where, r+ - r- is the net rate of Eq. (8.7). The exchange current is the forward and backward rate when Eq. (8.7) is in equilibrium. The ability of a given metal to catalyze the hydrogen evolution reaction is usually measured by the exchange current density, which is the rate of hydrogen evolution per surface area at the electrode potential when the reaction is at equilibrium. The

exchange current density (J_0) is defined to be the current density at zero overpotential. The catalytic effect originates from improving the rate of charge transfer at the interface between the electrode and electrolyte or from lowering the activation energy barrier for a chemical reaction; these catalytic effects are represented by J_0. The higher J_0 indicates that electron transfer or the adsorption/desorption of protons at the electrode/electrolyte can occur more easily with a lower kinetic barrier. From the Tafel plot, J_0 can be obtained by extrapolating the plot in Figure 5b and extracting the current density at 0 V vs. RHE. The CNS-GC electrode shows an enhanced J_0 of 2.9×10^{-6} A/cm^2, which is higher than the J_0 of bare GC (1.63×10^{-6} A/cm^2). The J_0 of CNS is also compared with that of the monolayer graphene. J_0 of monolayer graphene is similar to exchange current density of CNS (2.7×10^{-6} A/cm^2). We are currently investigating to identify and quantify the active sites of CNS. From the Tafel analysis, CNS has the catalytic activity for the HER compared to that of the previous graphene based catalyst.

The passivation effect of CNS was also investigated. A chronoamperometray test of the bare Si and CNS-Si was also performed at 0 V vs. RHE (Figure 8.6 (a)) and the current densities normalized by their initial values were displayed as a function of time in Figure 8.6 (b). CNS-Si shows the suppressed degradation of the performance in the photocurrent density compared to that of the bare Si at pH 0 condition. The performance of the bare Si completely fails only after 1,000 sec. The CNS-Si electrode maintains more than 20% of the normalized current and -4 mA/cm^2 even at 6,000 sec. Thus, from the change of the current density at 0 V vs. RHE, it is known that CNS suppresses the degradation of the photoelectrochemical performance by the oxidation of Si surface.

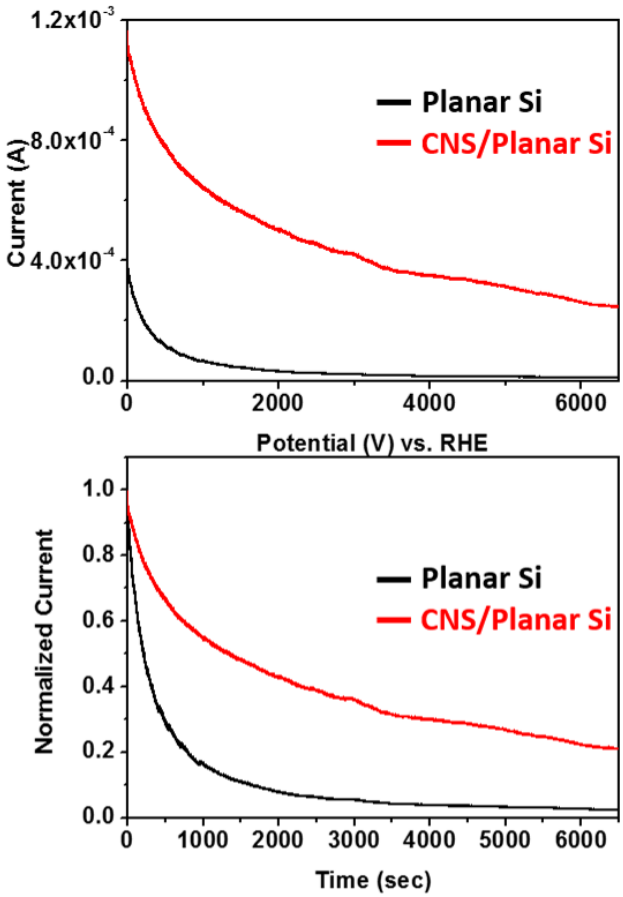

Figure 8.6. Chronoamperometry test of bare planar Si and CNS on Si photocathodes. (a) The change of photocurrent density at 0 V vs. RHE of bare planar Si (black line) and CNS-Si (red line) electrodes with the increase of time at 0. (b) The change of normalized photocurrent density (*J* divided by initial *J*) at 0 V vs. RHE with the increase of time at pH 0. The initial *J* is the initial current density in the chronoamperometry test.

To confirm the passivation effect of CNS on Si surface, the surface state of Si was investigated before and after the chronoamperometry test at 0 V vs. RHE for 6,000 sec. XPS spectra of bare Si and CNS-Si were measured in the Si $2p_{3/2}$ region. The Si peak can be assigned at 99.3 eV, and SiO_2 peak can be

assigned at 103.3 eV. From XPS spectra of bare Si, the peak of Si-O increases after the chronoamperometry test. In case of CNS-Si samples, after the long-term test, there is only slight increase in the Si-O peak. These results indicate that graphene suppresses the oxidation of Si surface during the photoelectrolysis.

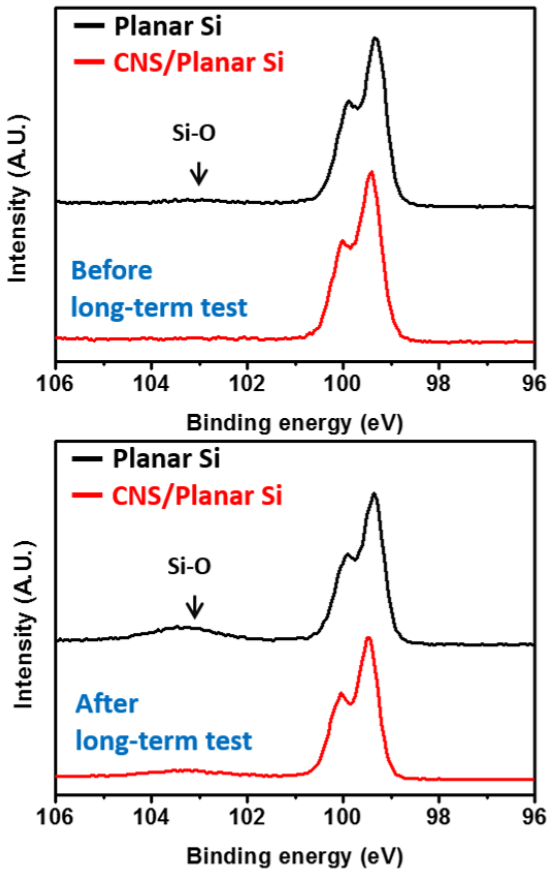

Figure 8.7. High resolution XPS spectra of Si 2p region of bare planar Si and CNS-Si electrodes. XPS spectra of each sample (a) before the chronoamperometry test and (b) after the chronoamperometry test at 0 V vs. RHE for 6,000 sec. Narrow-scan data of the Si 2p region were collected using pass energy of 40 eV and 0.05 eV/step.

8.3 Conclusion

We have presented carbon nanosheets as a catalyst for solar-driven hydrogen evolution reaction on Si photocathode. Carbon nanosheet has an excellent catalytic activity for photoelectrochemical cell. Our approach in this study exploits a strategy to develop metal-free carbon-based catalysts with high efficiency for solar-driven hydrogen fuel production.

Bibliography

8.1. Heller, A. Aharon-Shalom, E. Bonner, W. A. and Miller, B., Hydrogen-evolving semiconductor photocathodes: nature of the junction and function of the platinum group metal catalyst. *J. Am. Chem. Soc*. **104**, 6942-6948 (1982)

8.2. Hou, Y. Abrams, B. L. Vesborg, P. C. K. Björketun, M. E. Herbst, K. Bech, L. Setti, A. M. Damsgaard, C. D. Pedersen, T. Hansen, O. Rossmeisl, J. Dahl, S. Nørskov, J. K. and Chorkendorff, I., Bioinspired molecular co-catalysts bonded to a silicon photocathode for solar hydrogen evolution. *Nature Mater.* **10**, 434-438 (2011)

8.3. Reece, S. Y. Hamel, J. A. Sung, K. Jarvi, T. D. Esswein, A. J. Pijpers, J. J. H. and Nocera, D. G., Wireless Solar Water Splitting Using Silicon-Based Semiconductors and Earth-Abundant Catalysts. *Science* **334**, 645-648 (2011)

8.4. Li, Y. Wang, H. Xie, L. Liang, Y. Hong, G. and Dai, H., MoS2 nanoparticles grown on graphene: an advanced catalyst for the hydrogen evolution reaction. *J. Am. Chem. Soc*. **133**, 7296-7299 (2011)

8.5. Li, R. Parvez, K. Hinkel, F. Feng, X. and Mullen, K. Bioinspired wafer-scale production of highly stretchable carbon films for transparent conductive electrodes. *Angew. Chem. Int. Ed*. **52**, 5535–5538 (2013)

8.6. Sim, U.; Yang, T.-Y.; Moon, J.; An, J.; Hwang, J.; Seo, J.-H.; Lee, J.; Kim, K. Y.; Lee, J.; Han, S.; Hong, B. H.; Nam, K. T., N-doped monolayer graphene catalyst on silicon photocathode for hydrogen production. *Energy & Environmental Science* 2013, **6** (12), 3658-3664.

8.7. Fujishima, A.; Honda, K., Electrochemical photolysis of water at a

semiconductor electrode. *Nature* **238**, 37-38, (1972)

8.8. Maeda, K.; Domen, K., Photocatalytic water splitting: recent progress and future challenges. *J. Phys. Chem. Lett*. **1**, 2655-2661, (2010)

8.9. Kudo, A.; Miseki, Y., Heterogeneous photocatalyst materials for water splitting. *Chem. Soc. Rev*. **38**, 253-278, (2009)

8.10. Allam, N. K.; Poncheri, A. J.; El-Sayed, M. A., Vertically oriented Ti–Pd mixed oxynitride nanotube arrays for enhanced photoelectrochemical water Splitting. *ACS Nano* **5**, 5056-5066, (2011)

8.11. Yun, H. J.; Lee, H.; Kim, N. D.; Lee, D. M.; Yu, S.; Yi, J., A combination of two visible-light responsive photocatalysts for achieving the Z-Scheme in the solid state. *ACS Nano* **5**, 4084-4090, (2011)

8.12. Walter, M. G.; Warren, E. L.; McKone, J. R.; Boettcher, S. W.; Mi, Q.; Santori, E. A.; Lewis, N. S., Solar water splitting cells. *Chem. Rev.* **110**, 6446-6473, (2010)

8.13. Hou, Y.; Abrams, B. L.; Vesborg, P. C. K.; Björketun, M. E.; Herbst, K.; Bech, L.; Setti, A. M.; Damsgaard, C. D.; Pedersen, T.; Hansen, O.; Rossmeisl, J.; Dahl, S.; Nørskov, J. K.; Chorkendorff, I., Bioinspired molecular co-catalysts bonded to a silicon photocathode for solar hydrogen evolution. *Nat. Mater*. **10**, 434-438, (2011)

8.14. Chen, Y. W.; Prange, J. D.; Dühnen, S.; Park, Y.; Gunji, M.; Chidsey, C. E. D.; McIntyre, P. C., Atomic layer-deposited tunnel oxide stabilizes silicon photoanodes for water oxidation. *Nat. Mater.* **10**, 539-544, (2011)

8.15. Matsumura, M.; Roy Morrison, S., Anodic properties of n-Si and n-Ge electrodes in HF solution under illumination and in the dark. *J. Electroanal. Chem. and Inter. Electrochem*. **147**, 157-166, (1983)

8.16. Boettcher, S. W.; Warren, E. L.; Putnam, M. C.; Santori, E. A.; Turner-Evans, D.; Kelzenberg, M. D.; Walter, M. G.; McKone, J. R.; Brunschwig, B. S.; Atwater, H. A.; Lewis, N. S., Photoelectrochemical hydrogen evolution using Si microwire arrays. *J. Am. Chem. Soc*. **133**, 1216-1219, (2011)

8.17. Cook, T. R.; Dogutan, D. K.; Reece, S. Y.; Surendranath, Y.; Teets, T. S.; Nocera, D. G., Solar energy supply and storage for the legacy and nonlegacy worlds. *Chem. Rev*. **110**, 6474-6502, (2010)

8.18. Novoselov, K. S.; Geim, A. K.; Morozov, S. V.; Jiang, D.; Katsnelson, M. I.; Grigorieva, I. V.; Dubonos, S. V.; Firsov, A. A., Two-dimensional gas of massless Dirac fermions in graphene. *Nature* **438**, 197-200, (2005)

8.19. Liang, Y.; Li, Y.; Wang, H.; Zhou, J.; Wang, J.; Regier, T.; Dai, H., Co_3O_4 nanocrystals on graphene as a synergistic catalyst for oxygen reduction reaction. *Nat. Mater*. **10**, 780-786, (2011)

8.20. Qiu, J.-D.; Wang, G.-C.; Liang, R.-P.; Xia, X.-H.; Yu, H.-W., Controllable Deposition of platinum nanoparticles on graphene as an electrocatalyst for direct methanol fuel cells. *J. Phys. Chem. C* **115**, 15639-15645, (2011)

8.21. Xiang, Q.; Yu, J.; Jaroniec, M., Graphene-based semiconductor photocatalysts. *Chem. Soc. Rev*. **41**, 782-796, (2012)

8.22. Li, R.; Parvez, K.; Hinkel, F.; Feng, X.; Müllen, K., Bioinspired wafer-scale production of highly stretchable carbon films for transparent conductive electrodes. *Angew. Chem. Int. Ed*. **52**, 5535-5538, (2013)

8.23. Lee, H.; Dellatore, S. M.; Miller, W. M.; Messersmith, P. B., Mussel-inspired surface chemistry for multifunctional coatings. *Science*, **318**, 426-430, (2007)

8.24. Yu, X.; Fan, H.; Liu, Y.; Shi, Z.; Jin, Z., Characterization of

carbonized polydopamine nanoparticles suggests ordered supramolecular structure of polydopamine. *Langmuir* **30**, 5497-5505, (2014)

8.25. Huang, J. Y., HRTEM and EELS studies of defects structure and amorphous-like graphite induced by ball-milling. *Acta Materialia* **47**, 1801-1808, (1999)

8.26. Huang, Z.; Zhong, P.; Wang, C.; Zhang, X.; Zhang, C., Silicon nanowires/reduced graphene oxide composites for enhanced photoelectrochemical properties. *ACS Appl. Mater. & Inter*. **5**, 1961-1966, (2013)

8.27. Allen J. Bard, L. R. F., *Electrochemical methods: fundamentals and applications*. John Wiley & Sons, Inc. **864**, (2001)

8.28. Li, Y.; Wang, H.; Xie, L.; Liang, Y.; Hong, G.; Dai, H., MoS2 nanoparticles grown on graphene: an advanced catalyst for the hydrogen evolution reaction. *J. Am. Chem. Soc*. **133**, 7296-7299, (2011)

8.29. J. Larminie, A. Dicks, M. S. McDonald, *Fuel cell systems explained*, Vol. **2**, Wiley New York, 2003.

8.30. Nørskov, J. K.; Bligaard, T.; Logadottir, A.; Kitchin, J. R.; Chen, J. G.; Pandelov, S.; Stimming, U., Trends in the exchange current for hydrogen evolution. *J. Electrochem. Soc*. **152**, J23-J26, (2005)

Chapter 9 Biomimetic Iron Sulfur/Carbon-based Catalyst

9.1. Introduction

Development of sustainable energy sources is an urgent issue to meet growing demand in world energy consumption.[9.1] Among the various types of sustainable energy, hydrogen is the most promising renewable energy source with a high energy density. [9.2] The discovery of efficient catalysts represents one of the most important and challenging issues for the implementation of hydrogen production by electrolysis. [9.3] A critical requirement for outstanding electrocatalysts for water splitting is not only an ability to boost the kinetics of a chemical reaction but also a durability against electrochemical degradation. [9.4, 9.5] Generally, precious metals, such as platinum, exhibit superior performance in these requirements; however, high cost of the precious metal is the biggest barrier to widespread commercial use. [9.6, 9.7] To address this critical and long-standing technical barrier, many researches have focused on an intense search for efficient, durable, and inexpensive alternative catalysts. [9.8, 9.9]

Lessons from the biomolecular catalysts such as an enzyme or photosystem in nature provides clues to resolve the related kinetic issues. Biological systems, with their ability to create materials with precisely defined architecture in nanoscale, offer an unprecedented approach in dealing with this problem. For example, hydrogenase, which occurs in bacteria, archaea, and some eukarya, catalyzes a proton into HER with high activity very near the thermodynamic efficiency limit. [9.10] Functional protein assemblies surrounding a metal active site act as ligands for the metals, pockets for the

catalytic reaction, pathways for reactants and products, and transfer charge electron very effectively. Another example, in photosystem II of plant chloroplasts, manganese calcium clusters are stabilized and surrounded by specific peptides. [9.11, 9.12] These complexes exhibit unique electrochemical properties that is not achievable in synthetic manganese calcium crystals alone.

Up to now, researches have been conducted to enhance the hydrogen production efficiency using hydrogenase or hydrogenase inspired materials. For example, it is reported that [FeFe] hydrogenase is extracted from *Desulfovibrio desulfurcans (DdH)* directly and grafted to the electrode for the evaluation of hydrogen production. [9.13] Analysis of the specific structure of hydrogenase provides insight for the synthesis of an artificial hydrogenase using organometallic chemistry method. [9.14] Recently, synthesis of inorganic catalysts containing similar component from hydrogenase such as Fe and S has also been conducted. [9.15, 9.16] However, these approach has a disadvantage of low stability and relatively low property of hydrogen evolution.

The observation of natural phenomena can be breakthrough for discovery of novel materials and pathway of innovative technology. Among the many biomimetic researches, surface coating process using by polydopamine which motivated by mussel adhesives proteins (MAPs) is suitable examples of this discovery. [9.17] Mussel can adhere to virtually all types of surfaces by secreting adhesives protein. MAPs are composed to several amino acids, which are abundant in 3,4-dihydroxy-L-phenylalanine (DOPA) and lysine. By oxidative polymerization leading to bulk solidification, DOPA and other catechol compound can covalently (or noncovalently) attached to diverse surface. Polydopamine has similar structure with naturally occurring melanin (eumelanin) that incorporates many functional groups such as catechol, hydroxyl, amine and imine. For the preparation of the N-doped carbon nanosheet, polydopamine coated substrate is pyrolyzed in tube furnace under H_2 and Ar atmosphere. Inspired by natural biomolecular system, we have

designed enzyme-mimetic carbon-based catalyst for hydrogen evolution reaction and investigated the effect of each component with a systematic approach. Based on the understanding about the synthesis of the biomimetic carbon platform, earth-abundant metal active sites have been incorporated with high controllability and tunability, which results in a further decrease in kinetic overpotential. Annealing process after incorporation of iron and sulfur precursor shows the 3D porous structure of Fe_7S_8 with carbon platform. As a result, Fe_7S_8 with carbon platform catalyst exhibits superior electrocatalytic performance than those of any other reported iron sulfur-based catalyst. Moreover, Fe_7S_8 with carbon platform catalyst also shows both the good property and the long-term stability in the acid, the neutral, the base condition.

9.2 Results and Discussion

Fe_7S_8 with carbon platform catalyst is synthesized using following process. Dopamine (2 mg) is mixed in tris-(hydroxy-methyl) aminomethane solution (10 mM, pH 8.5). Dopamine as monomer is added into an alkaline solution and oxidized with oxygen as oxidant without any complicated reactant or harsh condition. Oxidized dopamine immediately turns into quinone form which can be oligomer, and finally self-aggregated as a porous 3D network structure or coated on substrate with dense polymer film. This hetero-aromatic polymer structure can be controllably chelated on several metal ion or attached on substrate in the thickness range of a few tens of nanometer depending on the immersion time. Iron precursor of $FeSO_4 \cdot 7H_2O$ (2 mM, 4 mM, 8 mM, 12 mM, or 16 mM) and $(NH_4)_2S_3$ (8.5 mM) were incorporated into dopamine solution, consequently. For carbonization, solution was dried then placed in a tube furnace for thermal treatment at elevated temperatures from 400 ^oC to 800 ^oC in a nitrogen atmosphere.

The surface characterization suggests that the synthesized catalyst is Fe_7S_8 with carbon platform. Fe_7S_8 nanoparticle is uniformly embedded onto a 3D

porous structure of carbonized polydopamine network by the SEM image when the annealing temperature is 600 ^{o}C as shown in Figure 9.1 (a). XRD analysis shows that the iron sulfur nanoparticle is the monoclinic pyrrhotite Fe_7S_8 structure (Figure 9.1 (b)) above the annealing temperature of 500 ^{o}C. Interestingly, with increasing temperature above 700 ^{o}C, characteristic peaks of hexagonal Fe_9S_{10} are appeared (Figure 9.6). The surface structure is also confirmed by TEM analysis (Figure 9.7) and the schematic of the crystal structure of monoclinic Fe_7S_8 is addressed in Figure 9.1 (c).

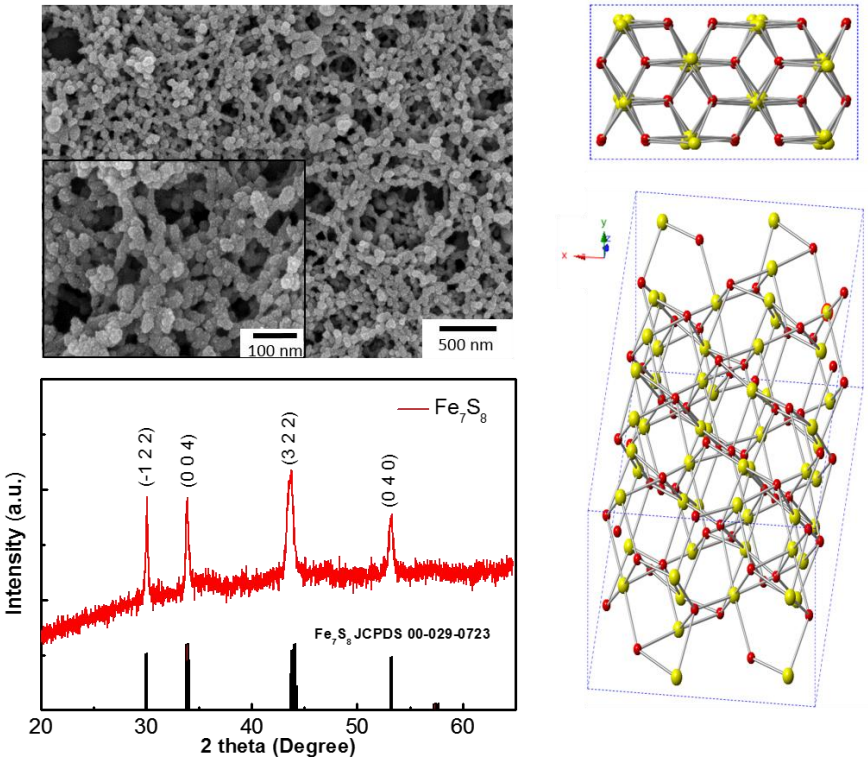

Figure 9.1. Surface characterization of Fe_7S_8 with carbon (Fe_7S_8/C) catalyst. (a) SEM image of Fe_7S_8/C. Inset is the magnified SEM image. (b) XRD result of Fe_7S_8/C annealed at 600 ^{o}C. (c) Schematic of monoclinic pyrrhotite of Fe_7S_8.

To investigate the electrocatalytic activity of the Fe_7S_8 with carbon platform (Fe_7S_8/C), cyclic voltammetry was measured using a rotating disk electrode (RDE) system in a three-electrode cell. As shown in Figure 9.2 (a), in the current density to potential curves (*J-E)* obtained by the RDE measurements, the current density associated with the hydrogen evolution reaction (HER) exponentially increases when the potential is swept from 0.15 V to -0.3 V vs. RHE at the pH 0 condition. When annealing temperature is increased from 400 ^{o}C to 800 ^{o}C, all samples show positive shifts of the overall current density-potential (*J-E*) photoresponse curve compared to that of bare glassy carbon (not shown here). Interestingly, the *J-E* curve of sample annealed at 600 ^{o}C shows the largest positive shift. The potential at -10 mA/cm^2 is -0.93 V vs. RHE, indicating a positive shift of 275 mV compared with bare GC (-0.368 V vs. RHE). Thereafter, the potential at -10 mA/cm^2 decreases with increasing annealing temperature (Figure 9.2 (a)). For the optimized catalytic property, the incorporation of the iron precursor was varied from 2 mM to 16 mM during synthesis with maintaining the annealing temperature of 600 ^{o}C and the sample in case of the incorporation of 8 mM showed the best catalytic activity for HER. For comparison, the RDE result of a bare Fe_7S_8 and Pt catalyst were also measured. The overpotential of Fe_7S_8/C is 170 mV higher than that of bare Fe_7S_8 without carbon platform. To our knowledge, the value is the lowest among iron sulfur-based catalysts reported up to date and is comparable to that of the best-performing metal-based catalysts (Table 9.1 and Figure 9.9). Moreover, Fe_7S_8/C catalyst is also highly active at the neutral and base condition as well as at the acid condition (Figure 9.9 (c)). The overpotential at -10 mA/cm^2 is 46 mV vs. RHE at the neutral condition (pH 7) and 106 mV vs. RHE at the base condition (pH 14), respectively. For comparison with the potential for the HER, the potential required to attain 10

mA/cm^2 of HER current density (overpotential at 10 mA/cm^2) is plotted with previous catalyst reported to date (Figure 9.9). A stability test also demonstrates the high stability of the Fe_7S_8/C catalyst. A chronoamperometry measurement was performed at -0.1 V vs. RHE and the current densities normalized by their initial values were displayed as a function of operation time as shown in Figure 9.2 (d). The Fe_7S_8/C catalyst maintains hydrogen evolution reaction stably even at 6,000 sec and more than 80 % of the normalized initial current in the acid and neutral condition, and more than 50 % of the normalized initial current at the base condition. This result indicates that the Fe_7S_8/C catalyst exhibit good stability as well as the efficient electrocatalytic activity toward the HER.

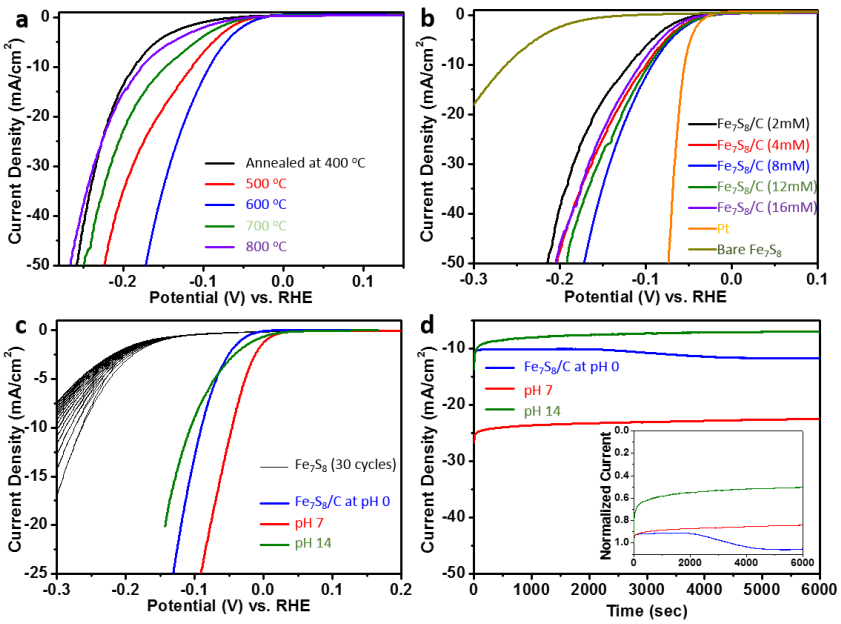

Figure 9.2. Electrochemical response of Fe_7S_8/C catalyst. (a) Current density-potential (*J-E*) curves of Fe_7S_8/C catalyst with increasing annealing temperature from 400 ^oC to 800 ^oC. (b) *J-E* curves of Fe_7S_8/C catalyst with increasing the injection of the molar ratio of Fe precursor from 2 mM to 16

mM. For comparison, Pt catalyst and bare Fe_7S_8 without carbon were plotted. (c) *J-E* curves of Fe_7S_8/C catalyst at the acid (pH 0), neutral (pH 7), base (pH 14) condition. *J-E* of bare Fe_7S_8 without carbon at the pH 0 gradually decreases during 30 cycles of cyclic voltammetry. (d) Chronoamperometry operation of Fe_7S_8/C catalyst at various pH condition. The change of photocurrent density at -0.1 V vs. RHE of Fe_7S_8/C catalyst at the pH 0 (blue line), pH 7 (red line), and pH 14 (green line) condition with increasing the operation time. Inset image is the change of normalized photocurrent density (J/J_{init}) at -0.1 V vs. RHE of each condition with increasing the operation time.

To evaluate the detailed hydrogen evolution reaction mechanism, pH dependency test was also performed in the pH range from pH 0 to pH 14 with increasing pH by 0.5 (Figure 9.3 (a)). From the pH dependency test, the partial derivative of potential with respect to pH, $\left(\frac{\partial E}{\partial pH}\right)_j$ is calculated as 60.3 mV/pH (Figure 9.3 (b)). And the average Tafel slope is 69.2 mV/dec and this is expressed as the partial derivative of potential with respect to log current density, $\left(\frac{\partial E}{\partial log j}\right)_{pH}$. The Tafel slope is an inherent property of the catalyst that is determined by the rate-limiting step for HER. Typically, Tafel slope of 60~80 mV/dec indicates proton-coupled one-electron transfer is involved prior to rate determining step and Tafel slope of 110~130 mV/dec suggests that single-electron transfer step is considered during HER. Proton activity dependence on current density could be derived as;[9.18]

$$\left(\frac{\partial E}{\partial pH}\right)_j = -\left(\frac{\partial log j}{\partial pH}\right)_E \left(\frac{\partial E}{\partial log j}\right)_{pH} \qquad (1)$$

Substituting the value of $\left(\frac{\partial \mathrm{E}}{\partial \mathrm{pH}}\right)_j$ and the Tafel slope $\left(\frac{\partial E}{\partial log j}\right)_{pH}$ into the partial differential equation (1) results in $\left(\frac{\partial log j}{\partial pH}\right)_E$ = 0.87, which indicates that the

reaction rate follows a nearly first-order dependence on the proton activity. As a result, the electrochemical law of Fe_7S_8/C catalyst is follow as; [9.18]

$$i = k_0(a_{H^+})^{0.87} e^{\frac{0.85EF}{RT}} \qquad (2)$$

where, k_0, a_{H+}, *and* F are potential-independent constant, proton-activity and Faraday constant, respectively. Although the whole HER catalysis process was not fully verified yet, it can be conjectured that one electron and one proton are involved prior to rate determining step.

To investigate the origin of the change in the catalytic activity, electrochemical impedance measurements were also performed. Figure 9.3 (d) shows a Nyquist plot representing a typical impedance result with only one semicircle. The one semicircle indicates that the equivalent circuit for the electrocatalysis is characterized by one time constant. Compared with the bare Fe_7S_8 (733 Ωcm^2), Fe_7S_8/C shows a much smaller semicircle, which corresponds to lower charge-transfer resistance (33.2 Ωcm^2 at pH 0, 24.8 Ωcm^2 at pH 7, 37.5 Ωcm^2 at pH 14, respectively). The charge-transfer resistance is related to a kinetic barrier energy for the faradaic reactions (HER) across the interface between catalysts and the electrolyte.[9.19] The charge-transfer resistance is also inversely proportional to the exchange current for the faradaic reaction, as described by the Butler-Volmer equation.[9.20] The Fe_7S_8/C with a lower charge-transfer resistance promotes the HER, which is related to relatively low charge transfer resistance, thus enhancing HER with a lower overpotential. Thus, impedance analysis also proves the enhanced catalytic property of the Fe_7S_8/C combined with the above-mentioned mechanism from Tafel analysis.

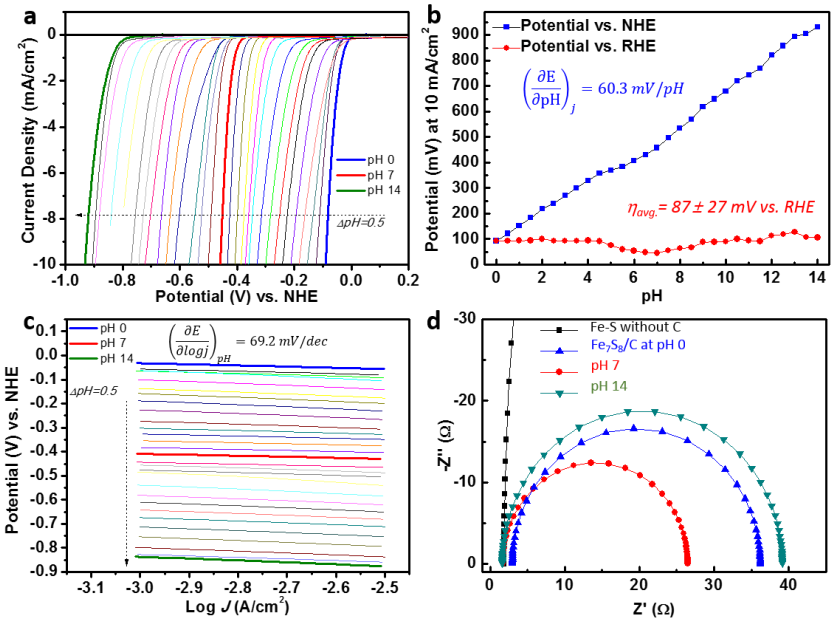

Figure 9.3. Detailed hydrogen evolution mechanism of Fe_7S_8/C catalyst. (a) *J-E* curves of Fe_7S_8/C catalyst with increasing pH condition of electrolyte from pH 0 to pH 14 by 0.5. (b) Potential vs. NHE (blue line) and a potential vs. RHE (red line) at -10 mAcm^2 of the Fe_7S_8/C catalyst with increasing the pH value. Linearly fitted $\left(\frac{\partial E}{\partial pH}\right)_j$ is calculated as 60.3 mVpH and the average overpotential to attain -10 mA/cm^2 is estimated as 87± 27 mV vs. RHE. (c) Tafel plots derived from *J-E* data. The average Tafel plot, $\left(\frac{\partial E}{\partial logj}\right)_{pH}$ is estimated as 69.2 mV/dec. (d) Impedance result of the Fe_7S_8/C catalyst. Nyquist plot of Fe_7S_8/C catalyst at the pH 0, pH 7, and pH 14 condition at a constant potential of -0.1 V vs. RHE. For comparison, bare Fe_7S_8 without carbon is also measured.

Continuous wave electron paramagnetic resonance (CW-EPR) spectra was measured to check the stability of Fe valency state during hydrogen evo lution reaction (Figure 9.4). The g-value can be calculated using following equation of $h\nu = g\beta B$ and thus, g=71.4484ν/B (mT). ν is 9.64 GHz for X band perpendicular mode.[21] At the resting state, Fe^{3+} and carbon radical signal were detected at the g-value of 4.24 and 2.00, respectively. After the bulk electrolysis at the potential of -0.5 V vs. RHE, Fe^{1+} signal was detected at the g-value of 2.082 in the vicinity of carbon radical signal, while the Fe^{3+} signal was decreased. And the carbon radical signal was also increased. This suggests that iron species involves during hydrogen evolution reaction and the iron valency changes from 3^+ to 1^+ with the low spin state because of the relatively high difference between e_g and t_{2g} energy level (Figure 9.4 (b)). This result is also similar to the hydrogen evolution by natural hydrogenase. It is known that carbonyl group or cyanide group adjacent to iron active sites also induces for iron species to make low valency with the low spin state and this effect promotes the efficient hydrogen evolution.

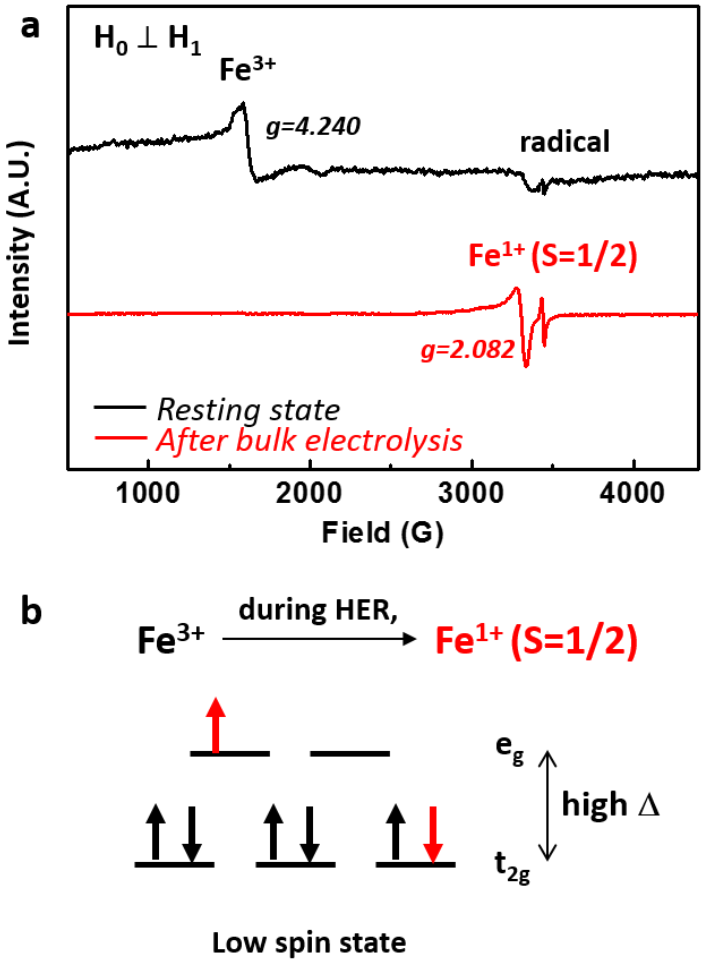

Figure 9.4. Fe valency change during hydrogen evolution reaction. (a) Perpendicular mode continuous wave electron paramagnetic resonance (CW-EPR) spectra at the resting state and after bulk electrolysis at the potential of -0.1 V vs. RHE for 5 min. (b) Schematic of the change in Fe spin state during hydrogen evolution reaction.

9.3 Conclusion

We have designed the bio-mimetic iron sulfur/carbon-based catalysts with enhanced HER property and long-term stability at the acid, the neutral, and the base condition. This significant enhancement achieved in this study emphasizes the strategies for the application of bioinspired materials as the hydrogen evolution reaction catalyst. Our bioinspired catalysts paradigm can revolutionize the catalyst materials that have traditionally made by alloying inorganic metal composite or have had little interest in surrounding carbon platform, opening the way to the design of atomic-scale controlled catalysts, materials inspired from biomolecular precursor approach, and learning design rules for interfacing semiconductor and catalysts.

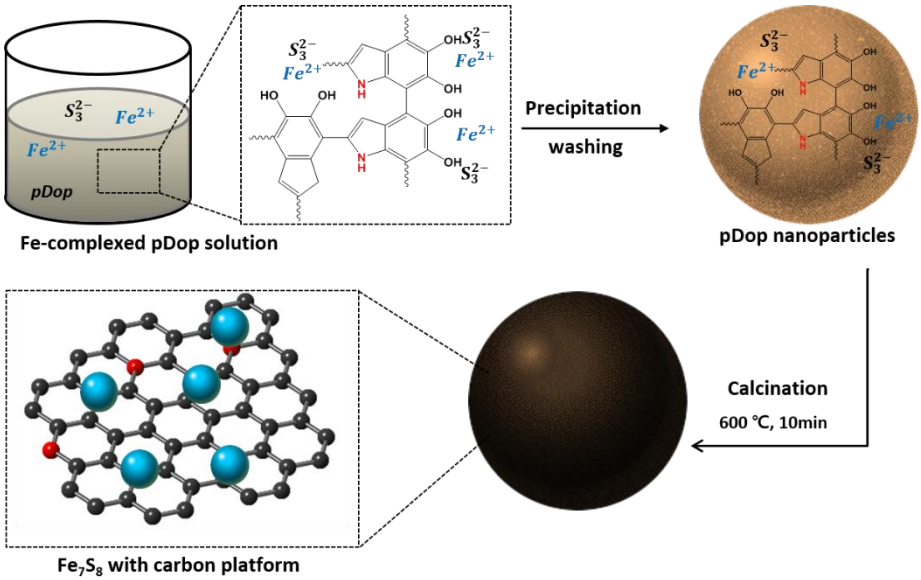

Figure 9.5. Schematic of the synthesis process of Fe_7S_8 with carbon platform.

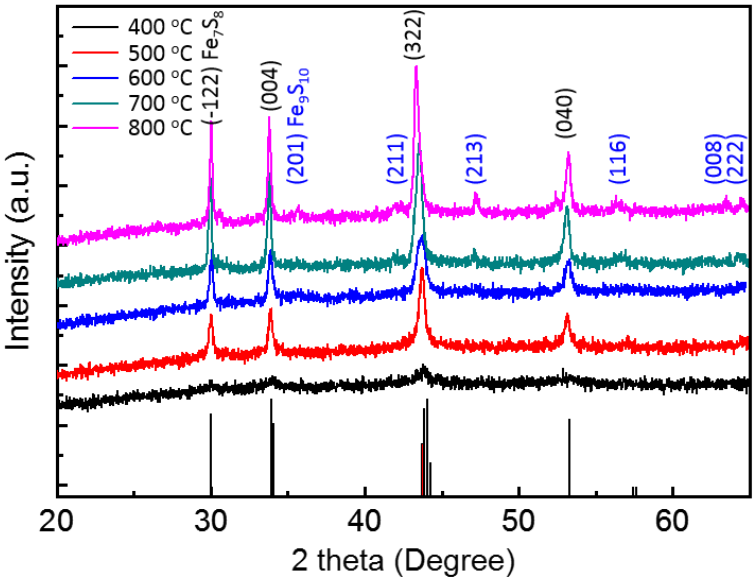

Figure 9.6. XRD analysis of Fe_7S_8 with carbon platform with increasing temperature from 400 ^oC to 800 ^oC.

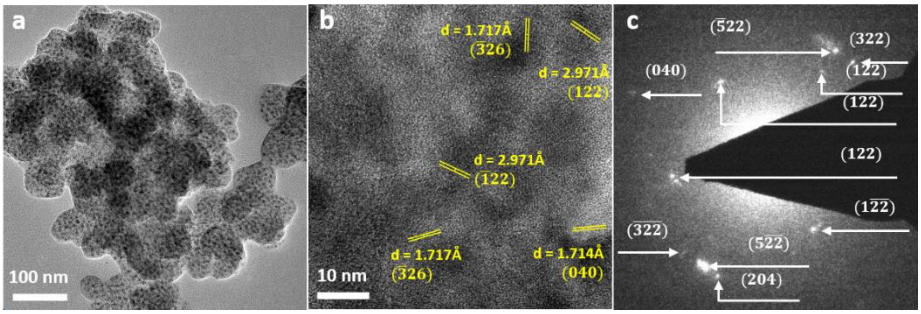

Figure 9.7. Structure of Fe_7S_8/pDop catalyst. (a)-(b) High-resolution of TEM images of Fe_7S_8/C catalyst. Fe_7S_8 is embedded carbon nanosheets. (c) The selective area electron diffraction (SAED) of Fe_7S_8/C catalyst.

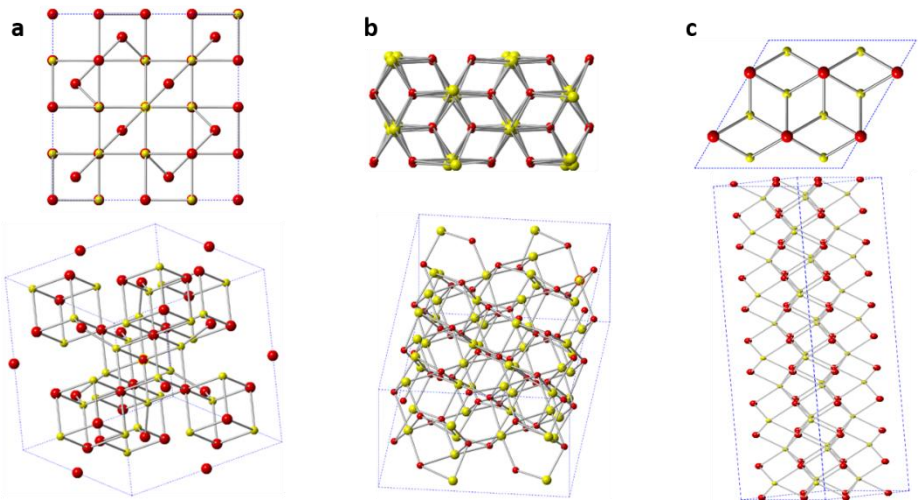

Figure 9.8. Top view and 3D view of representative iron sulfur structure.(a) Isometric hexoctahedral Fe_3S_4 (Greigite). (b) Monoclinic Fe_7S_8 (Pyrrhotite) (c) Hexagonal Fe_9S_{10} (Pyrrhotite).

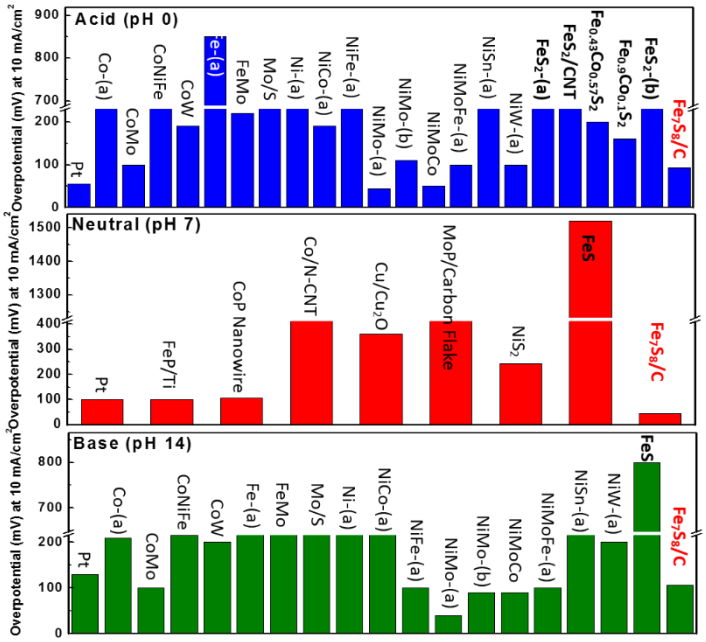

Figure 9.9. Overpotential to attain 10 mA/cm^2 of various hydrogen evolution reaction catalysts at the acid, the neutral, and the base condition.

Catalyst (Electrode)	Synthesis method	Electrolyte	Onset Potential vs. RHE (V) at -1 mA/cm^2	Potential (V) at -10 mA/cm^2	Tafel Slope (mV/dec)	Exchange Current density (A/cm^2)	Ref. (Year)
FeS_2 (GC)	Thermal vapor sulfurization	0.5M H_2SO_4	-0.21*	-0.26*	68.3	9.1x10^{-7}	[1](2013)
$Fe_{0.43}Co_{0.57}S_2$ (GC)			-0.155*	-0.2*	59.1	5.1x10^{-8}	
FeS (GC)	Solvothermal synthesis	0.1M K_3PO_4 (pH 7)	-0.67	-	150	6.6 x10^{-7}	[2](2014)
FeS_2/CNT (GC)	Solvothermal synthesis	0.5M H_2SO_4	-0.165*	-0.23*	65*	1.95x10^{-6}*	[3](2015)
$Fe_{0.95}Co_{0.05}S_2$/CNT (GC)			-0.12*	-0.175*	55*	6.58x10^{-6}*	
$Fe_{0.9}Co_{0.1}S_2$/CNT (GC)			-0.1*	-0.16*	46	5.01x10^{-6}*	
$Fe_{0.66}Co_{0.34}S_2$/CNT (GC)			-0.15*	-0.22*	70*	7.20x10^{-6}*	
$Fe_{0.37}Co_{0.63}S_2$/CNT (GC)			-0.15*	-0.225*	75*	1.00x10^{-5}*	
FeS_2 (GC)	Thermal vapor sulfurization	0.5M H_2SO_4	-0.217	-	56.4	1.44x10^{-7}	[4](2014)
$(Fe_{0.07}Ni_{0.93})S_2$(GC)			-0.196	-	58.7	4.469x10^{-8}	
$Fe_{0.48}Co_{0.52}S_2$ (GC)			-0.143	-0.196	47.5	9.59x10^{-7}	
Fe_7S_8/pDop (CFP)	Thermal annealing	0.5M H_2SO_4	-0.041	-0.093	63.6	3.67x10^{-4}	Our Study
		1M PBS	-0.056	-0.140	62.1	1.33x10^{-4}	

*: Values were measured and extrapolated by our group referring to the figures and data from the references.

Table 9.1. Summary of the electrochemical data of various catalysts on hydrogen evolution reaction electrodes

Bibliography

9.1. N. S. Lewis and D. G. Nocera, *Proceedings of the National Academy of Sciences*, 2006, **103**, 15729-15735.

9.2. J. A. Turner, *Science*, 2004, **305**, 972-974.

9.3. T. R. Cook, D. K. Dogutan, S. Y. Reece, Y. Surendranath, T. S. Teets and D. G. Nocera, *Chemical Reviews*, 2010, **110**, 6474-6502.

9.4. U. Sim, T.-Y. Yang, J. Moon, J. An, J. Hwang, J.-H. Seo, J. Lee, K. Y. Kim, J. Lee, S. Han, B. H. Hong and K. T. Nam, *Energy & Environmental Science*, 2013, **6**, 3658-3664.

9.5. U. Sim, J. Moon, J. An, J. H. Kang, S. E. Jerng, J. Moon, S.-P. Cho, B. H. Hong and K. T. Nam, *Energy & Environmental Science*, 2015, **8**, 1329-1338.

9.6. I. Oh, J. Kye and S. Hwang, *Nano Letters*, 2011, **12**, 298-302.

9.7. U. Sim, H.-Y. Jeong, T.-Y. Yang and K. T. Nam, *Journal of Materials Chemistry A*, 2013, **1**, 5414-5422.

9.8. A. Kudo and Y. Miseki, *Chemical Society Reviews*, 2009, **38**, 253-278.

9.9. U. Sim, K. Jin, S. Oh, D. Jeong, J. Moon, J. Oh and K. T. Nam, in *Handbook of Clean Energy Systems*, John Wiley & Sons, Ltd, 2015, DOI: 10.1002/9781118991978.hces223.

9.10. W. Lubitz, H. Ogata, O. Rüdiger and E. Reijerse, *Chemical Reviews*, 2014, **114**, 4081-4148.

9.11. J. Barber, *Chemical Society Reviews*, 2009, **38**, 185-196.

9.12. J. Yano, J. Kern, K. Sauer, M. J. Latimer, Y. Pushkar, J. Biesiadka, B. Loll, W. Saenger, J. Messinger, A. Zouni and V. K. Yachandra, *Science*, 2006, **314**, 821-825.

9.13. A. Adamska, A. Silakov, C. Lambertz, O. Rüdiger, T. Happe, E. Reijerse and W. Lubitz, *Angewandte Chemie International Edition*, 2012, **51**, 11458-11462.

9.14. G. Berggren, A. Adamska, C. Lambertz, T. R. Simmons, J. Esselborn, M. Atta, S. Gambarelli, J. M. Mouesca, E. Reijerse, W. Lubitz, T. Happe, V. Artero and M. Fontecave, *Nature*, 2013, **499**, 66-69.

9.15. C. Di Giovanni, W.-A. Wang, S. Nowak, J.-M. Grenèche, H. Lecoq, L. Mouton, M. Giraud and C. Tard, *ACS Catalysis*, 2014, **4**, 681-687.

9.16. D.-Y. Wang, M. Gong, H.-L. Chou, C.-J. Pan, H.-A. Chen, Y. Wu, M.-C. Lin, M. Guan, J. Yang, C.-W. Chen, Y.-L. Wang, B.-J. Hwang, C.-C. Chen and H. Dai, *Journal of the American Chemical Society*, 2015, **137**, 1587-1592.

9.17. H. Lee, S. M. Dellatore, W. M. Miller and P. B. Messersmith, *Science*, 2007, **318**, 426-430.

9.18. Y. Surendranath, M. W. Kanan and D. G. Nocera, *Journal of the American Chemical Society*, 2010, **132**, 16501-16509.

9.19. D. Merki, H. Vrubel, L. Rovelli, S. Fierro and X. Hu, *Chemical Science*, 2012, **3**, 2515-2525.

9.20. L. R. F. Allen J. Bard, *John Wiley & Sons, Inc.*, 2001, 864.

9.21. D. M. Murphy, *Journal of Chemical Technology & Biotechnology*, 2004, **79**, 103-103.

Chapter 10. Concluding remarks

Development of sustainable energy sources is an urgent issue to meet growing demand in world energy consumption. Among the various types of sustainable energy, hydrogen is the most promising renewable energy source with a high energy density. The discovery of efficient catalysts represents one of the most important and challenging issues for the implementation of photoelectrochemical (PEC) hydrogen production. A critical requirement for outstanding catalysts in a PEC cell is not only an ability to boost the kinetics of a chemical reaction but also a durability against electrochemical and photo-induced degradation. Generally, precious metals, such as platinum, exhibit superior performance in these requirements; however, high cost of the precious metal is the biggest barrier to widespread commercial use. To address this critical and long-standing technical barrier, I have focused on an intense search for efficient, durable, and inexpensive alternative catalysts. My research have been concentrated on four subjects; (1) new possibilities of an atomic-scale catalyst as the efficient hydrogen evolution reaction (HER) catalyst, (2) interface control between electrode and catalysts for lower activation energies and higher current density, (3) new type of the enzyme-mimetic carbon-based catalyst for greener and more environmentally benign approach, (4) the application to the co-catalysts for the PEC cell with high efficiency and long-term stability. I pioneered the field of the graphene-based catalyst for HER in PEC cell that have never been made before. Inspired by biomolecular approach, we also have made a breakthrough in the limit of recent photo-to-current efficiency through the incorporation of a non-noble transition metal into carbon-based catalysts.

Carbon-based nanomaterials have emerged as promising candidate catalyst for HER. The design of carbon-based catalysts represent an important

research direction in the search for non-precious, environmentally benign, and corrosion resistant catalysts. Especially, graphene possesses excellent transmittance and superior intrinsic carrier mobility, thus there have been several attempts to use graphene as a catalyst. It has been reported that reduced graphene oxide containing catalytic active materials exhibited improved activity in HER, oxygen evolution reactions, and oxygen reduction reactions. In most cases, the role of carbon materials is limited to an electrical conducting substrate or a supporter that enhances the performance of other decorated active catalysts. There is no report of the application of monolayer graphene to hydrogen production. For the first time, I investigated new possibilities for monolayer graphene as an electrocatalyst for efficient HER and found that atomic defect engineering such as nitrogen doping through treatment with N2 plasma improved the catalytic activity. This study has also attracted particular interest to the materials and chemical society in that it has demonstrated the role of carbon-based catalysts with comprehensive electrochemical analysis as well as the first demonstration of monolayer graphene as the HER catalyst.

The understanding of the correlated interaction between solid catalysts/electrode and liquid electrolyte during HER operation is also very important for efficient hydrogen production. However, few researches have been conducted before to study the interface between carbon catalysts/semiconductor electrode and aqueous solution. In the present work, I have explored to develop an enabling technology and design rules for the efficient and durable catalyst/electrode system. Moreover, as an intermediate stage of extension from the single 2D platform to a complicate 3D structure, I have transferred multi-layer graphene as a well-defined model of the atomically-defined pseudo-3D system and investigated the layer dependence of catalytic activity. Comprehensive electrochemical analysis shows that the double-layer graphene exhibits the best catalytic activity and the highest

charge transfer rate among carbon-based catalysts reported to date. Based on the in-depth electrochemical and electrical analysis, the band structure of the graphene/silicon semiconductor shows much smaller work function than that of bare electrode, which accelerates electron to hydrogen production potential for enhanced catalytic activity.

Lessons from the biomolecular catalysts such as an enzyme or photosystem in nature provides clues to resolve the related kinetic issues. Biological systems, with their ability to create materials with precisely defined architecture in nanoscale, offer an unprecedented approach in dealing with this problem. For example, hydrogenase, which occurs in bacteria, archaea, and some eukarya, catalyzes a proton into HER with high activity very near the thermodynamic efficiency limit. Functional protein assemblies surrounding a metal active site act as ligands for the metals, pockets for the catalytic reaction, and pathways for reactants and products. Another example, in photosystem II of plant chloroplasts, manganese calcium clusters are stabilized and surrounded by specific peptides. These complexes exhibit unique electrochemical properties that is not achievable in synthetic manganese calcium crystals alone. Inspired by biomolecular system, I have designed enzyme-mimetic carbon-based catalyst for HER and investigated the effect of each component with a systematic approach. Carbon nanosheet is synthesized by polydopamine, which are natural adhesive proteins secreted by marine mussels. Based on the understanding about the synthesis of the biomimetic carbon platform, earth-abundant metal active sites have been incorporated with high controllability and tunability, which results in a further decrease in kinetic overpotential. Fe-doped carbon nanosheet exhibits better photoelectrochemical performance in terms of the applied bias photon-to-current efficiency than those of any other reported non-noble metal-based catalyst/p-Si system. This significant enhancement achieved in this study emphasizes the strategies for the application of bioinspired materials as the

HER catalyst. My bioinspired catalysts paradigm can revolutionize the catalyst materials that have traditionally made by alloying inorganic metal composite or have had little interest in surrounding carbon platform, opening the way to the design of atomic-scale controlled catalysts, materials inspired from biomolecular precursor approach, and learning design rules for interfacing semiconductor and catalysts.

My synthetic bioinspired HER catalyst is also highly transparent and is applicable to the co-catalyst for the PEC cell. The results indicate the applied bias photon-to-current efficiency of 2.29%, which is higher than any other carbon-based PEC catalysts reported to date. In PEC cell system, negative effects from metal-based catalysts should be considered: reflection by the overlaid catalyst, an unfavorable band structure such as a Schottky barrier, photocorrosion, and recombination sites at the interface. To design catalysts for PEC water splitting, the optical properties, stability, and interfacial issues must be comprehensively considered. Silicon, the most promising photocathode material for absorbing of large part of visible spectrum, precise controllability, and its abundancy, however, cannot durably operate in aqueous electrolyte because of surface oxidation. Thus, passivation of silicon surface is essential for the durable operation of the silicon photocathode in neutral water. My transparent carbon catalysts on silicon acts as a passivation layer against surface oxidation without attenuating the photon incidence. Controlling a surface structure of the light-absorbing photoelectrode and the deposition with the co-catalyst also represent a significant step toward enhancing the hydrogen production. This transparent catalysts with a capability of passivation effect can result in a paradigm shift for catalytic materials research and discovery for energy application.

The significant meaning of this research is the construction of transparent catalyst that only consists of carbon materials and the possibility of extension to a variety of biomimetic HER catalysts with excellent activity. Scientifically,

it provides an importance to understand the interactions at the solid/solution interface to exploit its amazing potential. The conducted research would advance my understanding how the carbon-based catalysts can alter the band structure of the electrode and its photo-electrochemical behaviors. This understanding would allow development of catalysts with unique and highly tunable properties with broad energy applications as well as the efficient solar-driven hydrogen production.

Publication List

Papers:

1. **Uk Sim**, Junsang Moon, Junghyun An, Heonjin Ha, Kyoungsuk Jin, Hyo-Yong Ahn, and Ki Tae Nam, "Biomimetic Iron Sulfide/Carbon-based Catalyst for Efficient and Stable H_2 Production in Acid, Neutral, and Base condition", *Submitted*
2. **Uk Sim**†, Joonhee Moon†, Junghyun An, Hyo-Yong Ahn, Dong Jin Kim, Heonjin Ha, Jin Hyoun Kang, Byung Hee Hong and Ki Tae Nam, "Double-layer Graphene Outperforming Monolayer as Catalyst on Silicon Photocathode for Hydrogen Production", *Submitted*
3. **Uk Sim**†, Joonhee Moon†, Hyo-Yong Ahn, Dong Jin Kim, Junghyun An, Heonjin Ha, Chelho Jeon, Ki Tae Nam, and Byung Hee Hong, "Hierarchical Branching Carbon Nanowire Catalyzed by Copper-vapor on Silicon Nanowire for Hydrogen Evolution Reaction", *Submitted*
4. **Uk Sim**†, Vinayak S. Kale†, Heonjin Ha, Ki Tae Nam, and Taeghwan Hyeon, "Metal-free S-doped Graphitic Carbon Nitride Nanostructures as an Excellent Oxygen Evolution Electrocatalyst Inspired from Naturally Occurring Geodes", *Submitted*
5. **Uk Sim**†, Joonhee Moon†, Junghyun An, Jin Hyoun Kang, Sung Eun Jerng, Junsang Moon, Sung-Pyo Cho, Byung Hee Hong and Ki Tae Nam, "N-doped Graphene Quantum Sheets on Silicon Nanowire Photocathode for Hydrogen Production", *Energy & Environmental Science* **8**, 1329 (2015)
6. **Uk Sim**, Kyoungsuk Jin, Seungtaeg Oh, Donghyuk Jeong, Junsang Moon, Jihun Oh and Ki Tae Nam, "Hydrogen Production by Electrolysis and Photoelectrochemical System", *Handbook of Clean Energy System (Jinyue Yan (Eds.)*, Wiley-Blackwell, NJ, USA **5**, 1 (2015)
7. **Uk Sim**†, Tae-Youl Yang†, Joonhee Moon†, Junghyun An, Jinyeon

Hwang, Jung-Hye Seo, Jouhahn Lee, Kye Yeop Kim, Joohee Lee, Seungwu Han, Byung Hee Hong, and Ki Tae Nam, "N-doped Monolayer Graphene Catalyst on Silicon Photocathode for Hydrogen Production", *Energy & Environmental Science* **6**, 3658 (2013) → **This week's HOT articles from Royal Society of Chemistry publishing**

8. **Uk Sim**, Hui-Yun Jeong, Tae-Youl Yang and Ki Tae Nam, "Nanostructural dependence of hydrogen production in silicon photocathode", *Journal of Materials Chemistry A* **1**, 5414 (2013)
9. Joonhee Moon†, Junghyun An†, **Uk Sim**, Sung-Pyo Cho, Jin Hyoun Kang, Chul Chung, Jung-Hye Seo, Jouhahn Lee, Ki Tae Nam, and Byung Hee Hong "One-Step Synthehsis of N-doped Graphene Quantum Sheets from Monolayer Graphene by Nitrogen Plasma", *Advanced Materials* **26**, 3501 (2014)
10. Ki Dong Yang, Yoonhoo Ha, **Uk Sim**, Junghyun An, Chan Woo Lee, Kyoungsuk Jin, Younghye Kim, Jimin Park, Jung Sug Hong, Jun Ho Lee, Hye-Eun Lee, Hui-Yun Jeong, Hyungjun Kim and Ki Tae Nam, "Graphene Quantum Sheet Catalyzed Silicon Photocathode for Selective CO_2 Conversion to CO", *Advanced Functional Materials*, (2015) Article first published online 2 Dec 2015.
11. Kyoungsuk Jin, Arim Chu, Jimin Park, Donghyuk Jeong, Sung Eun Jerng, **Uk Sim**, Hui-Yun Jeong, Chan Woo Lee, Yong-Sun Park, Ki Dong Yang, Gajendra Pradhan, Donghun Kim, Nark-Eon Sung, Sun Hee Kim, and Ki Tae Nam, "Partially Oxidized Sub-10 nm MnO Nanocrystals with High Activity for Water Oxidation Catalysis", *Scientific Reports* **5**:10279 (2015)
12. Kyoungsuk Jin, Jimin Park, Joohee Lee, Ki Dong Yang, Gajendra Kumar Pradhan, **Uk Sim**, Donghyuk Jeong, Hae Lin Jang, Sangbaek Park, Donghun Kim, Nark-Eon Sung, Sun Hee Kim, Seungwu Han, Ki Tae Nam "Hydrated Manganese (II) Phosphate ($Mn_3(PO_4)_2$-$3H_2O$) as a

Water Oxidation Catalyst", *Journal of the American Chemical Society* **136**, 7435 (2014)

13. Tae-Youl Yang, Ho-Young Kang, Kyoungsuk Jin, Sangbaek Park, Ji-Hoon Lee, **Uk Sim**, Hui-Yun Jeong, Young-Chang Joo, and Ki Tae Nam, "Iron Oxide Photoanode with Hierarchical Nanostructure for Efficient Water Oxidation", *Journal of Material Chemistry A* **2**, 2297 (2013)
14. Tae-Youl Yang, Ho-Young Kang, **Uk Sim**, Young-Joo Lee, Ji-Hoon Lee, Byungjin Koo, Ki Tae Nam and Young-Chang Joo, "A New Hematite Photoanode Doping Strategy for Solar Water Splitting: Oxygen Vacancy Generation", *Physical Chemistry Chemical Physics* **15**, 2117 (2013)
15. Se Won Seo, Sangbaek Park, Hui-Yun Jeong, Sang Hyeon Kim, **Uk Sim**, Chan Woo Lee, Ki Tae Nam and Kug Sun Hong, "Enhanced Performance of $NaTaO_3$ using Molecular Co-catalyst $[Mo_3S_4]^{4+}$ for Water Splitting into H_2 and O_2", *Chemical Communication* **48**, 10452 (2012)
16. Jungsub Kim, Changjae Yang, **Uk Sim**, Gun-Do Lee, Jinsub Park, Youngsoo Lee, and Euijoon Yoon, "Growth Mechanism of Highly Uniform InAs/GaAs Quantum Dot with Periodic Arsine Interruption by Metalorganic Chemical Vapor Deposition", *Journal of Applied Physics* **110**, 044302 (2011)
17. Changjae Yang, Jungsub Kim, **Uk Sim**, Jaeyel Lee, Won Jun Choi, and Euijoon Yoon, "Competitive Growth Mechanisms of InAs Quantum Dots on $In_xGa_{1-x}As$ Layer during Post Growth Interruption", *Thin Solid Films*, **518**, 6361 (2010)
18. Jungsub Kim, Changjae Yang, **Uk Sim**, and Euijoon Yoon, "Enhancement of Optical Properties of InAs Quantum Dots Grown by using Periodic Arsine Interruption", *Thin Solid Films*, **517**, 3963 (2009)

19. Jungsub Kim, Changjae Yang, **Uk Sim**, Euijoon Yoon, Youngsoo Lee, and Won Jun Choi, "Effect of the Well Layer on the Emission Wavelength of InAs/InGaAs Dot-in a-Well Structure", *Journal of the Korean Physical Society*, **52**, S34 (2008)

Patent:

1. **Uk Sim**, Joonhee Moon, Junghyun An, Ki Tae Nam, and Byung Hee Hong, "N-doped Graphene Quantum Sheets Catalyst for Hydrogen Evolution Reaction", (No. 1020150143133 (2015.12.23))

Presentations:

1. **Uk Sim**, Junghyun An, Sungsoo Kim, and Ki Tae Nam, "Enzyme-mimetic Carbon-Based Catalyst for Hydrogen Production", 2015 Materials Research Society Fall Meeting, 2015.11.29~12.04, Boston, USA

2. Ki Dong Yang, **Uk Sim**, Junghyun An, Chan Woo Lee, Kyoungsuk Jin, Younghye Kim, Kimin Park, Jung Sug Hong, Jun Ho Lee, Hye-Eun Lee, Hui-Yun Jeong, and Ki Tae Nam, "Highly Selective Photoelectrochemical Reduction of CO_2 to CO with N-Doped Graphene Quantum Sheets on Silicon Nanowire", 2015 Materials Research Society Fall Meeting, 2015.11.29~12.04, Boston, USA

3. Vinayak S Kale, **Uk Sim**, Ki Tae Nam, and Taeghwan Hyeon, "Electrocatalytic Applications of Heteroatom-Doped g-C_3N_4 Nanostructures", 2015 Materials Research Society Fall Meeting, 2015.11.29~12.04, Boston, USA

4. **Uk Sim** and Ki Tae Nam, "Bioinspired Carbon based Catalyst for Hydrogen Evolution Reaction", The 114th Fall Meeting in Korea Chemical Society 2014.10.15~2014.10.17, Gwangju, Korea

5. **Uk Sim**, Joonhee Moon, Junghyun An, Byung Hee Hong, and Ki Tae Nam, "Nitrogen doped Monolayer Graphene Catalyst on Silicon Photoelectrochemical Cell for Highly Efficient Hydrogen Production", 2014 15th Korea-Japan Students' Symposium: Properties and Applications of Next Generation Energy Materials, 2014.11.11, Seoul, Korea

6. Junghyun An, Joonhee Moon, **Uk Sim**, Sung-Pyo Cho, Chul Chung, Byung Hee Hong, and Ki Tae Nam, "Nitrogen plasma-assisted synthesis of N-doped Graphene quantum dots form monolayer

graphene", 2014 15th Korea-Japan Students' Symposium: Properties and Applications of Next Generation Energy Materials, 2014.11.11, Seoul, Korea

7. Joonheee Moon, Junghyun An, Sung-Pyo Cho, Chul Chung, **Uk Sim**, Jouhahn Lee, Ki Tae Nam, Byung Hee Hong, "One-Step Synthesis of N-Doped Graphene Quantum Dots from Monolayer Graphene", 2014 Materials Research Society Spring Meeting, 2014.04.23, San Francisco, USA

8. **Uk Sim**, Tae-Youl Yang, Joonhee Moon, Jung Hyun Ahn, Jinyeon Hwang, Jung-Hye Seo, Jouhahn Lee, Kye Yeop Kim, Joohee Lee, Seungwu Han, Byung Hee Hong, and Ki Tae Nam, "Graphene Catalyst on Silicon Photocathode for Hydrogen Production", 2013 Materials Research Society Fall Meeting, 2013.12.01~06, Boston, USA

9. Kyoungsuk Jin, Jimin Park, Hae Lin Jang, Joohee Lee, Ki Dong Yang, Nam Hee Kim, Donghun Kim, **Uk Sim**, Seungwu Han, Sun Hee Kim, Ki Tae Nam, "New Manganese Phosphate Hydrate Crystal as Water Oxidation Catalyst", 2013 Materials Research Society Fall Meeting, 2013.12.01~06, Boston, USA

10. Tae-Youl Yang, Ho-Young Kang, Kyoungsuk Jin, Ji-Hoon Lee, **Uk Sim**, Hui-Yun Jeong, Ki Tae Nam and Young-Chang Joo, "All-iron oxide based hierarchical photoanode for efficient solar water oxidation", Electrochemical Society 224th meeting, 2013.10.27~ 11.01 San Francisco, USA

11. Junghyun An, Joonhee Moon, **Uk Sim**, Sung-pyo Cho, Chul Chung, Byung Hee Hong and Ki Tae Nam, "Preparation and Characterization of Nitrogen-doped Graphene Quantum Dot via Nitrogen Plasma

Treatment", 2013 Korea Ceramic Society Fall Meeting, 2013.10.16~18, Jeju, Korea

12. Sung Eun Jerng, **Uk Sim**, and Ki Tae Nam, "Visible Light Driven Photoelectrochemical Cell for Water Splitting Using a Hydrophobic Ruthenium Polypyridine Dye", The 3rd Fall Meeting in Sensor & Energy, 2013.06.20, Korea

13. **Uk Sim**, Jungsub Kim, Changjae Yang, Jaeyel Lee, and Euijoon Yoon, "The growth of InAs quantum dots with post-growth antimony exposure by metal organic chemical vapor deposition and their optical properties", The 3rd Seoul National University-National Taiwan University Student Workshop, 2008. 12.15~16, Seoul, Korea

14. Jungsub Kim, **Uk Sim**, Changjae Yang, Jaeyel Lee and Euijoon Yoon, "The effect of Sb surfactant during the post growth interruption on InAs QD growth by metal organic chemical vapor deposition", The IEEE Nanotechnology Materials and Devices Conference 2008, 10. 20~22, Kyoto, Japan

15. **Uk Sim**, Jungsub Kim, Changjae Yang, Jaeyel Lee and Euijoon Yoon, "The study of bimodal phenomena of InAs quantum dots through post-growth antimony exposure by metalorganic chemical vapor deposition", The IEEE Nanotechnology Materials and Devices Conference 2008, 10. 20~22, Kyoto, Japan

16. Jungsub Kim, Changjae Yang, **Uk Sim** and Euijoon Yoon, "The growth of InAs quantum dots grown by the periodic arsine interruption", The 1st International Conference on Microelectronics and Plasma Technology, 2008. 08. 18~20, Jeju, Korea

17. **Uk Sim**, Jungsub Kim, Changjae Yang, and Euijoon Yoon, "The antimony surfactant mediated growth of InAs quantum dots by

metalorganic chemical vapor deposition", The 1st International Conference on Microelectronics and Plasma Technology, 2008. 08. 18~20, Jeju, Korea

18. Jungsub Kim, Changjae Yang, **Uk Sim**, and Euijoon Yoon, "The growth of InAs/InGaAs dot-in-a-well structures with periodic arsine interruption by metal organic chemical vapor deposition", The 5th International Conference on Semiconductor Quantum Dots, 2008. 05. 11~16, Gyeongju, Korea

19. **Uk Sim**, Jungsub Kim, Changjae Yang, and Euijoon Yoon, "The effect of post-growth antimony exposure on the formation of InAs quantum dots by metal-organic chemical vapor deposition", The 5th International Conference on Semiconductor Quantum Dots, 2008. 05. 11~16, Gyeongju, Korea

20. Changjae Yang, Jungsub Kim, **Uk Sim**, and Euijoon Yoon, "Effects of strained buffer layer on growth of InAs quantum dots with post growth interruption", The 5th International Conference on Semiconductor Quantum Dots, 2008. 05. 11~16, Gyeongju, Korea

21. Changjae Yang, Jungsub Kim, **Uk Sim**, and Euijoon Yoon, "The influence of In content in InGaAs strain buffer layer to the InAs quqntum dot growth by metal organic chemical vapor deposition", The 5th International Conference on Advanced Materials and Devices, 2007.12.12~14, Jeju, Korea

22. Jungsub Kim, Changjae Yang, **Uk Sim**, and Euijoon Yoon, "The growth of InAs/InGaAs dot-in-a-well structures with periodic arsine interruption by metal organic chemical vapor deposition", The 5th International Conference on Advanced Materials and Devices, 2007.12.12~14, Jeju, Korea

23. Changjae Yang, Jungsub Kim, **Uk Sim**, and Euijoon Yoon, "Effect of the well layer on the emission wavelength of InAs QDs in dot-in-a-well structure", SNU (Seoul National Univ.)-NTU (National Taiwan Univ.) Student Workshop, 2007.11.20. National Taiwan Univ., Taiwan

24. Jungsub Kim, Changjae Yang, **Uk Sim**, and Euijoon Yoon, "The Growth of InAs/GaAs Quantum Dot Structure with Periodic Arsine Interruption by Metal Organic Chemical Vapor Deposition", SNU (Seoul National Univ.)-NTU (National Taiwan Univ.) Student Workshop, 2007.11.20. National Taiwan Univ., Taiwan

25. Changjae Yang, Jungsub Kim, **Uk Sim**, Youngsoo Lee and Euijoon Yoon, "Effects on surface modulation by periodic AsH_3 interruption(PAI) in the InAs/InGaAs/GaAs quantum dot growth", The 34th International Symposium on Compound Semiconductors (ISCS 2007), 2007.10.15~18, Kyoto, Japan

26. J. Kim, C. J. Yang, **U. Sim**, Y. S. Lee and E. Yoon, "Suppression of large island formation in self-assembled InAs/GaAs quantum dot structure with periodic arsine interruption method", 2007 The Korean Association of Crystal Growth (KACG), 2007.06.01, Dongshin University, Naju, Korea

27. J. Kim, C.J. Yang, P. Moon, **U. Sim** and E. Yoon, "Suppression of large island formation in InAs QD structure with periodic AsH_3 interruption method", The 1st International Conference on Nano-manufacturing and Directed Self-Assembly processes, 2007.06.27~29, Kookmin University, Korea

28. C. J. Yang, J. Kim, **U. Sim** and E. Yoon, "Homogeneous InAs/GaAs Quantum Dots growth wirh Periodic AsH_3 interruption", The 4th International Workshop on Nanoscale Semiconductor Devices, 2007.

04. 05~06, Jeju, Korea

29. **Uk Sim**, Jungsub Kim, Changjae Yang, Jaeyel Lee and Euijoon Yoon, "The effect of the antimony surfactant during the post growth interruption on InAs quantum dots grown by metal-organic chemical vapor deposition", The 16th Korean Conference on Semiconductors, 2009.02.18~20, Jeju, Korea

30. **Uk Sim**, Jungsub Kim, Changjae Yang, and Euijoon Yoon, "Growth mechanism of InAs/GaAs quantum dots on GaAs(001) by metal organic chemical vapor deposition with periodic AsH_3 interruption", The 33rd Annual Conference of the Korean Vacuum Society, 2007.08.15~17, Jeju, Korea

31. Changjae Yang, Jungsub Kim, **Uk Sim**, and Euijoon Yoon, "Surface modulation by periodic AsH_3 interruption(PAI) in the InAs/InGaAs/GaAs quantum dot growth", The 33rd Annual Conference of the Korean Vacuum Society, 2007.08.15~17, Jeju, Korea

32. Jungsub Kim, Changjae Yang, **Uk Sim**, and Euijoon Yoon, "Optical properties of InAs/InGaAs dot-in-a-well structure grown by periodic arsine interruption method", The 33rd Annual Conference of the Korean Vacuum Society, 2007.08.15~17, Jeju, Korea

초 록

전 세계적인 에너지 소비량의 급증으로 인하여 신 재생 에너지의 필요성은 더욱더 중요한 이슈로 자리매김하고 있다. 현재 에너지원은 주로 화석연료를 사용하는데, 화석연료의 고갈과 이산화탄소 배출로 인한 환경오염에 대한 우려로 인하여 자연친화적인 신재생에너지에 대한 갈망은 증가하고 있다. 이러한 이유로 최근 수소에너지가 주목을 받고 있다. 수소에너지는 반응 생성물이 물과 열이며 이산화 탄소 배출이 없어 친환경적이다. 현재 전체 수소 에너지의 약 96%는 기체 개질(gas reforming)을 통해 얻어지고 4% 정도가 물 전기분해 또는 광전기화학적 물분해를 통해 얻어지고 있다. 그러나 기체 개질은 수소 에너지를 생산하는 과정에서 비친환경 물질인 이산화탄소를 부산물을 생성해 낼 뿐 아니라, 고온 고압과 같은 어려운 조건에서 반응이 진행되어 위험성을 지니고 있다. 이와는 달리, 물 전기 분해 또는 광전기화학적 물분해는 수소를 생산하는 과정에서 오직 산소만을 부산물로 만들어내고 상온에서도 반응이 가능하기 때문에 최근 들어 주목을 받고 있는 추세이다. 따라서 저렴한 가격으로 수소 에너지를 생산하기 위해 물 전기분해 관련 연구의 필요성이 대두되고 있다. 하지만 현재 수소 생산 비용은 상용화된 기체 개질을 통한 방법보다는 여전히 비싸므로 이를 낮추려는 노력이 중요하다. 지금까지 개발된 효율 높은 촉매들은 귀금속 기반의 촉매들로서 가격 경쟁력 확보가 시급하다. 따라서, 이러한 전기화학적 반응을 이용한 수소 생산에 있어서 효율적인 촉매의 개발은 매우 중요하며, 시급히 해결해 나가야 할 문제이다.

자연계의 생체 촉매 또는 효소들은 이러한 문제를 해결해 나가는데 있어서 중요한 교훈을 제공해 주고 있다. 예를 들어, 자연계에 존재하는 수소화효소(hydrogenase) 는 박테리아, 고생물균, 진핵생물에 존재하는 생체촉매로써, 중성 조건에서 시간당 9000 moles의 수소를 발생시킬 정도로 수소발생능력이 매우 우수하다. 지금까지 이 같은 hydrogenase의 높은 성능을 모방하려는 연구들이 진행되어 왔는데 그 흐름은 (1) hydrogenase를 직접 추출하여 전극에 붙여 활용하려는 시도, (2) 구조내에 존재하는 metal active site 의 구조를 분석하여, 비슷한 구조로 합성을 진행하려는 시도 및 (3) hydrogenase를 구성하는 주성분인 Fe, Ni, 또는 S 를 이용하여 무기 촉매를 합성하려는 시도로 나누어 질 수 있다. 하지만, (1) 의 경우, 효소를 그대로 추출하여 이용하면, 수소 발생 성능이 매우 낮고, 안정성이 매우 취약한 단점을 가지며, (2) 의 연구들 또한, 합성이 매우 어렵고, hydrogenase의 구조를 최대한 정확하게 모방하려는 시도에 그쳤을 뿐, 실제 수소 발생 능력과 안정성이 낮으며, 전극에 붙여 활용하기 힘든 단점을 가진다. (3) 의 경우, hydrogenase 를 구성하고 있는 metal active site 의 역할에만 집중, 그 구성성분만을 이용하여 무기 촉매를 합성하려는 시도로 인해, hydrogenase 대비하여 성능을 비교하기에는 아직도 낮은 수준을 가진다. 따라서, metal active site 만을 모방하는 것이 아닌, hydrogenase를 이루고 있는 여러 가지 다른 요소들의 역할들을 전체적으로 조망해보고, 그에 따른 교훈을 활용하여 촉매 합성에 응용하려는 시도가 필요하다고 판단된다. 실제로 hydrogenase 는 proton reduction 반응이 일어나는 장소인 metal active site 이외에도 이를 둘러싸고 있는 functional protein assemblies 들이 metal을 안정화 시키는 리간드 역할 및 반응물과 생성물을 효과적으로 이동시키는 통로 역할을 하며, metal

active site 주위에 존재하는 Fe-S로 구성된 보조 인자 cluster 들이 수소 발생 반응이 일어나는데 필요한 전자를 효과적으로 전달시켜주는 역할을 한다. 즉 metal active site의 주변에 존재하는 supporter의 역할이 반응의 효율과 안정성을 향상시키는데 중요한 역할을 함을 알 수 있다.

이에, 우리는 hydrogenase의 구조의 교훈으로부터, systematic approach를 실시하여 먼저 Fe-S로 구성된 metal active sites를 디자인하고, 성능을 극대화 할 수 있는 플랫폼 역할을 할 수 있는 군을 탐색하여, 두 성분들이 최적의 구성비율을 가지고 분포된 catalyst를 디자인하여 합성하고자 한다. Supporter 탐색의 후보군으로써 기존의 연구들은 reduced graphene oxide 나 carbon nanotube 등의 전도성 높은 탄소 유도체 물질들에 집중하였는데, 이러한 물질들은 단순히 전자 전달을 위한 지지체의 역할에 그치는 연구로써, 촉매로서의 활용능력은 뛰어나지 못할 뿐만 아니라, 물질 특성상 불투명한 특성을 지녀, 광전기화학셀의 조촉매로의 적용은 불가능했다. 또한 정확한 로딩양 조절이 어려워 active site를 체계적으로 튜닝하고 관찰하는데 어려움이 있다. 따라서 본 연구에서는 이러한 탄소 기반 전도체의 역할 뿐 아니라, 촉매의 특성을 동시에 지니는 모델 플랫폼으로 그래핀 레이어를 선정하였다.

가장 단순한 탄소 기반 플랫폼의 형태로 2D monolayer 그래핀의 수소 발생 반응 촉매특성이 있음을 최초로 확인을 하였고, 수소 발생 반응 메커니즘을 분석하였다. 실리콘 광전극에 적용하여, 입사광의 손실 없이 효과적인 투명 조촉매로 작용할 뿐 아니라, 실리콘의 산화를 방지하여 장기안정성에 뛰어난 특성을 보임을 확인하였다. 나아가, 2D 구조에서 복잡한 3D 구조를 탐구하기 위한

중간 단계인 준 3D 구조로써, 층별로 쌓은 멀티레이어 그래핀들을 제작하여, 층별 의존도가 있음을 확인하였고, 전극/촉매/Electrolyte 간의 계면의 charge transfer rate, capacitance 의 변화 및 work function 의 영향을 탐구하였다. 특히, double-layer 그래핀이 물분해 반응에 가장 효과적인 촉매로 작동함을 확인할 수 있었다.

촉매의 수소 발생 반응 사이트를 좀더 체계적으로 조절하기 위해 플라즈마 처리를 도입하게 되었고, 질소 도핑 및 결함 사이트를 조절하여 특성을 비약적으로 향상 시켰으며, 플라즈마 처리 과정에서, 또다른 준-3D 구조인 그래핀 양자 시트를 만들어, 반응 메커니즘 분석 실시 및 평면 광전극에만 적용가능했던 기존의 그래핀 촉매를 다양한 나노구조의 광전극에도 적용할 수 있게 되어, 광전변환 물분해 성능을 비약적으로 향상 시킬 수 있게 되었다.

지금까지 탄소 기반의 그래핀 촉매 연구에서 배운 교훈을 바탕으로, 좀 더 효과적인 촉매를 디자인하기 위해, 그 후보군 중의 하나로써, 자연계에 존재하는 홍합으로부터 분비되는 접착 단백질을 구성하는 polydopamine이라는 물질에 주목하였는데, 이 물질은 접착력에 관여하는 catechol 작용기로 인해 수용액상에서 표면 특성에 관계없이 다양한 표면을 매우 안정하게 형성하며, carbonization 후에는 전도성 또한 매우 뛰어난 특성을 보일 뿐 아니라, metal ion과도 잘 결합하여 다양한 melanin 구조체를 합성할 수 있는 장점을 가진다. 이러한 Biomimetic polydopamine을 기반으로, dopa-HCl과 Fe, S 전구체 소스를 이용하여, 매우 간단한 방법으로 carbon이 둘러싸인 새로운 구조의 Iron Sulfide/Carbon-based Catalyst를 합성하였다. 해당 촉매의 수소 발생 촉매 특성을 살펴 본 결과, 중성에서만 작동할 수 있는 hydrogenase와는 달리 산성, 중성, 염기성 등 모든 pH 범위에서 수소 발생 능력이 매우 뛰어날 뿐

아니라, 안정성도 좋은 것을 확인할 수 있었고, 지금까지 보고된 Fe-S 계열의 촉매들과 비교하여 산성, 중성, 염기성 모두 수소발생 특성이 가장 뛰어남을 확인하였다. 효과적인 성능의 원인을 파악하기 위해, Impedance 분석을 통해 metal active site를 감싸고 있는 carbonized dopamine이 반응에 필요한 electron을 효과적으로 transfer를 할 수 있게 도와주는 것을 확인하였고, pH 의존도 실험을 통해, 해당 촉매의 Proton coupled electron transfer 능력이 매우 뛰어남을 확인할 수 있었을 뿐만 아니라, Electon paramagnetic resonance 분석을 실시하여, Fe valency 의 변화가 물분해 효율 향상에 긍정적인 영향을 미치는 것을 확인할 수 있었다.

결론적으로, 자연계의 생체 촉매의 구조 및 성분을 모방하여, 그 교훈으로부터 뛰어난 특성과 안정성을 가진 비귀금속 탄소기반 수소 발생 반응 촉매 개발을 달성해 낼 수 있었다.

주요어: 광전기화학셀, 탄소, 촉매, 생체모방, 물분해, 수소발생

학 번: 2011-30188